

This work is protected by copyright and other intellectual property rights and duplication or sale of all or part is not permitted, except that material may be duplicated by you for research, private study, criticism/review or educational purposes. Electronic or print copies are for your own personal, non-commercial use and shall not be passed to any other individual. No quotation may be published without proper acknowledgement. For any other use, or to quote extensively from the work, permission must be obtained from the copyright holder/s.

First-principles investigation of
the interaction between pentacene
molecules and monolayer
transition metal dichalcogenides

Edward James Black

Doctor of Philosophy

School of Chemical and Physical Sciences, Keele University

December 2024

Abstract

The search for new materials for photonic applications continues to expand, and one promising route is that of van der Waals heterostructures. Assembled layer by layer from atomically thin materials, there are combinations of materials with promising emergent properties. TMDs are strong candidates for photovoltaic and transistor technologies, and the addition of thin films of organic molecules to MoS₂ has been shown to lead to beneficial exciton dynamics. Here we investigate two-dimensional pentacene/MX₂ (M = Mo, W, X = S, Se) heterostructures in a systematic manner with varying concentration and molecular orientation using *ab initio* methods. Using DFT and hybrid methods to establish baseline parameters, we examine material band structure and resulting heterostructure band alignments.

We analyze the tuning of the electronic structure of our materials due to heterostructure formation in the various concentrations and molecular orientations, which results in changes to the heterojunction type from that predicted by comparison of the materials out of heterostructure.

This research contributes to understanding how organic molecules can modify the electronic structure of TMDs, offering valuable insights for the development of high-performance, flexible photonic devices. Our results highlight the importance of precise control over molecular interactions and band alignment in designing advanced materials for photovoltaic applications.

Preface

Acknowledgements

I would like to express appreciation for those who supported me throughout the period of research and writing. Firstly, I am grateful to my supervisor and principle investigator of this project, Dr. Juliana Morbec, whose expertise, guidance, and patience were invaluable to my progress. I thank the German Research Foundation (DFG, project number 406901005) and Keele University for their financial support, as well as Keele University for providing resources and facilities necessary for conducting the research. Additionally, thanks are warranted to the Cirrus UK National Tier-2 HPC Facility for providing the computational resources used in our calculations. Acknowledgement is in order for those who assisted in the research process: Dr. Juliana Morbec, who besides her supervisory role additionally took an active role in the process of our group's journal publication, Prof. Peter Kratzer, who assisted with the same process and publication.

Special thanks are warranted to my wife, who tried very hard to pretend to be interested in what I was doing for so long, but nevertheless was tremendously and unwaveringly supportive and encouraging. Special thanks as well as to my parents and brother, whose support eased the challenges of this project.

A note on nomenclature and symbols

Throughout this work there are some variables that use the same character representation. It is always clear from context what is meant in the cases of standard representations e.g. the imaginary unit, i , where i is also used as a counting index in other parts of the thesis. In cases where it may not be entirely obvious, variables are clearly defined in the nearby prose. Also of note is the use of the term ‘Brillouin zone’. Unless otherwise specified, or clear from context, this refers to the first Brillouin zone. In contexts where a distinction is required, the term ‘first Brillouin zone’ will be used, with ‘Brillouin zone’ being more general.

Font changes are used to represent the types of mathematical objects, with scalars in regular typeset, vectors in bold and matrices or higher rank tensors in sans serif bold. For the case of operators, some are not uniquely identified as such due to their simplicity or ubiquity e.g. the one dimensional position operator, x , is trivial and simply represented as a scalar. For cases where the identification of an object as an operator is more important, we use calligraphic typeset e.g. \mathcal{H} .

So far this overview of nomenclature has all been fairly standard, but there is nomenclature specific to this work. It is related to the heterostructures themselves, and how they are to be discussed in text. The abbreviation PEN/TMD refers to the heterostructures in general, with e.g. PEN/MoS₂ referring to only the heterostructures involving the specified TMD. When discussing pentacene concentrations, they will be referred to as low or high concentration regimes, or by their corresponding underlying substrate dimensions i.e. 7×4 or 6×3 . A subscript on PEN, without being followed by a TMD, denotes the state of its cell considered during calculation, and is without a substrate e.g. PEN_{6×3} denotes pentacene in a cell of size defined by the 6×3 substrate lattice, but without the substrate being present. Similarly, there is use of subscripts denoting the rotation of pentacene upon the substrate, as in PEN_{60°}/WSe₂, which refers to the pentacene-tungsten diselenide heterostructure where pentacene is rotated by 60° with respect to the underlying substrate. If there is no angle given in subscript, it is either a general reference or relates to unrotated (0°) systems. Which will be clear from

context.

Abbreviations, when used, will be defined in text with the first use. Exceptions are experimental techniques, which are often first specifically introduced in comparison tables of literature results. There is nothing particularly exotic, with the abbreviations being:

- Adsorption spectra, AS
- Angle-resolved photoemission spectroscopy, ARPES
- Angle-resolved X-ray photoelectron spectroscopy, ARXPS
- Photoluminescence, PL
- Scanning tunnelling spectroscopy, STS
- X-ray diffraction, XRD
- X-ray adsorption spectroscopy, XAS

Chapters are numerically labelled, starting with the introductory chapter as Chapter 1. Appendices follow the main work, and are labelled alphabetically.

Contents

Preface	ii
Acknowledgements	ii
A note on nomenclature and symbols	iii
1 Introduction	1
1.1 The current literature gap	3
1.2 Project overview and objectives	6
2 Physical theory and background	10
2.1 Quantum treatment of solids	11
2.1.1 Drude-Sommerfeld (free electron) model	11
2.1.2 Bloch's theorem	17
2.1.3 Semiclassical model	23
2.1.4 Self-consistent field methods	29
2.2 Energy bands and band structure	39
2.2.1 The nearly-free electron model	42
2.2.2 Wannier functions	48
2.2.3 Spin-orbit coupling	49
2.3 Semiconductors	51
2.3.1 Doping	55
2.3.2 Inhomogeneous semiconductors	58
2.3.3 Photovoltaics	71
2.4 Nanoscale phenomena	76

2.4.1	Edge effects	76
2.4.2	Confinement	80
2.5	Van der Waals (vdW) forces	82
3	Computational theory	90
3.1	Density functional theory	91
3.1.1	Kohn-Sham DFT	93
3.1.2	Exchange-correlation functionals	110
3.1.3	Van der Waals corrections	115
3.1.4	Hybrid functionals	118
3.2	Pseudopotentials	120
3.2.1	Orthogonalized plane waves	121
3.2.2	Norm-conserving pseudopotentials	123
3.2.3	Projector augmented wave method	127
3.3	Numerical algorithms and calculation overview	131
3.3.1	Numerical algorithms and computational techniques	131
3.3.2	Details of calculations	137
3.3.3	Workflow	139
3.3.4	Quantum ESPRESSO parameters	141
4	Determining properties before heterostructure formation	145
4.1	Computational details	148
4.2	Convergence testing	149
4.2.1	MoS ₂	151
4.2.2	MoSe ₂	153
4.2.3	WS ₂	155
4.2.4	WSe ₂	157
4.2.5	Pentacene	159
4.3	Geometry	161
4.3.1	MoS ₂	164

4.3.2	MoSe ₂	165
4.3.3	WS ₂	166
4.3.4	WSe ₂	167
4.3.5	Pentacene	168
4.4	Electronic structure	171
4.4.1	MoS ₂	174
4.4.2	MoSe ₂	178
4.4.3	WS ₂	181
4.4.4	WSe ₂	185
4.4.5	Pentacene	189
4.4.6	Band alignment	195
5	Low concentration pentacene heterostructures	198
5.1	The heterostructures	202
5.2	Electronic properties	208
5.2.1	Density of states	208
5.2.2	Charge transfer and work function	213
6	The effect of molecular concentration and rotation on PEN/TMD heterostructures	219
6.1	Investigating pentacene concentration	221
6.1.1	High concentration pentacene heterostructures: structure	221
6.1.2	High concentration pentacene heterostructures: electronic properties	226
6.1.3	Comparison of pentacene concentrations	233
6.2	Investigating pentacene rotation	246
6.2.1	Low concentration pentacene heterostructures: structure	246
6.2.2	Low concentration pentacene heterostructures: electronic properties	250
6.2.3	High concentration pentacene heterostructures: structure	252
6.2.4	High concentration pentacene heterostructures: electronic properties	255
6.2.5	Comparison of pentacene rotation angles	256

7 Conclusion	269
7.1 Future projects within the materials group and investigations of interest . .	271
A Central equation	273
B Bloch electron velocity	276
C Semiclassical equations of motion	279
D Vanishing current contribution of filled bands	281
E Spin-orbit coupling	283
F Scattering	286
G Derivative discontinuity	291
H Minimizing the Kohn-Sham energy functional	294
I Pentacene’s atomic deviation from the molecular plane	297

Chapter 1

Introduction

The search for effective materials for the construction of photonic devices is an ongoing area of intense research, with varied and diverse sub-fields and applications. Monolayer materials are a promising group of candidates which has a growing dictionary of materials that can be relatively easily produced and combined into heterostructures. Combinations of these materials are proving to demonstrate emergent effects, and given that these layered combinations are bound by the van der Waals (vdW) interaction, layer-by-layer construction is a relatively simple matter. If a given material can be grown as or exfoliated to a monolayer with no or few dangling bonds, physically placing the sample over another is enough for heterostructure formation.

One such group of materials that can be easily exfoliated in such a manner are the transition metal dichalcogenides (TMDs) [1, 2], which are themselves a diverse category of often semiconducting crystals. Group VI dichalcogenides in particular exhibit favorable optical absorption properties [3, 4] that lend themselves to applications such as photovoltaics [5], light-emitting diodes [6], and transistor technologies [7, 8], with variation in band gap energy and band gap depth, while being amenable to exfoliation to monolayer and stable in air [9, 10] and at temperatures appropriate for the applications. We focus here on the transition metals molybdenum and tungsten, and the chalcogens sulfur and selenium, giving us four TMDs: MoS_2 , MoSe_2 , WS_2 and WSe_2 . These are probably the most researched TMDs, with MoS_2 in particular being a popular target of investigation due to its favorable properties for photonics.

Heterostructures comprised of monolayer TMDs are well investigated [11,12], but not all layers of a heterostructure need be monolayer crystals, much less TMDs specifically. An important result from Homan et al. [13] was that the deposition of a thin layer of pentacene, $C_{22}H_{14}$, a polycyclic aromatic hydrocarbon with five benzene rings, on to monolayer MoS_2 produced a heterostructure that exhibited rapid exciton dissociation and slow recombination effects. Hole transfer from the TMD layer to the organic film occurred faster than all hole relaxation mechanisms except for surface defect trapping (a subpicosecond phenomena), but due to the reduced interlayer coupling compared to TMD-TMD heterostructures excitons remained dissociated for much longer than in TMD-TMD structures. This is a favorable property for photovoltaic devices in particular, in combination with the heterostructure band gap of 1.1 eV, setting a relatively high theoretical limit on the open-circuit voltage of any resultant device. Other organic compounds have been investigated in heterostructure with TMDs, showing tuning of the TMD's electronic structure, as well as exhibition of potentially complimentary properties for photonic applications [14,15].

Upon the background of the increasing monolayer and heterostructure research space, this motivated our research group to investigate the adsorption of organic molecules on monolayer TMDs. This particular flavor of heterostructure has potential in the realm of lightweight, flexible photovoltaic devices as both materials having readily controllable thickness and possess complementary properties to each other for such an application. In this project we probe the structural and electronic properties of heterostructures of pentacene adsorbed on to monolayers of MoS_2 , $MoSe_2$, WS_2 and WSe_2 , as well as the changes to the same due to variation in molecular concentration and orientation compared to the TMD substrate. Competing effects that lead to changes in these properties are also decoupled and considered.

1.1 The current literature gap

The TMDs investigated in this project are already well known in the literature. They form hexagonal crystals of MX_2 ($\text{M} = \text{Mo}, \text{W}$ and $\text{X} = \text{S}, \text{Se}$) comprising layers of transition metal atoms covalently bonded to six chalcogens each in a trigonal prism (see Figure 1.1). There are two forms in monolayer, 1T and 1H [16]. We consider only the 1H form here, as the 1T form is metastable and metallic [17–19].

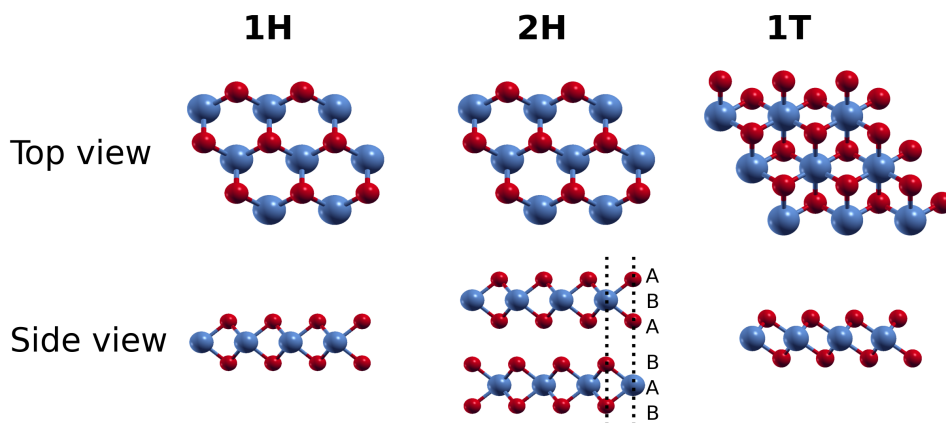


Figure 1.1: The structure of TMD monolayers and their forms. Blue atoms are transition metals, and red atoms are chalcogens. The 2H form is defined by the stacking relationship of a TMD bilayer, where each layer is a 1H monolayer with alternating orientation.

All four of the considered monolayer TMDs have band gap energies between 1 and 2 eV, in the near infrared to visible range. They exhibit an indirect Γ -Q band gap in bulk, which transitions to a direct \mathbf{K} - \mathbf{K} band gap in monolayer [20]. Experimentally, MoS_2 has been shown to have a monolayer band gap (E_G) of between 1.8 and 1.9 eV [21–24], MoSe_2 between 1.5 and 1.7 eV [25, 26], WS_2 approximately 2 eV [27], and WSe_2 approximately 1.7 eV [28].

Carrier mobility is a concern for photonic devices, where in the case of photovoltaics, a larger carrier mobility allows for greater excitonic spatial dissociation within a given time, and so provides a lower chance of recombination. Bulk TMDs exhibit good carrier mobility, but monolayer TMDs have reduced carrier mobility, even when their structure reflects that of the bulk sample [10]. Nevertheless, carrier mobilities have been measured as high as $\mu = 80 \text{ cm}^2\text{V}^{-1}\text{s}^{-1}$ at room temperature in monolayer MoS_2 [29], thin MoSe_2 at approximately $200 \text{ cm}^2\text{V}^{-1}\text{s}^{-1}$ at room temperature for electrons and $150 \text{ cm}^2\text{V}^{-1}\text{s}^{-1}$

for holes [30], approximately $50 \text{ cm}^2\text{V}^{-1}\text{s}^{-1}$ at room temperature and as high as $140 \text{ cm}^2\text{V}^{-1}\text{s}^{-1}$ at low ($< 100 \text{ K}$) temperatures for monolayer WS_2 [31], and a lower $7 \text{ cm}^2\text{V}^{-1}\text{s}^{-1}$ for monolayer WSe_2 at room temperature for electrons, although hole mobility was higher at $90 \text{ cm}^2\text{V}^{-1}\text{s}^{-1}$ [32]. These values are at least an order of magnitude larger than that for pentacene, our organic molecule of interest. Pentacene's carrier mobility has been experimentally determined as $0.26 \text{ cm}^2\text{V}^{-1}\text{s}^{-1}$ [33]. There are large ranges associated with experimental determination of carrier mobility, as it is highly dependent on sample quality. However, it is clear that pentacene has a much lower carrier mobility than do monolayer TMDs; examples of high (relative to other values reported for pentacene) carrier mobility in thin-film pentacene device are approximately $0.6 \text{ cm}^2\text{V}^{-1}\text{s}^{-1}$ [34] and $0.6 \text{ cm}^2\text{V}^{-1}\text{s}^{-1}$ [35], although measured values less than $10^{-3} \text{ cm}^2\text{V}^{-1}\text{s}^{-1}$ are not unknown for similar devices [36].

By combining the organic molecule pentacene with monolayer TMDs into a van der Waals heterostructure, we hope that advantage can be taken of the good carrier mobility of TMDs and favorable properties inherent to thin devices (lightweight, flexible etc), as well as enhance the optical absorption efficiency of the resultant heterostructure compared to the TMD alone, due to the comparatively higher absorption coefficient of organic molecules [15]. In order to do so, however, we must first assure ourselves of the band alignment between materials of any resultant heterostructure. This was one of the primary goals of this project. It has been shown previously that pentacene forms a Type-II heterojunction with monolayer MoS_2 [13,37], as does pentacene with WSe_2 [38]. WS_2 forms a Type-II heterojunction with the similar organic molecule, tetracene [39]. Type-II band alignment is required for the p-n junction of photovoltaics, although there are other applications for band alignments other than the staggered gap. A Type-I alignment, which has been shown for the case of pentacene/ MoSe_2 has been reported, although not in a manner particularly similar to the structures we investigated here; there was a third layer of graphene oxide on the opposite pentacene surface to that in contact with MoSe_2 [40].

Despite the TMDs and pentacene being well investigated, the specific heterostructures that we have targeted are not. There is limited theoretical literature on favorable

adsorption sites of molecular pentacene on monolayer TMDs, and the effect on molecular concentration and molecular orientation on the structure and electronic properties of resultant heterostructures is non-existent. Existing literature focuses on heterostructures with MoS₂, and is primarily concerned with thin films of pentacene, rather than two-dimensional structures [41, 42]. As such, there is an identified literature gap for a systematic study of the interaction between molecular pentacene and monolayer TMD substrates. The band alignment of molecular pentacene with TMDs and its variation with concentration is an important metric for photonic devices, and the manner in which pentacene tends to adsorb on to an underlying TMD substrate may be important for interface engineering concerns. Additionally, how the electronic structure of the materials and resultant heterostructures is changed by competing effects due to adsorption, variational concentration, and molecular rotation with respect to the substrate are potential subjects of interest for device design and tuning.

1.2 Project overview and objectives

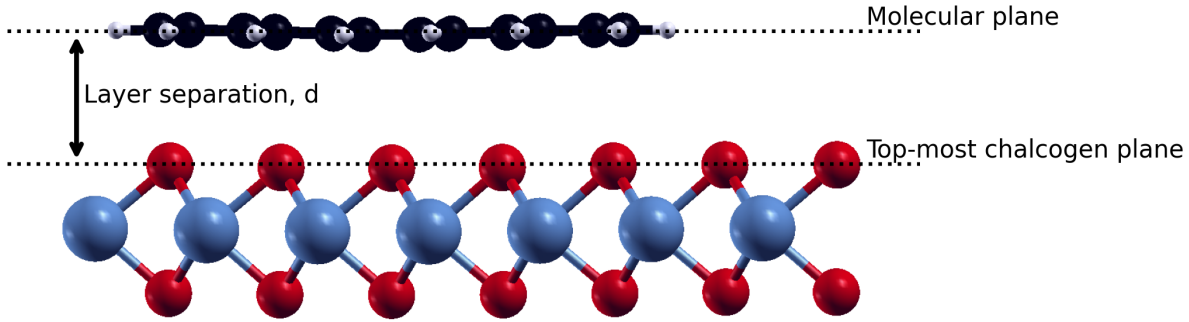


Figure 1.2: Side view of pentacene adsorbed on a 7×4 supercell of TMD. The molecular plane and top-most chalcogen plane are marked and labelled. Layer separation is also labelled, but is defined as the difference in z-coordinate of the center of mass of pentacene and the average position of chalcogens in the top-most chalcogen plane, not the difference between the molecular plane and top-most chalcogen plane (although these values will be very similar).

The aim of this project is to work towards filling the literature gap discussed in Section 1.1 by investigating the preferred adsorption sites of pentacene on to each of the four TMD monolayers, in the manner of Figure 1.2, and probing the structural and electronic properties of these heterostructures. We will demonstrate in which manner pentacene tends to adsorb on to the monolayers and how molecular concentration affects this, and through what mechanisms. Given the favorably adsorbed heterostructures, we will show to what degree the electronic properties of the TMDs and pentacene molecules are modulated by adsorption, examine the mechanisms through which this modulation occurs, and discuss the overall properties of the resultant heterostructures.

The first stage of the project, found in the first project chapter of the thesis (Chapter 4), was concerned with determining computational parameters that were needed going forward, baseline properties of the TMD monolayers and pentacene molecules when isolated from each other, and an analysis of likely band alignments between materials before their electronic properties are modulated through interacting with each other. This was performed using *ab initio* methods within density functional theory (DFT), using the Perdew-Burke-Ernzerhof (PBE) exchange correlation functional [43] (a generalized

gradient approximation (GGA) functional), and the projector-augmented wave (PAW) pseudopotential method [44]. We used Monkhorst-Pack [45] \mathbf{k} -point meshes for our sampling grids. Our calculations were performed using the Quantum ESPRESSO suite [46,47], a popular open-source plane wave pseudopotential package for electronic structure calculations.

The computational methods used in this project were selected based on characteristics of cost and accuracy. We did not wish to use an empirical functional in order to satisfy as many theoretical exact conditions as possible. Additionally, as we investigated structures which had yet to be studied to a significant degree, and that are combinations of organic molecules and TMDs, errors in non-empirical functionals would be likely to be systematic (e.g. underbinding in the local density approximation, or underestimation of the band gap with DFT in general), and so somewhat predictable in nature, if not necessarily in magnitude. Using an empirical functional that was designed for use on organic molecule, for example, could fail on predictions relating to the TMDs within the structure.

The local density approximation compares unfavorably to GGA functionals for atoms with highly-localized electrons, such as those found in our transition metal d-orbitals, as the electronic density is highly non-uniform. Additionally, LDA functionals tend to underestimate band gaps to a greater degree than do GGA functionals [48]. Therefore, we chose from GGA functionals; hybrid functionals were deemed to be too computationally expensive for our large heterostructure systems. Reviews of the performance of various functionals fairly consistently report that popular GGA functionals are similar in accuracy to each other, with small advantages in specific systems or for specific parameters [49,50]. One in particular that consistently performs well, and satisfies our previously mentioned concerns, is the PBE functional [43], which is the functional we proceeded with for the majority of our calculations.

As we are dealing with vdW heterostructures, it is expected that the vdW interaction plays a significant role in their structure and binding. The van der Waals correction method of Grimme's D3 [51] is a very effective choice for two-dimensional heterostructures, as well as molecules [52].

The next stage of the project, described in Chapter 5, was to investigate the preferred adsorption sites of pentacene on to the TMD monolayers at a fixed concentration. This concentration was controlled through the number of molecular units of TMD substrate within a single supercell, containing one pentacene molecule; a larger underlying substrate sheet results in a lower molecular concentration. We selected a supercell consisting of 7 TMD molecular units by 4 TMD molecular units, referred to as a 7×4 cell. We must of course modulate the length of the sides of this substrate monolayer in integer steps, and chose the side length ratio based on the shape of pentacene. A larger 8×5 supercell would be too computationally expensive, and the 7×4 cell provided good separation between pentacene molecules across periodic boundary conditions already. Using DFT, we calculated the total energy of heterostructures and compared this to that of isolated materials to determine the adsorption energy of pentacene in a number of adsorption sites. This allowed a direct comparison of favorability between adsorption sites, where we then probed the electronic structure of the favorably adsorbed heterostructures with density of states calculations. Additionally, differential charge density was calculated.

Following this, we performed the same investigation on higher concentration pentacene (by using a smaller supercell) and compared the two, allowing discussion of the effect of concentration on the calculated properties (see Chapter 6). The supercell was defined by an underlying substrate of dimensions 6×3 molecular units, shrinking the distance in both x- and y-directions between pentacene by one unit each. A greater reduction would result in almost overlapping pentacene molecules. We also looked at pentacene in the favorable adsorption sites across both concentrations, but rotated around its centre of mass within the plane of the underlying substrate. This allowed for a comparative analysis of the effect of rotation of pentacene.

Finally, we returned to the materials out of heterostructure for a more computationally intensive, but more accurate, investigation. We did this using a hybrid functional, which was the Heyd-Scuseria-Ernzerhof (HSE) functional [53]. This choice was due to its consistently strong performance in predicting structural and electronic properties of semiconductors [54]. It would not have been computationally feasible to deploy such a

functional on to the heterostructures, being such large supercells. While we performed this level of analysis near the end of the project chronologically, it is reported in Chapter 4 as it pertains to the isolated systems and is more useful as a side-by-side comparison at that point of this work.

The thesis is laid out thusly: an introductory chapter, which is the present chapter, followed by an overview of the background theory required for performing this research (Chapters 2 and 3, where there is a somewhat nebulous division between physical and computational theory), the chapters directly describing the methods and results of the project (Chapters 4-6), and wrapping up with a summary chapter at the end (Chapter 7). There is additionally an Appendix associated with this work, found at the end of the thesis.

Chapter 2

Physical theory and background

To understand the behavior of two-dimensional van der Waals heterostructures and their constituent materials (here organic molecules and transition metal dichalcogenides) as photovoltaic and optoelectronic candidates, we must first understand the underlying theory of solids, primarily semiconductors. This chapter discusses the relevant quantum theory of solids (Section 2.1), and the band theory of semiconductors and the photovoltaic effect (Sections 2.2 and 2.3). A description of phenomena that arise in these materials due to their small size and quantum nature is in section 2.4, followed by a discussion of the theory of van der Waals forces that are so important for the formation of the heterostructures in this project (section 2.5). Background information on the properties of organic molecules and transition metal dichalcogenides, and the way in which their heterostructures exhibit hybrid or emergent properties are discussed later in Chapter 3, as is the theoretical basis for, and the practical use of, the computational methods deployed in this work.

2.1 Quantum treatment of solids

2.1.1 Drude-Sommerfeld (free electron) model

Drude proposed his model of electron behavior in metals in 1900 [55] to explain the excellent electrical and thermal conductivity of metallic materials. Electrons themselves had been recently discovered by Thomson in 1897 [56], and so Drude applied kinetic theory to these new particles, treating them as a gas that moved among heavier and unmoving particles of opposite charge (metallic ions). In this model, electron gas particles move in straight paths until perturbed by collisions with the immobile metal ions. Interactions and collisions with other electrons are ignored, as are non-collisional interactions between electron and ions (such as interactions with fields). These two assumptions are known as the *independent electron approximation* and the *free electron approximation*, respectively. The relaxation time of an electron, τ , is assumed to be independent of the electron's position and velocity, and is defined by an electron's probability of undergoing a collision with an ion in time δt as $\frac{\delta t}{\tau}$. These collisions are then modelled as instantaneous, with immediate effect on the velocity of the electron, and only occur upon collision with ions. In addition, electron-ion collisions are assumed to be the sole process by which electrons attain thermal equilibrium with the background structure, and their post-collision velocity magnitude is determined by the temperature at the position of the collision.

The limitations of the Drude model resulting from classical approximations led Sommerfeld to update it with the Fermi-Dirac distribution in 1927 [57], resulting in quantum mechanical descriptions of electronic behavior in metals. The Sommerfeld theory of metals describes the electrons as a free electron gas, keeping the free electron approximation and the independent electron approximation of the Drude model. The major change to the Drude model is the replacement of the distribution function and a quantum treatment of the free electron gas.

Classical descriptions of electrons in a metal work well enough when the precision to which an electron's position must be described is sufficiently low such that its momentum does not become too imprecise, as described by the Heisenberg indeterminacy

principle [58], $\Delta x \sim \frac{\hbar}{\Delta p}$, where \hbar is the reduced Planck constant, and Δx and Δp are the uncertainties in position and momentum, respectively. With an uncertainty in momentum of an electron in a metal small enough, i.e. smaller than the typical metallic electron momentum of $\hbar k_F$, where k_F is the Fermi wavevector (defined shortly), the uncertainty in position approaches that of the radius of a sphere whose volume is the space taken up by one conduction electron. A classical description of electronic behavior in metals is sufficient for many cases, so long as field variations occur over much larger displacements than Δx of an electron, and mean free paths remain large in comparison as well. When discussing metals at room temperature, where mean free path is long enough, or when dealing with lower energy electromagnetic fields than ultraviolet radiation, classical descriptions of metallic behavior can be sufficient. Notice, however, that while the overall description of *metallic* behavior may be satisfactory, the behavior of a given electron is poorly described classically, as they obey Fermi-Dirac statistics and not the Maxwell-Boltzmann statistics of classical theory. Considering then the Sommerfeld theory of metals, using Fermi-Dirac statistics, the non-classical electronic energy distribution can be applied to Drude's model. This improves the prediction of the mean free path and thermal conductivity, although in this case not changing the value much, as Drude's classical model had mathematically cancelling inaccuracies. Hall coefficients, magnetoresistance and electrical conductivity are unchanged by the Sommerfeld theory compared to the Drude model, as they are independent of energy or velocity distribution.

Momentum

Consider the system of non-interacting electrons confined to a cubic volume V , with sides of length L . Evaluating the Schrödinger Equation,

$$\begin{aligned}
 H\psi(\mathbf{r}) &= \epsilon\psi(\mathbf{r}) \ , \\
 H &= -\frac{\hbar^2}{2m}\nabla^2 + U(\mathbf{r}) \ ,
 \end{aligned}
 \tag{2.1}$$

for this system with the travelling plane wave solution, we obtain the energy of a free electron,

$$\epsilon_{\mathbf{k}} = \frac{\hbar^2}{2m_e} k^2. \quad (2.2)$$

In the ground-state, where energy levels are filled up in ascending order, a system of N free particles will occupy allowed positions inside of a sphere of volume V within \mathbf{k} -space that has radius k_F . The energy at the surface of this sphere (the energy of the highest occupied orbital in the ground state) is ϵ_F , the Fermi energy. The Fermi momentum, p_F , can be calculated using the quantum mechanical momentum operator, $p = -i\hbar\nabla$, such that

$$p_F = \hbar k_F \quad (2.3)$$

(or more generally, $\mathbf{p} = \hbar\mathbf{k}$), which relates to the Fermi velocity,

$$v_F = \frac{\hbar k_F}{m_e}. \quad (2.4)$$

These properties can also be discussed in terms of their more general values, importantly the velocity,

$$\mathbf{v} = \frac{\hbar\mathbf{k}}{m_e}, \quad (2.5)$$

which is a function of wavevector and independent of temperature, in contrast to classical models.

As the wavevector components must satisfy

$$k_i = \pm \frac{2n_i\pi}{L}, \quad (2.6)$$

there exists one allowed combination of the quantum numbers k_x , k_y and k_z within each volume element of $(\frac{2\pi}{L})^3$. For electrons then, with two permitted spin states, there exist

two allowed states for each allowed combination of k_i . As such, the total number of orbitals in a spherical space is twice the volume of the sphere with radius k_F divided by the volume element of a single permitted k_i triplet, $(\frac{2\pi}{L})^3$. The Fermi wavevector, in terms of the electronic density, $n = \frac{N}{V}$, $V = L^3$, is then

$$k_F = (3\pi^2 n)^{\frac{1}{3}}. \quad (2.7)$$

Density of States

The total internal energy density, u , is the integral over all allowed \mathbf{k} within a volume of \mathbf{k} -space of the energy per \mathbf{k} value i.e. the integral over \mathbf{k} -space of the number of electrons per level times the energy of that level:

$$u = \int \frac{1}{4\pi^3} \epsilon(\mathbf{k}) f_{\text{FD}}(\epsilon) \delta\mathbf{k}. \quad (2.8)$$

By using spherical coordinates to remove dependence on the vector form of \mathbf{k} we can express u as an integral over the radial coordinate, k :

$$\begin{aligned} u &= \frac{1}{4\pi^3} \int_0^{2\pi} \delta\phi \int_0^\pi \sin\theta \delta\theta \int_0^\infty k^2 \epsilon f_{\text{FD}}(\epsilon) dk \\ &= \frac{1}{\pi^2} \int_0^\infty k^2 \epsilon f_{\text{FD}}(\epsilon) dk \end{aligned} \quad (2.9)$$

Substituting in for k and δk through

$$\frac{\delta k}{\delta \epsilon} = \sqrt{\frac{m_e \epsilon}{2\hbar^2}}, \quad (2.10)$$

we get

$$u = \int_{-\infty}^{\infty} \sqrt{\frac{2m_e^3 \epsilon^3}{\pi^2 \hbar^4}} f_{\text{FD}}(\epsilon) \delta\epsilon \quad (2.11)$$

where the limits between $-\infty$ and ∞ will give the same result as between 0 and ∞ due to the physical constraints on the system ($\epsilon > 0$), but are left as they are due to our later use of the Sommerfeld expansion. Our physical interpretation of u being the internal

energy density, i.e. the number of single electron states (occupied or unoccupied) in an energy range $\delta\epsilon$ per unit volume, times the probability of these levels having an electron present, times the energy of such an electron, leads us to the interpretation that the term $\sqrt{2m_e^3\epsilon\pi^{-2}\hbar^{-4}}\delta\epsilon$ is the number of single electron states in an energy range $\delta\epsilon$ per unit volume. This is the density of states, a concept that is important later in the project and of physical significance for computational analysis of semiconductors, and we will represent it as

$$D(\epsilon) = \frac{1}{2\pi^2} \left(\frac{2m_e}{\hbar^2} \right)^{\frac{3}{2}} \epsilon^{\frac{1}{2}} \quad (2.12)$$

It can be similarly recovered from the relations between the Fermi wavevector and electronic density, where it is $D(\epsilon) = \frac{1}{V} \frac{\delta N}{\delta \epsilon}$.

We can represent u as a function of density of states,

$$u = \int_{-\infty}^{\infty} \epsilon D(\epsilon) f_{\text{FD}}(\epsilon) \delta\epsilon, \quad (2.13)$$

where $f_{\text{FD}}(\epsilon)$ is temperature dependent. The behavior of $f_{\text{FD}}(\epsilon)$ is such that its form for temperatures where they remain solid at standard pressure only differs significantly from that at $T = 0$ K around $\epsilon = \mu$. An example is shown for 1500 K in Figure 2.1, a fairly typical melting point of pure metals at standard pressure, so when dealing with low-to-room temperatures u can be well represented by the value of u at 0 K plus the Taylor expansion of $\epsilon D(\epsilon)$ centered on $\epsilon = \mu$. The value of u at 0 K is simply

$$u_{T=0} = \int_{-\infty}^{\epsilon_F} \epsilon D(\epsilon) \delta\epsilon, \quad (2.14)$$

as at $T = 0$ K all states below ϵ_F have a probability of 1 to be occupied, and all above ϵ_F a probability of occupation of 0 (by definition). The expansion is known as the Sommerfeld expansion:

$$u = \int_{-\infty}^{\mu} \epsilon D(\epsilon) \delta\epsilon + \sum_{n=1}^{\infty} (k_B T)^{2n} A_n \frac{\delta^{2n-1}}{\delta \epsilon^{2n-1}} \epsilon D(\epsilon) \Big|_{\epsilon=\mu}, \quad (2.15)$$

where A_n are dimensionless coefficients.

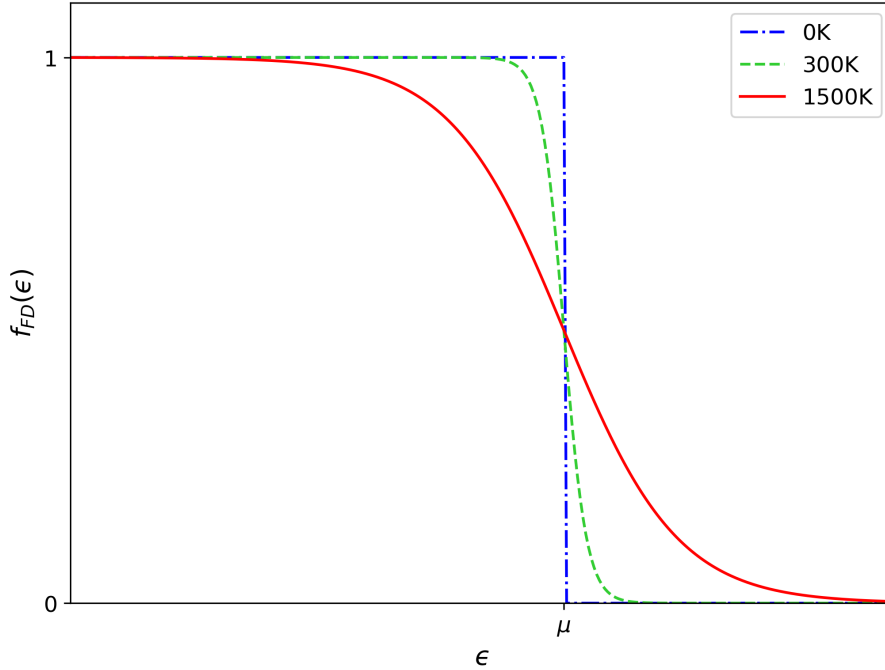


Figure 2.1: The Fermi-Dirac distribution for a metal at 1500 K, compared to 0 K and room temperature. Note the difference in distributions is only marked around μ , and the range over which this occurs is very small at room temperature.

This expansion is performed (with differences in notation) in Sommerfeld's 1927 paper [57].

Terms in the expansion fall off as $\mathcal{O}\left(\frac{k_B T}{\mu}\right)^2$, so we can consider only the first term of the expansion, and recognize that the integral limits in the $u_{T=0}$ term can be changed as negative energy is unphysical, giving us

$$u = \int_0^\mu \epsilon D(\epsilon) \delta\epsilon + \frac{\pi^2}{6} (k_B T)^2 \left(\mu \frac{\delta D(\mu)}{\delta\epsilon} + D(\mu) \right). \quad (2.16)$$

Following the above procedure again, we can similarly expand the expression for electronic density, n , as the integral over \mathbf{k} -space of the number of electrons per state (as a probability per state):

$$\begin{aligned} n &= \int \frac{1}{4\pi^3} f_{\text{FD}}(\epsilon) \delta\mathbf{k} = \int_{-\infty}^{\infty} D(\epsilon) f_{\text{FD}}(\epsilon) \delta\epsilon \\ &= \int_0^\mu D(\epsilon) \delta\epsilon + \frac{\pi^2}{6} (k_B T)^2 \frac{\delta D(\mu)}{\delta\epsilon} \end{aligned} \quad (2.17)$$

If the difference in μ between its value at 0 K and temperatures of interest is small, we

can approximate

$$\int_0^\mu D(\epsilon) \delta\epsilon = \int_0^{\epsilon_F} D(\epsilon) \delta\epsilon + (\mu - \epsilon_F) D(\epsilon_F) \quad (2.18)$$

and so

$$n = \int_0^\mu D(\epsilon) \delta\epsilon + (\mu - \epsilon_F) D(\epsilon_F) + \frac{\pi^2}{6} (k_B T)^2 \frac{\delta D(\mu)}{\delta\epsilon}. \quad (2.19)$$

However, if we keep volume constant the electronic density must be independent of temperature, so at constant volume n is equal to its value at 0 K, therefore

$$\begin{aligned} (\mu - \epsilon_F) D(\epsilon_F) + \frac{\pi^2}{6} (k_B T)^2 \frac{\delta D(\mu)}{\delta\epsilon} &= 0 \\ \therefore \mu &= \epsilon_F - \frac{\pi^2}{6} (k_B T)^2 \frac{1}{D(\epsilon)} \frac{\delta D(\epsilon)}{\delta\epsilon} \\ &= \epsilon_F \left(1 - \frac{1}{3} \left(\frac{\pi k_B T}{2\epsilon_F} \right)^2 \right) \end{aligned} \quad (2.20)$$

We see that the variation with temperature of μ is indeed small at low-to-room temperatures. Figure 2.2 shows this temperature-dependent variation in μ . Even at 1500 K, where we can expect issues with the solid state of the material, the variation in μ is only around 1%.

2.1.2 Bloch's theorem

Periodicity and Fourier series expansion

Solid structure generally falls in to one of three categories, being crystalline, polycrystalline and amorphous. These categories relate to the order of the material's microscopic structure, with crystalline materials, crystals, having periodic structure throughout their volume. Poly-crystalline materials, crystallites, are composed of multiple periodic regions arranged in a non-periodic manner, and amorphous solids have no microscopic periodicity over long range. These categories are represented in Figure 2.3. Crystals are the best understood and simplest materials in the context of solid state

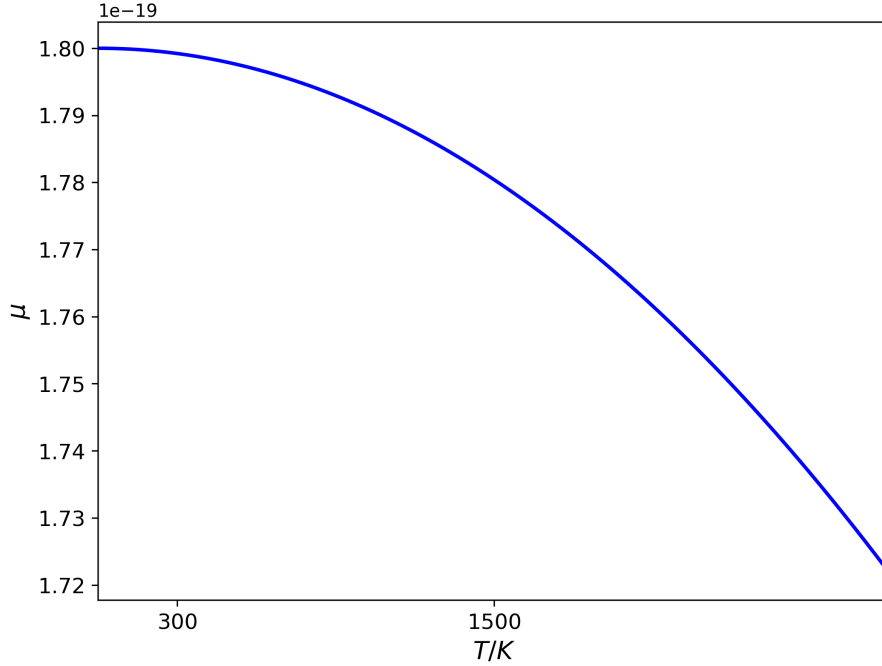


Figure 2.2: The variation of μ with temperature, as by Equation 2.20. As can be seen by the scale, even a large increase in temperature results in only a small decrease in μ .

physics, and the materials used in this project are crystalline. We therefore consider in our discussion a pristine crystalline solid, with ions arranged in a periodic array. This results in a periodic electronic potential, $U(\mathbf{r})$, throughout the material that is experienced by our electrons. The periodicity of this potential for a region suitably far from a spatial boundary (or we can assume an infinite crystal) is determined by the Bravais lattice of the material. For Bravais lattice vectors \mathbf{R} , this periodicity in the potential is described by $U(\mathbf{r} + \mathbf{R}) = U(\mathbf{r})$. Continuing to use the independent electron approximation here, we allow any specifics in the form of the potential due to electron-electron interactions to be included in $U(\mathbf{r})$, making it an effective potential.

Due to this periodicity, we can establish Fourier components of the potential (as well as other periodic properties, such as electron density and a spatial description of the lattice itself). The concept of the reciprocal lattice arises from the Fourier series expansion of the direct lattice, and is a useful tool for determining crystal properties. The Fourier series expansion of some function periodic in space over period \mathbf{a} , and invariant under translation $\mathbf{T} = u_1\mathbf{a}_1 + u_2\mathbf{a}_2 + u_3\mathbf{a}_3$, where $u_i \in \mathbb{Z}$ and \mathbf{a}_i are the crystal axes can be given

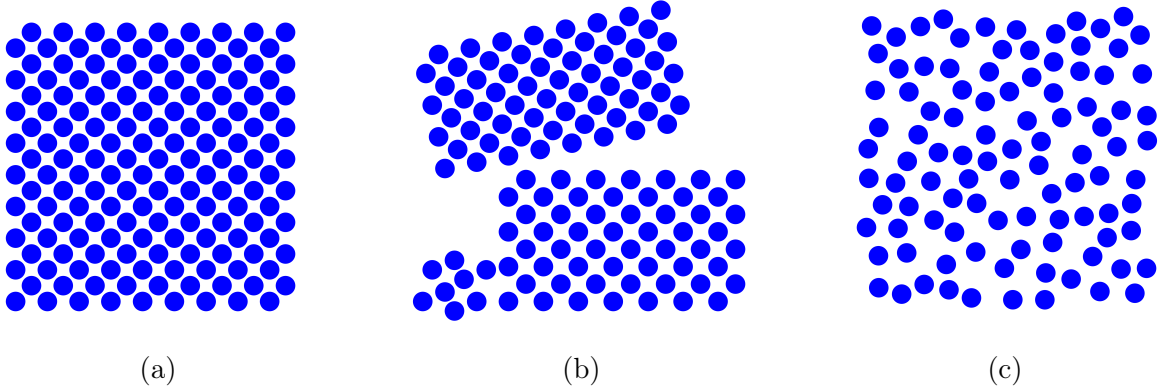


Figure 2.3: The three categories of solid structure: (a) crystalline structure (crystals), with long range order, (b) poly-crystalline structure (crystallites) with regions of order that are unordered with respect to each other., and (c) amorphous solids, with no long range order or periodicity.

as

$$f(\mathbf{r}) = \sum_{v_1} \sum_{v_2} \sum_{v_3} f_{v_1, v_2, v_3} e^{i(v_1 \mathbf{b}_1 \cdot \mathbf{r} + v_2 \mathbf{b}_2 \cdot \mathbf{r} + v_3 \mathbf{b}_3 \cdot \mathbf{r})}, \quad (2.21)$$

or more compactly as

$$f(\mathbf{r}) = \sum_{\mathbf{G}} f_{\mathbf{G}} e^{i\mathbf{G} \cdot \mathbf{r}} = \int_{\text{BZ}} f_{\mathbf{G}} e^{i\mathbf{G} \cdot \mathbf{r}} \delta \mathbf{G}, \quad (2.22)$$

where $f_{\mathbf{G}}$ are the Fourier coefficients and the integral is over the Brillouin Zone. The summation form is more useful for our purposes here, with the integral form seeing use in Chapter 3. Here $\mathbf{G} = v_1 \mathbf{b}_1 + v_2 \mathbf{b}_2 + v_3 \mathbf{b}_3$, $v_i \in \mathbb{Z}$, with \mathbf{b}_i as primitive vectors of the reciprocal lattice if they are constructed such that they are orthogonal to two crystal lattice primitive vectors, i.e. $\mathbf{b}_i \cdot \mathbf{a}_j = 2\pi \delta_{ij}$. δ_{ij} is the Kronecker delta function. The constructions that satisfy this requirement are

$$\mathbf{b}_i = \frac{2\pi}{V} (\mathbf{a}_{i+1} \times \mathbf{a}_{i+2}) \quad i \in \mathbb{Z}^+ \text{ mod } 3, \quad (2.23)$$

where the volume of the crystal lattice primitive cell is the triple product $V = \mathbf{a}_1 \cdot \mathbf{a}_2 \times \mathbf{a}_3$. The 2π term is included in the definition as convenience for later physical interpretation of angular wavevectors. As such, this Fourier series remains invariant under

crystal translation with \mathbf{T} , as

$$f(\mathbf{r} + \mathbf{T}) = \sum_{\mathbf{G}} f_{\mathbf{G}} e^{i\mathbf{G}\cdot\mathbf{r}} e^{i\mathbf{G}\cdot\mathbf{T}}, \quad (2.24)$$

where $e^{i\mathbf{G}\cdot\mathbf{T}} = 1$ due to the orthogonality of the vectors and assurance from construction that the product $u_i v_j \in \mathbb{Z}$.

The central equation and Bloch's theorem

Applying the Born-von Karman periodic boundary condition that a given wavefunction in our crystal must be periodic on the lattice, $\psi(\mathbf{r} + N_i \mathbf{a}_i) = \psi(\mathbf{r})$, $N_i \in \mathbb{Z}$ where $N = \prod_{i=1}^3 N_i$ is the total number of primitive cells in the crystal, we can consider the Fourier series expansion of a wavefunction in the crystal,

$$\psi(\mathbf{r}) = \sum_{\mathbf{k}} C_{\mathbf{k}} e^{i\mathbf{k}\cdot\mathbf{r}}, \quad (2.25)$$

where \mathbf{k} is a wavevector belonging to those plane waves in a set satisfying our boundary condition. Our boundary condition imposes that

$$e^{i\mathbf{k}\cdot(\mathbf{r}+\mathbf{a})} = e^{i\mathbf{k}\cdot\mathbf{r}} = e^{i\mathbf{k}\cdot\mathbf{r}} e^{i\mathbf{k}\cdot\mathbf{a}}, \quad (2.26)$$

$$e^{i\mathbf{k}\cdot\mathbf{a}} = 1, \quad (2.27)$$

and therefore

$$\mathbf{k} \cdot \mathbf{a} = 2\pi n, \quad n \in \mathbb{Z}, \quad (2.28)$$

i.e. \mathbf{k} is quantized. As the set N_i is orthogonal, so is our set of plane waves, $e^{i\mathbf{k}\cdot\mathbf{r}}$. Our periodic effective potential $U(\mathbf{r})$ can of course similarly be transformed as

$$U(\mathbf{r}) = \sum_{\mathbf{G}} U_{\mathbf{G}} e^{i\mathbf{G}\cdot\mathbf{r}}. \quad (2.29)$$

As the crystal lattice vector \mathbf{a} must be real, and $e^{i\mathbf{k}\cdot\mathbf{a}} = 1$, we see then that the Born-von Karman periodic boundary condition additionally requires that wavevector \mathbf{k} be real. Changing the potential by an additive constant does not affect the periodicity, so we can do so to set the average over a primitive cell of the potential to zero, i.e. $U_0 = 0$. Substituting our Fourier series expansions of $\psi(\mathbf{r})$ and $U(\mathbf{r})$ in to the time-independent Schrödinger equation (Equation 2.1) gives the central equation,

$$(\lambda_{\mathbf{k}} - E) C_{\mathbf{k}} + \sum_{\mathbf{G}} U_{\mathbf{G}} C_{\mathbf{k}-\mathbf{G}} = 0 , \quad (2.30)$$

the derivation of which is in Appendix A, and where the wavelength is given by

$$\lambda_{\mathbf{k}} = \frac{\hbar^2 k^2}{2m} . \quad (2.31)$$

The central equation is a restatement of the time-independent Schrödinger equation in \mathbf{k} -space. Due to the form of the $C_{\mathbf{k}-\mathbf{G}}$ coefficients, and as \mathbf{G} are reciprocal lattice vectors, we see that for each allowed value of \mathbf{k} in the first Brillouin zone there is an independent problem with solutions containing only the original wavevector and wavevectors differing by a reciprocal lattice vector. We can take advantage of this fact; as a given wavevector \mathbf{k} only takes values $\mathbf{k} - \mathbf{G}$ (allowing $\mathbf{G} = 0$), we see our wavefunction is of the form

$$\psi(\mathbf{r}) = \sum_{\mathbf{G}} C_{\mathbf{k}-\mathbf{G}} e^{i(\mathbf{k}-\mathbf{G})\cdot\mathbf{r}} = e^{i\mathbf{k}\cdot\mathbf{r}} \left(\sum_{\mathbf{G}} C_{\mathbf{k}-\mathbf{G}} e^{-i\mathbf{G}\cdot\mathbf{r}} \right) . \quad (2.32)$$

This wavefunction has infinite solutions; one for each allowed \mathbf{k} in the Brillouin zone. The physical interpretation of these eigenstates leads us to the band index, n : the index given to the discrete energy levels, or electronic energy bands. The energy, $\epsilon_n(\mathbf{k})$, varies continuously with \mathbf{k} , but \mathbf{k} takes discrete values. Changing the subscript to agree with this convention in notation gives us Equation 2.33, Bloch's theorem.

$$\psi_{n\mathbf{k}}(\mathbf{r}) = e^{i\mathbf{k}\cdot\mathbf{r}} u_{n\mathbf{k}}(\mathbf{r}) \quad (2.33)$$

Bloch's theorem, developed by Felix Bloch and published in 1928 [59], shows that the

eigenstates of the single-electron Hamiltonian H (Equation 2.1) in a Bravais lattice with a periodic potential can be expressed as plane waves modulated by a function with the periodicity of the Bravais lattice. Electrons described in this manner are Bloch electrons. In the free electron case (subsection 2.1.1), the wavevector \mathbf{k} is proportional to momentum,

$$\mathbf{k} = \frac{\mathbf{p}}{\hbar}. \quad (2.34)$$

Drude electrons, however, do not in general have a wavefunction that is a momentum eigenstate; \mathbf{k} is not proportional to \mathbf{p} . By applying the momentum operator to the wavefunction of a Drude electron, we get

$$\begin{aligned} -i\hbar\nabla\psi_{n\mathbf{k}} &= -i\hbar\nabla(e^{i\mathbf{k}\cdot\mathbf{r}}u_{n\mathbf{k}}(\mathbf{r})) \\ &= \hbar\mathbf{k}\psi_{n\mathbf{k}} - i\hbar e^{i\mathbf{k}\cdot\mathbf{r}}\nabla u_{n\mathbf{k}}, \end{aligned} \quad (2.35)$$

which is a non-proportional relation. Due to the similarity to the free electron case, $\hbar\mathbf{k}$ is referred to as the crystal momentum, but is not a true momentum itself. The velocity of a Bloch electron can be shown to be

$$\mathbf{v}_n(\mathbf{k}) = \frac{1}{\hbar} \frac{\delta\epsilon_n(\mathbf{k})}{\delta\mathbf{k}}, \quad (2.36)$$

a non-vanishing mean velocity (derived in Appendix B): the ionic lattice does not degrade its velocity, which is a stationary state for a given band index.

Improvements over the free electron model

By introducing periodicity conditions of the lattice to electronic potential, wavevectors \mathbf{k} are required to take discrete values. This leads to the emergence of discrete energy levels, or bands, previously not described by the free electron model. This has pronounced effects on the behavior of solids, and will be expanded upon in following subsections. As the materials of interest for this project have periodic crystal structure, a description of electronic behavior under a periodic potential is necessary, and the Bloch theorem provides the framework for the next update to modelling electronic behavior in solids; the

semiclassical model.

2.1.3 Semiclassical model

Equations of motion

The force acting on electrons experiencing a field (an electric field, \mathbf{E} , or a magnetic field, \mathbf{H}) is classically the Lorentz force, and using the Sommerfeld description of momentum ($\mathbf{p} = \hbar\mathbf{k}$, see subsection 2.1.1), where it can be described classically so long as we do not need to describe its position on the scale of interelectronic distances, we have

$$\frac{\delta\mathbf{r}}{\delta t} = \frac{\hbar\mathbf{k}}{m_e}, \quad (2.37)$$

and

$$\hbar\frac{\delta\mathbf{k}}{\delta t} = -e\mathbf{E} - \frac{e\mathbf{v}}{c} \times \mathbf{H}. \quad (2.38)$$

This behavior is for particulate electrons, so is of little use with an entirely wave-like description. However, by modelling this particle as a wave packet of free electron levels, we can update the classical model with a method to describe quantum systems, providing the semiclassical model. The wavefunction of such a free electron wave packet is

$$\psi(\mathbf{r}, t) = \sum_{\mathbf{k}'} g_{\mathbf{k}}(\mathbf{k}') e^{i(\mathbf{k}' \cdot \mathbf{r} - \epsilon_{\mathbf{k}'} t)}, \quad (2.39)$$

with the interpretations that \mathbf{r} and \mathbf{k} are the mean position and momentum of the wave packet, respectively, and where the coefficient $g_{\mathbf{k}}(\mathbf{k}')$ is a very small bin or discretization interval, $|\mathbf{k}' - \mathbf{k}| > \Delta k$, and we let Δk be much smaller than the size of the Brillouin zone, maintaining a well described momentum. Using the relations that follow from the Sommerfeld model (subsection 2.1.1), the semiclassical electronic equations of motion are

$$\begin{aligned}\dot{\mathbf{r}}_n(\mathbf{k}) &= \frac{1}{\hbar} \frac{\delta \epsilon_n(\mathbf{k})}{\delta \mathbf{k}} \\ \hbar \dot{\mathbf{k}} &= -e \left[\mathbf{E}(\mathbf{r}, t) + \frac{1}{c} \dot{\mathbf{r}}_n(\mathbf{k}) \times \mathbf{H}(\mathbf{r}, t) \right]\end{aligned}\tag{2.40}$$

where dot notation represents a time derivative, and are discussed further in Appendix C.

The electrical conductivity of a perfect periodic crystal is infinite, as the mean electronic velocity in a Bloch level may only vanish if the term

$$\frac{\delta \epsilon_n(\mathbf{k})}{\delta \mathbf{k}}\tag{2.41}$$

vanishes, although real crystals are imperfect over long range and there are thermal vibrations of the ions (producing phonons) thus far unaccounted for that perturb the periodicity. Interactions between Bloch electrons and lattice ions are taken into account already if the Schrödinger equation has solutions of a Bloch form. The periodicity, if perfect, permits wave propagation across infinite distance due to coherent scattering of electron waves without energy loss. In the semiclassical treatment of Bloch electrons, we accept some form of scattering mechanism, but it need not be due electron-ion collision. The wavefunction of a Bloch electron wave packet is

$$\psi_n(\mathbf{r}, t) = \sum_{\mathbf{k}'} g_{\mathbf{k}'}(\mathbf{k}') \psi_{n\mathbf{k}'} e^{-\frac{i}{\hbar} \epsilon_n(\mathbf{k}') t},\tag{2.42}$$

and as Δk is small compared to the size of the Brillouin zone, the change in $\epsilon_n(\mathbf{k})$ within the wave packet is also small. As $\Delta k \ll \frac{2\pi}{a}$, the uncertainty principle leads us to the fact that a wave packet well defined in momentum space on the scale of the Brillouin zone is poorly defined in real space on the scale of a primitive cell; $\Delta x \gg \frac{a}{2\pi}$. As such, the semiclassical model can be used in the limit that applied fields can be treated classically (they do not vary over the dimensions of the wave packet) and the periodic field has a period smaller than the dimensions of the wave packet.

Limitations and holes

The periodic lattice potential experienced by a Bloch electron cannot play a role in its true momentum (within the model); this would require localization of position on scales within a primitive cell (over which the periodic potential varies), which is inconsistent with our wave packets being spread over many primitive cells, $\Delta x \gg \frac{a}{2\pi}$. The semiclassical rate of change of crystal momentum, $\hbar \dot{\mathbf{k}}$ (Equation 2.40), only considers external fields acting on the electron, which must vary over longer length scales for the semiclassical model to hold validity. Additionally, band transitions are forbidden within the semiclassical model as the band index is a constant. As electrons tend towards free electrons (as periodic potential $U(\mathbf{r}) \rightarrow 0$) and experience only a uniform electric field, they may increase their kinetic energy ceaselessly (within a relativistic limit). As the model requires that the electrons remain energetically circumscribed within the band's energy limits, there exists a minimum periodic potential experienced by the electrons to maintain the appropriateness of the semiclassical model.

Despite its limitations, the semiclassical model is an improvement over the free electron theory of the Drude and Drude-Sommerfeld models (subsection 2.1.1) in the matters of electron transport and dynamics. Importantly, it provides an explanation for the existence of non-metallic materials, and for the variation in the sign of a metal's Hall coefficient.

Consider an electronic band in a crystal where each permitted state has energy below the Fermi energy, ϵ_F . With two spin states per energy level, and a \mathbf{k} -space volume of $(2\pi)^3$, the contribution of electrons in this band with wavevectors within a volume $\delta\mathbf{k}$ to total electronic density is $\frac{\delta\mathbf{k}}{4\pi^3}$. Within six-dimensional $\mathbf{r}\mathbf{k}$ -space (phase space), the density of electrons of a filled semiclassical band is $\frac{1}{4\pi^3}$, as the number of electrons within the \mathbf{k} -space volume $\delta\mathbf{k}$ in a given real space volume $\delta\mathbf{r}$ is $\delta\mathbf{r} \frac{\delta\mathbf{k}}{4\pi^3}$.

Liouville's theorem [60,61] asserts that the volume of a system in phase space remains constant in time. The phase space electronic density is therefore constant, as semiclassical electrons cannot undergo interband transitions (so neither the volume nor the number of electrons may vary). The general solution to the semiclassical equation of motion

(Equation 2.40) is

$$\mathbf{k}(t) = \mathbf{k}(0) - \frac{e\mathbf{E}t}{\hbar}, \quad (2.43)$$

which shows that over time interval t every wavevector undergoes the same shift, i.e. the electrons move through phase space together, further demonstrating the constancy of electronic density in phase space. Electrons within a volume element $\delta\mathbf{k}$ about the point \mathbf{k} have velocity

$$\mathbf{v}_n(\mathbf{k}) = \frac{1}{\hbar} \frac{\delta\epsilon_n}{\delta\mathbf{k}}, \quad (2.44)$$

and so the contribution of this filled band to the electric current density is

$$\mathbf{j} = -e \int_{\text{BZ}} \frac{1}{4\pi^3\hbar} \frac{\delta\epsilon(\mathbf{k})}{\delta\mathbf{k}} \delta\mathbf{k}, \quad (2.45)$$

where integration is over all \mathbf{k} in the Brillouin zone and considers only a single band, so the band index dependence has been dropped. The contribution to the energy current density is similarly just

$$\mathbf{j}_\epsilon = \int_{\text{BZ}} \frac{1}{4\pi^3\hbar} \epsilon(\mathbf{k}) \frac{\delta\epsilon(\mathbf{k})}{\delta\mathbf{k}} \delta\mathbf{k}. \quad (2.46)$$

Note that $\epsilon(\mathbf{k})$ is a function periodic over the Brillouin zone (the volume over which we are integrating), and so the contribution to the electric current density of a filled band is equal to zero. This is also true for the energy current density, and is shown in Appendix D. Due to the electronic passivity of filled bands, only those bands which are partially filled with electrons need be considered, providing an explanation for why the Drude's model use of atomic valence to determine an atom's contribution to conduction electrons was fairly rewarding; often an atom's valence electrons are the only ones occupying partially filled bands. The number of energy levels in each band is related to the number of primitive cells in the crystal; for crystals with a single atom in a primitive cell, there are two allowed energy levels in each band per primitive cell. Such solids with an odd number of electrons

per primitive cell must have partially filled bands, and is an electrical conductor (and has a high electronic contribution to its thermal conductivity as well). Solids with an even number of electrons per primitive cell may have only full and empty bands, causing a band gap and exhibiting insulating or semiconducting properties. They may still be conductors, however, as while they have the correct number of electrons to precisely fill a number of bands without remainder, they do not necessarily do so in cases where band energies overlap.

Considering now a band that is not necessarily filled, the contribution of electrons in the band to the current density is

$$\mathbf{j} = -\frac{e}{4\pi^3} \int_{\text{occupied}} \mathbf{v}(\mathbf{k}) \delta(\mathbf{k}) , \quad (2.47)$$

and as a filled band is inert we deduce that

$$\left(-\frac{e}{4\pi^3}\right) \int_{\text{occupied}} \mathbf{v}(\mathbf{k}) \delta(\mathbf{k}) + \left(-\frac{e}{4\pi^3}\right) \int_{\text{unoccupied}} \mathbf{v}(\mathbf{k}) \delta(\mathbf{k}) = 0 \quad (2.48)$$

and consequently we see that

$$\mathbf{j} = \frac{e}{4\pi^3} \int_{\text{unoccupied}} \mathbf{v}(\mathbf{k}) \delta(\mathbf{k}) \quad (2.49)$$

is an alternate way of representing the current density of a partially filled band, where the integrals are over permitted wavevectors that either do (occupied) or do not (unoccupied) have wave packets present with that wavevector. This shows the equivalence between treatments of a band partially filled with electrons, and the same band with those previously filled levels being unoccupied and the previously unoccupied levels being now occupied with particles of opposite electronic charge. This is perhaps the greatest revelation to come from the semiclassical model: a description of holes. Holes are the absence of an electron, but one may consider them to be the charge carriers, and consider electrons to be the absence of holes. As electrons have their wavevector and position uniquely determined by the semiclassical equations of motion at any time given these

variables at some other time, positions in phase-time space that lack electrons are also uniquely determined i.e. the paths taken through phase-time space of two electrons share no overlap. For a band with unoccupied states there will, therefore, be paths (or orbits) in phase-time space that have no electron in them, and these orbits will remain unoccupied with the evolution of time. The topography of these paths depends on the semiclassical equations of motion through their respective wavevector, and they remain the same regardless of whether they are actually occupied or not; these unoccupied paths can be considered to be the paths on which holes travel in phase space with the evolution of time. This concept is illustrated in Figure 2.4.

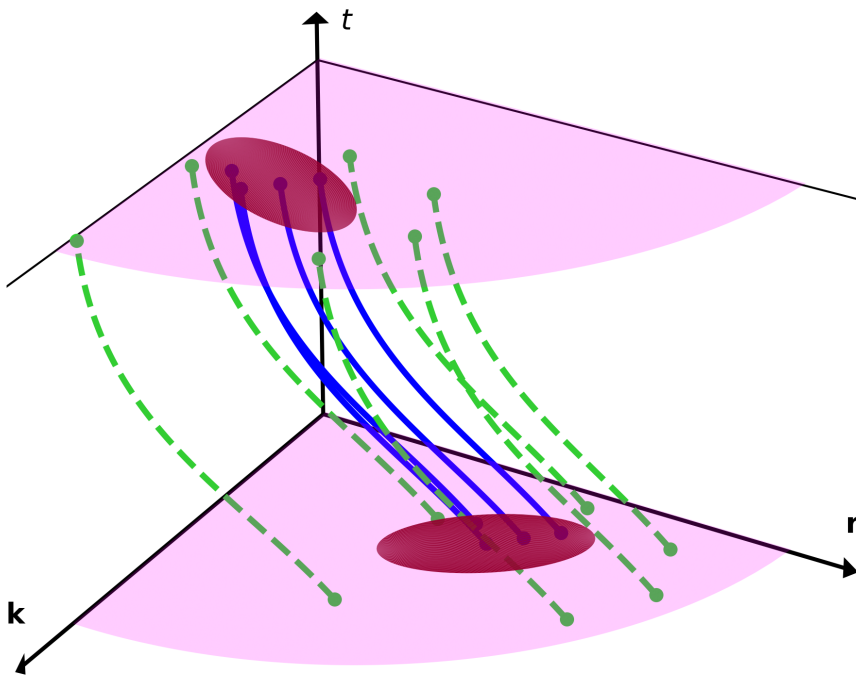


Figure 2.4: A schematic representation of phase space, as the position-wavevector plane (\mathbf{rk} plane), against time. The movement of charge carriers is displayed with solid blue lines for electrons, and dashed green lines for holes; the volume in \mathbf{rk} - t that these move through represent occupied and unoccupied bands, respectively. The phase space density remains constant with time, with the same number of electrons occupying the same amount of space throughout.

2.1.4 Self-consistent field methods

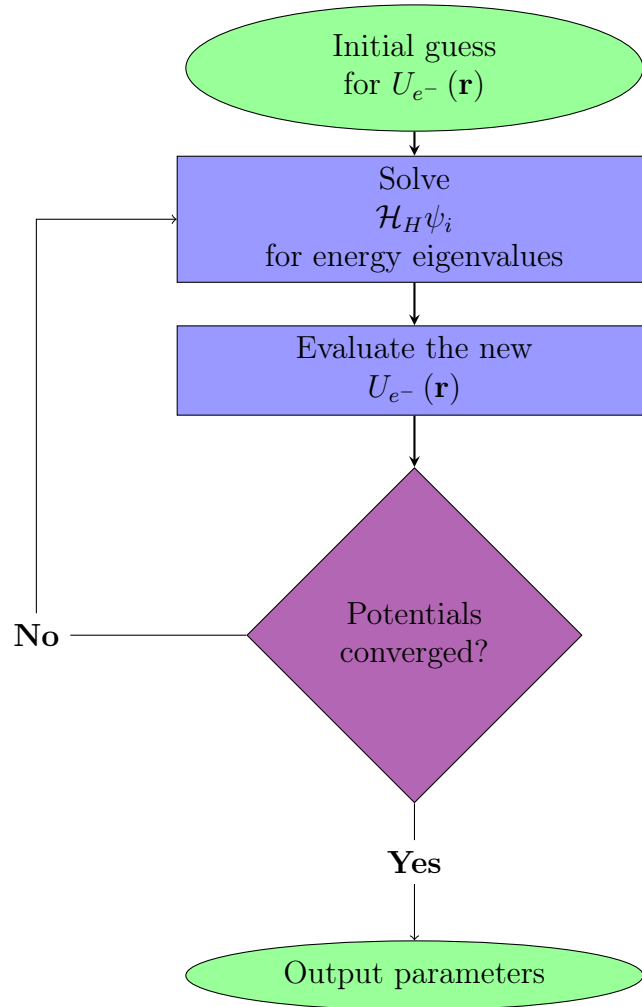


Figure 2.5: The process map for the Hartree self consistent field equations (Equation 2.53). Convergence in the potential is to a desired precision.

So far we have ignored electron-electron interactions. For a large system of N electrons, each single electron is affected by the $N - 1$ other electrons. As such, attempting for an exact solution to the Schrödinger equation for such a system is simply quixotic, especially if considering the practicalities of computational resource allocation. Instead it is more practical to choose a form of $U(\mathbf{r})$ that is physical but computationally feasible. The method used in this project is just such a computationally manageable one, and uses self-consistent field calculations. These do not belong to a category of new ideas, although the specifics have evolved over time. We discuss in this subsection early self-consistent field theory as an attempt to lift the independent electron approximation, holding the discussion of the modern form for its own section (Section 3.1).

We can consider the wavefunction of a single electron in a periodic solid that undergoes electron-electron interactions, but we do not consider each other electron individually. We first say that our single electron of interest here interacts with N , and not $N - 1$, other electrons. If N is large, we can ignore the difference of a single additional charge. We then treat the N electrons as a smooth background of negative charge, that effects a potential on our single electron of

$$U_{e^-}(\mathbf{r}) = -e \int \frac{\rho(\mathbf{r}')}{|\mathbf{r} - \mathbf{r}'|} \delta\mathbf{r}', \quad (2.50)$$

The electron also interacts with positively charged ions at positions \mathbf{R} belonging to the Bravais lattice. The potential felt by such an electron due to the ions is Coulombic, of form

$$U_{\odot}(\mathbf{r}) = -e^2 \sum_{\mathbf{R}} \frac{Z_{\mathbf{R}}}{|\mathbf{r} - \mathbf{R}|} \quad (2.51)$$

where $Z_{\mathbf{R}}$, the atomic number of the atom at position \mathbf{R} , is constant and outside the summation for a monatomic material. If the other electrons with wavefunctions $\psi_j(\mathbf{r}')$ do not interact with each other for the purposes of determining the density of the background negative charge (an acceptable compromise, considering we have already modelled the other electrons as a distribution of charge instead of distinct entities), and contribute to the charge density independently, the total electronic charge density is

$$\rho(\mathbf{r}) = -e \sum_j \psi_j^*(\mathbf{r}) \psi_j(\mathbf{r}). \quad (2.52)$$

Our single-electron Schrödinger equation is then one of a set of equations for single electron wavefunctions, ψ_i , that are to be solved iteratively, the Hartree equations:

$$-\frac{\hbar^2}{2m} \nabla^2 \psi_i(\mathbf{r}) - e^2 \sum_{\mathbf{R}} \frac{Z_{\mathbf{R}}}{|\mathbf{r} - \mathbf{R}|} \psi_i(\mathbf{r}) + e^2 \sum_j \int \frac{|\psi_j(\mathbf{r}')|^2}{|\mathbf{r} - \mathbf{r}'|} \delta\mathbf{r}' \psi_i(\mathbf{r}) = \epsilon_i \psi_i(\mathbf{r}) \quad (2.53)$$

$$\mathcal{H}_H = -\frac{\hbar^2}{2m} \nabla^2 + U_{\odot}(\mathbf{r}) + U_{e^-}(\mathbf{r})$$

These equations also define what we will call the Hartree Hamiltonian operator, \mathcal{H}_H .

The iterative method to solve such equations is given in Figure 2.5, and goes as follows: A starting potential for electron-electron interaction, determined through guesswork, previous iterations or empiricism, is used to solve the Hartree equations (Equation 2.53). This produces a solved set for the form of ψ_i , which is used to produce an updated U_{e^-} . This potential is then substituted back in to the Hartree equations to solve for a new set of ψ_i , and so on. This continues until a result of U_{e^-} is no different than the previous iteration to within the desired precision.

Hartree-Fock exchange

An N -electron wavefunction that satisfies the Hartree equations is a product of single electron levels,

$$\Psi(\mathbf{r}_1 s_1, \dots, \mathbf{r}_N s_N) = \psi_1(\mathbf{r}_1 s_1) \dots \psi_N(\mathbf{r}_N s_N) , \quad (2.54)$$

which in order to obey the Pauli exclusion principle must under particle exchange behave as

$$\Psi(\mathbf{r}_1 s_1, \dots, \mathbf{r}_i s_i, \dots, \mathbf{r}_j s_j, \dots, \mathbf{r}_N s_N) = -\Psi(\mathbf{r}_1 s_1, \dots, \mathbf{r}_j s_j, \dots, \mathbf{r}_i s_i, \dots, \mathbf{r}_N s_N). \quad (2.55)$$

The only way in which the product of single-electron wavefunctions form of Ψ can satisfy this antisymmetry requirement is if Ψ vanishes at all points in its domain i.e. the initial configuration and the exchanged configuration of electrons cannot exist in superposition; the single-electron product form of Ψ is not appropriate and the Hartree equations are inadequate. A solution to this is to modify the form of the wavefunction to be a linear combination of the product of single-electron wavefunctions with the products of the same single-electron wavefunctions with all combinations of particle exchange, with summation weights of positive or negative unity depending on the term's symmetry requirements.

This is a Slater determinant, and can be displayed as an $N \times N$ matrix

$$\Psi(\mathbf{r}_1 s_1, \dots, \mathbf{r}_N s_N) = \psi_1(\mathbf{r}_1 s_1) \dots \psi_N(\mathbf{r}_N s_N) - \psi_1(\mathbf{r}_2 s_2) \psi_2(\mathbf{r}_1 s_1) \dots \psi_N(\mathbf{r}_N s_N) + \dots \quad (2.56)$$

$$= \frac{1}{\sqrt{N!}} \begin{vmatrix} \psi_1(\mathbf{r}_1 s_1) & \psi_1(\mathbf{r}_2 s_2) & \dots & \psi_1(\mathbf{r}_N s_N) \\ \psi_2(\mathbf{r}_1 s_1) & \psi_2(\mathbf{r}_2 s_2) & \dots & \psi_2(\mathbf{r}_N s_N) \\ \vdots & \vdots & \ddots & \vdots \\ \psi_N(\mathbf{r}_1 s_1) & \psi_N(\mathbf{r}_2 s_2) & \dots & \psi_N(\mathbf{r}_N s_N) \end{vmatrix} \quad (2.57)$$

$$= \frac{1}{\sqrt{N!}} \det(\psi_i(\mathbf{r}_j s_j)) , \quad (2.58)$$

where the $\frac{1}{\sqrt{N!}}$ is a normalization term. Evaluating the expectation value of the Hartree Hamiltonian of the N -electron system represented by the Slater determinant results in

$$\begin{aligned} \langle \mathcal{H}_H \rangle_\Psi &= \sum_i \int \psi_i^*(\mathbf{r}) \left(-\frac{\hbar^2}{2m} \nabla^2 + U_\odot(\mathbf{r}) \right) \psi_i(\mathbf{r}) \delta \mathbf{r} \\ &+ \frac{1}{2} \sum_{i,j} \int \frac{e^2}{|\mathbf{r} - \mathbf{r}'|} \psi_i^*(\mathbf{r}) \psi_i(\mathbf{r}) \psi_j^*(\mathbf{r}') \psi_j(\mathbf{r}') \delta(\mathbf{r}) \delta(\mathbf{r}') \\ &- \frac{1}{2} \sum_{i,j} \int \frac{e^2}{|\mathbf{r} - \mathbf{r}'|} \delta_{s_i s_j} \psi_i^*(\mathbf{r}) \psi_i(\mathbf{r}') \psi_j^*(\mathbf{r}') \psi_j(\mathbf{r}) \delta \mathbf{r} \delta \mathbf{r}' \end{aligned} \quad (2.59)$$

where the Kronecker delta $\delta_{s_i s_j}$ enforces spin orthogonality. Minimizing this expectation value with respect to ψ_j^* leads to the Hartree-Fock equation:

$$\mathcal{H}_H \psi_i(\mathbf{r}) - \sum_j \int \frac{e^2}{|\mathbf{r} - \mathbf{r}'|} \psi_j^*(\mathbf{r}') \psi_i(\mathbf{r}') \psi_j(\mathbf{r}) \delta_{s_i s_j} \delta \mathbf{r}' = \epsilon_i \psi_i(\mathbf{r}) . \quad (2.60)$$

The Hartree-Fock Hamiltonian operator, \mathcal{H}_{HF} is the Hartree Hamiltonian operator, \mathcal{H}_H , plus the Hartree-Fock exchange term, V_X :

$$\mathcal{H}_{HF} = \mathcal{H}_H + V_X . \quad (2.61)$$

This term is an integral operator, where the operand is integrated as part of the operation. Examining the second term on the left hand side of Equation 2.60 we see that for an

operand $f(\mathbf{r}, \mathbf{i}) = \psi_i(\mathbf{r})$ the term takes on the form of

$$V_X f(\mathbf{r}, i) = \sum_j \int f(t) K(t, j) \delta t \quad (2.62)$$

and so is a sum-integral operator with $t = \mathbf{r}'$ and a kernel

$$K(t, j) = -\frac{e^2}{|\mathbf{r} - \mathbf{r}'|} \psi_j^*(\mathbf{r}') \psi_j(\mathbf{r}) \delta_{s_i s_j} . \quad (2.63)$$

The Hartree-Fock equations are, in general, not exactly solvable (the special case exception is the free electron gas), and so approximations are used for the exchange term and any other perturbations not so far considered. The approximate terms are used to solve for updated potentials in the same iterative manner as the Hartree equations.

Correlation

The Hartree equations do not take into account electron correlation: how much the motion of an electron is affected by the motion of the other $N - 1$ electrons. The updated Hartree-Fock equations do not attempt to take it into account, either. This is due to the modelling of other electrons as the smooth background charge of density $\rho(\mathbf{r})$, which both sets of equations use. So, we can update Equation 2.60 with an additional correlation term, \mathcal{C} , that for now shall remain defined by all unaccounted for perturbations to the Hartree-Fock equations. This term, as well as computationally tractable approximations to the exchange term, can be considered together as the exchange-correlation term. This is discussed further in Section 3.1, and holds significant relevance to density functional theory as the choice of this term determines the accuracy of any calculations.

Thomas-Fermi screening

Consider a free electron gas in a periodic lattice of positive ions. The positive ions attract electrons to them, and so an electron will feel the charge of these ions reduced by any negative charge between itself and the ion i.e. our ion is screened by other electrons relative to our target electron. These electrons may be core electrons, which are not

a part of the electron gas beyond their role of screening the full ionic charge of Z , or they may be free electrons that have been attracted closer to the ions than has our target electron. The electrostatic potential of the ion, ϕ_{\odot} , leads to the spatial charge distribution of

$$\nabla \cdot \mathbf{E}_{\odot}(\mathbf{r}) = -\nabla^2 \phi_{\odot}(\mathbf{r}) = 4\pi\rho_{\odot}(\mathbf{r}) . \quad (2.64)$$

An electron will not feel the entire potential due to screening from other electrons between itself and the ion, but instead will experience

$$\nabla \cdot \mathbf{E} = -\nabla^2 \phi(\mathbf{r}) = 4\pi\rho(\mathbf{r}) , \quad (2.65)$$

where values without subscript denote the screened values i.e. those physically felt by an electron at position \mathbf{r} . We can consider the screened charge density to be a sum of the ion's charge density and the charge density of the perturbed electron gas around the ion, ρ_{\sim} . We note that ϕ_{\odot} has its source arising from charges outside of the medium of the electron gas (although intrinsic to the lattice) and ϕ is the total effect experienced by our target electron. This is the same relationship as between the electric displacement field and the electric field in dielectric media, so we assume it follows the same relation,

$$\phi_{\odot}(\mathbf{r}) = \int \varepsilon(\mathbf{r} - \mathbf{r}') \phi(\mathbf{r}') \delta\mathbf{r}' , \quad (2.66)$$

where here ε represents the relative permittivity of the metal. If we take the convolution of $\varepsilon(\mathbf{r})$ and $\phi(\mathbf{r})$ using a spatial dummy vector, $\boldsymbol{\tau}$, we get

$$\phi(\mathbf{r}) * \varepsilon(\mathbf{r}) = \int \phi(\boldsymbol{\tau}) \varepsilon(\mathbf{r} - \boldsymbol{\tau}) \delta\boldsymbol{\tau} , \quad (2.67)$$

which if we let $\boldsymbol{\tau} = \mathbf{r}'$ (which we are free to do) leads us to recognize that

$$\phi_{\odot}(\mathbf{r}) = \phi(\mathbf{r}) * \varepsilon(\mathbf{r}) . \quad (2.68)$$

Through the convolution theorem, then we have that

$$\phi_{\odot}(\mathbf{q}) = \phi(\mathbf{q}) \varepsilon(\mathbf{q}) , \quad (2.69)$$

where $\phi(\mathbf{q})$ and $\varepsilon(\mathbf{q})$ are the Fourier transforms of our functions and \mathbf{q} is the wavevector associated with the spatial variation of ϕ and ε .

Similarly taking the Fourier transform of our Poisson relationships for ρ , and using the property of Fourier transforms that

$$\mathcal{F}\left\{\frac{\delta f(x)}{\delta x}\right\}(k) = -ik\mathcal{F}\{f(x)\}(k) , \quad (2.70)$$

we get

$$\mathcal{F}\{-\nabla^2\phi_{\odot}(\mathbf{r})\}(\mathbf{q}) = q^2\phi_{\odot}(\mathbf{q}) = 4\pi\rho_{\odot}(\mathbf{q}) , \quad (2.71)$$

and the equivalent expression for ρ . If we assume that ρ_{\sim} has a linear response with perturbation in ϕ , valid for small perturbations and weak potentials, we see that through analogy with the above convolution of ϕ and ε , and the introduction of a linear response function related to $\varepsilon(\mathbf{r})$ that we will remove later, $\chi(\mathbf{r})$,

$$\rho_{\sim}(\mathbf{q}) = \chi(\mathbf{q})\phi(\mathbf{q}) . \quad (2.72)$$

Physical interpretation of $\chi(\mathbf{q})$ is that it is the linear susceptibility in Fourier space and requires the linearity condition we are working under, but is of yet undetermined form. Using the Fourier transforms of the Poisson equations above, we see that

$$\phi(\mathbf{q}) - \phi_{\odot}(\mathbf{q}) = \frac{4\pi}{q^2}(\rho(\mathbf{q}) - \rho_{\odot}(\mathbf{q})) = \frac{4\pi}{q^2}\rho_{\sim}(\mathbf{q}) , \quad (2.73)$$

giving the relationship between ϕ and ρ_{\sim} i.e. ϕ depends on the charge density that ϕ itself has induced. We can use the above relationships to express ε in terms of χ , which

will be used later:

$$\varepsilon(\mathbf{q}) = \frac{\phi_{\odot}(\mathbf{q})}{\phi(\mathbf{q})} = 1 - \frac{4\pi\rho_{\sim}(\mathbf{q})}{q^2\phi(\mathbf{q})} = 1 - \frac{4\pi}{q^2}\chi(\mathbf{q}) \quad (2.74)$$

This gives rise to a self-consistent single-electron Schrödinger equation with energy Hamiltonian

$$\mathcal{H} = -\frac{\hbar^2}{2m}\nabla^2 - e\phi(\mathbf{r}) . \quad (2.75)$$

Again assuming linear relationships from small perturbations in potential and the restrictions from the semiclassical model (see subsection 2.1.3), from this Hamiltonian we get the energy of an electron in a self-consistent field to simply be the energy of a free electron plus an energy perturbation resulting from the local potential, $-e\phi(\mathbf{r})$. The induced charge density is similarly

$$\rho_{\sim} = -en(\mathbf{r}) + en_0 , \quad (2.76)$$

where n is the electron number density from subsection 2.1.1 modified with the new perturbed potential, and n_0 is this in the limit that the electrostatic potential from the ions $\phi_{\odot} = 0$,

$$n(\mathbf{r}) = \int \frac{1}{4\pi^3} \frac{\delta\mathbf{k}}{e^{\frac{\epsilon - \mu - e\phi(\mathbf{r})}{k_B T} + 1}} , \quad (2.77)$$

where ϵ is the classical energy, $\frac{\hbar^2 k^2}{2m_e}$. We note that n_0 may be expressed as a function of μ , $n_0(\mu)$, where then $n(\mathbf{r}) = n_0(\mu')$ if $\mu' = \mu + e\phi(\mathbf{r})$ i.e. $n(\mathbf{r}) = n_0(\mu + e\phi(\mathbf{r}))$. This results in a self-consistent relationship between induced electronic charge density and local electron number density,

$$\rho_{\sim}(\mathbf{r}) = -e[n_0(\mu + e\phi(\mathbf{r})) - n_0(\mu)] . \quad (2.78)$$

Expanding this around $\phi = 0$ gives

$$\begin{aligned}
\rho_{\sim}(\mathbf{r}) &= \rho_{\sim}(\mathbf{r}) \Big|_{\phi=0} + \frac{\delta\rho_{\sim}(\mathbf{r})}{\delta\phi} \Big|_{\phi=0} \phi + \mathcal{O}\phi^2 + \dots \\
&= -e[n_0(\mu) - n_0(\mu)] - e \frac{\delta n_0}{\delta(\mu + e\phi)} \frac{\delta}{\delta\phi} (\mu + e\phi) \Big|_{\phi=0} \phi + \mathcal{O}\phi^2 + \dots \\
&= -e^2 \frac{\delta n_0}{\delta\mu} \phi
\end{aligned} \tag{2.79}$$

by the chain rule and dropping terms of order ϕ^2 and above. From the linearity of Fourier transforms, and since $\rho_{\sim}(\mathbf{q}) = \chi(\mathbf{q})\phi(\mathbf{q})$, we see that

$$\chi(\mathbf{q}) = -e^2 \frac{\delta n_0}{\delta\mu} \tag{2.80}$$

and so

$$\varepsilon(\mathbf{q}) = 1 + \frac{k_s^2}{q^2}, \tag{2.81}$$

where the Thomas-Fermi wavevector, k_s , is

$$k_s = \sqrt{4\pi e^2 \frac{\delta n_0}{\delta\mu}}. \tag{2.82}$$

Considering our ion has positive charge Z concentrated within a small region of nuclear radius, we can treat this as a point charge for all displacements outside the nucleus (a perfectly reasonable physical restriction for electrons). The electrostatic potential due to this ion in Fourier space is simply $\phi_{\odot}(\mathbf{q}) = \frac{4\pi Z}{q^2}$, as for a point charge

$$\rho_{\odot}(\mathbf{r}) = Z\delta_D(\mathbf{r}), \tag{2.83}$$

where $\delta_D(\mathbf{r})$ is the Dirac delta function. The Fourier transform of this charge density is then

$$\rho_{\odot}(\mathbf{q}) = \int \rho_{\odot}(\mathbf{r}) e^{-i\mathbf{q}\cdot\mathbf{r}} \delta\mathbf{r} = Z \int \delta_D(\mathbf{r}) e^{-i\mathbf{q}\cdot\mathbf{r}} \delta\mathbf{r}, \tag{2.84}$$

which is non-zero only at $\mathbf{r} = 0$, giving

$$\rho_{\odot}(\mathbf{q}) = Z \int \delta_D(\mathbf{r}) \delta \mathbf{r} , \quad (2.85)$$

which is just the Dirac delta function normalized over all space (1 by definition), times the ionic charge, Z . So, the total electrostatic potential is then $\phi_{\odot}(\mathbf{q})$ divided by $\epsilon(\mathbf{q})$ as

$$\phi(\mathbf{q}) = \frac{4\pi Z}{q^2 + k_s^2} . \quad (2.86)$$

Inverting this transform to regain dependence on spatial coordinates, we have

$$\phi(\mathbf{r}) = \frac{Z}{r} e^{-k_s r} . \quad (2.87)$$

In Thomas-Fermi screening, therefore, there is a damping term to reduce the Coulombic electrostatic potential rapidly with increasing displacement from ions of scale $\frac{1}{k_s}$. The value of k_s can be estimated by recognizing that for a free electron gas far below the Fermi temperature, $\frac{\delta n_0}{\delta \mu}$ is the density of states at the Fermi energy, as $\mu \approx \epsilon_F$, i.e.

$$\frac{\delta n_0}{\delta \mu} = D(\epsilon_F) = \frac{m_e k_F}{\hbar^2 \pi^2} , \quad (2.88)$$

and therefore

$$k_s = \sqrt{\frac{4k_F m_e e^2}{\pi \hbar^2}} = \sqrt{\frac{4k_F}{\pi a_B}} , \quad (2.89)$$

where a_B is the Bohr radius,

$$a_B = \frac{\hbar^2}{m_e e^2} , \quad (2.90)$$

with the permittivity of free space being set to $\epsilon_0 = 1$ for natural units. This is the form used by Perdew, Burke and Ernzerhof [43] for their PBE functional, used in this project. It will be discussed in more detail later in Chapter 3.

2.2 Energy bands and band structure

In this section we will be returning to some previous assumptions and approximations in order to discuss instructive and simple cases of how band structure arises e.g. the free and independent electron approximations. Considering the free electron case, where an electron has energy

$$\epsilon(\mathbf{k}) = \frac{\hbar^2 \mathbf{k}^2}{2m_e}, \quad (2.91)$$

we notice from the discussions in subsection 2.1.2 that in a periodic lattice our wavevectors are such that

$$\mathbf{k}' = \mathbf{k} + \mathbf{G}, \quad (2.92)$$

where \mathbf{k} is a wavevector in the first Brillouin zone (FBZ) and \mathbf{G} represents the reciprocal lattice vectors. This is the origin of the computational parameter of energy cut-off, discussed more in Chapter 3; the plane wave basis set used in our calculations can be expanded or contracted by changing the highest energy (largest \mathbf{G}) plane wave considered in the set. We simplify for the purposes of explanation to a one-dimensional ‘empty’ lattice in the spatial x-dimension, with lattice point spacing of a and where the Bravais lattice vectors are then simply

$$\mathbf{R} = na\hat{x}, \quad n \in \mathbb{Z}. \quad (2.93)$$

The empty lattice approximation is one where we keep the periodicity of a lattice, but each lattice point is empty; there are no ions acting as sources of collisions or potentials. As such, our reciprocal lattice vectors are

$$\mathbf{G} = n \frac{2\pi}{a} \hat{k}_x. \quad (2.94)$$

Due to the periodicity condition that $\psi(\mathbf{r}) = \psi(\mathbf{r} + \mathbf{R})$, we can state the energy equivalently as

$$\epsilon(\mathbf{k}) = \frac{\hbar^2}{2m_e} (\mathbf{k} + \mathbf{G})^2 = \frac{\hbar^2}{2m_e} (k_x + G_{x_n})^2 = \frac{\hbar^2}{2m_e} \left(k_x + n \frac{2\pi}{a} \right)^2. \quad (2.95)$$

The FBZ has width in k_x of $\frac{2\pi}{a}$, and so when centred on 0 runs from $-\frac{\pi}{a}$ to $\frac{\pi}{a}$. k_x itself runs between $-\infty$ and ∞ , but values outside of the FBZ can be represented by k_x values within the FBZ plus a reciprocal lattice vector, with both representations being exactly equivalent. We can use this property to represent energy states within the FBZ in the reduced zone scheme by modulating the k_x values by a reciprocal lattice vector of the appropriate index, n . We do not change k_x values between $-\frac{\pi}{a}$ and $\frac{\pi}{a}$, we modulate those outside that range but up to $\pm \frac{2\pi}{a}$ by G_{x_2} , and so on.

We can also consider the simple cubic three-dimensional case with side of length a , where now

$$\epsilon(\mathbf{k}) = \frac{\hbar^2}{2m_e} (\mathbf{k} + v_1 \mathbf{b}_1 + v_2 \mathbf{b}_2 + v_3 \mathbf{b}_3)^2 = \frac{\hbar^2}{2m_e} \left(\mathbf{k} + v_1 \frac{2\pi}{a} \hat{k}_x + v_2 \frac{2\pi}{a} \hat{k}_y + v_3 \frac{2\pi}{a} \hat{k}_z \right)^2. \quad (2.96)$$

In the three-dimensional case we will represent reciprocal lattice vectors in terms of their component coefficients v_1, v_2 and v_3 i.e., the reciprocal lattice vector of the band for which $\mathbf{v} = v_1, v_2, v_3 = 1, 0, 0$ is $\mathbf{G} = \frac{2\pi}{a} \hat{k}_x$. Due to the directional dependence of energy, if we wish to display the band structure in a two-dimensional plot, we must define a direction along which to define the energy. Here we will use [100], the x-direction. The lowest lying band is where $\mathbf{G} = 0$, and so the band energy is k_x^2 (in units such that $\frac{\hbar^2}{2m_e} = 1$). Beyond the FBZ this band can be equivalently represented within the FBZ by other values of \mathbf{G} , as discussed in the one-dimensional case. Bands arising from reciprocal lattice vectors that are not parallel to the direction of plotting give a more complex picture than in the one-dimensional case. In this instance, where we are considering the [100] direction, this lowest energy band is represented within the FBZ by shifting those values outside the FBZ by the appropriate choice of \mathbf{G} , which gives values equivalent to those from the band

represented by $\mathbf{v} = 1, 0, 0$ for $-\frac{\pi}{a} \leq k_x \leq \frac{\pi}{a}$. Consider the band for which $\mathbf{v} = 0, 1, 0$. The energy of such a band is

$$\begin{aligned} (\mathbf{k} + \mathbf{G})^2 &= \left(k_x + v_1 \frac{2\pi}{a}\right)^2 + \left(k_y + v_2 \frac{2\pi}{a}\right)^2 + \left(k_z + v_3 \frac{2\pi}{a}\right)^2 \\ &= (k_x + 0)^2 + \left(k_y + \frac{2\pi}{a}\right)^2 + (k_z + 0)^2 . \end{aligned} \quad (2.97)$$

Along the [100] direction $k_y = k_z = 0$, so

$$(\mathbf{k} + \mathbf{G})^2 \Big|_{\mathbf{v}=010} = (k_x)^2 + \left(\frac{2\pi}{a}\right)^2 . \quad (2.98)$$

At $k_x = 0$, this energy is the same as for the band represented by $1, 0, 0$, i.e. $\epsilon(0) = \left(\frac{2\pi}{a}\right)^2$. However, at a non-zero value of k_x within the FBZ the energy differs between these two bands, where the band for which $\mathbf{v} = 1, 0, 0$ has energy $\epsilon(k_x) = \left(k_x \pm \frac{2\pi}{a}\right)^2$. This more complex band structure arising from increasing dimensionality is displayed in Figure 2.6.

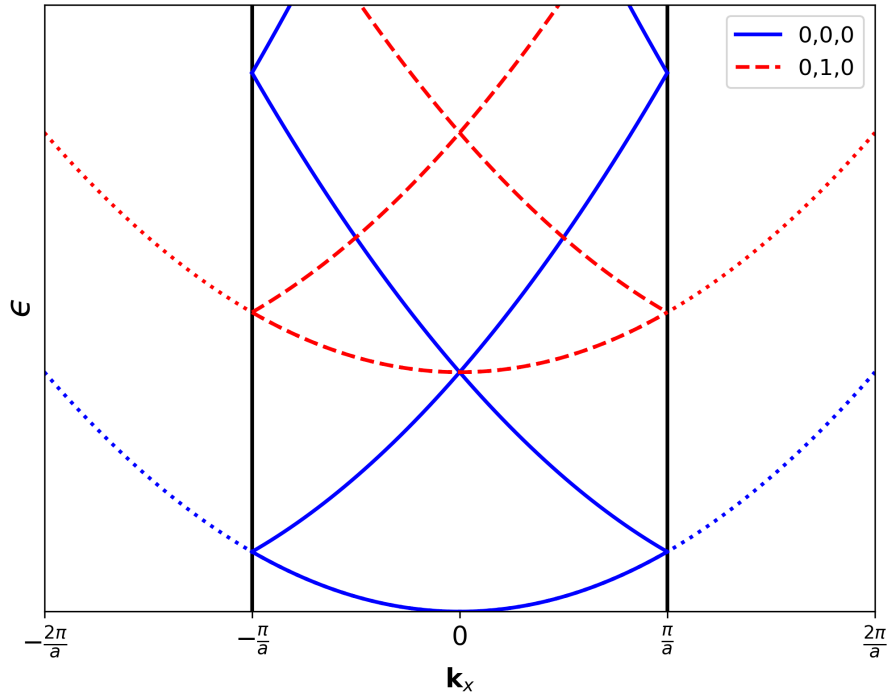


Figure 2.6: A plot of energy in the [100] direction (in units such that $\frac{\hbar^2}{2m_e} = 1$) against k_x for a three-dimensional empty lattice with free electron energy, in the reduced zone scheme. The solid blue line is for energy corresponding to the \mathbf{k} -point within the FBZ (i.e. $\mathbf{v} = 0, 0, 0$), and the dashed red line is that for $\mathbf{v} = 0, 1, 0$. The FBZ is delineated with solid vertical bars.

A more complex system than a simple cubic cell will produce a more complex band structure, but the procedure is the same. Consider a face-centered cubic cell in the same approximations as above. The primitive lattice vectors are $\mathbf{a}_1 = \frac{a}{2}\hat{y} + \frac{a}{2}\hat{z}$, $\mathbf{a}_2 = \frac{a}{2}\hat{x} + \frac{a}{2}\hat{z}$ and $\mathbf{a}_3 = \frac{a}{2}\hat{x} + \frac{a}{2}\hat{y}$ where a is the side length of the conventional unit cell. The reciprocal lattice vectors are therefore $\mathbf{b}_1 = \frac{2\pi}{a}(\hat{k}_y + \hat{k}_z - \hat{k}_x)$, $\mathbf{b}_2 = \frac{2\pi}{a}(\hat{k}_x + \hat{k}_z - \hat{k}_y)$ and $\mathbf{b}_3 = \frac{2\pi}{a}(\hat{k}_x + \hat{k}_y - \hat{k}_z)$, which is a body-centered cubic cell with conventional cell side of length $\frac{4\pi}{a}$.

The first Brillouin zone of such a system is displayed in Figure 2.7a, along with the positions of some critical points. It is typical to plot band structure between these critical points, and we can see that the Γ point is at the reciprocal cell origin and the X point is at $\frac{2\pi}{a}\hat{k}_y$. This is equivalent to points at $\pm\frac{2\pi}{a}$ in any cardinal direction. Plotting the energy between Γ and X leads us to define $\mathbf{k}' = \alpha\frac{2\pi}{a}\hat{x}$, where $0 \leq \alpha \leq 1$. $\alpha = 0$ represents the Γ point and $\alpha = 1$ represents the X point. As $\mathbf{k} = \mathbf{k}' + \mathbf{G}$, we notice that

$$\mathbf{k} = \alpha\frac{2\pi}{a}\hat{x} + v_1\mathbf{b}_1 + v_2\mathbf{b}_2 + v_3\mathbf{b}_3. \quad (2.99)$$

We can use this to plot energy along the $\Gamma \rightarrow X$ direction, with different reciprocal lattice vectors \mathbf{G} (differing in their v_1 , v_2 and v_3 values) to keep our wavevector within the FBZ. In units where $\frac{\hbar^2}{2m_e} = 1$, the energy of an electron is

$$\epsilon = k^2 = \frac{4\pi^2}{a^2} \left[(\alpha - v_1 + v_2 + v_3)\hat{k}_x + (v_1 - v_2 + v_3)\hat{k}_y + (v_1 + v_2 - v_3)\hat{k}_z \right]^2. \quad (2.100)$$

We let v_1 , v_2 and v_3 run through $-1 \leq v \leq 1$, $v \in \mathbb{Z}$ and plot the energy against k_x between Γ and X , shown in Figure 2.7b.

2.2.1 The nearly-free electron model

An improvement can be made to the above discussion of band structure, by maintaining the independent electron approximation, but dropping the empty lattice approximation i.e. we introduce a weak periodic potential as in subsection 2.1.2. This is the ‘nearly free electron’ model, and it works well to describe some metals where the contribution of

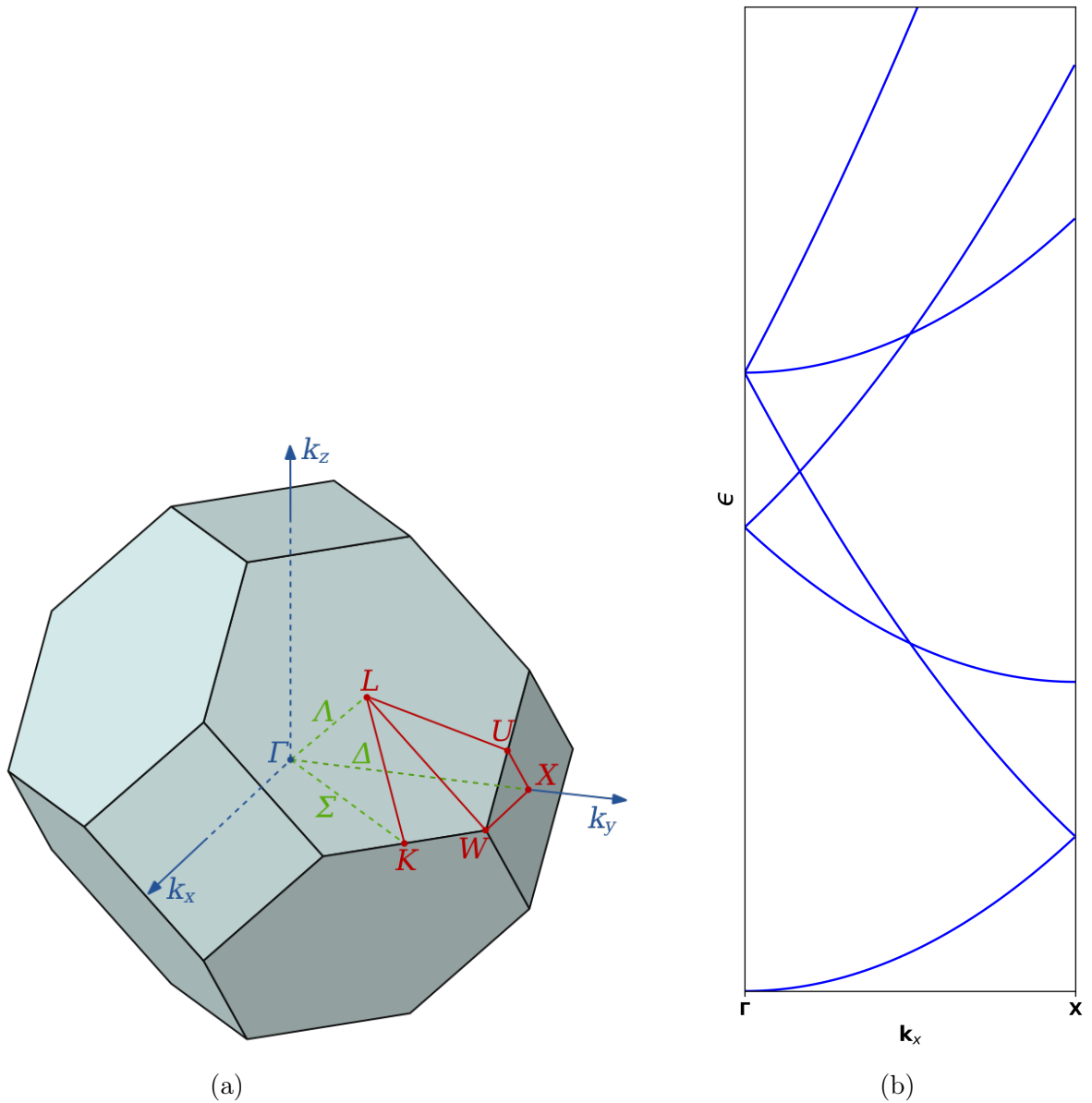


Figure 2.7: (a) The first Brillouin zone of a face-centered cubic lattice, where the planes delineating the FBZ are perpendicular planar bisectors of vectors between the lattice point at the centre of the conventional reciprocal cell and its nearest lattice points, such that any point in the space enclosed by the polyhedron is closer to the lattice point at the origin than any other. (b) A plot of energy between Γ and X in the FBZ of a face-centered cubic lattice against k_x in the empty lattice approximation with free electron energy, in the reduced zone scheme.

electron-electron and electron-ion interactions to the total potential felt by a conduction electron are significantly damped by the behavior of core electrons. The Pauli exclusion principle ensures that conduction electrons maintain a notable displacement from ions, not being able to get past the core electrons, and screening effects reduce the potential felt at larger displacements.

We can use the equivalent variation of the central equation (Equation 2.30) that is given in Appendix A, with solutions of the Bloch wavefunction form $\psi_{\mathbf{k}}(\mathbf{r}) = \sum_{\mathbf{G}} C_{\mathbf{k}-\mathbf{G}} e^{i(\mathbf{k}-\mathbf{G})\cdot\mathbf{r}}$ to show that in the case of a free electron ($U_{\mathbf{G}} = 0$), we have

$$\left(\frac{\hbar^2}{2m_e} (\mathbf{k} - \mathbf{G})^2 - \epsilon \right) C_{\mathbf{k}-\mathbf{G}} = 0 . \quad (2.101)$$

Non-trivial solutions require then that $\frac{\hbar^2}{2m_e} (\mathbf{k} - \mathbf{G})^2 = \epsilon$, which in the case of a non-degenerate system of electrons, may only occur for a single \mathbf{G} , which we shall denote \mathbf{G}_1 .

The non-degenerate case

Considering the non-degenerate case where there is only one reciprocal lattice vector, \mathbf{G}_1 , for which the equality $\frac{\hbar^2}{2m_e} (\mathbf{k} - \mathbf{G})^2 = \epsilon$ is true (in the free electron case). We introduce such a system to a periodic lattice, and treat the kinetic energy term as that of a free electron. As there is only one electron energy level satisfying this case, $\frac{\hbar^2}{2m_e} (\mathbf{k} - \mathbf{G}_1)^2 \neq \frac{\hbar^2}{2m_e} (\mathbf{k} - \mathbf{G}_n)^2$, $n \neq 1$, $n \in \mathbb{Z}$, and the difference between this energy level and any other is much larger than U . For all $\mathbf{G} \neq \mathbf{G}_1$ and fixed \mathbf{k} we therefore have $C_{\mathbf{k}-\mathbf{G}} = 0$. Our central equation is now in the form

$$(\epsilon - \epsilon_{\mathbf{k}-\mathbf{G}_1}) C_{\mathbf{k}-\mathbf{G}_1} = \sum_{\mathbf{G}} U_{\mathbf{G}-\mathbf{G}_1} C_{\mathbf{k}-\mathbf{G}} , \quad (2.102)$$

where for the purposes of reducing clutter we have made the notational substitution for an energy level corresponding to wavevector \mathbf{k} of

$$\epsilon_{\mathbf{k}} \equiv \frac{\hbar^2}{2m} \mathbf{k}^2 . \quad (2.103)$$

Expressing our central equation in terms of $C_{\mathbf{k}-\mathbf{G}}$, and separating the case of $\mathbf{G} = \mathbf{G}_1$ explicitly out of the the summation because of the requirement that it is much larger than for other \mathbf{G} (as a part of our initial premise), we have

$$\begin{aligned}
C_{\mathbf{k}-\mathbf{G}} &= \sum_{\mathbf{G}'} \frac{U_{\mathbf{G}'-\mathbf{G}} C_{\mathbf{k}-\mathbf{G}'}}{\epsilon - \epsilon_{\mathbf{k}-\mathbf{G}}} \\
&= \frac{U_{\mathbf{G}_1-\mathbf{G}} C_{\mathbf{k}-\mathbf{G}_1}}{\epsilon - \epsilon_{\mathbf{k}-\mathbf{G}}} + \sum_{\mathbf{G}' \neq \mathbf{G}_1} \frac{U_{\mathbf{G}'-\mathbf{G}} C_{\mathbf{k}-\mathbf{G}'}}{\epsilon - \epsilon_{\mathbf{k}-\mathbf{G}}} \\
&= \frac{U_{\mathbf{G}_1-\mathbf{G}} C_{\mathbf{k}-\mathbf{G}_1}}{\epsilon - \epsilon_{\mathbf{k}-\mathbf{G}}} + \mathcal{O}(U^2) ,
\end{aligned} \tag{2.104}$$

where the last term is of order U^2 because $C_{\mathbf{k}-\mathbf{G}'}$ vanishes in the limit of vanishing U for $\mathbf{G}' \neq \mathbf{G}_1$ i.e. it follows the order of U , where in the \mathbf{G}_1 case it does not.

Substituting this expression of $C_{\mathbf{k}-\mathbf{G}}$ in to Equation 2.102, we find that

$$\epsilon = \epsilon_{\mathbf{k}-\mathbf{G}_1} + \sum_{\mathbf{G}} \frac{|U_{\mathbf{G}-\mathbf{G}_1}|^2}{\epsilon_{\mathbf{k}-\mathbf{G}_1} - \epsilon_{\mathbf{k}-\mathbf{G}}} + \mathcal{O}(U^3) , \tag{2.105}$$

where we can see that energy levels, $\epsilon_{\mathbf{k}-\mathbf{G}}$, above that of $\epsilon_{\mathbf{k}-\mathbf{G}_1}$ decrease ϵ by an amount of order $\mathcal{O}(U^2)$, and energy levels below increase ϵ by the same order. That is to say that in the case of non-degeneracy, the value of ϵ for free electrons is of second order in U .

The near-degenerate case

We now consider the near-degenerate case, where we choose a value of \mathbf{k} such that there are a number, n , of \mathbf{G} values producing energy levels $\epsilon_{\mathbf{k}-\mathbf{G}_n}$ all close in energy to each other on the scale of U , but differing from any other energy levels not in this set of n , $\epsilon_{\mathbf{k}-\mathbf{G}}$, by an amount much greater than U . Our central equation is then a set of n equations, where we again separate the terms from the sum that do not have vanishing coefficients with vanishing U . The coefficients for a given energy level in near-degeneracy, $C_{\mathbf{k}-\mathbf{G}_i}$, $1 \leq i \leq n$, $i \in \mathbb{Z}$, where the energy levels that it is nearly degenerate with are $C_{\mathbf{k}-\mathbf{G}_j}$, $i \neq j$, $1 \leq j \leq n$, $j \in \mathbb{Z}$, and where the other energy levels that do not share

near-degeneracy have coefficients $C_{\mathbf{k}-\mathbf{G}}$ are then

$$\begin{aligned}
C_{\mathbf{k}-\mathbf{G}_i} &= \frac{1}{\epsilon - \epsilon_{\mathbf{k}-\mathbf{G}}} \left[\sum_{j=1}^n U_{\mathbf{G}_j-\mathbf{G}} C_{\mathbf{k}-\mathbf{G}_j} + \sum_{\mathbf{G}' \neq \mathbf{G}_i} U_{\mathbf{G}'-\mathbf{G}} C_{\mathbf{k}-\mathbf{G}'} \right] \\
&= \frac{1}{\epsilon - \epsilon_{\mathbf{k}-\mathbf{G}}} \sum_{j=1}^n U_{\mathbf{G}_j-\mathbf{G}} C_{\mathbf{k}-\mathbf{G}_j} + \mathcal{O}(U^2) , \quad (2.106) \\
\mathbf{G}_i &= \mathbf{G}_1, \dots, \mathbf{G}_n ,
\end{aligned}$$

which is in analogy with the above non-degenerate case. Evaluating the set of central equations with these coefficients gives

$$\begin{aligned}
(\epsilon - \epsilon_{\mathbf{k}-\mathbf{G}_i}) C_{\mathbf{k}-\mathbf{G}_i} &= \sum_{j=1}^n U_{\mathbf{G}_j-\mathbf{G}_i} C_{\mathbf{k}-\mathbf{G}_j} + \sum_{j=1}^n \left[\sum_{\mathbf{G}' \neq \mathbf{G}_i} \frac{U_{\mathbf{G}-\mathbf{G}_i} U_{\mathbf{G}_j-\mathbf{G}}}{\epsilon - \epsilon_{\mathbf{k}-\mathbf{G}}} \right] C_{\mathbf{k}-\mathbf{G}_j} + \mathcal{O}(U^3) , \\
\mathbf{G}_i &= \mathbf{G}_1, \dots, \mathbf{G}_n . \quad (2.107)
\end{aligned}$$

This leads to a larger change in the energy level value due to band repulsion when compared with the non-degenerate case (of order U compared to U^2), so we will consider the simplified case of two electrons in near-degeneracy for further discussion of how the nearly free electron model treats band repulsion and predicts the band gap.

Band gaps from the nearly free electron model

Consider now two electron levels in near degeneracy with each other, but energetically dissimilar from all other levels. The central equation for these levels becomes

$$\begin{aligned}
(\epsilon - \epsilon_{\mathbf{q}}) C_{\mathbf{q}} &= U_{\mathbf{G}} C_{\mathbf{q}-\mathbf{G}} \\
(\epsilon - \epsilon_{\mathbf{q}-\mathbf{G}}) C_{\mathbf{q}-\mathbf{G}} &= U_{-\mathbf{G}} C_{\mathbf{q}} = U_{\mathbf{G}}^* C_{\mathbf{q}} , \quad (2.108)
\end{aligned}$$

where $U(\mathbf{r})$ is real and $\mathbf{q} = \mathbf{k} - \mathbf{G}_1$, $\mathbf{G} = \mathbf{G}_2 - \mathbf{G}_1$ have been substituted to avoid notational clutter. If these levels were truly degenerate then their energies are equivalent, $\epsilon_{\mathbf{q}} = \epsilon_{\mathbf{q}-\mathbf{G}}$, and their wavevectors will meet in \mathbf{k} -space at the same point and have the same magnitude. As their vector origins differ by a reciprocal lattice vector that point will

be on a Bragg plane. As the energy levels are nearly degenerate with each other but far in energy value from all other levels, this condition is only met for wavevectors differing by the specific $\mathbf{G} = \mathbf{G}_2 - \mathbf{G}_1$ from our notation; importantly, not those levels $\epsilon_{\mathbf{q}-\mathbf{G}'}$, $\mathbf{G}' \neq \mathbf{G}$. This means that the point at which the degenerate level's wavevectors meet must only lie on the Bragg plane of \mathbf{G} , and not other \mathbf{G}' i.e. in the case of near-degeneracy, \mathbf{q} must be close to a Bragg plane, but cannot be near a point where multiple Bragg planes intersect.

Our central equations for the two nearly degenerate energy levels are coupled equations that can be represented as

$$\begin{bmatrix} \epsilon - \epsilon_{\mathbf{q}} & -U_{\mathbf{G}} \\ -U_{\mathbf{G}}^* & \epsilon - \epsilon_{\mathbf{q}-\mathbf{G}} \end{bmatrix} \begin{bmatrix} C_{\mathbf{q}} \\ C_{\mathbf{q}-\mathbf{G}} \end{bmatrix} = \begin{bmatrix} 0 \\ 0 \end{bmatrix} . \quad (2.109)$$

This has non-trivial solutions when the leading matrix is singular i.e.

$$\begin{vmatrix} \epsilon - \epsilon_{\mathbf{q}} & -U_{\mathbf{G}} \\ -U_{\mathbf{G}}^* & \epsilon - \epsilon_{\mathbf{q}-\mathbf{G}} \end{vmatrix} = 0 \quad (2.110)$$

$$\therefore (\epsilon - \epsilon_{\mathbf{q}}) (\epsilon - \epsilon_{\mathbf{q}-\mathbf{G}}) - |U_{\mathbf{G}}|^2 = 0 , \quad (2.111)$$

which can be rearranged for

$$\epsilon = \frac{\epsilon_{\mathbf{q}} + \epsilon_{\mathbf{q}-\mathbf{G}}}{2} \pm \sqrt{\left(\frac{\epsilon_{\mathbf{q}} + \epsilon_{\mathbf{q}-\mathbf{G}}}{2}\right)^2 + |U_{\mathbf{G}}|^2} . \quad (2.112)$$

This has the effect of perturbing bands near Brillouin zone boundaries, such that when $\mathbf{q} = \frac{\mathbf{G}}{2}$, the energy is reduced by $|U_{\mathbf{G}}|$ from its free electron energy; this produces a band gap of $2|U_{\mathbf{G}}|$, as the equivalent band approaching the Bragg plane from the other direction in \mathbf{k} -space (due to periodicity of the lattice) is increased by $|U_{\mathbf{G}}|$. This is displayed in Figure 2.8 and is responsible for the formation of band gaps, the structure of which need not be as simple as displayed.

A categorical distinction can be made between band gaps of two natures: direct and indirect. A direct band gap occurs when the valence band maximum and conduction band

minimum both occur at the same point in \mathbf{k} -space, as in Figure 2.8. An indirect band gap occurs when these energies occur at different points in \mathbf{k} -space. This has consequences for electron energy transitions, discussed in subsection 2.3.3.

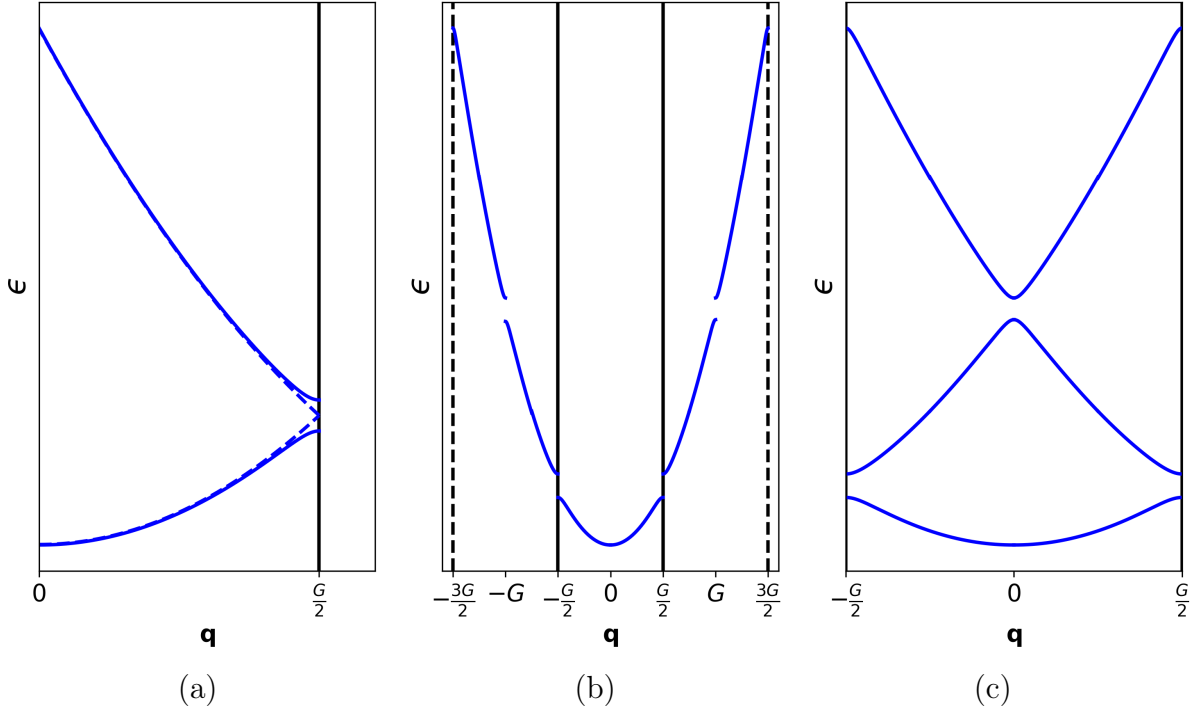


Figure 2.8: (a) Band repulsion in the simple one-dimensional case for two near-degenerate electrons (solid lines) compared to the free electron case (dashed lines). The difference between the two at a Bragg plane (here the positive \mathbf{q} boundary of the FBZ, $\mathbf{q} = \frac{G}{2}$), is $|2U_{\mathbf{G}}|$. The boundary of the FBZ is demarcated by solid vertical lines. (b) Band repulsion of the system shown in the extended zone scheme across additional Bragg planes. The boundary of the second Brillouin zone is additionally demarcated by dashed vertical lines. (c) The same system displayed in the reduced zone scheme. The y-axis scale is twice that in (b) and (c) as that in (a).

2.2.2 Wannier functions

A given band can be described by Bloch functions as a function of atomic wavefunctions. These wavefunctions for a crystalline system are Wannier functions, $\phi_{\mathbf{R}}$, and describe localized molecular orbitals. Our chosen band has a Fourier expansion of its Bloch states in the direct lattice, i.e.

$$\psi_{\mathbf{k}}(\mathbf{r}) = \sum_{\mathbf{R}} \phi_{\mathbf{R}}(\mathbf{r}) e^{i\mathbf{R}\cdot\mathbf{k}}. \quad (2.113)$$

The Fourier coefficients are the Wannier functions, which form an orthonormal set with dependence in \mathbf{R} :

$$\phi_{\mathbf{R}} = \frac{1}{V} \int_{\text{FBZ}} e^{-i\mathbf{R}\cdot\mathbf{k}} \psi_{\mathbf{k}}(\mathbf{r}) \delta\mathbf{k} . \quad (2.114)$$

The integration is over the FBZ, and V is the volume of the FBZ in \mathbf{k} -space. Wannier functions provide a real-space representation of electrons in a crystal, and so are a useful tool for describing phenomena local to an atomic site i.e. molecular bonding. By applying the correct choice of phase change to the Bloch states, which always results in valid Bloch states, one can localize the system's Wannier functions around lattice sites, where they will then vanish rapidly with increasing displacement from \mathbf{R} , greatly simplifying any problem. This process of transforming the Bloch states, which describe electron wavefunctions in reciprocal space, into localized Wannier functions in real-space is known as Wannierization. The process of Wannier interpolation is deployed in this project for extracting the band structure of hybrid functional calculations, the reasons for using and description of this method are given in subsection 3.3.1.

2.2.3 Spin-orbit coupling

An electron moving in an electric field (such as the periodic ion field in a crystal) experience a magnetic field in its frame of reference. This field interacts with the electron's magnetic moment, perturbing the Hamiltonian. As the magnetic moment originates from the particle's spin, this interaction is known as spin-orbit coupling, or the spin-orbit interaction. The interaction produces degeneracy splitting within energy levels due to opposing electronic spin states. In the non-relativistic limit, $\gamma \approx 1$, the magnetic field experienced by an electron around a hydrogenic atom in its own reference frame is

$$\mathbf{B} = \frac{1}{rm_e c^2} \frac{\delta U(\mathbf{r})}{\delta r} \mathbf{L} , \quad (2.115)$$

(see Appendix E) where \mathbf{L} is the angular momentum of the electron, U is the potential energy of the electron, and r here is the displacement from the ion. The perturbation to

the Hamiltonian by the spin-orbit interaction is

$$H_{SO} = H_L + H_T = \mu_B \frac{g_s - 1}{r \hbar m_e c^2} \frac{\delta U(\mathbf{r})}{\delta r} \mathbf{L} \cdot \mathbf{S} \quad (2.116)$$

where μ_B is the Bohr magneton, g_s is a proportionality constant, and the L and T subscripts denote Hamiltonian corrections due to the Larmor and Thomas interaction energies, respectively (see Appendix E), and \mathbf{S} is the spin angular momentum vector. The dot product $\mathbf{L} \cdot \mathbf{S}$ is a function of the electron's total angular momentum, j , orbital angular momentum, l , and spin, s , quantum numbers:

$$\mathbf{L} \cdot \mathbf{S} = \frac{\hbar^2}{2} (j(j+1) - l(l+1) - s(s+1)) . \quad (2.117)$$

Spin-orbit coupling can be an important phenomenon when discussing the band structure and energies of materials, as it lifts energy level degeneracy. This can alter the band gap of semi-conducting systems when compared to modelling without the spin-orbit interaction. The energy shift due to spin-orbit coupling depends on Z through r , so heavier elements suffer a greater effect. Beyond this, the spin-orbit interaction can induce magnetic anisotropy [62, 63] where the magnetic properties depend on the orientation of the magnetic field with respect to the underlying crystal lattice, and influences spin-dependent phenomena studied in the field of spintronics [64].

2.3 Semiconductors

Insulators and semiconductors are materials with only fully filled bands at 0 K and a band gap between the highest occupied band and the lowest unoccupied band, a range of energies for which there exists no permitted states i.e. the density of states is 0. If the band gap is large, few electrons will gain enough energy to move into the unoccupied band, and so no current will flow. This is an insulator. Semiconductors, however, have band gaps small enough that enough electrons can gain energy and jump to the lowest unoccupied level that charge can flow in an appreciable amount. The line between insulator and semiconductor is not well defined, and a poor insulator may well be considered a semiconductor.

A way in which electrons in the highest occupied band can gain enough energy to jump the band gap is through thermal excitation; the higher the temperature, the more electrons can transition to the next band (the lowest unoccupied band at 0 K). These bands are no longer fully occupied or unoccupied, and so will be called the valence band and the conduction band, respectively (collectively referred to as the frontier bands in reference to frontier orbitals, a subtly different concept). Now the conduction band is only mostly, but not completely, empty. This allows the electrons in the band to flow through unoccupied spaces and carry current. The valence band is similarly only mostly full, and the holes left by the transitioned electrons can also carry current. As such, the number of charge carriers is a function of temperature, increasing with temperature as $e^{-\frac{1}{T}}$. For metals, charge carrier density is independent of temperature, and so conductivity is reduced with increasing temperatures due to increased electron-phonon scattering. A pure material that displays semiconducting properties in the described manner is an intrinsic semiconductor. Semiconducting properties of an impure material can arise via the introduction of charge carriers through the impurities. This material would be an extrinsic semiconductor (which may also have intrinsic semiconducting qualities).

The number of charge carriers in the conduction band per unit volume of a semiconductor is the integral over the appropriate energy range of the density of states times the probability of any given electron being found within that energy range

with respect to energy. We denote this as $n_c(T)$ to demonstrate the temperature dependence, and similarly subscript the density of states of the conduction band as $D_c(\epsilon)$. So we have

$$n_c(T) = \int_{\epsilon_c}^{\infty} D_c(\epsilon) \frac{1}{e^{\frac{\epsilon-\mu}{k_B T}} + 1} \delta\epsilon \quad (2.118)$$

and similarly the number of charge carriers in the valence band,

$$p_v(T) = \int_{-\infty}^{\epsilon_v} D_v(\epsilon) \left(1 - \frac{1}{e^{\frac{\epsilon-\mu}{k_B T}} + 1} \right) \delta\epsilon = \int_{-\infty}^{\epsilon_v} D_v(\epsilon) \frac{1}{e^{\frac{\mu-\epsilon}{k_B T}} + 1} \delta\epsilon, \quad (2.119)$$

where we have used $p_v(T)$ to represent the number density of valence band charge carriers as these charge carriers will be holes with positive charge, and ϵ_c and ϵ_v are the energies at the bottom of the conduction band and top of the valence band, respectively. We assume that the impurity levels are not so high that the material becomes a degenerate semiconductor: a semiconductor with such a contribution to charge carriers from impurities that its behavior approaches that of a metal and no longer increases conductivity with temperature. In this case, $\epsilon_c - \mu \gg k_B T$ for ϵ above the conduction band minimum, and $\mu - \epsilon_v \gg k_B T$ for ϵ below the valence band maximum. We can test the validity of these assumptions in a self-consistent manner given specific information about impurity levels and the chemical potential of a real sample. So in the case of a non-degenerate semiconductor we have

$$n_c(T) \approx \int_{\epsilon_c}^{\infty} D_c(\epsilon) e^{-\frac{\epsilon-\mu}{k_B T}} \delta\epsilon \quad (2.120)$$

and

$$p_v(T) \approx \int_{-\infty}^{\epsilon_v} D_v(\epsilon) e^{-\frac{\mu-\epsilon}{k_B T}} \delta\epsilon. \quad (2.121)$$

We can define temperature functions that vary slowly compared to the exponential terms

required in $n_c(T)$ and $p_v(T)$ such that

$$n_c(T) = N_c(T) e^{-\frac{\epsilon_c - \mu}{k_B T}} \quad (2.122)$$

and

$$p_v(T) = P_v(T) e^{-\frac{\mu - \epsilon_v}{k_B T}}. \quad (2.123)$$

These functions are then

$$N_c(T) = \int_{\epsilon_c}^{\infty} D_c(\epsilon) e^{-\frac{\epsilon - \epsilon_c}{k_B T}} \delta\epsilon \quad (2.124)$$

and

$$P_v(T) = \int_{-\infty}^{\epsilon_v} D_v(\epsilon) e^{-\frac{\epsilon_v - \epsilon}{k_B T}} \delta\epsilon. \quad (2.125)$$

The charge carriers in frontier bands will tend to be close in energy to the band extrema, ϵ_c and ϵ_v , as the excited electrons must first cross the semiconductor band gap, $\epsilon_g = \epsilon_c - \epsilon_v$. As excitation energy increases, the likelihood of carriers transitioning far from these extrema decreases due to the higher energy barrier. As such, the energy-wavevector relation of charge carriers in such a semiconductor can be approximated as the local band structure close to the band extrema:

$$\epsilon(\mathbf{k}) = \epsilon_c + \frac{\hbar^2 \mathbf{k}^2}{2m_e^*} = \epsilon_c + \hbar^2 \sum_{ab} k_a (\mathbf{M}_e^{-1})_{ab} k_b \quad (2.126)$$

for electrons in the conduction band, and similarly

$$\epsilon(\mathbf{k}) = \epsilon_v - \frac{\hbar^2 \mathbf{k}^2}{2m_h^*} = \epsilon_v - \hbar^2 \sum_{ab} k_a (\mathbf{M}_h^{-1})_{ab} k_b \quad (2.127)$$

for holes, where m^* and \mathbf{M} are the effective particle mass and the effective mass tensor. Due to this approximation, and by using Equation 2.12, we can say that the density of

states function for the frontier bands can be approximated as

$$D_{c,v}(\epsilon) = \sqrt{2|\epsilon - \epsilon_{c,v}|} \frac{m_{c,v}^{\frac{3}{2}}}{\hbar^3 \pi^2}, \quad (2.128)$$

where $m_{c,v}^{\frac{3}{2}}$ is the determinant of the effective mass tensor for electrons in the conduction band i.e. the product of its principle values, or equivalent for holes in the valence band. Substituting this in to our slow varying temperature functions, we get

$$N_c(T) = \frac{1}{4} \left(\frac{2m_c k_B T}{\pi \hbar^2} \right)^{\frac{3}{2}} \quad (2.129)$$

and

$$P_v(T) = \frac{1}{4} \left(\frac{2m_v k_B T}{\pi \hbar^2} \right)^{\frac{3}{2}} \quad (2.130)$$

We can remove the dependence on μ from the carrier densities n_c and p_v by taking their product, resulting in the law of mass action,

$$n_c p_v = N_c P_v e^{-\frac{\epsilon_G}{k_B T}}. \quad (2.131)$$

As this is independent of μ , if the concentration of one type of carrier is known, so is the other. This is regardless of the levels of impurity in a sample, although if impurities contribute significantly to the semiconductor's behavior the treatment of this equation becomes more complicated through μ : both intrinsic and extrinsic semiconductors obey this law so long as they maintain their non-degeneracy.

In an intrinsic semiconductor where the impact of impurities on carrier density is insignificant,

$$n_c(T) = p_v(T) \quad (2.132)$$

where we can commonly represent these parameters as the intrinsic number density, n_i .

As such,

$$n_i(T) = [N_c(T) P_v(T)]^{\frac{1}{2}} e^{-\frac{\epsilon_G}{2k_B T}} . \quad (2.133)$$

Assessing our above expressions for $n_i(T)$ and $p_v(T)$ as an equality, we find that

$$n_i(T) = p_v(T) \quad (2.134)$$

and

$$[N_c(T) P_v(T)]^{\frac{1}{2}} e^{-\frac{\epsilon_G}{2k_B T}} = P_v(T) e^{-\frac{\mu - \epsilon_v}{k_B T}} \quad (2.135)$$

which is true in that μ is the intrinsic chemical potential, μ_i ,

$$\mu = \mu_i = \epsilon_v + \frac{1}{2}\epsilon_G + \frac{3k_B T}{4} \ln \frac{m_v}{m_c} . \quad (2.136)$$

We can see that as $T \rightarrow 0$, $\mu_i \rightarrow \epsilon_v + \frac{1}{2}\epsilon_G$ i.e. at absolute zero the intrinsic chemical potential lies in the middle of the band gap. As the effective masses of holes and electrons are similar, the temperature dependent term will not exceed order $k_B T$, and so the intrinsic chemical potential will not vary from the centre of the band gap by more than order $k_B T$. At low enough temperatures that the band gap is large compared to $k_B T$, then, the intrinsic chemical potential will not approach the edges of the band gap, ϵ_c or ϵ_v . Our original assumption to treat our semiconductor as non-degenerate holds in the intrinsic case so long as the band gap is large compared to $k_B T$, a condition that is true at room temperature for almost all pure semiconductors.

2.3.1 Doping

While high levels of impurities can cause degeneracy, in the case of a non-degenerate extrinsic semiconductor where impurities are an important contributor to carrier concentration but the law of mass action (Equation 2.131) still holds, the additional

carriers from the impurities can be treated in a term for carrier density deviation from the intrinsic case, $\Delta n = n_c - p_v$. Considering deviation from the intrinsic case,

$$n_c - p_v = \Delta n , \quad (2.137)$$

where we make a substitution in terms of the intrinsic number density for

$$n_c - \frac{n_i^2}{n_c} - \Delta n = 0 , \quad (2.138)$$

and therefore

$$n_c = -\frac{-\Delta n \pm \sqrt{(-\Delta n)^2 - 4(-n_i^2)}}{2} . \quad (2.139)$$

The two alternate solutions here physically represent the carrier concentration of electrons or holes, and which one is represented by the plus or minus is dependent on the particular impurity. So, in terms of intrinsic behavior, the extrinsic carrier concentrations are

$$n_c = \frac{1}{2} (\Delta n^2 + 4n_i^2)^{\frac{1}{2}} + \frac{\Delta n}{2} \quad (2.140)$$

and

$$p_v = \frac{1}{2} (\Delta n^2 + 4n_i^2)^{\frac{1}{2}} - \frac{\Delta n}{2} , \quad (2.141)$$

where we allow the sign of the value of Δn to hold the information specific to the particular source of impurity. In the extrinsic case, then, we can see that either electrons or holes will be the dominant carrier type; for positive Δn (where impurities contribute extra electrons) and as $\frac{n_i}{\Delta n} \rightarrow 0$, $n_c \rightarrow \Delta n$ and $p_v \rightarrow 0$. The opposite is true for negative Δn , the case where impurities contribute holes instead. This results in extrinsic semiconductors with primarily electrons as charge carriers, referred to as a negative-type semiconductor (n-type), or primarily holes as charge carriers, referred to as a positive-type semiconductor (p-type). For the purposes of device engineering, it can be beneficial to intentionally

add impurities to an intrinsic semiconductor in a process known as doping. The dopant can be either a donor or acceptor, referring to whether the introduced impurity donates an electron to the conduction band (to create an n-type semiconductor) or accepts an electron to create a hole in the valence band (to create a p-type semiconductor).

In the case of a substitutional defect, an impurity in which an atom of the pristine crystal is replaced by another, we can model a donor impurity as a perturbation of the crystal equivalent to adding a positive point charge at a lattice site and additional valence electrons. For a simple case where the added point charge is of magnitude e and only one additional electron is added, we can consider a silicon lattice with a phosphorus substitutional defect. The point charge can bind this additional electron, but as it occurs in the medium of the existing semiconductor, the binding energy is reduced by the static relative permittivity of the silicon lattice. As the electron is moving in the crystal medium, it is described by the semiclassical energy

$$\epsilon(\mathbf{k}) = \epsilon_c + \frac{\hbar^2 \mathbf{k}^2}{2m_e^*} . \quad (2.142)$$

The additional electron has energy states of the conduction band, perturbed by the impurity point charge, $+e$ i.e. the second energy term can be modelled as a hydrogenic problem with electronic effective mass m^* around a charge $+e/\epsilon$. This gives a ground-state binding energy of

$$\epsilon_b = \frac{e^4 m^*}{\hbar^2 \epsilon^2} , \quad (2.143)$$

resulting in a very small binding energy compared to the case of the atom in free space. Since semiconductors by their nature have an electronic structure that permits charge carrier transition, they have high relative permittivity. This fact, in addition to the low effective masses of such impurity electrons, results in the binding energy of our donor impurity and an electron being significantly less than the band gap observed in semiconductors. This binding energy has the effect of pulling the electronic energy level down from where the electron would otherwise be (the bottom of the conduction band),

introducing a permitted donor energy state, $\epsilon_D = \epsilon_c - \epsilon_b$. As ϵ_b is much smaller than ϵ_G , this new state arising from the introduced impurity sits near the top of the band gap. The analogue to this is the expected outcome for an acceptor impurity e.g. boron in a silicon lattice, where the new permitted acceptor energy state is $\epsilon_A = \epsilon_v + \epsilon_b$.

2.3.2 Inhomogeneous semiconductors

Inhomogeneous semiconductors are characterized by spatial variations in their composition or structure, leading to non-uniform electronic properties across different regions or interfaces within the material. This phenomenon is best illustrated in the case of an impurity gradient across a short distance and centred on a simple spatial plane in a single crystal, resulting in distinct n-type behavior on one side of the sharply gradated region and p-type behavior on the other. Such a region is known as a p-n junction. We will here consider an abrupt junction at $x = 0$, where the donor impurity density is zero at $x < 0$ and the acceptor impurity density is zero at $x > 0$, and are both otherwise positive and constant.

The diffusion of majority carriers across the p-n junction leaves behind charged impurity ions that cannot diffuse, resulting in an electrostatic potential, $\phi(x)$. This potential will balance thermal migration, as the resultant electric field reduces diffusion and reaches an equilibrium state.

The semiclassical energy of an electron in band n in a potential ϕ is $\epsilon_n - e\phi$, and so our carrier densities from the previously discussed homogeneous case are now

$$n_c(x) = N_c(T) e^{-\frac{\epsilon_c - e\phi(x) - \mu}{k_B T}} \quad (2.144)$$

and

$$p_v(x) = P_v(T) e^{-\frac{\mu - \epsilon_v + e\phi(x)}{k_B T}} \quad (2.145)$$

in the inhomogeneous case. These densities can be determined self-consistently. Far from the p-n junction, we have potentials of $\phi(x) = \phi(\infty)$ where the concentration of donor

atoms is $N_D = n_c(\infty)$, and $\phi(x) = \phi(-\infty)$ where the concentration of acceptor atoms is $N_A = p_v(-\infty)$. The potential drop across the junction between the n-side and p-side, $\Delta\phi_0 = \phi(\infty) - \phi(-\infty)$, for the case of thermal equilibrium (where μ is constant) is

$$\Delta\phi_0 = \frac{1}{e} \left(\epsilon_G + k_B T \ln \left[\frac{N_D N_A}{N_c P_v} \right] \right) . \quad (2.146)$$

The subscript denotes that this is the potential drop across the junction in the case of zero applied voltage.

We define frontier energies and local impurity energies as functions of position and use these alongside a constant μ to represent band energies across the p-n junction, i.e.

$$\epsilon_c(x) = \epsilon_c - e\phi(x) \quad (2.147)$$

$$\epsilon_v(x) = \epsilon_v - e\phi(x) \quad (2.148)$$

$$\epsilon_D(x) = \epsilon_D - e\phi(x) \quad (2.149)$$

$$\epsilon_A(x) = \epsilon_A - e\phi(x) . \quad (2.150)$$

A plot of these energies considered in this manner is given in Figure 2.9. The effect of perturbation of energy levels near the p-n junction with respect to a constant μ is called band bending.

The overall charge density due to carriers and impurities is

$$\rho(x) = e(N_D(x) - N_A(x) + p_v(x) - n_c(x)) . \quad (2.151)$$

If we assume that ϕ varies only over a small region around $x = 0$ between the boundaries of a depletion layer at positions $-d_p$ and d_n , then outside of this region ϕ approaches its value at $\phi(\pm\infty)$, depending on which side of the p-n junction is considered. At values of $x > d_n$, the donor atoms are too far from the p-n junction for their donated electrons to migrate across the junction, and so $n_c = N_D$, and in our simple case we also have $N_A = p_v = 0$ at these positions. For values of $x < d_p$, the equivalent is true for acceptors and holes; $p_v = N_A$ and $N_D = n_c = 0$. Therefore, outside of the depletion

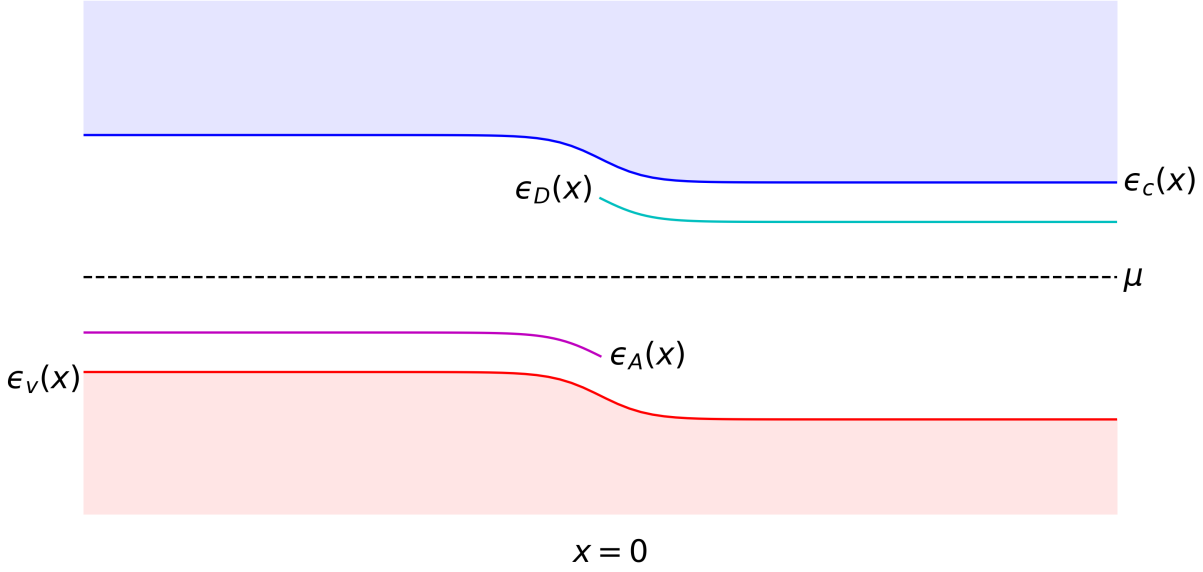


Figure 2.9: Energy against x position of an inhomogeneous semiconductor with an abrupt p-n junction in the plane $x = 0$. With μ set as a constant between the p- and n-side, ϵ_c and ϵ_v are functions of position, as are the impurity levels ϵ_D and ϵ_A . The effect of the internal potential ψ is to produce band bending near the p-n junction.

layer, $\rho(x) = 0$. Within the depletion layer far from the boundaries the charge carriers do migrate across the p-n junction, and so $n_c \ll N_D$ and $p_v \ll N_A$, resulting in a charge density $\rho(x) = e(N_D(x) - N_A(x))$. If the depletion layer is large on the scale of interatomic distance, we can consider Poisson's equation of electrostatics to relate the charge density to the potential, and so at values not near the boundaries of the depletion layer,

$$\nabla^2 \phi(x) = \begin{cases} 0, & x < -d_p \\ \frac{4\pi e N_A}{\epsilon}, & -d_p < x < 0 \\ -\frac{4\pi e N_D}{\epsilon}, & d_n > x > 0 \\ 0, & x > d_n. \end{cases} \quad (2.152)$$

We note that ϕ outside of the depletion layer is $\phi(\pm\infty)$ by construction, so we can apply the condition that this and its first derivative is continuous across the boundaries $x = d_n$ and $x = -d_p$, and thus integrate the above terms to recover $\phi(x)$ within the depletion

layer:

$$\nabla\phi(x) = \begin{cases} 0, & x < -d_p \\ \frac{4\pi e N_A}{\varepsilon} (x + d_p), & -d_p < x < 0 \\ -\frac{4\pi e N_D}{\varepsilon} (x - d_n), & d_n > x > 0 \\ 0, & x > d_n, \end{cases} \quad (2.153)$$

$$\phi(x) = \begin{cases} \phi(-\infty), & x < -d_p \\ \phi(-\infty) + \frac{2\pi e N_A}{\varepsilon} (x + d_p)^2, & -d_p < x < 0 \\ \phi(\infty) - \frac{2\pi e N_D}{\varepsilon} (x - d_n)^2, & d_n > x > 0 \\ \phi(\infty), & x > d_n. \end{cases} \quad (2.154)$$

If we insist that excess charge on either side of the p-n junction is equivalent to the other i.e. ϕ and its first derivative are continuous at $x = 0$, then

$$\frac{4\pi e N_A}{\varepsilon} (x + d_p) \Big|_{x=0} = -\frac{4\pi e N_D}{\varepsilon} (x - d_n) \Big|_{x=0}, \quad (2.155)$$

and therefore

$$N_A d_p = N_D d_n, \quad (2.156)$$

and

$$\phi(-\infty) + \frac{2\pi e N_A}{\varepsilon} (x + d_p)^2 \Big|_{x=0} = \phi(\infty) - \frac{2\pi e N_D}{\varepsilon} (x - d_n)^2 \Big|_{x=0}, \quad (2.157)$$

and therefore

$$\Delta\phi_0 = \frac{2\pi e}{\varepsilon} (N_A d_p^2 + N_D d_n^2). \quad (2.158)$$

We can use these expressions to determine the size of the depletion layer:

$$\Delta\phi_0 = \frac{2\pi e}{\varepsilon} \left(N_A \left(\frac{N_D d_n}{N_A} \right)^2 + N_D d_n^2 \right) = \frac{2\pi e}{\varepsilon} d_n^2 \left(\frac{N_D^2 + N_D N_A}{N_A} \right) \quad (2.159)$$

$$\therefore d_n = \left(\frac{\varepsilon \Delta\phi_0}{2\pi e} \frac{N_A}{N_D (N_A + N_D)} \right)^{\frac{1}{2}} \quad (2.160)$$

and similarly

$$d_p = \left(\frac{\varepsilon \Delta\phi_0}{2\pi e} \frac{N_D}{N_A (N_A + N_D)} \right)^{\frac{1}{2}} . \quad (2.161)$$

These can be combined in the form

$$d_{n,p} = \left(\frac{\varepsilon \Delta\phi_0}{2\pi e} \frac{1}{(N_A + N_D)} \right)^{\frac{1}{2}} \left(\frac{N_A}{N_D} \right)^{\pm \frac{1}{2}} \quad (2.162)$$

$$d_t = \left(\frac{\varepsilon \Delta\phi_0}{2\pi e (N_A + N_D)} \right)^{\frac{1}{2}} \left(\sqrt{\frac{N_A}{N_D}} + \sqrt{\frac{N_D}{N_A}} \right) ,$$

where the positive index is for d_n and the negative for d_p , and the total size of the depletion layer is $d_t = d_n + d_p$.

Carrier dynamics under applied bias

So far we have considered the simple case of an abrupt p-n junction with constant impurity concentrations on each respective side of the junction, in the absence of external fields. We now consider the same junction with an applied voltage, V . We assume that the potential only varies around the depletion layer, warranted by the reduced charge carrier density in the depletion region increasing resistance significantly above that found at positions far from $x = 0$. The potential drop across the junction between the n-side and the p-side is then

$$\Delta\phi = \Delta\phi_0 - V , \quad (2.163)$$

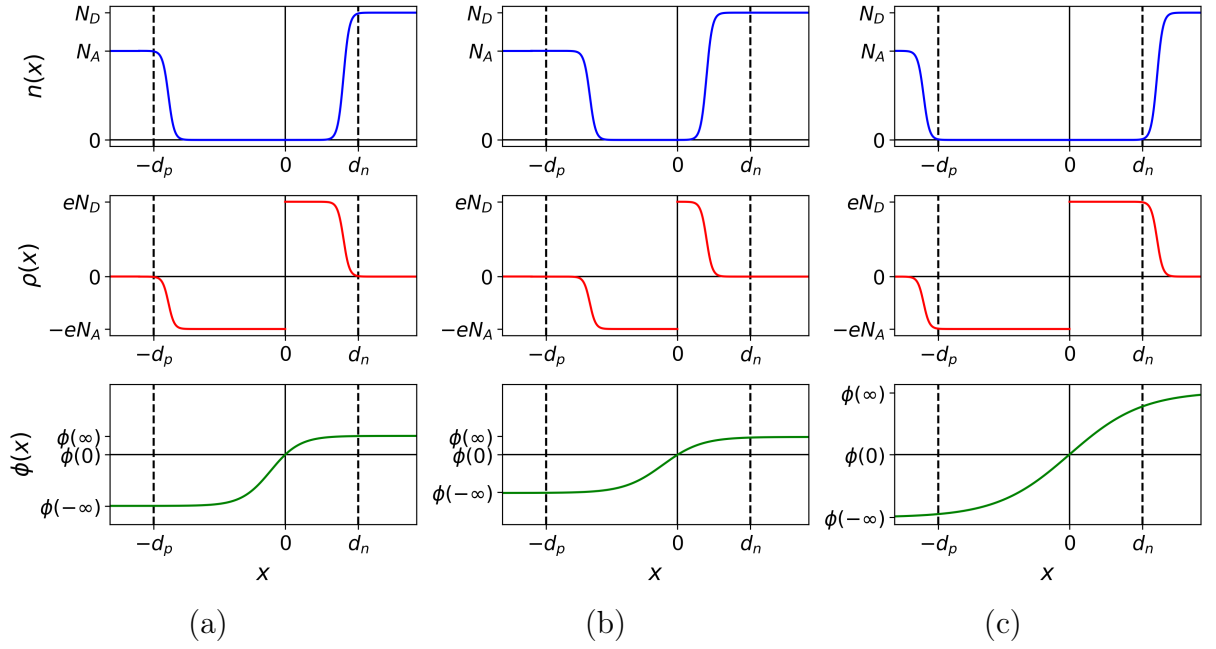


Figure 2.10: A comparison of carrier density $n(x)$, charge density $\rho(x)$, and potential $\phi(x)$, near a p-n junction at $x = 0$, under the conditions of (a) an unbiased junction ($V = 0$), (b) a forward biased junction, (c) a reverse biased junction. The edges of the depletion layer, $-d_p$ and d_n , are shown at their unbiased values for comparison.

which has V defined in the opposite direction to ϕ : a positive V increases the p-side potential with respect to the n-side. In the case of an inhomogeneous semiconductor device with applied voltage defined in this way, forward bias is a positive V and reverse bias is negative. We can replace the $\Delta\phi_0$ variable in Equation 2.162 with $\Delta\phi$ for an applied voltage-dependant expression of the size of the depletion layer,

$$d_{n,p}(V) = d_{n,p}(0) \left(1 - \frac{V}{\Delta\phi_0}\right)^{\frac{1}{2}}. \quad (2.164)$$

Examining our expressions for the spatial extent of the depletion layer and change in potential in response to applied bias leads us to say that a forward bias shrinks the depletion layer and the change in potential and a reverse bias does the opposite, with respect to the unbiased case. A comparison of bias cases is displayed in Figure 2.10.

Consider electrons in the p-type material, outside of the depletion layer ($x < -d_p$), where they are minority carriers. Some will be thermally excited out of the valence band and diffuse across the $x = -d_p$ boundary, where the induced electric field of the depletion layer will drive them to the n-side of the p-n junction. Such a flow of electrons is the

electron number generation current density, J_e^{gen} . The current is not dependant on the (non-zero) magnitude of the potential drop across the junction, only its direction and rate of diffusion: all electrons diffusing into the depletion layer from the p-side will be driven to the n-side by the induced electric field, and the field strength does not impact the number of electrons thus diffusing. There is an opposing current whereby electrons in the n-type material that possess sufficient thermal energy to overcome the induced electric field can flow across the p-n junction. Any carriers that undergo this process become excess minority carriers, and inevitably recombine with one of their opposite, more abundant, counterparts. As such, this current is that with electron number recombination current density, J_e^{rec} . The contrary currents for holes, J_h^{gen} and J_h^{rec} , operate in the same manner. In equilibrium with no applied voltage, the carrier recombination and generation currents must be equivalent, as there is no net current across the p-n junction. In either case, the number of electrons that can contribute to the recombination current is determined by their energy distribution. The concentration of carriers in non-degenerate semiconducting systems is low, so we can ignore electron-electron interactions and treat them as moving independently and following Maxwell-Boltzmann statistics. We then have

$$J_e^{\text{rec}} = J_e^{\text{gen}} , \quad V = 0 \quad (2.165)$$

where

$$J_e^{\text{rec}} \propto e^{-e \frac{\Delta\phi_0 - V}{k_B T}} , \quad (2.166)$$

therefore

$$\therefore J_e^{\text{rec}} = J_e^{\text{gen}} e^{\frac{eV}{k_B T}} , \quad (2.167)$$

and so

$$J_e = J_e^{\text{rec}} - J_e^{\text{gen}} = J_e^{\text{gen}} \left(e^{\frac{eV}{k_B T}} - 1 \right) . \quad (2.168)$$

The net electrical current density is then

$$j = j_h - j_e = eJ_h - (-e)J_e = e(J_e^{\text{gen}} + J_h^{\text{gen}}) \left(e^{\frac{eV}{k_B T}} - 1 \right) \quad (2.169)$$

This is an asymmetric function in V , leading to diode-like behavior. At $V = 0$, the net current density is 0. At positive V , the function increases exponentially, but at negative V the exponential term goes to 0 and the function quickly approaches an asymptotic value of

$$j_{\text{sat}} = -e(J_e^{\text{gen}} + J_h^{\text{gen}}) . \quad (2.170)$$

This is the saturation current density, providing the highest magnitude current possible under reverse bias. As the magnitude of the generation currents are small, this value of j_{sat} is small, giving the result that forward bias is the bias direction of good current flow, and reverse bias is the direction of greatly reduced flow.

The saturation current

To find the value of j_{sat} , we must determine a form for the generation current densities. Consider the drift current, that which is due to the electric field, and the diffusion current, that which is due to a carrier density gradient. The carrier number densities can be represented as a sum of these two currents modified by some constants:

$$J_e = -\mu_n n_c E - D_n \frac{\delta n_c}{\delta x} \quad (2.171)$$

$$J_h = \mu_p p_v E - D_p \frac{\delta p_v}{\delta x} . \quad (2.172)$$

The first term of each is the carrier drift current with positive proportionality constants μ . If there exists no electron density gradient in a system where we consider electrons to

be the sole charge carriers by construction, then

$$J_e = -\mu_n n_c E \quad (2.173)$$

$$j = -eJ_e = \sigma E , \quad (2.174)$$

where σ is the conductivity. The conductivity can be experimentally measured, and is given by the Drude model as

$$\sigma = \frac{ne^2\tau}{m_e} , \quad (2.175)$$

, which leads to

$$\mu_n = \frac{e\tau_n}{m_n^*} . \quad (2.176)$$

For a physical interpretation, we consider the electronic acceleration

$$a_n = \frac{F}{m_n^*} = -\frac{eE}{m_n^*} , \quad (2.177)$$

and velocity

$$v_n = a_n\tau_n = -\frac{e\tau_n}{m_n^*} E , \quad (2.178)$$

which leads to

$$v_n = -\mu_n E , \quad (2.179)$$

i.e. μ_n is the electron mobility. Similarly, the hole mobility is

$$\mu_p = \frac{e\tau_p}{m_p^*} . \quad (2.180)$$

The second term in our expressions for the carrier number densities is the diffusion current. In the case of thermal equilibrium, there must be no net current and so the drift current

must cancel out the diffusion current. Considering again an electron-only system, we have

$$0 = J_{\text{drift}} + J_{\text{diffusion}} = -\mu_n n_c E - D_n \frac{\delta n_c}{\delta x} . \quad (2.181)$$

For non-interacting particles like our low-concentration electrons or holes behaving according to Maxwell-Boltzmann statistics, the local potential energy, U , uniquely defines the particle density, n . For particles of charge q in one dimension, and dropping explicit terms for treating holes and electrons separately, we have then

$$\frac{\delta n}{\delta x} = \frac{\delta n}{\delta U} \frac{\delta U}{\delta x} = \frac{\delta n}{\delta U} qE , \quad (2.182)$$

therefore

$$-\mu_n E - D \frac{\delta n}{\delta U} qE = 0 , \quad (2.183)$$

where

$$D = -\frac{\mu_n}{q} \left(\frac{\delta n}{\delta U} \right)^{-1} . \quad (2.184)$$

For Maxwellian particles where A is a constant related to total particle number,

$$n = A e^{-\frac{U}{k_B T}} \quad (2.185)$$

and

$$\frac{\delta n}{\delta U} = -\frac{1}{k_B T} A e^{-\frac{U}{k_B T}} = -\frac{1}{k_B T} n . \quad (2.186)$$

We can then determine a relationship between the mobility constants and the diffusion constants;

$$D = \frac{\mu k_B T}{q} . \quad (2.187)$$

The rate of change of carrier density is determined by the rate of charge carrier flow across a region of interest, modified by the rate of generation and recombination of carriers, i.e.

$$\left(\frac{\delta n}{\delta t}\right)_{\text{total}} = \left(\frac{\delta n}{\delta t}\right)_{\text{gr}} - \frac{\delta J}{\delta x}, \quad (2.188)$$

where the subscript *gr* represents the rate of change of density due to generation and recombination. This rate of change in density depends on the equilibrium values of carrier densities, where the balance of generation against recombination will shift in order to move the system towards equilibrium; higher carrier densities result in more recombination and oppose generation. The rate of change of carrier density is then proportional to the difference between its current value and its expected value as determined by the law of mass action (Equation 2.131), the intrinsic number density, n_i , given the density of the other carrier. For electrons,

$$\left(\frac{\delta n_c}{\delta t}\right)_{\text{gr}} \propto n_c - \frac{n_i^2}{p_v}, \quad (2.189)$$

and for holes

$$\left(\frac{\delta p_v}{\delta t}\right)_{\text{gr}} \propto p_v - \frac{n_i^2}{n_c}. \quad (2.190)$$

The proportionality constant relates to the expected lifetime of a carrier between generation and recombination, τ_r , known as the recombination time:

$$\left(\frac{\delta n_c}{\delta t}\right)_{\text{gr}} = -\frac{1}{\tau_{r,n}} \left(n_c - \frac{n_i^2}{p_v}\right), \quad (2.191)$$

and similarly for holes. The term

$$-\frac{n_c}{\tau_{r,n}} \quad (2.192)$$

represents the number of electrons lost to recombination, and the term

$$+\frac{n_i^2}{p_v\tau_{r,n}} \quad (2.193)$$

represents those generated. If carrier densities are constant in time, such as with a static applied bias, we have the steady-state equilibrium conditions of

$$\frac{\delta J_e}{\delta x} + \frac{1}{\tau_{r,n}} \left(n_c - \frac{n_i^2}{p_v} \right) = 0 \quad (2.194)$$

$$\frac{\delta J_h}{\delta x} + \frac{1}{\tau_{r,p}} \left(p_v - \frac{n_i^2}{n_c} \right) = 0 . \quad (2.195)$$

In the case of a small electric field and constant majority carrier density, the minority carrier drift current is very small compared to the minority carrier diffusion current and can be ignored. Considering electrons, we have then

$$\lim_{E \rightarrow 0} J_e = -D_n \frac{\delta n_c}{\delta x} , \quad (2.196)$$

$$\frac{\delta J_n}{\delta x} = -D_n \frac{\delta^2 n_c}{\delta x^2} , \quad (2.197)$$

so therefore

$$D_n \frac{\delta^2 n_c}{\delta x^2} = \frac{1}{\tau_{r,n}} \left(n_c - \frac{n_i^2}{p_v} \right) , \quad (2.198)$$

and

$$D_p \frac{\delta^2 p_v}{\delta x^2} = \frac{1}{\tau_{r,p}} \left(p_v - \frac{n_i^2}{n_c} \right) \quad (2.199)$$

for holes.

Consider a position, $x_0 > 0$ in the n-type material (where the p-n junction is at $x = 0$) far enough away from the junction such that the density towards which the law of mass action tends towards $\left(\frac{n_i^2}{n_c}\right)$ is the minority carrier density of the n-type semiconductor at very large displacements, $p(\infty)$, but not so far from the depletion layer that the minority

charge carrier density has reached this equilibrium value. We can introduce a trial solution for the behavior of the minority charge carrier density, in this case $p_v(x)$, of

$$p_v(x) = p_v(\infty) + e^{-\frac{x-x_0}{L_p}} [p_v(x_0) - p_v(\infty)] , \quad (2.200)$$

where $L_p = \sqrt{\tau_{r,p}D_p}$. We test this trial solution in our above relations:

$$\begin{aligned} \frac{\delta^2 p_v(x)}{\delta x^2} &= \frac{1}{L_p^2} e^{-\frac{x-x_0}{L_p}} [p_v(x_0) - p_v(\infty)] \\ &= \frac{1}{L_p^2} [p_v(x) - p_v(\infty)] , \end{aligned} \quad (2.201)$$

therefore

$$\frac{D_p}{L_p^2} [p_v(x) - p_v(\infty)] = \frac{1}{\tau_{r,p}} \left(p_v - \frac{n_i^2}{n_c} \right) , \quad (2.202)$$

which for the stated L_p and above conditions on the equilibrium density, $p_v(\infty)$, is true, validating our trial solution. Examination of the above trial solution provides a physical interpretation of L_p : as L_p becomes large, the exponential term goes to 0. In this case, the hole density approaches its equilibrium density i.e. L_p is the distance scale over which the hole density returns to $p_v(\infty)$, the distance a hole is expected to travel before it is lost to recombination, the hole diffusion length. The electron case is the same, with $L_n = \sqrt{\tau_{r,n}D_n}$.

Finally, we see that an electron will have a reasonable chance of diffusion into the depletion layer if it is generated within L_n of the depletion layer boundary, and generation occurs at a rate of

$$\frac{n_i^2}{p_v \tau_{r,n}} \approx \frac{n_i^2}{N_D \tau_{r,n}} \quad (2.203)$$

outside of the depletion layer. As such, the rate of flow across the depletion layer boundary into the depletion layer from the n-side, which is just the electron generation current

density, is

$$J_e^{\text{gen}} = \frac{L_n n_i^2}{N_D \tau_{r,n}}, \quad (2.204)$$

and the hole generation current density is

$$J_h^{\text{gen}} = \frac{L_p n_i^2}{N_A \tau_{r,p}}, \quad (2.205)$$

providing the terms of the saturation current density.

2.3.3 Photovoltaics

The properties arising from the p-n junction between inhomogeneous semiconductors can be utilized for a number of applications. The directional asymmetry in response to applied bias results in diode applications, charge carrier depletion results in transistor behavior, and the induced electric field can drive a current, resulting in photovoltaic devices.

Introducing a load between the p- and n-sides of the junction causes a potential difference to develop, effectively producing a small bias. This is the simplest classical photovoltaic device. The resultant current is known as the dark current. Incident photons on the device may excite electrons from the valence band into the conduction band, as long as the photon energy is equal or greater than the band gap energy, ϵ_G . The excited electrons readily diffuse with some entering the depletion zone, then being accelerated in the direction of the n-side, driving a current that can be extracted to perform work. The excitation of electrons from incident photons resulting in a forward voltage is the photovoltaic effect, and the resultant current the photocurrent. The voltage developed between isolated terminals in a device constructed around this junction, i.e. when no load is applied, is known as the open-circuit voltage.

The excitation of electrons between bands is complicated in the case of an indirect band gap. Incident photons can provide the required energy to raise the electron to the conduction band minimum, but cannot convey the required crystal momentum $\hbar\mathbf{k}$ to move the electron from its point in \mathbf{k} -space at the valence band maximum to that

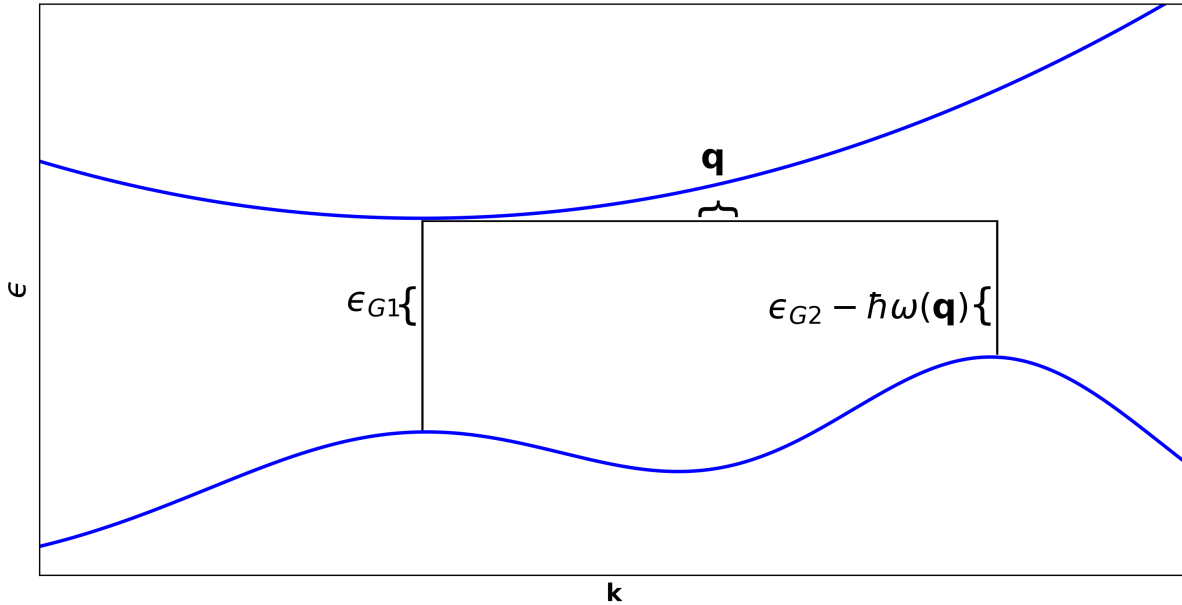


Figure 2.11: Band structure of a material exhibiting a direct band gap and a smaller indirect band gap. A direct transition requires the absorption of a photon of energy ϵ_{G1} , while an indirect transition requires both the absorption of a photon of energy $\epsilon_{G2} - \hbar\omega(\mathbf{q})$ ($\epsilon_{G1} > \epsilon_{G2}$), and transfer of crystal momentum from a phonon of wavevector \mathbf{q} . In such a material, transitions of both natures can be expected, with the relative rates dependent on the spectra of incident light.

of the conduction band minimum. The crystal momentum must come from a phonon of wavevector \mathbf{q} , which also carries a small amount of its own energy, $\hbar\omega(\mathbf{q})$, negligibly reducing the energy requirement of the incident photon. This is known as an indirect transition, and they occur over longer timescales than direct transitions of the same magnitude under the same conditions as they require the additional phonon interaction. Materials may have active direct and indirect band gaps simultaneously. These cases are displayed in Figure 2.11.

Excitons

The excitation of an electron to the conduction band leaves behind a hole in the valence band. In materials with significant screening effects, these charge carriers may be treated as separate, free entities with a binding energy much lower than $k_B T$. However, in cases with poor screening, such as low-dimensional systems or those with low electron density, interaction between the excited electron and resultant hole are important. We treat such bound electron-hole pairs as a neutrally charged quasiparticle: an exciton. The incident

photon energy need not exceed ϵ_G , and must only exceed the energy required to generate an exciton, the optical adsorption gap, ϵ_{opt} , in order to precipitate the photovoltaic effect. The difference between the conveyed energy to the exciton and the band gap is the binding energy of the exciton, ϵ_B . In order to act as charge carriers, the electron and hole must be separated.

This binding energy is Coulombic in nature and a function of separation of components: the excitonic radius. The radius, r , is that where the Coulomb attractive force between electron and hole balance the centrifugal force of their orbit, in analogy to the hydrogen atom. Ignoring the permittivity of the material and using the effective mass, μ ,

$$F_{\text{cent}} = F_{\text{Coul}} \quad (2.206)$$

$$-\frac{\mu v^2}{r} = -\frac{e^2}{r^2} \quad (2.207)$$

$$r = \frac{\mu (vr)^2}{e^2} = \frac{(\mu vr)^2}{\mu e^2}, \quad (2.208)$$

where v is the velocity of the electron and hole. The circumference of the orbital path traced by the exciton as a quasiparticle is an integer multiple of its wavelength, $\lambda = \frac{h}{\mu v}$,

$$2\pi r = n \frac{h}{\mu v}, \quad (2.209)$$

and therefore

$$\mu vr = n\hbar. \quad (2.210)$$

Substituting for μvr , we get

$$r = \frac{n^2 \hbar^2}{\mu e^2} = \frac{n^2 m_e}{\mu} \frac{\hbar^2}{m_e e^2} = \frac{n^2 m_e}{\mu} a_B \quad (2.211)$$

where a_B is the Bohr radius. With a_X as the radius of an exciton for the sake of consistent

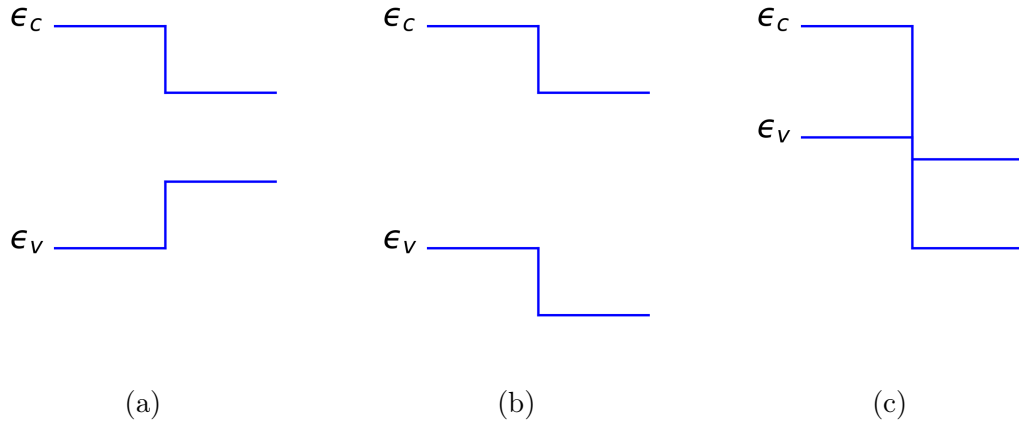


Figure 2.12: A schematic representation of band alignments between heterogeneous semiconductors at their junctions: (a) Type-I, or straddling gap, (b) Type-II, or staggered gap, and (c) Type-III, or broken gap. In the context of photovoltaic junctions, the semiconductor with higher conduction and valence band energies is the donor semiconductor, and the other is the acceptor semiconductors.

nomenclature, we arrive at Equation 2.212.

$$a_X = \frac{n^2 m_e}{\mu} a_B \quad (2.212)$$

Consider a heterojunction between semiconductors, where each semiconductor has an approximately similar band gap, but different chemical potentials. The conduction and valence band energies of the total system will suffer a sharp discontinuity across the junction, such that the band energies in the semiconductors are offset from each other; this is a staggered (or type-II) band alignment, and is the desired band alignment for this project. The semiconductor with the higher band energies is the known as the donor semiconductor, with the other being the acceptor semiconductor, for reasons outlined shortly. Band alignments are represented schematically in Figure 2.12. In the staggered gap alignment, an exciton generated from the valence band of the donor semiconductor may dissociate across the heterojunction if its energy exceeds that of the acceptor's conduction band, and it reaches the donor-acceptor interface before recombination. The hole remains in the donor's valence band, and the electron may act in the acceptor's conduction band. As such, what we called the donor semiconductor has donated an electron to the acceptor semiconductor. The immediate state where the electron in the acceptor and the hole in the donor are still bound through the Coulomb force is known

as a charge-transfer exciton. The charge-transfer exciton fully dissociates into free charge carriers due to further spatial separation driven by the electric field or via thermally assisted dissociation.

2.4 Nanoscale phenomena

In contrast to crystals extending infinitely in all directions, finite crystals introduce additional phenomena. Notably, edge effects emerge, while confinement effects arise due to the reduced dimensionality specific to this project.

2.4.1 Edge effects

Work function

The work function of a material is the thermodynamic work required to move an electron from the interior of the material to a point ‘just outside’ the surface: a macroscopically small, but atomically large, displacement. This is an important property for photovoltaic applications, as it affects energy requirements of charge carrier injection and collection.

Considering an infinite cubic crystal with inversion symmetry. The periodic potential energy is a sum of contributions from each repeating unit, i.e. each primitive Wigner-Seitz cell about their respective lattice points:

$$U_{\infty}(\mathbf{r}) = \sum_{\mathbf{R}} v(\mathbf{r} - \mathbf{R}) . \quad (2.213)$$

where $v(\mathbf{r} - \mathbf{R})$ is the potential energy of an electron at point \mathbf{r} due to the cell centered at \mathbf{R} . Treating a finite crystal as occupying a finite space, Ω , of an infinite crystal, but with the same configuration,

$$U_{\infty}(\mathbf{r}) = \sum_{\mathbf{R} \in \Omega} v(\mathbf{r} - \mathbf{R}) . \quad (2.214)$$

We are primarily interested with how rapidly this decays with increasing displacement, and so we examine the form of $v(\mathbf{r})$, the potential energy of an electron at point \mathbf{r} due to some charge distribution $\rho(\mathbf{r}')$. Considering a single Wigner-Seitz cell,

$$v(\mathbf{r}) = -e \int_{\text{cell}} \rho(\mathbf{r}') \frac{1}{|\mathbf{r} - \mathbf{r}'|} \delta\mathbf{r}' . \quad (2.215)$$

We can manipulate the term

$$|\mathbf{r} - \mathbf{r}'| = \sqrt{r^2 - 2\mathbf{r} \cdot \mathbf{r}' + r'^2} = r \sqrt{\left|1 - 2\frac{\hat{\mathbf{r}} \cdot \mathbf{r}'}{r} + \left(\frac{r'}{r}\right)^2\right|}, \quad (2.216)$$

leading to

$$\frac{1}{|\mathbf{r} - \mathbf{r}'|} = \frac{1}{r} (1 + \lambda)^{\frac{1}{2}}, \quad (2.217)$$

where

$$\lambda = -2\frac{\hat{\mathbf{r}} \cdot \mathbf{r}'}{r} + \left(\frac{r'}{r}\right)^2. \quad (2.218)$$

Applying the binomial expansion to Equation 2.217 gives

$$\begin{aligned} \frac{1}{|\mathbf{r} - \mathbf{r}'|} &\approx \frac{1}{r} \left(1 - \frac{1}{2}\lambda + \frac{3}{8}\lambda^2 - \frac{5}{16}\lambda^3 + \dots\right) \\ &= \frac{1}{r} + \frac{\hat{\mathbf{r}} \cdot \mathbf{r}'}{r^2} + \frac{3(\hat{\mathbf{r}} \cdot \mathbf{r}')^2 - r'^2}{r^3} + \frac{1}{r} \mathcal{O}\left(\frac{r'}{r}\right)^3, \end{aligned} \quad (2.219)$$

with terms collected by power of \mathbf{r} . Then the potential energy becomes

$$\begin{aligned} v(\mathbf{r}) &= -\frac{e}{r} \int_{\text{cell}} \rho(\mathbf{r}') \delta\mathbf{r}' - \frac{e}{r^2} \hat{\mathbf{r}} \cdot \left(\int_{\text{cell}} \mathbf{r}' \rho(\mathbf{r}') \delta\mathbf{r}' \right) + \mathcal{O}\left(\frac{1}{r^3}\right) \\ &= -e\frac{Q}{r} - e\frac{\mathbf{p} \cdot \hat{\mathbf{r}}}{r^2} + \frac{e}{r^3} \int_{\text{cell}} \rho(\mathbf{r}') [3(\mathbf{r}' \cdot \hat{\mathbf{r}})^2 - r'^2] \delta\mathbf{r}' + \mathcal{O}\left(\frac{1}{r^4}\right), \end{aligned} \quad (2.220)$$

where Q is the total charge of the cell and \mathbf{p} is the total cellular dipole moment. The crystal is overall neutral, and periodic across cells, so each cell must be electrically neutral, $Q = 0$. In our crystal, $\mathbf{p} = 0$ also, as it exhibits inversion symmetry; the contribution of a cell to the dipole moment must be zero. This is also true for the octupole moment, the term of order \mathbf{r}^{-4} (not shown above). Considering the \mathbf{r}^{-3} term,

$$(\mathbf{r}' \cdot \hat{\mathbf{r}})^2 = (r'_i \cos \theta) (r'_j \cos \theta) = r'_i r'_j \cos^2 \theta. \quad (2.221)$$

When $i \neq j$ this evaluates to zero, and when $i = j$, $r'_i r'_j = r'^2$. We then have

$$\begin{aligned} (\mathbf{r}' \cdot \hat{\mathbf{r}})^2 &= r'^2 \langle \cos^2 \theta \rangle = \frac{r'^2}{3} \\ \therefore \frac{e}{r^3} \int_{\text{cell}} \rho(\mathbf{r}') [3(\mathbf{r}' \cdot \hat{\mathbf{r}})^2 - r'^2] \delta \mathbf{r}' &= \frac{e}{r^3} \int_{\text{cell}} \rho(\mathbf{r}') \left[3 \left(\frac{r'^2}{3} \right) - r'^2 \right] \delta \mathbf{r}' = 0, \end{aligned} \quad (2.222)$$

i.e. the quadropole term also vanishes in this specific case of cubic symmetry. As such, the contribution of any given Wigner-Seitz cell to the potential energy of an electron decreases as \mathbf{r}^{-5} or faster. So, with the highest occupied state inside the crystal having energy of ϵ_F , and the potential outside the crystal very rapidly decaying to the vacuum level, the work required to move an electron from inside to a position external of the crystal where the contribution to the potential energy from nearby cells is negligible ('just outside'), with zero kinetic energy and in the absence of external fields, is

$$W = 0 - \epsilon_F = -\epsilon_F. \quad (2.223)$$

However, a finite crystal does not, in practice, maintain the same configuration as an infinite crystal; surface ions typically do not keep their ideal positions in the would-be lattice, and they need not exhibit the symmetry previously used to eliminate terms in the potential energy contribution. As such, local surface multipole moments need not be vanishing, the net electric field near the surface may be non-zero, and the work function must be modified with an additional term, W_S , the work required to carry an electron through the electric field near the surface:

$$W = W_S - \epsilon_F. \quad (2.224)$$

The form of W_S is dependent on the material and the quality and orientation of the surface. The potential energy of an electron outside the crystal returns to its zero value at large displacements, $U = 0$ in a vacuum. An example of a resultant potential energy function is shown in Figure 2.13.

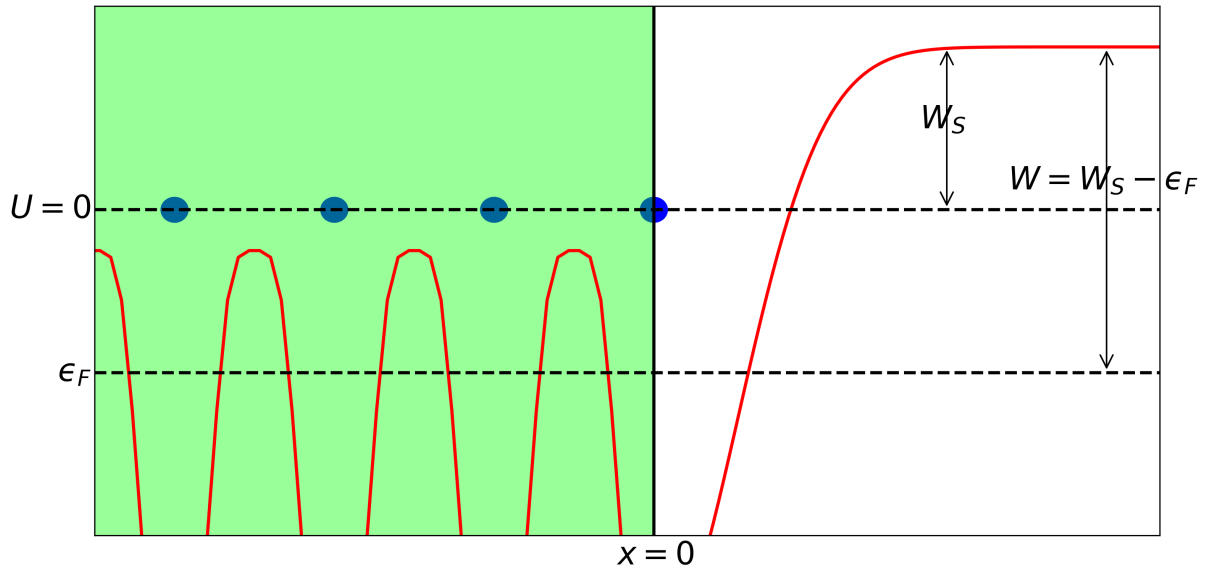


Figure 2.13: The potential energy of an electron, U , as a function of position in a finite crystal. The crystal-vacuum interface is at $x = 0$, and ionic spatial positions are represented by solid dots. The form of the perturbed potential near the boundary depends on the surface properties. The work required to move an electron to just outside the surface, W , is the sum of that required to overcome the infinite lattice potential, $-\epsilon_F$, and that required to overcome the surface electric field, W_S . The potential outside the infinite crystal would asymptote to the potential energy at vary large displacements outside the crystal: $U = 0$ in vacuum.

Dangling bonds and surface states

As crystals have a periodic structure, a break in this periodicity at a specimen edge can result in unsatisfied valences of the surface atoms. Where these atoms do not have enough suitable bonding partners, a dangling bond is found: valence electrons not engaged in a chemical bond, but that otherwise would be chemically active given a suitable nearby species. These may occur anywhere in a defective crystal, such as adjacent to a vacancy point defect, but will be plentiful along a surface of a crystal that has a geometry that properly satisfies each atom's valence only when the crystal continues in all directions e.g. diamond-structure silicon.

Surface dangling bonds are highly reactive, and can be optically active: their electrons adding an additional energy level between the conduction band and valence band, allowing for adsorption or emission of lower energy photons. Additionally, they may contribute to surface states, whereby the abrupt termination of crystal periodicity lifts the Born-von Karman boundary condition, in turn the requirement that the wavevector \mathbf{k} be real is

likewise lifted. Consider then the Bloch form with complex wavevector $\mathbf{k} = \boldsymbol{\kappa} + i\boldsymbol{\varkappa}$, where $\text{Re}\{\mathbf{k}\} = \boldsymbol{\kappa}$ and $\text{Im}\{\mathbf{k}\} = \boldsymbol{\varkappa}$:

$$\psi(\mathbf{r}) = u(\mathbf{r}) e^{i\mathbf{k}\cdot\mathbf{r}} = u(\mathbf{r}) e^{i\boldsymbol{\kappa}\cdot\mathbf{r}} e^{-\boldsymbol{\varkappa}\cdot\mathbf{r}} . \quad (2.225)$$

This additional term for the imaginary component of \mathbf{k} results in a wavefunction that grows in the opposite direction to $\boldsymbol{\varkappa}$. Far from a surface, the Born-von Karmann condition holds locally, and this term has no physical relevance. Near a surface the periodic boundary conditions are lifted, and for a surface perpendicular to $\boldsymbol{\varkappa}$ there are solutions to $\psi(\mathbf{r})$ that grow on approach to the surface, and then decay outside it (as the potential at infinite displacement outside the crystal must be determined only by external conditions, and the wavefunction must be continuous across the boundary). These described solutions are possible for a discrete set of $\boldsymbol{\varkappa}$, and are surface states. Precise microscopic calculations of the surface must take them into account by treating Bloch states without the requirement that \mathbf{k} be real near a surface.

2.4.2 Confinement

When the motion of charge carriers in a material is restricted to a small region on the scale of interatomic distance, altered band structure and electronic properties can emerge. This is clearly demonstrated by the permitted energy states emerging from the infinite potential well problem, where electrons are bound in a region of space along one axis by infinite potential barriers, separated by a displacement, d . The potential within these barriers is zero. If we say that the infinite potential barriers are plane perpendicular to the x-axis, the wavefunction solutions are then those of the well known one-dimensional well problem,

$$\psi_n(\mathbf{x}) = \sqrt{\frac{2}{d}} \sin \frac{n\pi x}{d} . \quad (2.226)$$

Substituting this in to the time independent Schrödinger equation (Equation 2.1), we get discrete energy eigenstates of

$$\epsilon_n = \frac{1}{2m_e^*} \left(\frac{\hbar n \pi}{d} \right)^2, \quad (2.227)$$

which depend on the size of the confined region as d^{-2} . As such, increasing spatial confinement results in increase the energies of permitted states by widening any gap between them. This affects the band structure of any material when confinement effects are pronounced, such as the edge of a specimen. Notably for this work, monolayer systems obviously only contain regions that are near an edge, and so these effects are pronounced throughout the crystal in the few-layer regime. A system that is spatially confined in this way, with one spatial dimension restricted and the other two free, is a quantum well. Also of note for this work are quantum dots, with spatial confinement in all three dimensions. With very large values of d , like in a bulk crystal, energy bands can appear continuous at low resolution: while levels within bands are still quantized, the differences between levels within the same band are very small. Increasingly smaller values of d result in the quantization becoming more obvious, and a splitting of energy levels occurs.

These changes to band structure have the typical effect of widening band gaps, but can sometimes be profound enough to change the nature of the band gap from direct to indirect, or vice-versa.

Another consequence of confinement is the emergence of the confinement energy of excitons. The components of an exciton are attractive, resulting in a binding energy that must be overcome to separate an exciton into constituent charge carriers. An exciton can be treated as being confined by its own radius, a_X (Equation 2.212). If the spatial region within which an exciton is confined due to the nature of the crystal media decreases below a_X , the binding energy can be treated as having another term for the added energy as a consequence of decreased radius, the confinement energy. This has the effect of enhancing the binding energy: excitons are easier to produce via photovoltaic effects, and harder to separate into constituent charge carriers.

2.5 Van der Waals (vdW) forces

Van der Waals (vdW) forces, named after Johannes Diderik van der Waals, are displacement-dependent forces between stable chemical species. They give rise to both overall repulsive and attractive effects, depending on the separation of the interacting species. The separation between particles within which the forces become repulsive while decreasing separation (due to overlapping electron clouds) is the van der Waals contact distance. At separations larger than this, the forces are weakly attractive due to interactions between induced and permanent fluctuating dipoles in the species (see Figure 2.14).

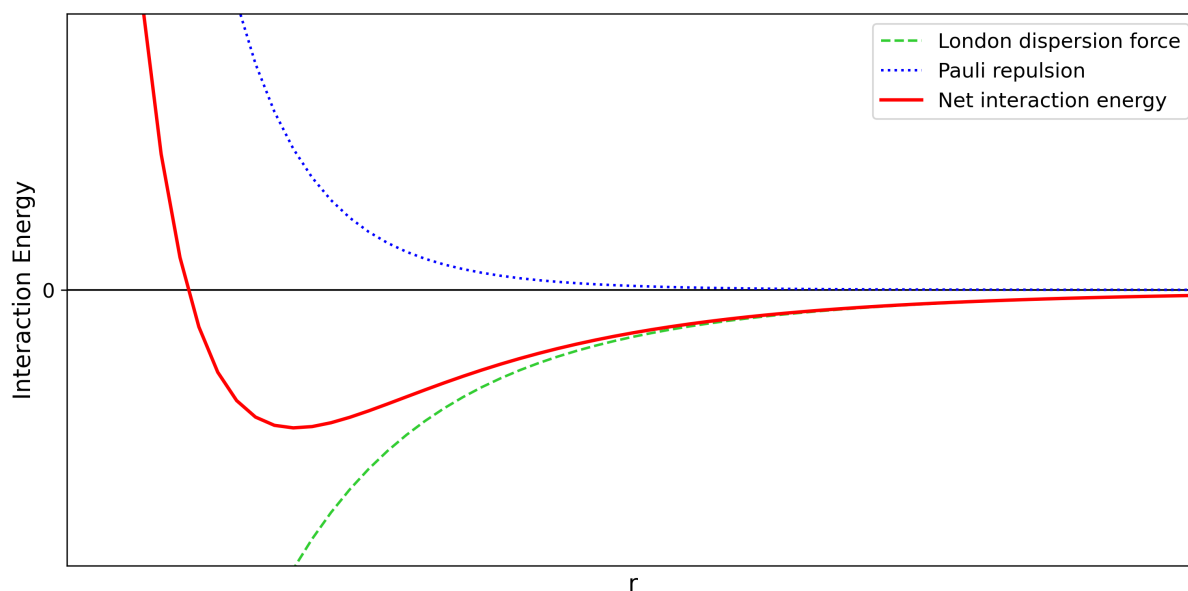


Figure 2.14: The London dispersion force (green, dashed) and Pauli repulsion (blue, dotted) as a function of separation between interacting species. The net interaction energy from these forces is in solid red, and where this crosses the y-axis is the van der Waals contact distance: below this separation, Pauli repulsion dominates and the net force is repulsive, and vice-versa for above.

These forces are potentially comprised of four components: the Keesom force, the Debye force, Pauli repulsion and London dispersion forces. Which of the four are included in the bracket ‘van der Waals forces’ is dependent on the context and the source of information. Here, we will concern ourselves only with London dispersion forces, and the discussions of vdW forces will relate only to the London dispersion force unless otherwise stated. This is because the computational method for handling vdW forces used in this

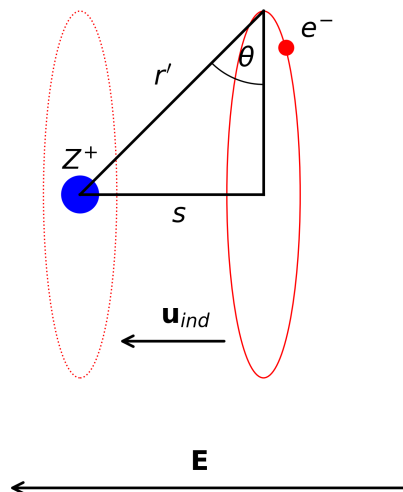


Figure 2.15: The deflection of an orbiting electron, in red, around a Bohr nucleus, in blue. The dotted ellipse is the orbit without an external field, \mathbf{E} , the solid ellipse is the deflected orbit. s is the spatial separation between the original and deflected orbits, resulting in the electron-nucleus displacement of r' at angle θ . This separation of charges results in the induced dipole moment \mathbf{u}_{ind} .

project (Grimme's DFT-D3 [65]) only considers the London dispersion force, but this is not because the London dispersion force is stronger than the others. Conversely, they are the weakest of the four aforementioned forces. However, Pauli repulsion is handled implicitly in the exchange-correlation terms, and both Keesom and Debye interactions require permanent dipoles within a polar molecule. As we are considering only crystals and the organic molecule pentacene (a non-polar molecule), we need not use a vdW correction in our calculations that considers the Keesom or Debye forces.

The London dispersion force

The London dispersion force is named for Fritz London, who proposed it as a form of intermolecular force in 1930 [66], and further described the general case of the interaction energy in 1937 [67].

Consider a Bohr atom of a nucleus and an orbiting electron, of charge $+e$ and $-e$, respectively. The displacement of the electron cloud relative to the nucleus due to an

external electric field, \mathbf{E} , causes polarization such that the induced dipole moment is

$$u_{\text{ind}} = es , \quad (2.228)$$

where s is the displacement of the electron from its unperturbed state. At equilibrium the force on the electron from the electric field, $F_{\mathbf{E}}$, must be balanced by the restoring force, F_R , which is the Coulombic attraction between the electron and nucleus as

$$F_{\mathbf{E}} = F_R , \quad (2.229)$$

which is

$$-eE = \frac{-e^2}{4\pi\epsilon r'^2} \sin\theta = \frac{-e^2}{4\pi\epsilon r'^2} \frac{s}{r'} = \frac{-eu_{\text{ind}}}{4\pi\epsilon r'^3} , \quad (2.230)$$

where ϵ is the permittivity, and θ is the angle between the unperturbed orbital radius vector and the perturbed displacement vector, \mathbf{r}' , at equilibrium under the effect of the field E (see Figure 2.15). We then have

$$u_{\text{ind}} = 4\pi\epsilon r'^3 E , \quad (2.231)$$

which can be expressed in terms of the electronic polarizability of our Bohr atom, α ,

$$u_{\text{ind}} = \alpha E , \quad (2.232)$$

where

$$\alpha = 4\pi\epsilon r'^3 . \quad (2.233)$$

In general, the induced dipole moment and so the polarizability are dependent on the frequency of the field. We will exclude this treatment for now, but it is considered in the Grimme's DFT-D3 [65] treatment of vdW corrections that we use in this project, and

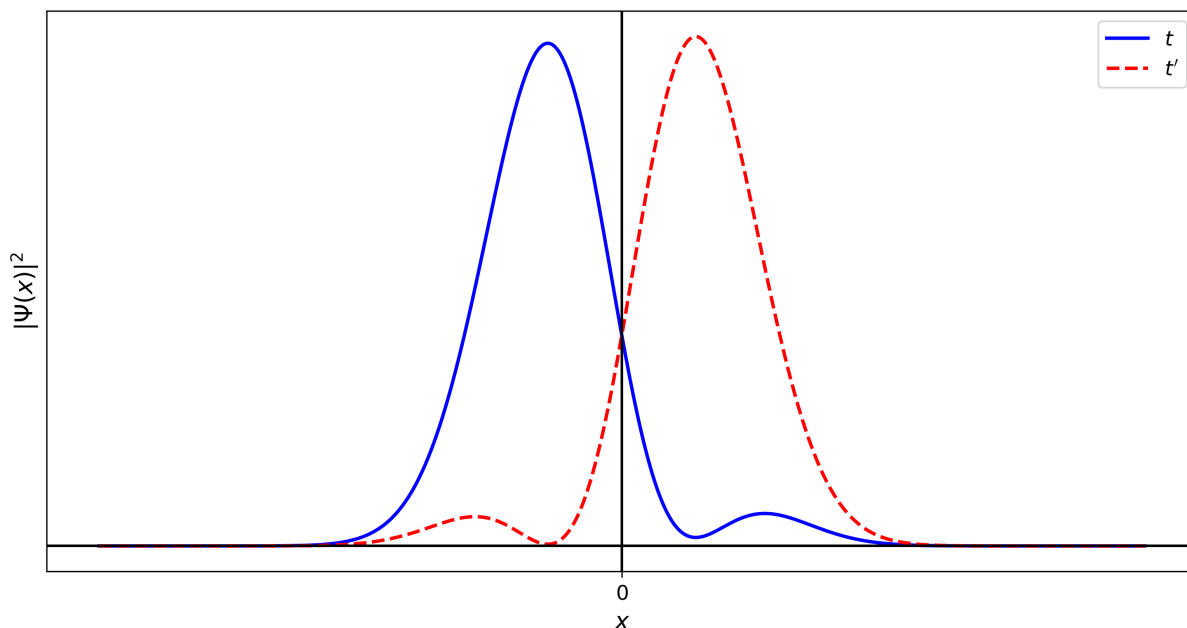


Figure 2.16: The probability distribution of a quantum harmonic oscillator's position. This is representative of the principle of transient dipole moments around an atom or molecule. The probability distribution is time dependent, and the transition between states t and t' results in a transition dipole moment.

discuss in subsection 3.1.3. In that subsection, a proper treatment serves to introduce an integral over all frequencies, which can be ignored for now.

Without the presence of an external field, neutral atoms and non-polar molecules have a time-averaged dipole moment of zero. However, the local charge density distribution around an atom or molecule is variable in time, with transient states of high charge density and low charge density in any particular part of local space, as represented in Figure 2.16. If the charge density is high in a region of local space, it will be low elsewhere, and vice-versa. At any given instant, there then exists a non-zero dipole moment. This transient, instantaneous dipole moment produces an electric field that polarizes nearby species, as described above, which generates its own electric field and results in the London dispersion force between the two.

Consider a point in space, A , separated from a Bohr atom with instantaneous dipole moment u by displacement r . Let the angle between \mathbf{r} and \mathbf{s} be θ , and the angle between the vectors \mathbf{d}_+ and \mathbf{d}_- be ϕ . \mathbf{d}_+ and \mathbf{d}_- are the vectors between A and the Bohr nucleus and the Bohr electron, respectively. The geometry of such a system is displayed in Figure

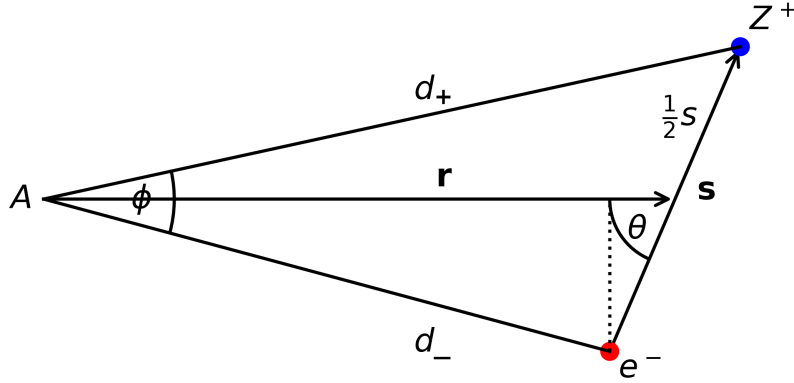


Figure 2.17: The geometry of the instantaneous dipole of a Bohr atom resulting in an electric field as considered in this section. We assume that the considered point in space, A , is far from the Bohr atom on the scale of its electron-nucleus separation.

2.17. If $r \gg s$, the magnitudes of \mathbf{d}_+ and \mathbf{d}_- can be approximated by

$$d_- \approx r - \frac{s}{2} \cos \theta, \quad (2.234)$$

and

$$d_+ \approx r + \frac{s}{2} \cos \theta \quad (2.235)$$

The electric field felt at point A due to the Bohr electron is

$$\begin{aligned} E_- &= \frac{e}{4\pi\epsilon d_-^2} = \frac{e}{4\pi\epsilon r^2 \left(1 - \frac{s}{2r} \cos \theta\right)^2} \\ &\approx \frac{e}{4\pi\epsilon r^2 \left(1 - \frac{s}{r} \cos \theta\right)}. \end{aligned} \quad (2.236)$$

Similarly, the electric field felt at point A due to the Bohr nucleus is

$$E_+ \approx \frac{e}{4\pi\epsilon r^2 \left(1 + \frac{s}{r} \cos \theta\right)}. \quad (2.237)$$

The parallel component of the total field from both contributions at A is

$$\begin{aligned}
 E_{\parallel} &= (E_- - E_+) \cos \frac{\phi}{2} \\
 &= \frac{e}{4\pi\epsilon r^2} \left(\frac{1}{1 - \frac{s}{r} \cos \theta} - \frac{1}{1 + \frac{s}{r} \cos \theta} \right) = \frac{e}{4\pi\epsilon r^2} \left(\frac{\frac{2s}{r} \cos \theta}{1 - \left(\frac{s}{r} \cos \theta\right)^2} \right) \\
 &\approx \frac{e}{4\pi\epsilon r^2} \frac{2s}{r} \cos \theta,
 \end{aligned} \tag{2.238}$$

as if ϕ is small, $\cos \frac{\phi}{2} \approx 1$. Similarly, $\sin \frac{\phi}{2} \approx \tan \frac{\phi}{2} = \frac{s}{2r} \sin \theta$, and so the perpendicular component of the total field from both contributions at A is

$$E_{\perp} \approx \frac{e}{4\pi\epsilon r^2} \frac{s}{r} \sin \theta. \tag{2.239}$$

Therefore, the magnitude of the total \mathbf{E} -field at point A due to the instantaneous dipole of a Bohr atom with separation \mathbf{r} is

$$E_u = \sqrt{E_{\parallel}^2 + E_{\perp}^2} = \frac{es}{4\pi\epsilon r^3} (4 \cos^2 \theta + \sin^2 \theta)^{\frac{1}{2}}, \tag{2.240}$$

which can be displayed more concisely as

$$E_u = \frac{u(1 + 3 \cos^2 \theta)^{\frac{1}{2}}}{4\pi\epsilon r^3} \tag{2.241}$$

If there is a point charge of $+e$ at point A , producing a field \mathbf{E}_A such that

$$E_A = \frac{e}{4\pi\epsilon r^2}, \tag{2.242}$$

the Bohr atom's induced dipole moment \mathbf{u}_{ind} will be aligned with \mathbf{E}_A and produces the anti-aligned reaction field

$$\begin{aligned}
 E_u &= \frac{-u_{\text{ind}}(1 + \cos^2 \theta)^{\frac{1}{2}}}{4\pi\epsilon r^3} = \frac{-2\alpha E_A}{4\pi\epsilon r^3} \\
 &= \frac{-2\alpha}{4\pi\epsilon r^3} \frac{e}{4\pi\epsilon r^2} = \frac{-2\alpha e}{(4\pi\epsilon)^2 r^5}.
 \end{aligned} \tag{2.243}$$

The attractive force between the charge at A and the Bohr atom is then

$$F(r) = eE_u \quad (2.244)$$

and the potential energy of this interaction, the interaction energy, $w(r)$, is

$$w(r) = - \int_{\infty}^r F(r) \delta r = - \frac{\alpha e^2}{2(4\pi\epsilon)^2 r^4} = - \frac{1}{2} \alpha E_A^2 . \quad (2.245)$$

Instead of a point charge, if there is another Bohr atom at point A then the interaction energy is angle-averaged as

$$w(r) = - \frac{1}{2} \alpha E_A^2 = - \frac{1}{2} \alpha u_{\text{ind}}^2 \frac{(1 + 3\langle \cos^2 \theta \rangle)}{(4\pi\epsilon)^2 r^6} = - \frac{\alpha u_{\text{ind}}^2}{(4\pi\epsilon)^2 r^6} . \quad (2.246)$$

For Bohr electrons at the first Bohr radius, a_B , their electrostatic potential energy is the Coulombic interaction with their nucleus. For a central potential, the Virial theorem states that the time-averaged kinetic, T , and potential, U , energies are related as $\langle T \rangle = -\frac{1}{2}\langle U \rangle$. As such, the sum of these energies gives the total energy, which is $\frac{1}{2}U$. The ionization energy required to free the electron from its bound state in the Bohr atom, I , is therefore half that of the potential energy from the Coulomb interaction:

$$\frac{e^2}{4\pi\epsilon a_B} = 2I \quad (2.247)$$

and so

$$a_B = \frac{e^2}{8\pi\epsilon I} . \quad (2.248)$$

As the induced dipole moments involved here are $u_{\text{ind}} = es = ea_B$, the interaction energy is then

$$w(r) = -\alpha \frac{e^2 a_B^2}{(4\pi\epsilon)^2 r^6} , = - (4\pi\epsilon a_B^3) \frac{e^2 a_B^2}{(4\pi\epsilon)^2 r^6} , \quad (2.249)$$

and so substituting in our expressions for a_B and α , we find to order unity that

$$w(r) \approx -\frac{\alpha^2 I}{(4\pi\epsilon)^2 r^6} . \quad (2.250)$$

This is the London dispersion interaction energy, differing from the original derivation found in London's 1930 paper [66] by only a coefficient of order unity (but derived and presented in a different manner), which can be generalised for two non-identical particles [67] as

$$w_L(r) = -\frac{3}{2} \frac{\alpha_1 \alpha_2}{(4\pi\epsilon)^2 r^6} \frac{I_1 I_2}{I_1 + I_2} . \quad (2.251)$$

Chapter 3

Computational theory

In this chapter we will discuss how the physical theory of Chapter 2 is applied to computation and electronic structure calculations. The chapter starts with an overview of the primary theory used in the project, density functional theory (DFT), and how functionals are used to make otherwise intractable problems computationally feasible. This is within Section 3.1, which includes the implementation of the important van der Waals correction. Pseudopotentials, approximations of real potentials, are used in electronic structure calculations to reduce computational cost, and their theory is discussed in Section 3.2, following which is background on some important numerical algorithms used within Quantum ESPRESSO, as well as an overview of Quantum ESPRESSO parameters in Section 3.3.

3.1 Density functional theory

The theory used in this project to calculate properties of our materials is density functional theory. It is a modelling method to extract the ground state electronic structure from a system based on its electronic density. A functional is a mapping from some space into the field of real or complex numbers. More loosely, in the context of a field of functions, it returns a scalar. An example is the area, A , between two functions, $f(x)$ and $g(x)$, denoted as $A[g, f]$. In the case of DFT, the functionals are of the ground state electronic density, $n_0(\mathbf{r})$. Modern DFT arose from Hohenberg and Kohn's 1964 paper on the matter [68], proving that a functional of the density exists that describes the ground state energy of the system under a general external potential, which is unique to the form of the density. Minimizing this functional then gives the ground state energy.

To show that $n_0(\mathbf{r})$ is unique to the potential, we can follow the proof by contradiction provided by Hohenberg and Kohn. Consider two external potentials, $V_1(\mathbf{r})$ and $V_2(\mathbf{r})$, that produce the same ground state density. There are associated Hamiltonians, $\mathcal{H}_{1,2}$, and wavefunctions, $\psi_{1,2}$, derived from these differing potentials, and so differing ground state energies, ϵ_1 and ϵ_2 . If the wavefunction ψ_2 is a solution to \mathcal{H}_1 , it is not the ground state solution, which can be shown simply:

$$\epsilon_1 = \langle \psi_1 | \mathcal{H}_1 | \psi_1 \rangle < \langle \psi_2 | \mathcal{H}_1 | \psi_2 \rangle = \langle \psi_2 | \mathcal{H}_2 | \psi_2 \rangle + \langle \psi_2 | (\mathcal{H}_1 - \mathcal{H}_2) | \psi_2 \rangle, \quad (3.1)$$

and therefore

$$\epsilon_1 < \epsilon_2 + \int [V_1(\mathbf{r}) - V_2(\mathbf{r})] n_0(\mathbf{r}) \delta\mathbf{r} \quad (3.2)$$

The wavefunction ψ_1 is not the ground state of \mathcal{H}_2 , so we also get

$$\epsilon_2 < \epsilon_1 + \int [V_2(\mathbf{r}) - V_1(\mathbf{r})] n_0(\mathbf{r}) \delta\mathbf{r}. \quad (3.3)$$

Adding these expressions together, we get

$$\epsilon_1 + \epsilon_2 < \epsilon_1 + \epsilon_2 , \quad (3.4)$$

and therefore conclude that two differing potentials cannot produce the same ground state electronic density i.e. the Hamiltonian is fully determined by $n_0(\mathbf{r})$; all properties can, in principle, be represented by functionals of the ground state density alone. We use the universal Hohenberg-Kohn functional, $F_{HK}[n]$, so-called as it is independent of the external potential, and so is identical for all electron systems,

$$F_{HK}[n] = T[n] + E_{\text{int}}[n] , \quad (3.5)$$

where $E_{\text{int}}[n]$ is the internal energy functional of an interacting electron system i.e. electron-electron interaction energy, and $T[n]$ is the kinetic energy term. The total energy functional is then

$$E_{HK}[n] = F_{HK}[n] + \int V_{\text{ext}}(\mathbf{r}) n(\mathbf{r}) \delta\mathbf{r} + E_I , \quad (3.6)$$

where E_I is the interaction term of the nuclei of a given system, and includes any nuclear terms that do not involve the electrons but do affect the system energy e.g. nucleus-nucleus interactions. We have then for the ground state density $n_1(\mathbf{r})$

$$\epsilon_1 = E_{HK}[n_1] = \langle \psi_1 | \mathcal{H} | \psi_1 \rangle , \quad (3.7)$$

and for some other density $n_2(\mathbf{r})$

$$\epsilon_2 = E_{HK}[n_2] = \langle \psi_2 | \mathcal{H} | \psi_2 \rangle . \quad (3.8)$$

Clearly $\epsilon_1 < \epsilon_2$, as $n_2(\mathbf{r})$ is not the ground state density i.e. minimization of $E_{HK}[n]$ with respect to $n(\mathbf{r})$ gives the ground state energy and density. This is the variational principle, where any approximated wavefunction solution results in a higher energy than

the true wavefunction. Local minima in the form of $E_{HK}[n]$ do not necessarily represent excited states, however.

Hohenberg-Kohn DFT does not itself describe how to model a many-body system in terms of density functionals; it is not simple to extract desired parameters from a known form of the density, and the formulation does not attempt to provide a method for doing so. It is, however, exact in principle.

3.1.1 Kohn-Sham DFT

In 1965, Kohn and Sham provided the method still used today for tractable DFT calculations [69], where an auxiliary system of independent electron approximation is created, and solutions found. Kohn-Sham DFT is not itself an independent electron approximation, but the constructed auxiliary system of independent particles gives the same density and total energy as the real, many-body system, so Kohn-Sham DFT still uses independent particle methods. This auxiliary system treats the effects of the real many-body terms in a functional, the exchange-correlation functional, $E_{XC}[n]$. This functional in Kohn-Sham theory is exact, but any practical implementation requires that it is approximated. This leads to the discrepancies between the results from a Kohn-Sham method of calculation and the true values, but the method in general provides perhaps the best trade-off between accuracy and computational resources for a large number of applications. A notable drawback is the underestimation of band gap energies, which results from the derivative discontinuity of energy with respect to number of electrons. This is explored in Appendix G.

In the Kohn-Sham DFT method (in this project the Kohn-Sham DFT method is used, so any mention of the DFT process in following sections and chapters refers to the Kohn-Sham variation, unless otherwise specified), calculations are performed on the auxiliary system using the Hamiltonian

$$\mathcal{H}_{KS} = -\frac{1}{2}\nabla^2 + V_{\text{eff}}(\mathbf{r}) \ , \quad (3.9)$$

with $V_{\text{eff}}(\mathbf{r})$ being the effective potential acting on an electron at position \mathbf{r} , and is of local form. Potential terms are in principle spin dependent, but we will here consider the spin symmetric case only as asymmetric spin is not featured in the project. The electronic density of the system is given by the sum of the square magnitude of the N wavefunctions, ψ_i , for each occupied orbital,

$$n(\mathbf{r}) = \sum_{i=1}^N |\psi_i(\mathbf{r})|^2, \quad (3.10)$$

and the Kohn-Sham kinetic energy is the sum of that of independent particles,

$$T_S = -\frac{1}{2} \sum_{i=1}^N \langle \psi_i | \nabla^2 | \psi_i \rangle, \quad (3.11)$$

where the subscript denotes a single-electron treatment i.e. the non-interacting kinetic energy. The Kohn-Sham energy functional, $E_{KS}[n]$, is similar to the Hohenberg-Kohn expression except that the internal energy is considered in two parts, with the Coulombic interaction energy, $E_H[n]$, treated explicitly and the exchange-correlation functional, $E_{XC}[n]$, taking up the rest:

$$E_{KS}[n] = T_S[n] + \int V_{\text{ext}}(\mathbf{r}) n(\mathbf{r}) \delta\mathbf{r} + E_H[n] + E_{XC}[n] + E_I, \quad (3.12)$$

where $V_{\text{ext}}(\mathbf{r})$ is the external potential, and the Coulombic interaction energy of a system of electrons of density profile $n(\mathbf{r})$ with itself is called the Hartree energy, due to its role in the Hartree equations in analogous form (Equation 2.53). As a functional of density, the Hartree energy is

$$E_H[n] = \frac{1}{2} \int \int \frac{n(\mathbf{r}) n(\mathbf{r}')}{|\mathbf{r} - \mathbf{r}'|} \delta\mathbf{r} \delta\mathbf{r}'. \quad (3.13)$$

The new exchange-correlation energy term groups the many-body effects from the true system, and noting that the total energy and the density of the auxiliary system matches those of the true system i.e. $E_{KS}[n] = E_{HK}[n]$, we compare the two energy relationships

to find

$$F_{KS}[n] + E_I + \int V_{\text{ext}}(\mathbf{r}) n(\mathbf{r}) \delta\mathbf{r} = T_S[n] + \int V_{\text{ext}}(\mathbf{r}) n(\mathbf{r}) \delta\mathbf{r} + E_H[n] + E_{XC}[n] + E_I , \quad (3.14)$$

which leads to

$$F_{KS}[n] = T_S[n] + E_H[n] + E_{XC}[n] . \quad (3.15)$$

Recognizing that the true kinetic energy functional can be expressed as the expectation value of the kinetic energy operator, and similarly for the internal energy functional, $E_{\text{int}}[n] = \langle \mathcal{V}_{\text{int}} \rangle$, we can express the exchange-correlation energy functional explicitly as the difference between the kinetic and internal energies of the true system and the independent-particle auxiliary system,

$$E_{XC}[n] = \langle \mathcal{T} \rangle + \langle \mathcal{V}_{\text{int}} \rangle - (T_S[n] + E_H[n]) . \quad (3.16)$$

This demonstrates that if the exchange-correlation functional was known, the more computationally tractable independent-particle auxiliary system can be used to find the exact ground state energy and density of the true many-body system. As such, finding solutions to the Kohn-Sham system can provide an approximation of the ground state energy to the degree of accuracy that the approximation of E_{XC} itself carries.

Varying the orbitals in the Kohn-Sham energy functional gives us the variational equation,

$$\frac{\delta E_{KS}}{\delta \psi_i^*} = \frac{\delta T_S}{\delta \psi_i^*} + \frac{\delta n}{\delta \psi_i^*} V_{\text{eff}}(\mathbf{r}) , \quad (3.17)$$

where we have reduced clutter by taking advantage of the chain rule of differentiation and introduced the effective potential, V_{eff} ,

$$V_{\text{eff}}(\mathbf{r}) \equiv \frac{\delta E_{\text{ext}}}{\delta n} + \frac{\delta E_H}{\delta n} + \frac{\delta E_{XC}}{\delta n} , \quad (3.18)$$

where E_{ext} is the energy due to the external potential,

$$E_{\text{ext}} = \int V_{\text{ext}}(\mathbf{r}) n(\mathbf{r}) \delta\mathbf{r} . \quad (3.19)$$

We see from expressions above that

$$\frac{\delta T_S}{\delta \psi_i^*} = -\frac{1}{2} \nabla^2 \psi_i(\mathbf{r}) \quad (3.20)$$

and

$$\frac{\delta n}{\delta \psi_i^*} = \psi_i(\mathbf{r}) . \quad (3.21)$$

In order to minimize E_{KS} within the constraints of orthonormality,

$$\langle \psi_i | \psi_j \rangle = \delta_{ij} , \quad (3.22)$$

we use the method of Lagrange multipliers, where λ_{ij} are the multipliers, to get

$$\left(-\frac{1}{2} \nabla^2 + V_{\text{eff}}(\mathbf{r}) \right) \psi_i(\mathbf{r}) = \sum_j \lambda_{ij} \psi_j(\mathbf{r}) \quad (3.23)$$

$$\lambda_{ij} = \delta_{ij} \epsilon_j .$$

This is outlined in Appendix H, and when $i = j$, we are left with the Schrödinger-like Kohn-Sham equations,

$$(\mathcal{H}_{KS} - \epsilon_i) \psi_i(\mathbf{r}) = 0 \quad (3.24)$$

These are independent-particle equations, and are solved self-consistently between the potential and the density. Note that there is no dependence on the specific form of E_{XC} : if it were to be exactly known, these equations would model the true many-body system and provide the exact ground state energy.

Self-consistent solutions

The coupled Kohn-Sham equations, Equation 3.24 (one for each electronic state, ψ_i), can be solved iteratively, with an initial guess for V_{eff} (subject to the given approximation of E_{XC}) to solve for the electronic density, with this result feeding back in a new solution for V_{eff} , until convergence is achieved. This is the same general process as outlined in subsection 2.1.4, with the Kohn-Sham process displayed in Figure 3.1. Finding the solution to the Kohn-Sham equations is the computationally expensive process within electronic structure calculations, scaling with the number of electrons within a system, N , as $\mathcal{O}(N^3)$, as diagonalization of an $M \times M$ Hamiltonian matrix scales as M^3 , and $M \propto N$; solving the Hamiltonian for N electrons is done by constructing the Hamiltonian matrix, \mathbf{H} ,

$$\mathbf{H} \equiv \begin{bmatrix} H_{11} & H_{12} & \dots & H_{1m} \\ H_{21} & H_{22} & \dots & H_{2m} \\ \vdots & \vdots & \ddots & \vdots \\ H_{l1} & H_{l2} & \dots & H_{lm} \end{bmatrix}, \quad (3.25)$$

where l and m are matrix component indices related to the set of basis functions, such that

$$\mathbf{H} \begin{bmatrix} c_{1n} \\ c_{2n} \\ \vdots \\ c_{mn} \end{bmatrix} = E_n \begin{bmatrix} c_{1n} \\ c_{2n} \\ \vdots \\ c_{ln} \end{bmatrix}, \quad (3.26)$$

for n eigenstates. We can construct an orthogonal matrix of eigenvectors,

$$\mathbf{C} = \begin{bmatrix} c_{11} & c_{12} & \dots & c_{1m} \\ c_{21} & c_{22} & \dots & c_{2m} \\ \vdots & \vdots & \ddots & \vdots \\ c_{l1} & c_{l2} & \vdots & c_{lm} \end{bmatrix}, \quad (3.27)$$

and use this to diagonalize the Hamiltonian matrix to recover eigenstates:

$$\mathbf{C}^T \mathbf{H} \mathbf{C} = \begin{bmatrix} E_1 & 0 & \dots \\ 0 & E_2 & \dots \\ \vdots & \vdots & \ddots \end{bmatrix} . \quad (3.28)$$

It is this process that leads to the scaling as $\mathcal{O}(N^3)$, as the matrix elements are related to the basis functions used, themselves being of a number proportional to N .

Total energies are in general calculated during the output stage, but some modern codes, including the Quantum ESPRESSO packages used in this project, use the energy functional as a self-consistency check and so calculate them at that stage instead.

Formally, the Kohn-Sham energy is a functional of the electronic density, but it may be practically considered to be a functional of the potential that is input to the Kohn-Sham equations during a self-consistent calculation. This is a method utilised by the *PWscf* package in the Quantum ESPRESSO suite used in this project [46]. This package calculates the Kohn-Sham energy as a functional of the input effective potential, V_{in} , as $E_{KS}[V_{\text{in}}]$, and also, separately, as an explicit functional of the input density; the Harris-Weinert-Foulkes functional form, E_{HWF} . The Harris-Weinert-Foulkes [70–72] functional is one where the total energy is given as an explicit functional of the input density whereas the Kohn-Sham functional is in terms of the output density:

$$E_{HWF}[n_{\text{in}}] = \sum_i \int \psi_i^*(\mathbf{r}) \left(-\frac{1}{2} \nabla^2 + V_{\text{ext}}(\mathbf{r}) + V_{\text{in}}(\mathbf{r}) \right) \psi_i \delta \mathbf{r} - \quad (3.29)$$

$$\int n_{\text{in}}(\mathbf{r}) V_{\text{in}}(\mathbf{r}) \delta \mathbf{r} + E_{HXC}[n_{\text{in}}] . \quad (3.30)$$

The Kohn-Sham energy functional (Equation 3.12) can be alternately expressed as

$$\begin{aligned} E_{KS}[n_{\text{out}}] &= \sum_i \int \psi_i^*(\mathbf{r}) \left(-\frac{1}{2} \nabla^2 + V_{\text{ext}}(\mathbf{r}) \right) \psi_i \delta \mathbf{r} + E_H[n_{\text{out}}] + E_{XC}[n_{\text{out}}] + E_I \\ &= \sum_i \int \psi_i^*(\mathbf{r}) \left(-\frac{1}{2} \nabla^2 + V_{\text{ext}}(\mathbf{r}) \right) \psi_i \delta \mathbf{r} + E_{HXC}[n_{\text{out}}] , \end{aligned} \quad (3.31)$$

where E_{HXC} is the sum of the Hartree, exchange-correlation and atomic interaction term.

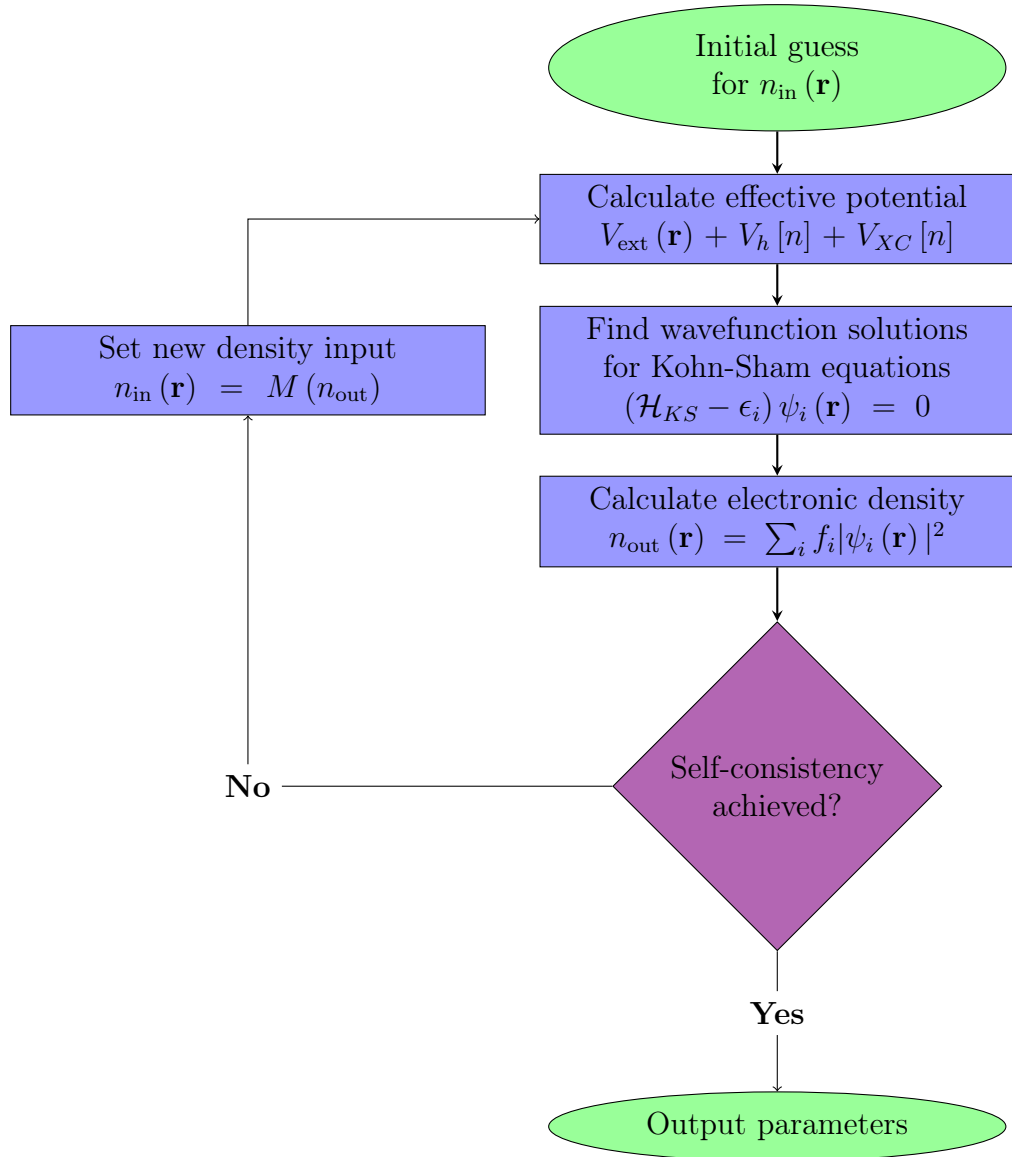


Figure 3.1: The process map for the Kohn-Sham DFT self-consistent loop. f_i is a weighting function to maintain the total electron number and $M(n_{\text{out}})$ is a mixing function, the nature of which is described later in this subsection.

For a given input density then the difference between these energies is only dependent on the difference between potential terms using input and output densities as

$$E_{KS} - E_{HWF} = E_{HXC} [n_{\text{out}}] - E_{HXC} [n_{\text{in}}] , \quad (3.32)$$

where the Hartree term is dominant, and so

$$\begin{aligned} E_{KS} - E_{HWF} &\approx E_H [n_{\text{out}}] - E_H [n_{\text{in}}] \\ &\approx \frac{1}{2} \int \int \frac{[n_{\text{out}}(\mathbf{r}) - n_{\text{in}}(\mathbf{r})][n_{\text{out}}(\mathbf{r}') - n_{\text{in}}(\mathbf{r}')]}{|\mathbf{r} - \mathbf{r}'|} \delta\mathbf{r} \delta\mathbf{r}' \\ &= \frac{1}{2} \int \int \frac{\Delta n \Delta n'}{|\mathbf{r} - \mathbf{r}'|} \delta\mathbf{r} \delta\mathbf{r}' , \end{aligned} \quad (3.33)$$

where $\Delta n = n_{\text{out}}(\mathbf{r}) - n_{\text{in}}(\mathbf{r})$ and is small. This is the way in which the *PWscf* package determines the degree of self-consistency during an iterative step [46] as at the self-consistent Kohn-Sham energy $E_{KS} = E_{HWF}$ and $\Delta n = 0$.

Mixing

At the end of the i^{th} iteration, if self-consistency has yet to be reached, a choice must be made for $n_{\text{in}}^{(i+1)}$. The simplest option is just to set it to $n_{\text{out}}^{(i)}$, but this typically results in large step sizes and, near the self-consistent solution, an $n_{\text{out}}^{(i)} = n_{\text{in}}^{(i+1)}$ that has stepped across the ground state density from $n_{\text{in}}^{(i)}$. This can occur for some number of iterations, with only very small improvements in Δn per iteration i.e. $n_{\text{in}}^{(i)} \approx n_{\text{in}}^{(i+2)}$, and similarly for n_{out} . The worst case scenario is that new iterates become restricted to a subspace of previous iterates, and the process will run indefinitely without convergence (or divergence). A simple solution to this is linear mixing, where $n_{\text{in}}^{(i)}$ is modified by some fraction of Δn to give $n_{\text{in}}^{(i+1)}$, as in Equation 3.34a below (with the more general form in Equation 3.34b, where \mathbf{f}_i is the residual, or error vector, between iterative steps), where this fraction is α :

$$|n_{\text{in}}^{(i+1)}\rangle = |n_{\text{in}}^{(i)}\rangle + \alpha \left(|n_{\text{out}}^{(i)}\rangle - |n_{\text{in}}^{(i)}\rangle \right) \quad (3.34a)$$

$$\mathbf{x}_{i+1} = \mathbf{x}_i + \alpha \mathbf{f}_i \quad (3.34b)$$

In this way the mixing parameter $\alpha \in 0,1$ determines the degree of influence that previous iterations have on the current iterate. A larger α will more closely replicate the case where $n_{\text{in}}^{(i+1)} = n_{\text{out}}^{(i)}$, and a smaller α may take a long time to converge due to very small step sizes. The specific choice of this parameter, and analogous parameters for the more complex mixing methods below, depends on the system and specific form of the space of density functions. Practically, it is chosen empirically.

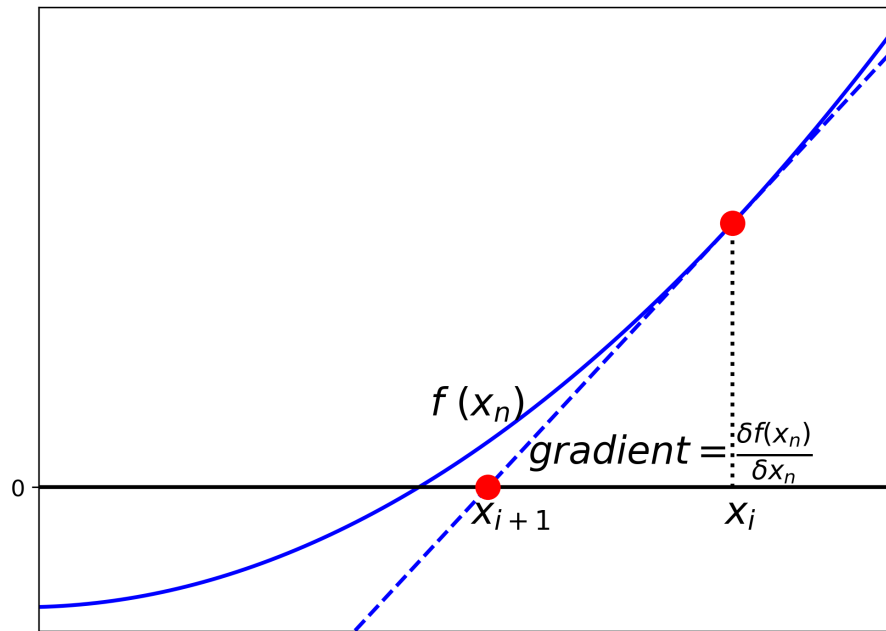


Figure 3.2: A schematic representation of the root-finding algorithm, the Newton-Raphson method. An iterative estimate x_i , is updated by the intercept of the derivative of the slope at x_i .

The basis for the Broyden method [73] of mixing is the well-known Newton-Raphson method, which is as follows: a set of m nonlinear equations

$$f_j(x_1, x_2, \dots, x_m) = 0 \quad (3.35)$$

for $j \in \mathbb{Z}, 1 \leq j \leq m$, can be expressed as the function application of the function operator

column vector \mathbf{f} to the column vector of independent variables \mathbf{x} , such that

$$\mathbf{f}(\mathbf{x}) = \begin{bmatrix} f_1(x_1, x_2, \dots, x_m) \\ f_2(x_1, x_2, \dots, x_m) \\ \vdots \\ f_m(x_1, x_2, \dots, x_m) \end{bmatrix} = 0. \quad (3.36)$$

Considering a plot of $\mathbf{f}(\mathbf{x})$ against \mathbf{x} in some abstracted vector space (or simply the two-dimensional scalar analogue), the Newton-Raphson method takes a tangent along $\mathbf{f}(\mathbf{x})$ at \mathbf{x}_i , and evaluates its horizontal axis intercept. As long as \mathbf{x}_i is not separated from the horizontal axis intercept of $\mathbf{f}_i(\mathbf{x})$ by a local minima (i.e. \mathbf{x}_i is close to the true root), then the intercept of the tangent will be closer to the root than is the value of \mathbf{x}_i , and so is taken as \mathbf{x}_{i+1} . This is visualized in Figure 3.2. The slope-intercept form of such a tangent can be seen to be

$$\mathbf{f}(\mathbf{x}) = \mathbf{J}_i(\mathbf{x} - \mathbf{x}_i) + \mathbf{f}_i, \quad (3.37)$$

where term \mathbf{f}_i is shorthand for $\mathbf{f}(\mathbf{x}_i)$. When this equation is evaluated at the root ($\mathbf{f}(\mathbf{x}) = 0$), at which point $\mathbf{x} = \mathbf{x}_{i+1}$, results in

$$\mathbf{x}_{i+1} = \mathbf{x}_i - \mathbf{J}_i^{-1} \mathbf{f}_i, \quad (3.38)$$

where the Jacobian matrix of $\mathbf{f}(\mathbf{x})$ within any given iteration is

$$\mathbf{J} = \frac{\delta \mathbf{f}(\mathbf{x})}{\delta \mathbf{x}} = \begin{bmatrix} \frac{\delta \mathbf{f}_1(\mathbf{x})}{\delta x_1} & \frac{\delta \mathbf{f}_1(\mathbf{x})}{\delta x_2} & \dots & \frac{\delta \mathbf{f}_1(\mathbf{x})}{\delta x_m} \\ \frac{\delta \mathbf{f}_2(\mathbf{x})}{\delta x_1} & \frac{\delta \mathbf{f}_2(\mathbf{x})}{\delta x_2} & \dots & \frac{\delta \mathbf{f}_2(\mathbf{x})}{\delta x_m} \\ \vdots & \vdots & \ddots & \vdots \\ \frac{\delta \mathbf{f}_m(\mathbf{x})}{\delta x_1} & \frac{\delta \mathbf{f}_m(\mathbf{x})}{\delta x_2} & \dots & \frac{\delta \mathbf{f}_m(\mathbf{x})}{\delta x_m} \end{bmatrix}. \quad (3.39)$$

This method can be very computationally expensive, with m^2 evaluations of $\frac{\delta \mathbf{f}_j(\mathbf{x})}{\delta x_m}$ per iteration if solved analytically, and numerical solutions are still excessive for systems of

interest to this project (and modern electronic structure applications in general); m here is proportional to the number of electrons in the system. Additionally, if the initial guess of \mathbf{x} is not sufficiently close to the root, there may be a failure of convergence altogether (as alluded to above in the requirement that \mathbf{x}_i be not separated from the root by a local minima).

In the context of Kohn-Sham DFT, we are trying to minimize Δn i.e. the output density of iteration i should equal the initial input density of iteration i after it is fed through the Kohn-Sham equations via the effective potential. The iterative method is used after the determination of n_{out} via the potential; we will discuss here only the selection of a new density where n_{out} is n_i and the subsequent new n_{in} is then n_{i+1} . The above $\mathbf{f}(\mathbf{x})$ is therefore specifically Δn , and the variables \mathbf{x} are the density n .

A method that reduces the large computational costs of the Newton-Raphson method is that of Broyden's second method, where we consider an approximation to the Jacobian matrix \mathbf{J} , calculate it once and then update it every iteration with a matrix that is more tractable. In the following, we use the notation \mathbf{H} and \mathbf{C} due to their use in the surrounding literature, but they no longer represent the Hamiltonian and eigenvector matrices that they did above. The approximate Jacobian matrix is denoted \mathbf{B} , and we additionally define

$$\mathbf{p}_i = -\mathbf{B}_i^{-1}\mathbf{f}_i , \quad (3.40)$$

and the above Newton-Raphson relationship becomes

$$\mathbf{x}_{i+1} = \mathbf{x}_i + t_i\mathbf{p}_i , \quad (3.41)$$

where t_i is a scalar coefficient that we will for now treat as arbitrary, but is chosen to prevent divergence (although it does not guarantee convergence). As such, our solution such that $\mathbf{f}(\mathbf{x}) = 0$ is

$$\mathbf{x} = \mathbf{x}_i + t\mathbf{p}_i . \quad (3.42)$$

For each of the nonlinear equations we have

$$\frac{\delta f_j}{\delta t} = \sum_k^m \frac{\delta f_j}{\delta x_k} \frac{\delta x_k}{\delta t} , \quad (3.43)$$

which implies that

$$\frac{\delta \mathbf{f}}{\delta t} = \mathbf{J} \mathbf{p}_i \quad (3.44)$$

where the left hand side is the vector consisting of derivatives of f_j with respect to t . If we could solve this analytically without unreasonable computational resources, we would not need this method in the first place. So, we look for approximations to the Jacobian matrix at the point \mathbf{x}_i . We can expand about t_i the term

$$\mathbf{f}(t_i - s) \approx \mathbf{f}_{i+1} - s \frac{\delta \mathbf{f}}{\delta t} \quad (3.45)$$

where s_i is chosen to be small and is the coefficient of the ratio between the Jacobian matrix and its estimate, \mathbf{B} (a ratio that should be approximately one for a good solution), used as a difference between consecutive steps of $\mathbf{f}(t_i)$. We have also excluded higher order terms in our Taylor expansion on the premise that s is small. When, therefore, \mathbf{f}_{i+1} and $\mathbf{f}(t_i - s_i)$ are known, an approximation of $\frac{\delta \mathbf{f}}{\delta t}$ and so the Jacobian matrix need not be computed directly. We can represent the above expansion as

$$\mathbf{f}_{i+1} - \mathbf{f}(t_i - s) \approx s_i \mathbf{J} \mathbf{p}_i , \quad (3.46)$$

and as we are aiming to improve the agreement between \mathbf{J} and \mathbf{B} with each step, we are trying to choose a \mathbf{B}_{i+1} that satisfies

$$\mathbf{f}_{i+1} - \mathbf{f}(t_i - s) = s_i \mathbf{B}_{i+1} \mathbf{p}_i . \quad (3.47)$$

In order to find the root of the initial problem, \mathbf{x} such that $\mathbf{f}(\mathbf{x}) = 0$, one needs to solve m equations of $\mathbf{p} = -\mathbf{B}_i^{-1} \mathbf{f}_i$. This can, however, be reduced to matrix-vector multiplication,

saving resources. For the purposes of reducing clutter we define

$$\mathbf{H}_i = -\mathbf{B}_i^{-1} \quad (3.48)$$

and

$$\mathbf{y}_i = \mathbf{f}_{i+1} - \mathbf{f}(t_i - s_i) \quad (3.49)$$

such that we have now

$$\mathbf{p}_i = \mathbf{H}_i \mathbf{f}_i \quad (3.50)$$

and

$$\mathbf{H}_{i+1} \mathbf{y}_i = -s_i \mathbf{p}_i = -s_i \mathbf{H}_i \mathbf{f}_i . \quad (3.51)$$

This equation describes the change in the value of the our function, $\mathbf{f}(\mathbf{x})$, between an evaluation at \mathbf{x}_{i+1} and $\mathbf{x}_i + (t_i - s_i) \mathbf{p}_i$. It does so through the gradient of the function in the direction of \mathbf{p}_i (through the estimate of our Jacobian matrix). If we consider this for some arbitrary vector, \mathbf{v}_i , we have two limit cases whereby if $\mathbf{v}_i^T \mathbf{y}_i = 0$ i.e. \mathbf{v}_i and \mathbf{y}_i are orthogonal to each other, and the case where $\mathbf{v}_i = \mathbf{y}_i$. In these two cases, then, the difference change in our matrix from an iterative step in the direction \mathbf{v}_i is

$$\mathbf{H}_{i+1} \mathbf{v}_i - \mathbf{H}_i \mathbf{v}_i = \begin{cases} 0 & \text{if } \mathbf{v}_i^T \mathbf{y}_i = 0 \\ -s_i \mathbf{p}_i - \mathbf{H}_i \mathbf{y}_i & \text{if } \mathbf{v}_i = \mathbf{y}_i \end{cases} . \quad (3.52)$$

The first case is justified by the fact that there is no information about the rate of change in directions other than \mathbf{y}_i . We chose then an updated matrix \mathbf{H}_{i+1} such that the change in our function $\mathbf{f}(\mathbf{x})$ in a direction orthogonal to \mathbf{y}_i is unaffected by iterative improvement of our matrix. We are in this manner directed towards finding a more satisfying expression

that obeys the above conditional equality, which is simply

$$\mathbf{v}_i (\mathbf{H}_{i+1} - \mathbf{H}_i) = (-s_i \mathbf{p}_i - \mathbf{H}_i \mathbf{v}_i) \frac{\mathbf{v}_i^T \mathbf{y}_i}{\mathbf{y}_i^T \mathbf{y}_i}. \quad (3.53)$$

Evaluating this where $\mathbf{v}_i = \mathbf{y}_i$, which is the original direction we are interested in anyway, we find through rearranging that

$$\mathbf{H}_{i+1} = \mathbf{H}_i - \frac{(s_i \mathbf{p}_i + \mathbf{H}_i \mathbf{y}_i) \mathbf{y}_i^T}{\mathbf{y}_i^T \mathbf{y}_i}. \quad (3.54)$$

Using this relation, the Jacobian matrix can be updated by a rank-one matrix, without having to solve for the Jacobian during every iteration. This is Broyden's second method, and in this project we use a modified version of this method by Johnson [74] to handle the choice of the next iteration's input density. Broyden's first method requires the storage of $N \times N$ matrices (which can be really quite large for systems of interest), whereas the second method does not; by using the inverse of the Jacobian matrix, it devolves to a problem of i vectors of length N . Johnson's modification builds additionally on a former modification by Vanderbilt and Louie [75], where information from historic iterations (and not just the single most recent) is used in order to improve the next guess of the Jacobian matrix. Doing so acts to improve the rate of convergence as it provides an additional check on overstepping the root, similar to the implementation of α in simple linear mixing. Johnson's work removed the storage requirement of $N \times N$ matrices by applying the same principle by Vanderbilt and Louie to Broyden's second method, with the inverse Jacobian matrix.

The following exposition is based on work by Johnson [74], with some changes in nomenclature to agree with our previous notation. First, a function is constructed that describes the weighted error in the current inverse Jacobian, and the weighted error in all previous inverse Jacobian matrices from iteration j if they were determined by the

current iteration's vector solutions. This function is

$$E = w_0^2 |\mathbf{H}_{i+1} - \mathbf{H}_i|^2 + \sum_{j=1}^i w_j^2 |\Delta \mathbf{x}_j + \mathbf{H}_{i+1} \Delta \mathbf{f}_j|^2, \quad (3.55)$$

where w_0 and w_j are the weights of the errors and $\Delta \mathbf{x}_j$ and $\Delta \mathbf{f}_j$ are the differences from iterations $j+1$ and j of \mathbf{x}_j and \mathbf{f}_j , scaled by $|\mathbf{f}_{j+1} - \mathbf{f}_j|$, respectively. As such, $\Delta \mathbf{f}_j^T \Delta \mathbf{f}_j = 1$.

Minimizing this function gives

$$\frac{\delta E}{\delta \mathbf{H}_{i+1}} = 0 = w_0^2 |\mathbf{H}_{i+1} - \mathbf{H}_i| + \sum_{j=1}^i w_j |\Delta \mathbf{x}_j + \mathbf{H}_{i+1} \Delta \mathbf{f}_j| |\Delta \mathbf{f}_j|, \quad (3.56)$$

and so

$$\mathbf{H}_{i+1} = \mathbf{H}_i - \sum_{j=1}^i \frac{w_j^2}{w_0^2} \Delta \mathbf{x}_j \Delta \mathbf{f}_j^T - \sum_{j=1}^i \frac{w_j^2}{w_0^2} \mathbf{H}_{i+1} \Delta \mathbf{f}_j \Delta \mathbf{f}_j^T, \quad (3.57)$$

which can be rearranged and displayed as

$$\mathbf{H}_{i+1} = \boldsymbol{\gamma}_{i+1} \boldsymbol{\beta}_{i+1}^{-1} \quad (3.58)$$

where

$$\boldsymbol{\gamma}_{i+1} = w_0^2 \mathbf{H}_i - \sum_{j=1}^i w_j^2 \Delta \mathbf{x}_j \Delta \mathbf{f}_j^T \quad (3.59)$$

and

$$\boldsymbol{\beta}_{i+1} = w_0^2 \mathbf{I} + \sum_{j=1}^i w_j^2 \Delta \mathbf{f}_j \Delta \mathbf{f}_j^T, \quad (3.60)$$

with \mathbf{I} as the identity matrix. To find the inverse of $\boldsymbol{\beta}_{i+1}$, an infinite Neumann series expansion of $(\mathbf{I} - \mathbf{X})^{-1} = \sum_0^k \mathbf{X}^k$ was performed, where here

$$\begin{aligned} \mathbf{X} &= (-1) \widetilde{\Delta \mathbf{f}_j} \widetilde{\Delta \mathbf{f}_j}^T, \\ \widetilde{\Delta \mathbf{f}_j} &\equiv \frac{w_j}{w_0} \Delta \mathbf{f}_j. \end{aligned} \quad (3.61)$$

As such, using Einstein notation to handle the notationally unwieldy summations, the infinite expansion is

$$\begin{aligned}
\boldsymbol{\beta}_{i+1}^{-1} &= w_0^{-2} (\mathbf{I} - \mathbf{X})^{-1} \\
&= w_0^{-2} \left[\mathbf{I} - \widetilde{\Delta \mathbf{f}}_j \widetilde{\Delta \mathbf{f}}_j^T + \left(\widetilde{\Delta \mathbf{f}}_j \widetilde{\Delta \mathbf{f}}_j^T \right)^2 - \left(\widetilde{\Delta \mathbf{f}}_j \widetilde{\Delta \mathbf{f}}_j^T \right)^3 + \dots \right] \\
&= w_0^{-2} \left[\mathbf{I} - \widetilde{\Delta \mathbf{f}}_j \widetilde{\Delta \mathbf{f}}_k^T \left(\delta_{jk} - \widetilde{\mathbf{A}}_{kj} + \widetilde{\mathbf{A}}_{ki} \widetilde{\mathbf{A}}_{ij} - \widetilde{\mathbf{A}}_{ki} \widetilde{\mathbf{A}}_{in} \widetilde{\mathbf{A}}_{nj} + \dots \right) \right],
\end{aligned} \tag{3.62}$$

where an extra summation index is included with each increasing power of the infinite series (k and n so far), and \mathbf{A} is defined as

$$\begin{aligned}
\mathbf{A}_{ij} &= w_i w_j \Delta \mathbf{f}_i \Delta \mathbf{f}_j^T, \\
\widetilde{\mathbf{A}}_{ij} &\equiv \frac{w_j}{w_0} \mathbf{A}_{ij}.
\end{aligned} \tag{3.63}$$

It is at this point that Johnson modifies the method that so far has been the same as that from Vanderbilt and Louie [75]; recognizing that the infinite series term is itself a Neumann series, it can be contracted, returned to the usual summation notation, and the weighting terms taken back out explicitly:

$$\boldsymbol{\beta}_{i+1}^{-1} = w_0^{-2} \left[\mathbf{I} - \sum_{j,k=1} w_j w_k \Delta \mathbf{f}_j \Delta \mathbf{f}_k^T (w_0^2 \mathbf{I} + \mathbf{A})_{kj}^{-1} \right] = w_0^{-2} \left(\mathbf{I} - \sum_{j,k=1} w_j w_k \mathbf{C}_{kj} \Delta \mathbf{f}_j \Delta \mathbf{f}_k^T \right), \tag{3.64}$$

where

$$\mathbf{C}_{kj} \equiv (w_0^2 \mathbf{I} + \mathbf{A})_{kj}^{-1}. \tag{3.65}$$

Johnson then substitutes this inverted term, $\boldsymbol{\beta}_{i+1}^{-1}$, into Equation 3.58 and factorises to get

$$\mathbf{H}_{i+1} = \mathbf{H}_i - \sum_{j,k=1} \mathbf{C}_{kj} (\mathbf{H}_i \Delta \mathbf{f}_j + \Delta \mathbf{x}_j) \Delta \mathbf{f}_k^T. \tag{3.66}$$

To put this in terms of \mathbf{H}_1 , Johnson uses a process of induction to produce the

relationship

$$\mathbf{H}_{i+1} = \mathbf{H}_1 - \sum_{k=1}^i \mathbf{z}_i^{(k)} \Delta \mathbf{f}_k^T, \quad (3.67)$$

where

$$\mathbf{z}_i^{(k)} = \sum_{k=1}^i \mathbf{C}_{kj} \mathbf{u}_j + w_0^2 \sum_{j=1}^{i-1} \mathbf{C}_{kj} \mathbf{z}_{i-1}^{(j)}, \quad (3.68)$$

and

$$\mathbf{u}_j = \mathbf{H}_1 \Delta \mathbf{f}_j + \Delta \mathbf{x}_j. \quad (3.69)$$

The matrices here are small $i \times i$ matrices, instead of the large $N \times N$ that would have to be dealt with using Vanderbilt and Louie's modification starting with the Jacobian, \mathbf{B} . Now, for small w_0 , the above expression can be recast as

$$\mathbf{H}_{i+1} = \mathbf{H}_1 - \sum_{j,k=1}^i \mathbf{C}_{kj} \mathbf{u}_j \Delta \mathbf{f}_k^T + \mathcal{O}(w_0^2). \quad (3.70)$$

In this limit \mathbf{H}_i can be expressed in terms of \mathbf{H}_1 and a sum over $i-1$ to update the general form of Equation 3.34 through α , given the final modified Broyden expression:

$$\mathbf{x}_{i+1} = \mathbf{x}_i + \mathbf{H}_1 \mathbf{f}_i - \sum_{j,k=1}^{i-1} w_j w_k \Delta \mathbf{f}_k^T \mathbf{f}_i \mathbf{C}_{kj} \mathbf{u}_j. \quad (3.71)$$

By examination of Equation 3.71 we see that in order to update our value for n each iteration, we must keep in memory the current vectors \mathbf{x} and \mathbf{f} , all previous iterations of the vectors \mathbf{u} and $\Delta \mathbf{f}^T$, and the matrix \mathbf{A} . This leads to the fairly modest storage requirement of an $i \times i$ matrix and i vectors of length N . The value of \mathbf{H}_1 is chosen empirically, and in the primary computational suite used in this project, Quantum ESPRESSO, it is $\alpha \mathbf{I}$, $0 < \alpha < 1$. With this definition, Equation 3.71 reduces to linear mixing with some correction, although subsequent iterations of \mathbf{H} cannot be represented by a scalar multiple of the identity matrix. Within Quantum ESPRESSO's *PWscf* package, the parameter

that controls \mathbf{H}_1 through α is the `mixing_beta` (despite the name, we have represented it here as α in keeping with the relevant literature surrounding the Broyden class of methods).

3.1.2 Exchange-correlation functionals

The Kohn-Sham DFT formulation is, in principle, an exact theory. The component that prevents practical attempts to wield the theory from being exact is the exchange-correlation functional. A good approximation to this component results in good approximations in output parameters, with a number of levels of theory existing as options. The simplest is the local density approximation (LDA), which is then built upon in subsequent improvements. The concept of the electron hole reappears here, but in a slightly different context; instead of being a region of relative positive charge due to a missing electron, it is the region surrounding an electron that has a decreased probability of containing a second electron due to the exchange (Pauli repulsion) and correlation (Coulomb repulsion) interactions.

We can express the exchange-correlation energy of Equation 3.12 in terms of each individual interacting electron as

$$E_{XC}[n] = \int n(\mathbf{r}) \epsilon_{XC}([n], \mathbf{r}) \delta\mathbf{r} , \quad (3.72)$$

where $\epsilon_{XC}([n], \mathbf{r})$ is the exchange-correlation interaction energy of a single electron at point \mathbf{r} as a functional of the density within a neighbourhood around \mathbf{r} . The energy of an electron interacting with its own hole is

$$\epsilon_{XC} = \frac{1}{2} \int \frac{n_{XC}(\mathbf{r}, \mathbf{r}')}{|\mathbf{r} - \mathbf{r}'|} \delta\mathbf{r} , \quad (3.73)$$

where $n_{XC}(\mathbf{r}, \mathbf{r}')$ is the hole around an electron at \mathbf{r} caused by exchange-correlation. We do not necessarily know the shape of this hole, but we do know that the electron density must integrate over all space to give the total number of electrons. So, as the exchange-correlation density reduces the electronic density around the reference point \mathbf{r} due to the

Pauli exclusion principle, in order to maintain the correct total electron count, N , we have that

$$\int n_{XC}(\mathbf{r}, \mathbf{r}') \delta \mathbf{r}' = -1, \quad (3.74)$$

known as the sum rule.

The local density approximation

The local density approximation (LDA) is the approximation that the exchange-correlation energy at each point \mathbf{r} is the same as that in a homogeneous electron gas with the same density as our system at that point \mathbf{r} (the density is local to the position \mathbf{r}). In the homogeneous case, the electron hole will be spherical in shape, and the exchange-correlation energy functional is

$$\begin{aligned} E_{XC}^{(\text{LDA})}[n] &= \int \epsilon_{XC}^{(\text{hom})}(n(\mathbf{r})) \delta \mathbf{r} \\ &= \int \epsilon_X^{(\text{hom})}(n(\mathbf{r})) \delta \mathbf{r} + \int \epsilon_C^{(\text{hom})}(n(\mathbf{r})) \delta \mathbf{r}. \end{aligned} \quad (3.75)$$

The exchange functional for a single electron, $\epsilon_X^{(\text{single})}(n(\mathbf{r}))$, is given in Equation 2.60 as the exchange term, i.e.

$$\epsilon_X^{(\text{single})}(n(\mathbf{r})) = - \sum_j \int \frac{e^2}{|\mathbf{r} - \mathbf{r}'|} \psi_j^*(\mathbf{r}') \psi_i(\mathbf{r}') \psi_j(\mathbf{r}) \delta \mathbf{r}', \quad (3.76)$$

for unpolarized spin cases. For wavefunctions of the plane wave form

$$\psi(\mathbf{r}) = e^{i\mathbf{k}\cdot\mathbf{r}} \quad (3.77)$$

and making use of the Fourier transform of the Coulomb term,

$$\frac{q^2}{|\mathbf{r} - \mathbf{r}'|} = 4\pi q^2 \int \frac{1}{(2\pi)^3} \frac{1}{k} e^{i\mathbf{k}\cdot(\mathbf{r}-\mathbf{r}')} \delta \mathbf{k}, \quad (3.78)$$

when $q = e$, via Equation 3.76 we reach the expression

$$\epsilon_X^{(\text{single})}(n(\mathbf{r})) = - \sum_j \int \left[4\pi q^2 \int \frac{1}{(2\pi)^3} \frac{1^2}{k} e^{i\mathbf{k}\cdot(\mathbf{r}-\mathbf{r}')} \right] \psi_j^*(\mathbf{r}') \psi_i(\mathbf{r}') \psi_j(\mathbf{r}) \delta\mathbf{r}' . \quad (3.79)$$

Letting $e = 1$ for natural units, this has the analytical solution

$$\epsilon_X^{(\text{single})}(n(\mathbf{r})) = -\frac{k_F}{\pi} F(x) , \quad (3.80)$$

where

$$F(x) = 1 + \frac{1-x^2}{2x} \ln \frac{1+x}{1-x} , \quad (3.81)$$

$$x = \frac{k}{k_F} . \quad (3.82)$$

The exchange energy per electron of a homogeneous electron gas, then, is this exchange energy of a single electron divided by two (to avoid double counting), with $F(x)$ evaluated as its average value of $\frac{3}{2}$:

$$\epsilon_X^{(\text{hom})}(n(\mathbf{r})) = \frac{E_X}{N} = -\frac{3}{4\pi} k_F = -\frac{3}{4} \left(\frac{3n^{(\text{hom})}}{\pi} \right)^{\frac{1}{3}} . \quad (3.83)$$

The correlation energy of an electron is the interaction energy of that with all other electrons. The holes produced by the other electrons act to screen these interactions, such that the long-range Coulomb interaction can be treated as exponentially decaying. The screening models used are saved for discussion later in the specific context of the exchange-correlation functional used during this project, but the correlation energy in general cannot be found analytically. Even in the simple system of a homogeneous electron gas, one must use interacting many-body methods, the gold standard of which is currently quantum Monte Carlo calculations.

The generalized gradient approximation

The LDA is based on the premise that our system of interest behaves similarly to a uniform electron gas with respect to exchange and correlation interactions. However, in the case of non-homogeneous systems (molecules, heterostructures, systems with defects, crystal that are not monatomic), there is a non-constant density, even over short range. In order to capture this variation in density, one might expect a more reasonable approximation for the exchange-correlation functional to include a term corresponding to the change in density with respect to position i.e. the gradient of the density.

A method for doing this is to expand the local density approximation as a series, and drop higher order terms, which is schematically

$$f = f^{\text{LDA}} (1 + \mu_1 s_1^2 + \mu_2 s_2^2 \dots) , \quad (3.84)$$

where often only the first term in s is included, for an s of form

$$s_m = \frac{|\nabla^m n|}{n^{1+\frac{m}{3}}} . \quad (3.85)$$

The denominator in s_m is to normalize to a dimensionless quantity (in natural units, $e = 1$), such that s is the reduced gradient. The specific form of s varies between functionals, but is modified to be a measure of how fast the density changes over particular scales. For our purposes here, we will drop all terms other than s_1 , simply referred to as s . μ is determined by the particulars of the functional: either empirically to result in good agreement with some previously determined reference results, or to meet some conditions of the formulation (as it is in the functional we use in this project, discussed shortly). The dependence of the exchange-correlation functional on both the density and the gradient of the density leads to the name of the class of functional, generalized gradient approximation (GGA) functionals.

The Perdew-Burke-Ernzerhof functional

The exchange-correlation functional that we use is the Perdew-Burke-Ernzerhof [43] GGA, which begins with the correlation functional as

$$E_C^{(PBE)} = \int n \left(\epsilon_C^{(\text{hom})}(r_s) + H(r_s, t) \right) \delta \mathbf{r} , \quad (3.86)$$

where both $\epsilon_C^{(\text{hom})}$ and H depend also on relative spin polarization, but we consider here only the unpolarized case. r_s is the local Seitz radius, the radius of a sphere with volume equal to that taken up by a single free electron,

$$r_s = \left(\frac{3}{4\pi n} \right)^{\frac{1}{3}} , \quad (3.87)$$

and t is the reduced gradient on the scale of Thomas-Fermi screening effects (see Section 2.1.4),

$$t = \frac{|\nabla n|}{2k_s n} , \quad (3.88)$$

where k_s is the Thomas-Fermi wavevector (see Equation 2.82). The specific form of H is determined by constraining it to certain conditions:

- it recovers the second-order gradient expansion above ($H \rightarrow \beta t^2$) in the limit that the gradient of density varies slowly, with the coefficient β determined numerically [76] ,
- it cancels the correlation term of the homogeneous electron gas in the limit of rapidly varying density ($t \rightarrow \infty$) such that correlation interaction energies vanish, and
- it scales uniformly between these two limits.

The final condition is so that it cancels the logarithmic divergence of the LDA correlation found by a perturbation expansion in powers of r_s [77] in the high density limit.

There are conditions placed on the formulation of the exchange energy as well. In the high density limit (the low reduced gradient limit), the functional must recover the LDA

value, and so is of form

$$E_X^{(PBE)} = \int n \epsilon_X^{(\text{hom})} F_X(s) \delta \mathbf{r} , \quad (3.89)$$

where $F_X(0) = 1$ and in this specific functional the reduced gradient is

$$s = \frac{|\nabla n|}{2k_F n} , \quad (3.90)$$

in order to normalize the gradient over the scale of the Fermi wavevector, k_F , introduced in Section 2.1. We also want the functional to be similar to the LDA for small density variations, as it is a good approximation [78], so we use a form of F_X such that as $s \rightarrow 0$,

$$F_X(s) \rightarrow 1 + \mu s^2 . \quad (3.91)$$

In order to also satisfy the Lieb-Oxford bound [79], the lower limit on the ‘indirect’ part of the Coulombic interaction energy (that part which arises from the quantum effects of exchange and correlation), such that

$$E_X \geq E_{XC} \geq -C e^2 \int n^{\frac{4}{3}} \delta \mathbf{r} , \quad (3.92)$$

where C has been improved upon over the years [79–82] but is stated as 1.679 in the original PBE formulation. In order to satisfy the Lieb-Oxford inequality and still recover the form above for small density variations, we recast our function as

$$F_X(s) = 1 + \kappa - \kappa \left(1 + \frac{\mu s^2}{\kappa} \right)^{-1} , \quad (3.93)$$

where in the case of $C = 1.679$, $\kappa = 0.804$.

3.1.3 Van der Waals corrections

A van der Waals correction can be included in the determination of the energy of a system, and so far the dispersion force has not yet been considered. The correction used in this

project is that of Grimme’s DFT-D3 [65], which is calculated and subtracted from the Kohn-Sham energy determined from a particular exchange-correlation functional. This specific correction has been chosen for its good results [52], low computational burden, and strong compatibility with our chosen exchange-correlation functional, PBE. Indeed, one of the goals of the correction’s development was compatibility with PBE (and other common functionals).

The dispersion correction is as follows:

$$E_{\text{DFT-D3}} = E_{KS} - E_{\text{disp}} , \quad (3.94)$$

where E_{disp} is the sum of the two- and three-body terms, respectively:

$$E_{\text{disp}} = E_{(2)} + E_{(3)} . \quad (3.95)$$

The two-body term is more important, and is a form of our previously determined Equation 2.251, but with a more proper treatment of the frequency-dependence of the polarizability, α . The two-body term for a system of interacting species, where AB is a pair of any particular species, is

$$E_{(2)} = \sum_{AB} \sum_{n=6,8,10,\dots} s_n \frac{C_{n,AB}}{r_{AB}^n} f_d , \quad (3.96)$$

where s is a scale factor that depends on which exchange-correlation functional the correction is being used with (as some hybrid functionals account for long-range dispersion already), f_d is a damping function to avoid near-singularity behavior at small radii r_{AB} , chosen to be numerically stable, and C_{AB} are the dispersion coefficients of the atomic pair AB ,

$$C_{6,AB} = \frac{3}{\pi} \int_0^\infty \alpha_A(i\omega) \alpha_B(i\omega) \delta\omega , \quad (3.97)$$

$$C_{8,AB} = 3C_{6,AB} \sqrt{(Z_A Z_B)^{\frac{1}{2}} \frac{\langle r_{AB}^4 \rangle}{\langle r_{AB}^2 \rangle}} , \quad (3.98)$$

where ω is the frequency of the field inducing the dipole moment, Z is the nuclear charge, and our terms in r^{-8} and beyond come from a multipole expansion. There are higher order terms in the two-body dispersion energy, but they are here ignored; while discussed in Grimme's paper [65], they are excluded from the correction as they make calculations of complicated systems unstable, and do not improve those of simpler systems by any significant degree. The damping term, f_d , is one introduced by Chai and Head-Gordon [83], originally to fix divergence of the dispersion correction within their functional at short nuclear distances,

$$f_d = \left[1 + 6 \left(\frac{r_{AB}}{s_{r,n} R_{0,AB}} \right)^{-a_n} \right]^{-1}, \quad (3.99)$$

where $s_{r,n}$ is again a scaling factor, R_0 is the interatomic distance region within which the dispersion energy is decreasing in magnitude (determined as part of the correction), and a_n is a steepness parameter, determined manually.

The three-body term contributes much less to the total dispersion correction than the two-body term (approximately 5 – 10%), and the leading term is given by [84]

$$E_{ABC} = \frac{C_{ABC} (3 \cos \theta_a \cos \theta_b \cos \theta_c + 1)}{(r_{AB} r_{BC} r_{CA})^3}, \quad (3.100)$$

where θ are the internal angles of the triangle formed by r , and

$$C_{ABC} = \frac{3}{\pi} \int_0^\infty \alpha_A(i\omega) \alpha_B(i\omega) \alpha_C(i\omega) \delta\omega. \quad (3.101)$$

Non-leading terms are excluded due to their negligible contribution, resulting in a three-body term of

$$E_{(3)} = \sum_{ABC} f_{d,3} E_{ABC}, \quad (3.102)$$

where the damping term is determined using the geometrically averaged r .

3.1.4 Hybrid functionals

Hybrid functionals are typically an improvement over DFT-only methods, where by combining the exchange-correlation functionals from DFT (that are density dependent) with Hartree-Fock-like functionals (that are orbital dependent), results closer to those of experiment can be obtained compared to those from either isolated method. The ratio of combination is usually selected empirically, with justification for hybridization from the underestimation of energies from DFT and the overestimation of Hartree-Fock methods, both of which lead to poor experimental agreement of band gaps in solids. The mixing parameter, α , is the fractional contribution of the Hartree-Fock-like functionals, so in general we have

$$E_{XC}^{(\text{hybrid})} = E_{XC}^{(\text{DFT})} + \alpha \left(E_X^{(\text{DFT})} - E_X^{(\text{HF})} \right), \quad (3.103)$$

where the correlation component is not considered in hybrid due to being a small comparative contribution to the final result. Some hybrid formulations use multiple mixing fractions and multiple exchange functionals e.g. B3LYP, which uses Lee-Yang-Parr (LYP) correlation [85] and Becke (B88) exchange [86], each with different mixing fractions, but the principle remains the same. This project uses only one hybrid functional, which does not do this: the Heyd-Scuseria-Ernzerhof (HSE) functional [53]. The HSE functional is based off of the PBE DFT functional that we use in this project, and has been demonstrated to provide consistently strong performance for analysis of semiconductors' structural and electronic properties [54].

The Heyd-Scuseria-Ernzerhof functional

Long-range Hartree-Fock-like Coulomb interactions are difficult to calculate efficiently due to the non-local nature of the problem. So, the HSE approach is to split the exchange interaction into a long- and short-range interaction, and hybridizes only the short-range

component:

$$E_{XC}^{(HSE)} = \alpha E_X^{(HF,SR)}(\omega) + (1 - \alpha) E_X^{(PBE,SR)}(\omega) + E_X^{(PBE,LR)}(\omega) + E_C^{(PBE)}, \quad (3.104)$$

where the *LR* and *SR* superscripts denote long- and short-range components respectively. The dependence on the adjustable screening parameter ω provides the division of the Coulomb term into long- and short-range components, which is determined by substituting in the following:

$$\frac{1}{r} = \frac{\operatorname{erfc}(\omega r)}{r} + \frac{\operatorname{erf}(\omega r)}{r}, \quad (3.105)$$

where the first term on the right hand side is the short-range term, and the second the long-range term. $\operatorname{erf}(\omega r)$ is the error function, a sigmoid function that is normally distributed and runs between -1 and 1 , and $\operatorname{erfc}(\omega r) = 1 - \operatorname{erf}(\omega r)$. The choice of this specific function is partially arbitrary, with the authors giving the justification for its use as it being analytically integrable [53]. ω dictates the rate of decay of the error function, and so determines the relative contribution from long- and short-range functions at a particular distance i.e. it is a screening parameter.

The use of HSE, then, hybridizes the PBE DFT functional in a manner which avoids added computational resources for solving the long-range Coulomb contribution and the correlation interaction, while improving the prediction of the exchange interaction over short range (with careful, empirical, choice of ω). Due to the use of Hartree-Fock exchange there is still an increase in computational resources, but this increased cost goes towards the most impactful components of the functional.

3.2 Pseudopotentials

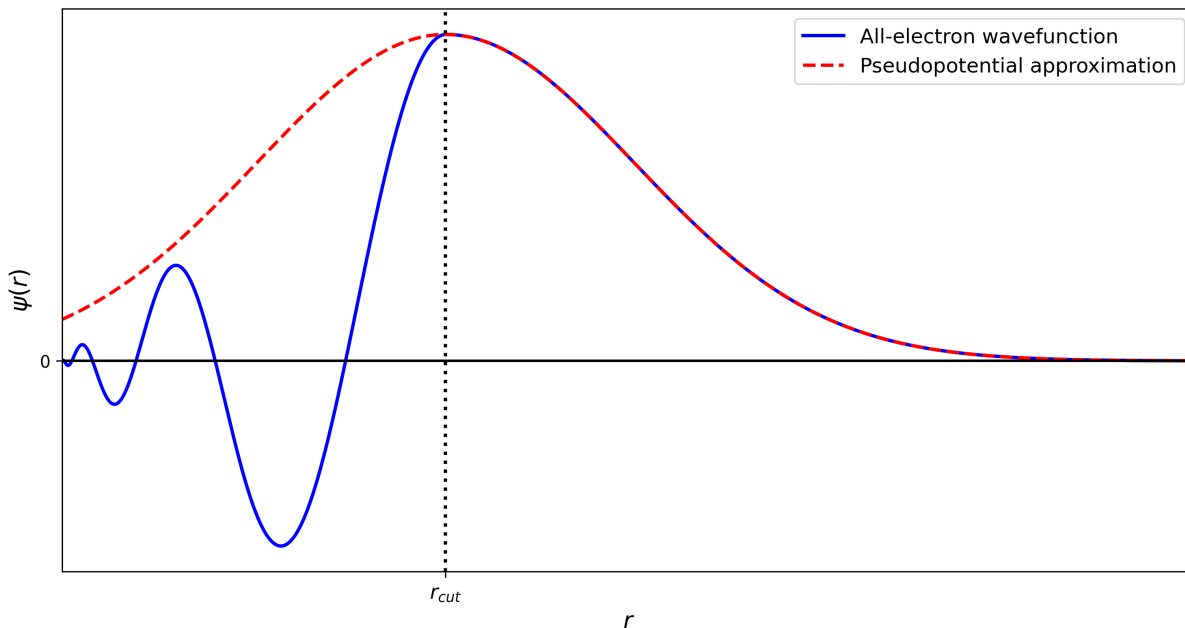


Figure 3.3: A comparison of the all-electron (solid, blue) and the pseudopotential approximation (dashed, red) of a wavefunction, ψ . The point beyond which the pseudopotential function matches the all-electron function is the cut-off radius, r_{cut} .

Pseudopotentials are replacements for real potentials that aim to reduce computational cost when determining properties that depend on that potential. As core electrons are chemically inert and do not contribute to bonding, for electronic structure calculations pseudopotentials replace the real electron density of electrons in the core with smoother approximations that give the same results within a desired precision of important properties. This is seen where the resultant potentials are the same for the exact and pseudopotential systems beyond a given atomic radial cut-off, r_{cut} . They result in much simpler electron wavefunctions, as in Figure 3.3. A pseudopotential as used in this project refers to that which describes the core electron density of a specific species, with particular considerations. These considerations are the type of exchange-correlation functional that is to be used, whether spin-orbit coupling needs considered, and the character of the pseudopotential (i.e. hardness and norm-conservation). To create a pseudopotential, atomic orbitals are calculated using DFT by solving self-consistent Kohn-Sham equations (Section 3.1) for one-electron states, for all electrons, including those in the core, typically in a simple system like a single spherical atom (due to

the cost of all-electron calculations; transferability to other systems is discussed in subsection 3.2.2). Smoother pseudo-orbitals are then mapped on to the ‘exact’ (within the limitations of the DFT exchange-correlation approximation) all-electron orbitals, and a pseudopotential function can be extracted that matches the all-electron potential beyond a desired r_{cut} , chosen such that the chemically active (valence) electrons are beyond this distance (Figure 3.4); repulsion from core electrons tends to maintain separation, and any the part of the valence orbitals that does potentially extend in to the core region is less important (otherwise core electrons would be more chemically active than they are). The pseudopotential does not match the all-electron potential at radial positions below r_{cut} , and instead is smoother and less computationally demanding to use in subsequent calculations. The pseudopotential is then validated by comparing electronic structure calculations using the pseudopotential and the all-electron potential. Future calculations using the pseudopotential assumes that the core electrons cannot change state, and keep their smoothed density defined by the pseudopotential; this is the frozen core approximation. The smoother pseudopotential has fewer Fourier modes, and so fewer plane waves must be considered to achieve an accurate result, i.e. the high energy plane waves that cause rapid oscillations in potential near the core can be ignored. This results in the concept of energy cut-off, the energy beyond which a calculation stops including plane waves. A smoother pseudopotential allows for lower energy cut-offs, saving computational resources.

3.2.1 Orthogonalized plane waves

The precursor to the modern pseudopotential method is the orthogonalized plane wave (OPW) method, developed by Conyers Herring in 1940 [87]. We will discuss this method here to provide some structural background for more modern pseudopotential formulations. The aim is effectively the same as the pseudopotential method; produce pseudowavefunctions for core electrons that are computationally less intensive to find solutions for than the true wavefunctions. The OPW method does this by defining a plane wave basis set for valence states which the pseudowavefunctions then follow from,

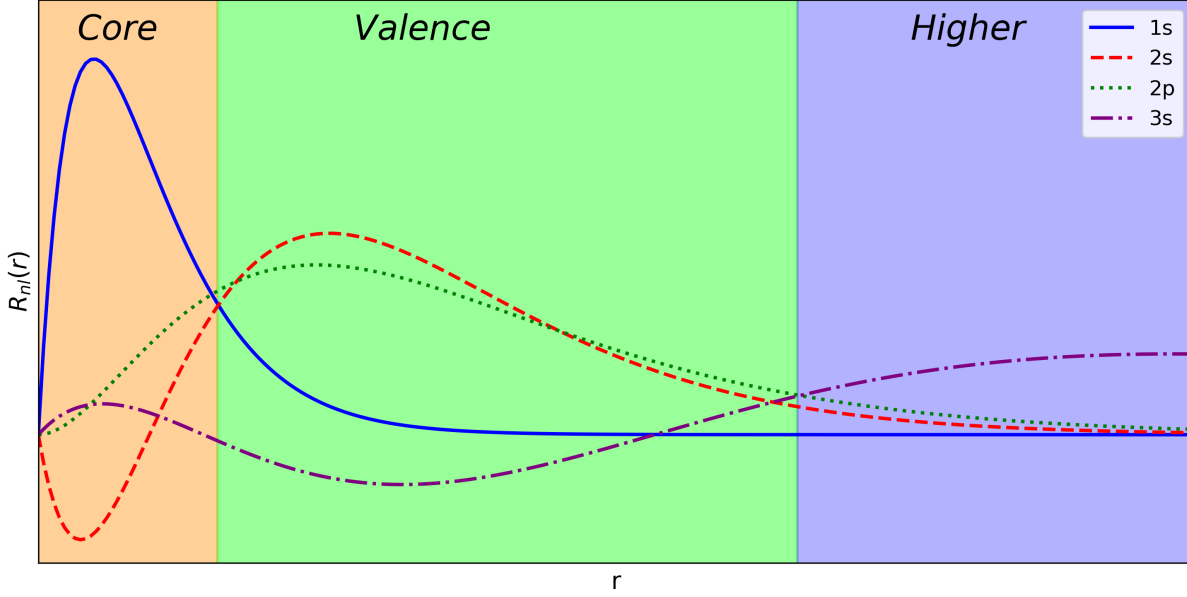


Figure 3.4: A general representation of the radial orbitals, $R_{nl}(r)$, of an atom, showing the probability density of radial position for some electrons. There is clear spatial separation between core states, valence states and unoccupied higher-energy states, allowing for selection of good r_{cut} values.

in contrast to pseudopotential methods that replace the atomic core potential.

To define the valence electron plane wave basis set, we subtract a correction term from the permitted plane wave set for all electrons. The correction term is the weighted overlap between permitted wavevectors and atomic core functions, $u_j(\mathbf{r})$, that are localized around the nucleus, representing core states. The plane wave basis functions are then

$$\chi_{\mathbf{q}}^{\text{OPW}}(\mathbf{r}) = \frac{1}{\Omega} \left[e^{i\mathbf{q}\cdot\mathbf{r}} - \sum_j \langle u_j | \mathbf{q} \rangle u_j(\mathbf{r}) \right], \quad (3.106)$$

where Ω is the volume of the crystal and \mathbf{q} is the wavevector associated with the plane wave. We can choose $u_j(\mathbf{r})$ such that the resultant wavefunction is separated into a smooth part of the function, approximating the core behavior, and an outer part that is equivalent to the true wavefunction. $\psi_l^v(\mathbf{r})$, the wavefunction of a valence electron of angular momentum l , is then represented by its Fourier expansion as

$$\psi_l^v(\mathbf{r}) = \int C_l(\mathbf{q}) \chi_{\mathbf{q}}^{\text{OPW}}(\mathbf{r}) \delta\mathbf{q} = \int C_l(\mathbf{q}) \frac{1}{\Omega} \left[e^{i\mathbf{q}\cdot\mathbf{r}} - \sum_j \langle u_j | \mathbf{q} \rangle u_j(\mathbf{r}) \right] \delta\mathbf{q}, \quad (3.107)$$

where C_l are the Fourier coefficients (see subsection 2.1.2). This is a superposition of the smoothed core function, $\tilde{\psi}_l^v$, and the term accounting for the part outside the core, as

$$\psi_l^v(\mathbf{r}) = \tilde{\psi}_l^v(\mathbf{r}) - \sum_j B_{l,j} u_{l,j}(\mathbf{r}) , \quad (3.108)$$

whose components have Fourier expansions

$$\tilde{\psi}_l^v(\mathbf{r}) = \int C_l(\mathbf{q}) e^{i\mathbf{q}\cdot\mathbf{r}} \delta\mathbf{r} , \quad (3.109)$$

$$B_{l,j} = \int C_l(\mathbf{q}) \langle u_j | \mathbf{q} \rangle \delta\mathbf{r} . \quad (3.110)$$

The wavefunctions resulting from the OPW basis functions have reduced amplitude and smoother structure near the nucleus compared to the true wavefunctions, but are not orthonormal.

3.2.2 Norm-conserving pseudopotentials

Consider the pseudopotential for a particular atomic species. We want it to be valid and computationally tractable when used in systems other than that within which it was created i.e. we want it to be transferable. As such, it should retain its validity when the atom is placed in a bound state within a molecule or crystal. When placed in a poly-atomic system, the valence orbitals experience a perturbation from other atomic cores, resulting in a shift in their energies (see section 2.2). In 1979, norm-conserving pseudopotentials (NCPPs) were developed by Hamann, Schlüter and Chiang from Bell Laboratories as an *ab initio* method of producing transferable pseudopotentials [88].

Applying our first constraint on the pseudo-wavefunction, the norm-conserving condition between the all-electron (ψ_{AE}) and pseudo-wavefunctions (ψ_{PP}),

$$|\langle \psi_{AE} | \psi_{AE} \rangle|^2 = |\langle \psi_{PP} | \psi_{PP} \rangle|^2 , \quad (3.111)$$

the integrated charge within r_{cut} must then agree between all-electron and pseudo-

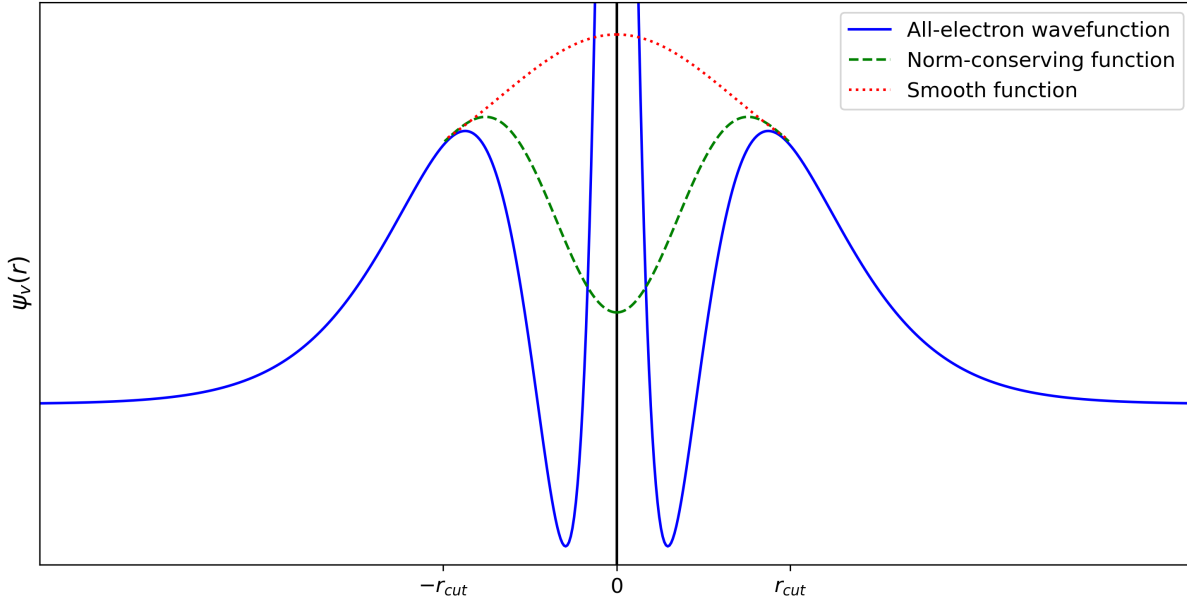


Figure 3.5: A schematic representation of a smooth function (dotted, red) in one dimension that matches a valence wavefunction (solid, blue) beyond the cut-off radius, r_{cut} . This is compared to a norm-conserving function (dashed, green) that also matches the wavefunction beyond r_{cut} .

wavefunctions, as the integrated charge therein is

$$Q_l = \int_0^{r_{\text{cut}}} r^2 |\psi_l(r)|^2 \delta r = \int_0^{r_{\text{cut}}} \phi_l(r)^2 \delta r . \quad (3.112)$$

where $\phi_l(r) \equiv r\psi_l(r)$ in spherical coordinates, which will be used later in place of the radial wavefunction to simplify some problems, and the fundamental unit of charge is being taken as 1. A comparison between norm-conserving and general smooth functions that match a wavefunction beyond some cut-off radius is given in Figure 3.5.

We apply a second constraint that the shift in energy resulting from being in a polyatomic system must be consistent between the all-electron wavefunction and the pseudo-wavefunction to a linear order beyond r_{cut} :

$$\psi_{AE}(r > r_{\text{cut}}) = \psi_{PP}(r > r_{\text{cut}}) , \quad (3.113)$$

$$\frac{\delta}{\delta r} \psi_{AE}(r > r_{\text{cut}}) = \frac{\delta}{\delta r} \psi_{PP}(r > r_{\text{cut}}) . \quad (3.114)$$

We divide these two equivalencies to get

$$\frac{\psi'_{AE}(r > r_{\text{cut}})}{\psi_{AE}(r > r_{\text{cut}})} = \frac{\psi'_{PP}(r > r_{\text{cut}})}{\psi_{PP}(r > r_{\text{cut}})}, \quad (3.115)$$

and therefore

$$\frac{\delta}{\delta r} \ln \psi_{AE}(r > r_{\text{cut}}) = \frac{\delta}{\delta r} \ln \psi_{PP}(r > r_{\text{cut}}). \quad (3.116)$$

We will define the logarithmic derivative,

$$D_l(\epsilon, r) \equiv r \frac{\delta}{\delta r} \ln \psi_l(\epsilon, r), \quad (3.117)$$

where the ϵ dependence is shown explicitly due to later use.

Using $\phi_{n,l}(r)$, the radial Schrödinger equation can be recast as

$$-\frac{1}{2} \frac{\delta^2}{\delta r^2} \phi_{n,l}(r) + \left[\frac{l(l+1)}{2r^2} + V(r) - \epsilon_{n,l} \right] \phi_{n,l}(r) = 0. \quad (3.118)$$

If we define a variable, ζ_l , as a modified logarithmic derivative, $D_l(\epsilon, r)$ as

$$\zeta_l(\epsilon, r) = \frac{1}{r} [D_l(\epsilon, r) + 1] = \frac{\delta}{\delta r} \ln \phi_l(r), \quad (3.119)$$

we can re-arrange the above radial equation as

$$\frac{1}{\phi_l(r)} \frac{\delta^2}{\delta r^2} \phi_l(r) = \frac{l(l+1)}{r^2} + 2[V(r) - \epsilon], \quad (3.120)$$

and as

$$\zeta_l(\epsilon, r) = \frac{\delta}{\delta \phi} \ln \phi_l(r) \frac{\delta \phi}{\delta r} = \frac{1}{\phi_l(r)} \frac{\delta \phi}{\delta r} \quad (3.121)$$

and

$$\begin{aligned} \frac{\delta \zeta_l}{\delta r} &= \frac{\delta \phi}{\delta r} \cdot \frac{\delta}{\delta r} \frac{1}{\phi_l(r)} + \frac{1}{\phi_l(r)} \cdot \frac{\delta^2 \phi}{\delta r^2} = \frac{\delta \phi}{\delta r} \cdot \left[\frac{\delta}{\delta \phi} \left(\frac{1}{\phi_l(r)} \right) \cdot \frac{\delta \phi}{\delta r} \right] + \frac{1}{\phi_l(r)} \cdot \frac{\delta^2 \phi}{\delta r^2} \\ &= -\frac{1}{\phi_l(r)^2} \left(\frac{\delta \phi}{\delta r} \right)^2 + \frac{1}{\phi_l(r)} \frac{\delta^2 \phi}{\delta r^2}, \end{aligned} \quad (3.122)$$

we can represent the radial equation as a nonlinear differential equation, as in Equation 3.123.

$$\frac{\delta \zeta}{\delta r} + \zeta(\epsilon, r)^2 = \frac{l(l+1)}{r^2} + 2[V(r) - \epsilon] \quad (3.123)$$

We now differentiate this with respect to energy, where a prime notation indicates differentiation with respect to r ,

$$\frac{\delta}{\delta \epsilon} \zeta'_l(\epsilon, r) + 2\zeta_l(\epsilon, r) \frac{\delta}{\delta \epsilon} \zeta_l(\epsilon, r) = -1. \quad (3.124)$$

Consider the expression

$$\frac{1}{\phi_l(r)^2} \frac{\delta}{\delta r} \left[\phi_l(r)^2 \frac{\delta \zeta}{\delta \epsilon} \right], \quad (3.125)$$

and differentiate explicitly as

$$\begin{aligned} \frac{1}{\phi_l(r)^2} \frac{\delta}{\delta r} \left[\phi_l(r)^2 \frac{\delta \zeta}{\delta \epsilon} \right] &= \frac{1}{\phi_l(r)^2} \left[\phi_l(r)^2 \frac{d^2 \zeta}{\delta r \delta \epsilon} + \frac{\delta \zeta}{\delta \epsilon} \frac{\delta}{\delta r} \phi_l(r)^2 \right] \\ &= \frac{d^2 \zeta}{\delta r \delta \epsilon} + 2 \frac{\delta \zeta}{\delta \epsilon} \frac{\phi'_l(r)}{\phi_l(r)} = \frac{d^2 \zeta}{\delta r \delta \epsilon} + 2 \frac{\delta \zeta}{\delta \epsilon} \zeta_l(\epsilon, r). \end{aligned} \quad (3.126)$$

This is the same expression as the left hand side of Equation 3.123 when differentiated with respect to ϵ , and so we rewrite this as

$$\frac{1}{\phi_l(r)^2} \frac{\delta}{\delta r} \left[\phi_l(r)^2 \frac{\delta \zeta}{\delta \epsilon} \right] = -1. \quad (3.127)$$

We then rearrange and integrate with respect to r between radii of 0 and the cut-off

radius, r_{cut} ,

$$\phi_l(r_{\text{cut}})^2 \frac{\delta\zeta}{\delta\epsilon} = - \int_0^{r_{\text{cut}}} \phi_l(r)^2 \delta r, \quad (3.128)$$

to find that at the cut-off radius

$$\frac{\delta\zeta}{\delta\epsilon} = - \frac{1}{\phi_l(r_{\text{cut}})^2} Q_l. \quad (3.129)$$

We can conclude from this that if the pseudopotential wavefunction, ϕ_{PP} , has the same magnitude at the cut-off radius as ϕ_{AE} (which it does by construction), as long as it is also norm-conserving i.e. the integrated charge within r_{cut} agrees between the two wavefunctions, then the first energy derivative of the logarithmic derivative ζ_l is the same between pseudo- and all-electron wavefunctions. In terms of our previously defined logarithmic derivative, $D_l(\epsilon, r_{\text{cut}})$, this is expressed as

$$\frac{\delta}{\delta\epsilon} D_l(\epsilon, r_{\text{cut}}) = - \frac{r_{\text{cut}}}{\phi_l(r_{\text{cut}})^2} Q_l \quad (3.130)$$

In this case, for a self-consistent potential, the scattering phase shifts, $\eta_l(\epsilon)$, which depend on D_l (see Appendix F) and therefore the energy shifts are the same i.e. our second constraint (energy shifts from being in a poly-atomic system are consistent between pseudo- and all-electron wavefunctions) is implied by the first (norm conservation). As such, NCPPs are transferable from the simple environment they are generated into more complex, poly-atomic systems.

3.2.3 Projector augmented wave method

The projector augmented wave (PAW) method is that used in this project. In this approach developed by Blöchl in 1994 [44], wavefunctions are evaluated as integrals of smooth functions plus contributions localized around atomic sites, which are radial integrations i.e. the wavefunctions are represented as spherical harmonics near nuclei, and smoother pseudo-wavefunctions elsewhere. These radial integrations are over what are

commonly called ‘muffin tin spheres’, where space is divided into two distinct categories: spheres surrounding nuclei, and the interstitial space in between these regions (the name coming from the appearance of this division in a two-dimensional plane being reminiscent of a muffin tin). Within the spheres, the effective potential is approximated as spherically symmetric, and constant outside of the spheres.

Using the frozen core approximation, we consider a smooth part of a valence wavefunction (like those in subsection 3.2.1), $\tilde{\psi}(\mathbf{r})$, where we have dropped the super- and subscript as we are only dealing with valence wavefunctions here. To obtain the smoothed wavefunction, we apply a linear transformation, \mathcal{T} , such that

$$\psi = \mathcal{T}\tilde{\psi} , \quad (3.131)$$

and assume that the transform is unity outside of the nuclear muffin tin sphere:

$$\mathcal{T} = \mathbf{1} + \sum_{\mathbf{R}} \mathcal{T}_{\mathbf{R}} , \quad (3.132)$$

where $\mathbf{1}$ is the identity transform, and \mathbf{R} denotes the spherical dependence of the partial wave solutions localized to each sphere. The smooth wavefunction can be treated as a sum of m partial waves within each sphere (expanded into plane waves), and so we have

$$|\tilde{\psi}\rangle = \sum_m C_m |\tilde{\psi}_m\rangle , \quad (3.133)$$

and

$$|\psi\rangle = \mathcal{T}|\tilde{\psi}\rangle = \sum_m C_m |\psi_m\rangle . \quad (3.134)$$

We can represent the all-electron wavefunction as the following, by both adding the pseudo-wavefunction and then subtracting it in its partial wave form:

$$|\psi\rangle = |\tilde{\psi}\rangle + \sum_{\mathbf{R}m} C_{\mathbf{R}m} \left[|\psi_{\mathbf{R}m}\rangle - |\tilde{\psi}_{\mathbf{R}m}\rangle \right] . \quad (3.135)$$

As the transformation \mathcal{T} is linear, we have for the coefficients C_m a projection in each sphere, with projection operator $\tilde{p}_{\mathbf{R}m}$, on to the pseudo-wavefunction

$$C_{\mathbf{R}m} = \langle \tilde{p}_{\mathbf{R}m} | \tilde{\psi} \rangle , \quad (3.136)$$

$$\langle \tilde{p}_{\mathbf{R}m} | \tilde{\psi}_{\mathbf{R}m'} \rangle = \delta_{mm'} , \quad (3.137)$$

such that we ensure

$$|\tilde{\psi}\rangle = \sum_{\mathbf{R}m} |\tilde{\psi}_{\mathbf{R}m}\rangle \langle \tilde{p}_{\mathbf{R}m} | \tilde{\psi} \rangle , \quad (3.138)$$

as required. So, we can see from examination of the above that the transformation, \mathcal{T} , is

$$\mathcal{T} = \mathbf{1} + \sum_{\mathbf{R}m} \left[|\psi_{\mathbf{R}m}\rangle - |\tilde{\psi}_{\mathbf{R}m}\rangle \right] \langle \tilde{p}_{\mathbf{R}m} | . \quad (3.139)$$

Some operator, \mathcal{A} , will have the same expectation value as its transformed operator, $\tilde{\mathcal{A}}$, when applied to the appropriate wavefunctions, i.e.

$$\sum_i f_i \langle \psi_i | \mathcal{A} | \psi_i \rangle = \sum_i f_i \langle \tilde{\psi}_i | \tilde{\mathcal{A}} | \tilde{\psi}_i \rangle , \quad (3.140)$$

where the sum is over states, i , f_i is the occupation of the state, and the transformed operator is given by

$$\tilde{\mathcal{A}} = \mathcal{T}^\dagger \mathcal{A} \mathcal{T} = \mathcal{A} + \sum_{mm'} |\tilde{p}_m\rangle \left[\langle \psi_m | \mathcal{A} | \psi_{m'} \rangle - \langle \tilde{\psi}_m | \mathcal{A} | \tilde{\psi}_{m'} \rangle \right] \langle \tilde{p}_{m'} | . \quad (3.141)$$

Using this operator relationship above, we consider the case where $\mathcal{A} = |\mathbf{r}\rangle\langle\mathbf{r}|$, i.e. the real-space projection operator, which has expectation value $n(\mathbf{r})$. We see that this is equivalent to the expectation value of the transformed operator acting on the transformed

wavefunction:

$$\begin{aligned}
n(\mathbf{r}) &= \sum_i f_i \langle \tilde{\psi}_i | \left[|\mathbf{r}\rangle\langle\mathbf{r}| + \sum_{mm'} |\tilde{p}_m\rangle \left(\langle \psi_m | \mathbf{r}\rangle\langle\mathbf{r} | \psi_{m'}\rangle - \langle \tilde{\psi}_m | \mathbf{r}\rangle\langle\mathbf{r} | \tilde{\psi}_{m'}\rangle \right) \langle \tilde{p}_{m'} | \right] | \tilde{\psi}_i\rangle \\
&= \sum_i f_i \left[\langle \tilde{\psi}_i | \mathbf{r}\rangle\langle\mathbf{r} | \tilde{\psi}_i\rangle + \sum_{mm'} \langle \tilde{\psi}_i | \tilde{p}_m\rangle \langle \psi_m | \mathbf{r}\rangle\langle\mathbf{r} | \psi_{m'}\rangle \langle \tilde{p}_{m'} | \tilde{\psi}_i\rangle - \right. \\
&\quad \left. \sum_{mm'} \langle \tilde{\psi}_i | \tilde{p}_m\rangle \langle \tilde{\psi}_m | \mathbf{r}\rangle\langle\mathbf{r} | \tilde{\psi}_{m'}\rangle \langle \tilde{p}_{m'} | \tilde{\psi}_i\rangle \right] \\
&\equiv \tilde{n}(\mathbf{r}) + n^{(1)}(\mathbf{r}) - \tilde{n}^{(1)}(\mathbf{r}) ,
\end{aligned} \tag{3.142}$$

where $\tilde{n}(\mathbf{r})$, $n^{(1)}(\mathbf{r})$ and $\tilde{n}^{(1)}(\mathbf{r})$ are the terms in their respective order, with the superscript (1) terms being the localized densities about each atom i.e. the muffin tins. The electronic density is equivalent to a smooth density function, $\tilde{n}(\mathbf{r})$, extending through all space except regions localized about nuclei (hence the subtraction of $\tilde{n}^{(1)}(\mathbf{r})$), plus the rapidly varying density localized about nuclei, $n^{(1)}(\mathbf{r})$. These integrals can be performed in spherical coordinates, and do not suffer problematic variations near the nucleus.

By (in principle) capturing core electron interactions accurately through $n^{(1)}$ and $\tilde{n}^{(1)}$ (and the equivalents for other observables), but allowing the interstitial region between muffin tin spheres to be augmented by the projector function and so allowing the plane wave expansion, the PAW method provides a computationally efficient, but accurate, modification of the pseudopotential method. The core states are, in practice, not represented by individually constructed pseudopotentials, but instead the total core density is used. The expansion of pseudo-wavefunctions into plane waves is truncated by an energy cut-off.

3.3 Numerical algorithms and calculation overview

This section is dedicated to the specifics of the calculations performed in this project that have not yet been discussed in the relevant theory sections. This includes important numerical algorithms deployed by the programs used, as well as a brief overview of the different types of calculations performed and their significant parameters.

3.3.1 Numerical algorithms and computational techniques

k-point grids

Performing electronic structure calculations frequently requires integrations over the Brillouin Zone. These can be difficult or intractable to perform analytically, so numerical methods are used. In a multidimensional analogy to integration by the trapezoid rule, we can define a grid of discrete points in \mathbf{k} -space, and sum their contributions to provide a numerical solution to the integral problem. This grid must be carefully selected, both for its concentration of points and the position of those points; there is a greater concentration requirement in areas where the integrand varies rapidly. The specific positions of these points can be selected such that symmetry can be taken advantage of, and integration must only be carried out over an irreducible Brillouin Zone (IBZ), as displayed in Figure 3.6.

By shifting the mesh such that there are no points at $\mathbf{k} = 0$, the number of inequivalent points in the IBZ can be reduced, which reduced the computational load of calculating the integral. One method for determining these points is the Monkhorst-Pack method [45]. This is one of the most popular methods for handling the mesh for numerical integration, and the primary method used in this project. The Monkhorst-Pack mesh points are positioned at

$$\mathbf{k}_{n_1, n_2, n_3} = \sum_i^3 \frac{2n_i - N_i - 1}{2N_i} \mathbf{G}_i, \quad (3.143)$$

where $1 \leq n_i \leq N_i$, $n_i \in \mathbb{Z}^+$ and \mathbf{G}_i are reciprocal lattice vectors. If the integrand is a periodic function whose Fourier components extend only to $N_i \mathbf{T}_i$, with \mathbf{T}_i being the

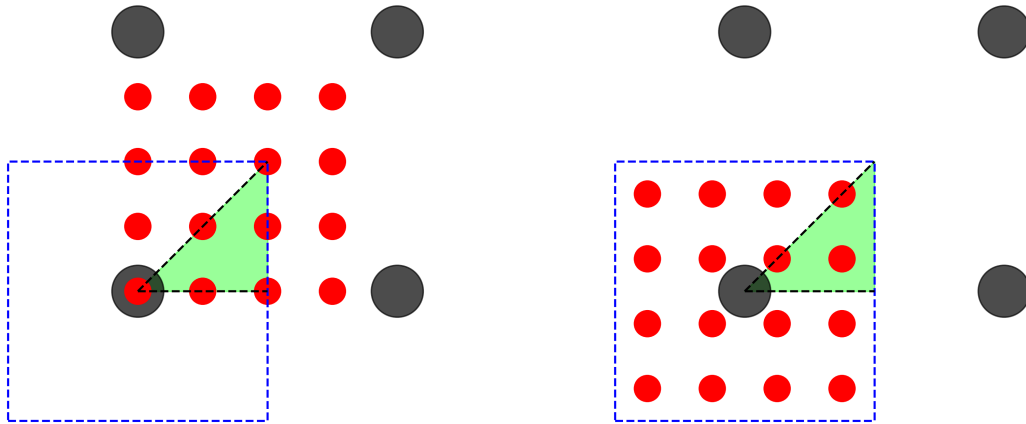


Figure 3.6: Grid points (red points) within the first Brillouin zone (delimited by the blue dashed squares) between reciprocal lattice points (gray points). Dashed black lines delimit the IBZ, shaded in green. With a grid centred on $\mathbf{k} = 0$ (left), the IBZ contains six inequivalent points over which integration must be carried out. By shifting the mesh off-center (right), the number of inequivalent points can be reduced, in this case to only three.

translation vectors of the crystal, then the sum over the uniform set of Monkhorst-Pack points gives the exact integration. This method provides then integrations as exact as permitted by the choice of energy cut-offs.

Fast Fourier transform

The fast Fourier transform (FFT) is an algorithm used to compute discrete Fourier transforms in a way that scales computational complexity much more favorably than decomposing a large number of components directly. Direct calculation has a complexity of $\mathcal{O}(n^2)$, as there are n outputs X_k , each requiring a sum over n terms:

$$X_k = \sum_{m=0}^{n-1} x_m e^{-i\frac{2\pi k}{n}m}, \quad 0 \leq k \leq n-1, k \in \mathbb{Z}^+. \quad (3.144)$$

The complexity of FFTs is much lower, $\mathcal{O}(n \log_2 n)$. Quantum ESPRESSO uses the FFTW subroutine library [89], which deploys specific FFT algorithms depending on the machine and data set. The most widely used FFT algorithm is the Cooley-Tukey

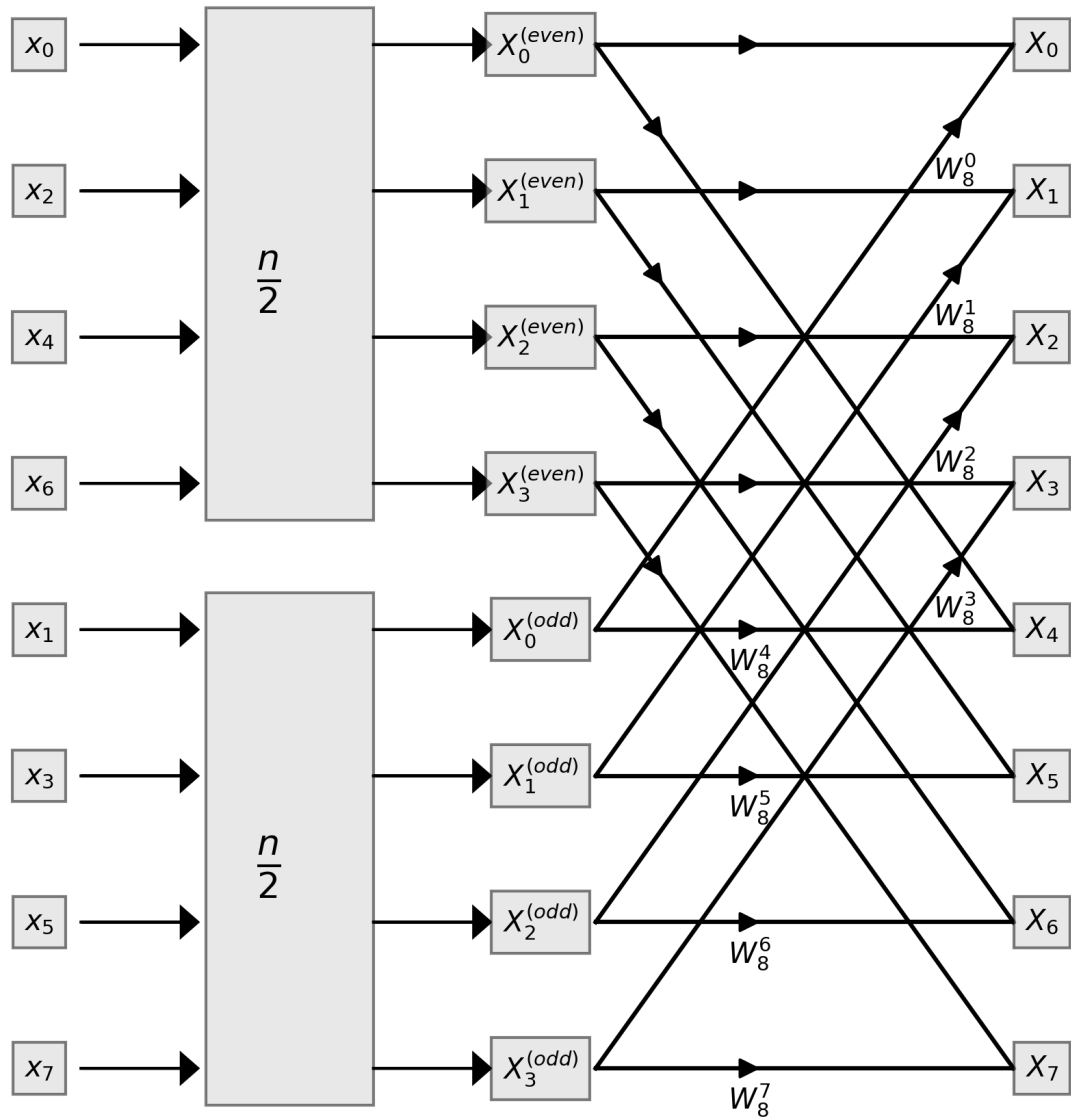


Figure 3.7: A simple block diagram of the Cooley-Tukey FFT method (broadly representative of most FFT methods) for $n = 8$. Arrows indicate a multiplication by the annotated value, with a multiplication of 1 for no annotation. Eight inputs, x_n , are split in a ‘divide-and-conquer’ technique and so resolving the discrete Fourier transform problem of length n into two of length $\frac{n}{2}$. They are thus solved with a lower complexity than the initial problem (and can be further split to smaller Fourier processes as described in the main text) for even- or odd-indexed outputs, $X_k^{(even, odd)}$. These are then fed in to Equation 3.153, and solved for the final outputs, X_k .

algorithm [90], which exploits symmetries in the exponential term above. Let this term be defined as W_n ,

$$W_n = e^{-i\frac{2\pi}{n}} , \quad (3.145)$$

which has properties of complex conjugate symmetry, and is periodic in m and k :

$$W_n^{k(n-m)} = W_n^{-km} = (W_n^{km})^* , \quad (3.146)$$

$$W_n^{km} = W_n^{k(n+m)} = W_n^{(k+n)m} , \quad (3.147)$$

as

$$W_n^{kn} = e^{-i2\pi k} = 1 . \quad (3.148)$$

The algorithm separates x_n into even- and odd-indexed subsequences, where here we assume that n is a power of two. This is not a requirement, but would otherwise complicate the following without adding instructiveness to the description of the core algorithm.

These subsequences can be represented as

$$X_k = \sum_{m=1}^{n-1} x_m W_n^{km} = \sum_{m \text{ even}} x_m W_n^{km} + \sum_{m \text{ odd}} x_m W_n^{km} . \quad (3.149)$$

For even indices, we have that $m = 2r$, and for odd indices $m = 2r + 1$, with $0 \leq r \leq \frac{n}{2} - 1$. This allows zero-indexing for computational deployment, and we can substitute and factorize:

$$\begin{aligned} X_k &= \sum_{r=0}^{\frac{n}{2}-1} x_{2r} W_n^{k2r} + \sum_{r=0}^{\frac{n}{2}-1} x_{(2r+1)} W_n^{(2r+1)k} \\ &= \sum_{r=0}^{\frac{n}{2}-1} x_{2r} (W_n^2)^{kr} + W_n^k \sum_{r=0}^{\frac{n}{2}-1} x_{(2r+1)} (W_n^2)^{kr} . \end{aligned} \quad (3.150)$$

We recognize that

$$W_n^2 = e^{-2i\frac{2\pi}{n}} = e^{-i\frac{2\pi}{(\frac{n}{2})}} = W_{\frac{n}{2}} , \quad (3.151)$$

and so

$$X_k = \sum_{r=0}^{\frac{n}{2}-1} x_{2r} W_{\frac{n}{2}}^{kr} + W_n^k \sum_{r=0}^{\frac{n}{2}-1} x_{2r+1} W_{\frac{n}{2}}^{kr} . \quad (3.152)$$

The first summation is an $\frac{n}{2}$ point discrete Fourier transform associated with the even samples, which we will denote $X_k^{(\text{even})}$, and the second is associated with the odd samples, $X_k^{(\text{odd})}$. The full discrete Fourier transform can then be denoted as

$$X_k = X_k^{(\text{even})} + W_n^k X_k^{(\text{odd})} . \quad (3.153)$$

This representation illuminates the simplification introduced by the algorithm so far, where the signal is split into two half-sized signals to be solved separately, giving solutions to be summed as increasing powers of W_n , up to W_n^m . This is displayed for the $m = 8$ case in Figure 3.7.

We can see from examination of Figure 3.7 that the algorithm so far requires $2\left(\frac{n}{2}\right)^2$ processes (solving both of the $\frac{n}{2}$ transforms), and then an additional n processes to produce the outputs, W_n^m . This splitting can be applied recursively, replacing the two $\frac{n}{2}$ transforms by four $\frac{n}{4}$ transforms and so on, ultimately resulting in $\frac{n}{2^p}$ transforms where they cannot be split any further. The limit to p is where $\frac{n}{2^p} = 1$, i.e. no more splitting can occur, so in this limit $p = \log_2 n$. In this case, the complexity of the transforms is $\frac{n^2}{n} = n$, and np for the multiplication processes to produce the outputs W_k , which for large n approximates to $\mathcal{O}(n \log_2 n)$, which scales very favorably compared to the direct calculation of $\mathcal{O}(n^2)$.

Wannier interpolation

When performing calculations with hybrid functionals such as HSE, only self-consistent calculations are supported by Quantum ESPRESSO. These calculations use a relatively

coarse grid of \mathbf{k} -points for sampling, and so are not particularly useful for the direct representation of detailed electronic structure (such as a band structure diagram) without further refinement. As such, non-self consistent field calculations are performed afterwards, using a single step on a much finer sampling grid with the output from preceding self-consistent field calculations as starting data. In order to produce something like band structure with a hybrid functional, then, as one cannot simply deploy a non-self consistent calculation, we must either perform a self-consistent calculation with a fine grid (which is expensive) and a hybrid functional (which is very expensive), or use an interpolation method. Here we use the Wannier interpolation method: using Wannier functions to interpolate existing data of the Hamiltonian on to a finer grid of \mathbf{k} -points, in order to mimic the use of an appropriately fine grid. To do this, we use the `wannier90` tool [91].

The Wannier interpolation method starts from previously determined energies (from `scf` calculations), $E_{n\mathbf{q}}$ and wavefunctions, $\psi_{n\mathbf{q}}(\mathbf{r}) = u_{n\mathbf{q}}(\mathbf{r}) e^{i\mathbf{q}\cdot\mathbf{r}}$ (see Equation 2.33). We use here wavevectors \mathbf{q} to represent those from previous calculation, and \mathbf{k} for those from the interpolation grid. In our case, the energies and wavefunctions have been determined in a self-consistent calculation using a relatively coarse grid of \mathbf{k} -points that has $N_{\mathbf{q}} = N_{\mathbf{q}}^{(1)} N_{\mathbf{q}}^{(2)} N_{\mathbf{q}}^{(3)}$ wavevectors within the reciprocal unit cell. We use an equivalent form of Equation 2.114 with our notation here to define a set of J Wannier functions:

$$|\phi_{\mathbf{R}n}\rangle = \frac{1}{N_{\mathbf{q}}} \sum_{\mathbf{q}} e^{-i\mathbf{q}\cdot\mathbf{R}} \sum_{m=1}^{J_{\mathbf{q}}} |\psi_{m\mathbf{q}}\rangle \mathbf{V}_{mn}(\mathbf{q}) , \quad (3.154)$$

where the matrices \mathbf{V}_{mn} are unitary and so preserve orthonormality, and contain the required information to ensure that the resulting Wannier functions are maximally localized i.e. the quadratic spread within the ‘home’ unit cell ($\mathbf{R} = 0$), Ω , of the Wannier functions is minimized with respect to $u_{n\mathbf{q}}(\mathbf{r})$,

$$\Omega = \sum_n \langle \phi_{0n} | r^2 | \phi_{0n} \rangle - \langle \phi_{0n} | \mathbf{r} | \phi_{0n} \rangle^2 . \quad (3.155)$$

Maximal localization ensures that the Wannier functions are a unique set of functions,

reducing redundancy and providing a physically meaningful description: localized molecular orbitals. The Bloch wavefunctions in this maximally localized Wannier gauge, then are

$$|\psi_{n\mathbf{k}}^{(W)}\rangle \equiv e^{i\mathbf{k}\cdot\mathbf{r}}|u_{n\mathbf{k}}^{(W)}\rangle \equiv \sum_{\mathbf{R}} e^{i\mathbf{k}\cdot\mathbf{R}}|\phi_{\mathbf{R}n}\rangle . \quad (3.156)$$

The elements of the Hamiltonian (energy) matrix, $\mathbf{H}_{ij} = \langle i|\mathcal{H}|j\rangle$, for states $|i\rangle$, $|j\rangle$ in terms of the wavefunctions in the Wannier gauge, is then

$$\mathbf{H}_{mn}(\mathbf{R}) \equiv \frac{1}{N_{\mathbf{q}}} \sum_{\mathbf{q}} e^{-i\mathbf{q}\cdot\mathbf{R}} \langle \psi_{m\mathbf{q}}^{(W)} | \mathcal{H} | \psi_{n\mathbf{q}}^{(W)} \rangle , \quad (3.157)$$

which is also representable in terms of the energies from previous self-consistent calculations,

$$\mathbf{H}_{mn}(\mathbf{R}) \equiv \frac{1}{N_{\mathbf{q}}} \sum_{\mathbf{q}} e^{-i\mathbf{q}\cdot\mathbf{R}} \sum_l V_{lm}^*(\mathbf{q}) E_{l\mathbf{q}} V_{ln}(\mathbf{q}) . \quad (3.158)$$

In order to extract energies at an arbitrary \mathbf{k} -point, i.e. to interpolate to a finer grid, we just need to construct the Wannier Hamiltonian matrix, with elements

$$\mathbf{H}_{mn}^{(W)}(\mathbf{k}) = \sum_{\mathbf{R}} \mathbf{H}_{mn}(\mathbf{R}) e^{i\mathbf{k}\cdot\mathbf{R}} , \quad (3.159)$$

and evaluate at our desired \mathbf{k} . By doing so for \mathbf{k} -points in between those already calculated in our self-consistent calculation, and along paths of interest (such as in Section 2.2), we can populate a finer grid for analysis of properties such as band structure.

3.3.2 Details of calculations

This subsection provides an overview of the calculations performed during the project, from the perspective of their practical use within the Quantum ESPRESSO suite. The primary code that is used is `pw.x` from the *PWscf* package. This deploys most of the calculations used. Post-processing is performed within the same package, but

uses different codes (one of which is `bands.x`, unfortunately the same name as one of the processing calculations in `pw.x`; it should be obvious from context which is being discussed). Here we consider data manipulation and reformatting (for plotting, analysis etc) that lacks calculation of physical parameters to be post-processing. Descriptions of calculations used in this project are provided in Table 3.1.

Table 3.1: A descriptive overview of the calculations used during this project, including post-processing codes. They are all within the Quantum ESPRESSO suite.

Calculation	Description
<code>scf</code>	This stands for ‘self-consistent field’, and is the main calculation of DFT where the Kohn-Sham equations are solved iteratively. Total energy, forces, and stresses are calculated as described in Section 3.1.
<code>relax</code> , <code>vc-relax</code>	These are calculations for geometric optimization i.e. finding the atomic positions that minimise the energy of the structure. The <code>relax</code> calculation allows atoms to move within a cell of fixed dimensions, whereas <code>vc-relax</code> allows the unit cell dimensions to vary as well (standing for ‘variable cell’). Series of self-consistent field calculations are performed at different atomic positions, and compared iteratively to find energy minima with respect to the underlying structure.
<code>nscf</code>	This stands for ‘non-self consistent field’, and performs only one step of the typical <code>scf</code> process with a fixed electron density. However, it also considers unoccupied electron states and should be performed with a denser \mathbf{k} -point grid. Both of these factors make it more expensive than the <code>scf</code> calculation per step. However, it can accept as a starting point previous <code>scf</code> calculation outputs. For cases where fine grids are required, it is overall more economical to perform an <code>scf</code> calculation on a coarse grid, and then an <code>nscf</code> on a finer grid as compared to just the <code>scf</code> calculation on the fine grid.
<code>bands (pw.x)</code>	This is similar to the <code>nscf</code> calculation, but only computes the Kohn-Sham states for specified \mathbf{k} -points. This is useful for band structure diagrams, where the energies at points along a particular path in \mathbf{k} -space are needed.
DOS, pDOS	These are the ‘density of states’ and ‘projected density of states’ post-processing calculations, respectively. They are post-processing codes, and simply extract information from previous calculations’ output files to be represented in a useful way.
<code>pp.x</code>	A post-processing code for extracting information from <code>pw.x</code> calculations in a format suitable for plotting or analyzing.
<code>bands.x</code>	Another post-processing code to reformat output data from the <code>pw.x bands</code> calculation for plotting.

3.3.3 Workflow

The standard workflow for DFT calculations depends on what data is available for the particular system of interest, with early calculations being skipped if the data they provide is already available. For a completely novel system where we are using a DFT-only (not hybrid) functional, the workflow is displayed in Figure 3.8.

It begins with `scf` calculations using a sensible guess for atomic positions and cell parameters (e.g. from existing literature). Convergence testing is performed, where repeat `scf` calculations are done on these test systems with increasingly more fine k -point meshes and increasing values of energy cut-offs. The results of these `scf` calculations are compared to determine the most coarse grid and lowest cut-offs that can be used while still providing the same results within some desired precision. Using these converged parameters, a `vc-relax` calculation, or just `relax` if the cell parameters are known from similar cases (e.g. the same substrate but different molecular binding site will not affect the cell parameters), is performed to optimize the system's geometry.

The main `scf` calculation is then performed with the new geometry and converged parameters to produce data on the occupied Kohn-Sham states. The energy output from this and the previous `vc-relax` or `relax` calculations should be very similar, differences arising from the fact that the plane wave basis set is determined by the input geometry.

In order to produce density of states information, an `nscf` calculation on a finer grid than that of the preceding `scf` calculation is performed, followed by post-processing `DOS` and `pDOS` steps. Similarly, to produce the band structure, a `bands` calculation is performed with the desired \mathbf{k} -point path and sampling concentration, followed by some simple post-processing.

The workflow of a hybrid calculation differs, with the initial convergence testing and geometry optimization stages being the same (and still using the DFT-only functional). After geometry optimization a further convergence test is performed, this time with the hybrid functional, but only for the parameters specific to the use of hybrid functionals i.e. the Fock mesh, another \mathbf{k} -point mesh for the Hartree-Fock-like calculations. During this convergence testing, an `scf` calculation with the correct parameters will necessarily

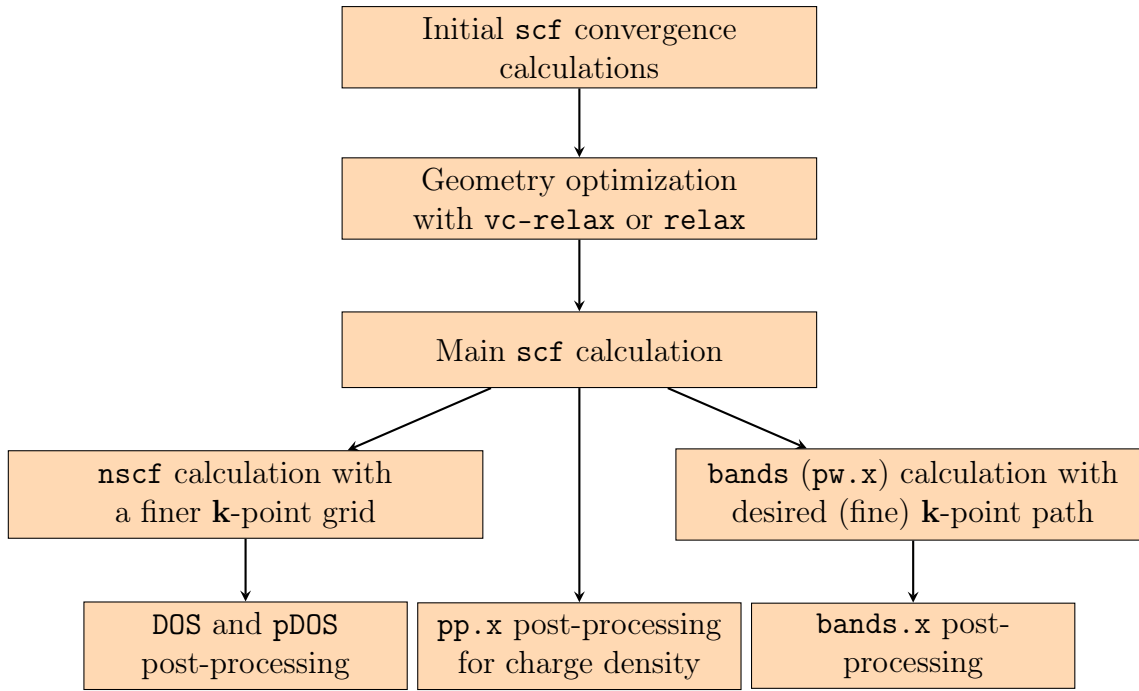


Figure 3.8: The normal workflow of a DFT calculation, indicating the prerequisites of each calculation.

have been performed. As discussed previously in subsection 3.3.1, non-self consistent calculations for hybrid functionals are not supported within Quantum ESPRESSO, and so band structure cannot be determined without the use of another technique. This technique is Wannier interpolation (also discussed in subsection 3.3.1), where the `wannier90` code is deployed to interpolate self-consistent field data to arbitrary \mathbf{k} -points and fill out a finer grid. This workflow is represented in Figure 3.9.

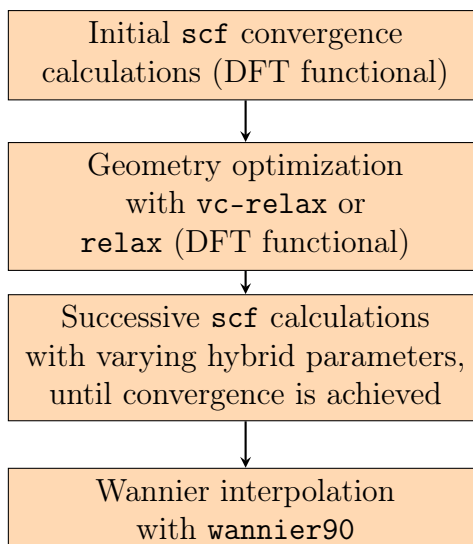


Figure 3.9: The normal workflow of a hybrid calculation, indicating the prerequisites of each calculation.

3.3.4 Quantum ESPRESSO parameters

This subsection provides an overview of the more important parameters available during normal workflow, with explanations of their purpose and justifications for their values. A lot of parameters were kept the same for all calculations that they applied to, some of which were the default values of the computational suite. In these cases, the parameters' default values have often been selected empirically, and there is no compelling reason to change them.

Convergence thresholds

These parameters dictate when an iterate is close enough to the previous value to be considered converged. This is convergence within a self-consistent calculation, not between `scf` calculations for convergence testing of other parameters.

`ecut_conv_thr` and `forc_conv_thr`: The convergence threshold on the total energy of the system and all components of all forces within the system, respectively. The difference between successive steps' energies and forces must both be below their respective values for convergence to be achieved.

`conv_thr`: Another total energy convergence threshold, but for the total calculation, not

successive iterative steps.

Energy cut-off

`ecutwfc`: The kinetic energy cut-off for electronic wavefunctions, which defines the size of the plane wave basis set to be used. A higher `ecutwfc` produces a larger, more accurate, more expensive plane wave basis set.

`ecutrho`: The kinetic energy cut-off for charge density. It plays the same role as `ecutwfc` for charge density.

`ecutfock`: This is the analogous term to `ecutrho` for Hartree-Fock-like functionals.

Occupations

In this project, we have used two arguments for this parameter, ‘`smearing`’ and ‘`tetrahedra`’. Due to the discrete nature of truncating the plane wave expansion with `ecutwfc`, the number of plane waves is a both discontinuous function of the energy cut-off, but also of the lattice parameters at a fixed energy cut-off (changing the spatial scope of the lattice may discretely introduce or remove lattice vectors to or from the energy range). So, the system energy as a function of the lattice parameters will suffer discontinuities, corresponding to a change in the number of plane waves.

`occupations = ‘smearing’`: Smearing methods broaden the occupation function to reduce the magnitude of the discontinuities, thus reducing numerical noise.

`occupations = ‘tetrahedra’`: Alternatively, Blöchl’s tetrahedral method [92] discretizes the Brillouin zone into tetrahedral cells with vertices at the sampled \mathbf{k} -points, and computes the occupation of electronic states within each cell by interpolating between the sampled points. This is typically more accurate than smearing methods, but can be more expensive. We use this option, then, for `nscf` calculations, and the smearing method for `scf`.

Mixing

`mixing_beta`: We always use Broyden mixing [73], with this parameter being the mixing parameter α from subsection 3.1.1.

k-points

The **k**-points over which the Brillouin zone is to be sampled can be determined in a number of ways using different arguments, followed by coordinates in the relevant format.

`automatic`: We typically use this option, where a uniform Monkhorst-Pack mesh [45] is generated with provided dimensions.

`gamma`: Alternatively, we can sample only the Γ point at $\mathbf{k} = 0$, suitable for large systems in real space where we accept rough results.

`crystal_b`: Instead of a mesh, we can define a **k**-point path over which to sample Kohn-Sham states, as well as the concentration of sampling along the path. This is appropriate for bands structure plots, and is used in `bands` calculations.

Fock mesh

`nqx1`, `nqx2`, `nqx3`: These are the dimensions of the Fock mesh, the Hartree-Fock-like equivalent of the **k**-point mesh. They cannot be larger than their respective **k**-point mesh.

Spin-orbit coupling

`noncolin`: A boolean parameter that allows or disallows non-collinear spin i.e. electronic spin axes do not have to be aligned. This is set to `.true.` for calculations that consider spin-orbit coupling.

`lspinorb`: Another boolean parameter, which if `.true.`, allows the code to use a pseudopotential with spin-orbit coupling.

Hybrid functionals

`input_DFT`: This dictates the exchange-correlation functional to use. By default it is read from pseudopotential files, but in the case of our HSE hybrid calculations it is set to `input_DFT = 'HSE'`.

`exx_fraction`: This is the fraction of Hartree-Fock-like functional to use for the hybrid calculation, α in subsection 3.1.4. The DFT functional to be used in combination is then read from pseudopotential files.

`screening_parameter`: For HSE and similar functionals, this parameter dictates the value of ω from subsection 3.1.4. This has been left as the default value, as tested and implemented by the original authors. Originally, it was stated by them to have been $\omega = 0.15a_0^{-1}$ in their testing [53], but this was later corrected in an erratum [93] to have been $\omega = \frac{0.15}{\sqrt{2}}a_0^{-1} \approx 0.106a_0^{-1}$ all along (the discrepancy not affecting the validity of their work). Sometimes literature will refer to the functional using the earlier, incorrect, implementation as HSE03, and the corrected implementation as HSE06. This project used HSE06, but will refer to it simply as HSE.

Chapter 4

Determining properties before heterostructure formation

The first step of this project was to classify the geometry of the materials that were to be investigated, as well as confirm their independent electronic structure. This initial analysis culminates in the comparison of pentacene's frontier orbital energies with those of each TMD, for a number of different computational frameworks. The frontier orbital energies were then compared between TMDs and pentacene, which gave us a coarse prediction of the type of heterojunction to expect later. The type of heterojunction is important in heterostructure semiconductor devices as it determines use cases of the device, so this is among the first things to be checked when considering combinations of materials in this context.

The TMDs investigated, MoS_2 , MoSe_2 , WS_2 and WSe_2 , are found in two phases when in monolayer: 1T and 1H [16]. The 1H monolayer is identical to any single layer in the 2H and 3R phases, with distinctions arising only with the addition of stacking layers and their orientation to each other. These schemes are displayed in the Introduction chapter, in Figure 1.1. As the 1T form is metastable and metallic [17–19], we did not investigate it. The computational frameworks used were DFT, using the PBE exchange-correlation functional (subsection 3.1.2), where we either did or did not include consideration of spin-orbit coupling, and hybrid calculations using the HSE functional (subsection 3.1.4), with

consideration of spin-orbit coupling. These frameworks will be referred to as PBE-nSOC, PBE-SOC and HSE, respectively.

As van der Waals forces are considered using Grimme's D3 method, a perturbation to the energy functional, we have not directly consider van der Waals interactions when calculating the electronic structure; the effect on electronic structure is indirect, arising from changes in the optimized geometry due to the perturbation. This introduces an error as an incorrect treatment of these forces, but there do exist functionals that include van der Waals interactions within DFT, notably the family of non-local van der Waals Density Functionals (vdW-DF) [94]. By considering long-range correlation effects through inclusion of a non-local component of the correlation functional that captures dispersion forces, vdW-DF methods provide a more intrinsic treatment of electronic structure. These effects can directly affect the electronic structure instead of effects arising solely from changes in geometry as in the methods used in this project. This results in a self-consistent description of dispersion effects. Computational cost is greatly increased over local and semi-local GGA only functionals, however, and so we did not proceed with the use of these functionals.

The inclusion of spin-orbit coupling is a more physically accurate framework, predicting spin splitting of energy bands which leads to a more correct treatment of frontier orbital energies, but it comes at an increased computational cost. Therefore, we included it at this early stage while using small unit cells, and did not include it later when using the much larger supercell approach for analysis of the heterostructures (seen later in Chapters 5 and 6). This allowed us to quantify the degree to which the inclusion of spin-orbit coupling affects the resulting energies, and establishes any change in pattern amongst the different TMDs.

We performed our HSE calculations without spin-orbit coupling on only monolayer MoS₂ and compared the computational cost to the same, but with inclusion of spin-orbit coupling, and found that the increase in cost was perfectly manageable for the small systems, especially in the context of naturally expensive HSE calculations. As HSE calculations are expensive without spin-orbit coupling anyway, we only performed

the HSE calculations on the other TMDs with spin-orbit coupling, avoiding performing two sets of expensive calculations on each TMD. This is also true for pentacene; we did not perform HSE calculations without spin-orbit coupling. As such, any time our HSE calculations are discussed, they include spin-orbit coupling unless otherwise specified.

With these considerations, we first performed convergence testing for computational parameters, followed by geometry optimization with these converged parameters, and then the electronic structure calculations required to describe the band structure and density of states of the systems.

4.1 Computational details

Some of the computational parameters for the project were determined following convergence testing, which follows in Section 4.2. Other details were determined due to decisions outlined previously in the introductory chapter (Chapter 1) or established default values within our plane-wave basis computational suite, Quantum ESPRESSO. These include the use of the generalized gradient approximation PBE [43] functional for DFT calculations and the hybrid HSE [93] functional (HSE06, where $\omega = 0.106a_0^{-1}$), Grimme's DFT-D3 [65] van der Waals force corrections, the projector-augmented wave [44] method using norm-conserving pseudopotentials, and a Monkhorst-Pack grid sampling method. The \mathbf{k} -point (and \mathbf{q} -point for hybrid calculations) grid dimensions required convergence testing, as did cut-off energies; both are discussed in the following section. The self consistent field convergence thresholds for total energy, force and individual electron energy were `etot_conv_thr` = $10^{-4}a.u.$, `forc_conv_thr` = $10^{-3}a.u.$ and `conv_thr` = $10^{-8}a.u.$, respectively. These values are used throughout the project. In Chapters 5 and 6 we use the supercell approach to construct our heterostructures, which use different computational parameters as a necessity of the size of the systems. These are discussed at the beginning of the relevant chapters.

4.2 Convergence testing

The parameters for DFT calculations that needed converging were the size of the \mathbf{k} -point mesh, represented by the dimensionality of the Monkhorst-Pack grid, and the plane wave kinetic energy cut-off for the electronic wavefunctions, `ecutwfc`.

The aim is to perform increasingly more expensive (and more accurate) calculations by varying the parameter to be converged, compare the output energies, and choose the parameter value of the cheapest calculation that produces the same output as the value to which increased parameter cost will converge to, within some predefined convergence threshold. This threshold is chosen based on the desired final precision.

Using initial guessed at geometry (from known experimental data for the lattice parameter of the crystal, and a hexagonal Bravais lattice) and a high-dimension \mathbf{k} -point mesh of $24 \times 24 \times 1$, successive `scf` calculations were performed with increasing `ecutwfc` and `ecutrho`. The frontier orbital energies following completion of the iterative self-consistent process were compared between calculations with different values of energy cut-offs. A threshold for frontier orbital convergence of 0.005 eV was chosen, where the cheapest calculation that gives frontier orbital energies equivalent, within this threshold, to that of subsequently more expensive (and more accurate) calculations provides the parameter value that we move forward with. Caveats are that the parameter must be flattening out with respect to increasing calculation cost, and that each subsequent calculation is also within the convergence threshold. We proceeded with early calculations on pentacene out of heterostructure using a slightly higher cut-off energy than was strictly required, due to previous work within the research group. This will not affect results, as shown by convergence testing. A similar process was then performed with varying densities of \mathbf{k} -point mesh, using the converged value of `ecutwfc` and `ecutrho`. Here we assess the Fermi energy, as we are ultimately interested in the band structure, for which the Fermi energy is a good proxy for convergence testing: we do not use the actual frontier orbital energies as before. This is because with changing Monkhorst-Pack grids the positions sampled from the Brillouin zone change, which may miss the position of the VBM and CBM for some choices of grid i.e. by changing the grid density, changes in the

frontier orbital energies reported are not necessarily improvements towards a converged value, but are simply sampling a different region farther from the actual frontier orbital position. A threshold for Fermi energy convergence of 0.02 eV was selected, although for cheap calculations performed earlier in the project, denser \mathbf{k} -point grids were occasionally selected than required for this particular threshold. As we were also interested in geometry and, later in the project, binding energies of heterostructures, we also converged the total system energy. In all cases, this converged much faster, and to within a much smaller range (less than 10^{-5} eV), than the Fermi or frontier orbital energies, and so did not affect any decisions.

As HSE calculations use DFT-optimized geometry as inputs, and only the self-consistent steps are performed with the hybrid functional, the parameters used in an HSE calculation that must also be converged in order to perform the previous DFT calculations are already decided upon, as discussed in subsection 3.3.3. We therefore used the same `ecutwfc` and `ecutrho` as we did for DFT calculations, only increasing them if required due to a restriction of the software implementation. This was the case for both sulfur systems, discussed in their relevant subsections below.

However, due to the computational cost of HSE calculations, a dense \mathbf{k} -point grid was not a feasible choice. Additionally, there is a \mathbf{q} -point mesh (or Fock mesh) that must be used alongside the usual \mathbf{k} -point mesh. This is for the exact (Hartree-Fock-like) part of the hybrid calculation, as discussed in subsection 3.1.4. The Fock mesh must match with the \mathbf{k} -point mesh, being divisible into it. Convergence testing operates slightly differently for our HSE calculations, as we already have geometry from DFT and cannot perform non-self consistent field calculations: we perform convergence testing on the `scf` calculation, which is the only calculation performed with HSE anyway, before moving on to Wannier interpolation to fill out a denser grid. As such, we perform calculations with successively more dense Fock meshes until convergence is reached in the Fermi energy to a slightly higher threshold of 0.05 eV. Once we do reach convergence, we will have already performed the calculation needed during this process. This means that we end up using the results from the most expensive (and accurate) calculation we performed despite knowing, albeit

retroactively, that the second-most accurate would have been sufficient.

We performed HSE calculations on MoS₂ without spin-orbit coupling initially, but found that hybrid calculations both with and without spin-orbit coupling were similar to each other in cost. As such, we abandoned further HSE calculations without spin-orbit coupling, and we shall only discuss HSE results with the inclusion of the proper spin-orbit coupling treatment.

4.2.1 MoS₂

DFT

The results of convergence testing for energy cut-off are shown in the left panel of Figure 4.1, where the VBM and CBM values are within the colored bars that represent the threshold of 0.005 eV around the result from the most accurate calculation from the very first calculation. As such, we simply use the lowest energy cut-offs of `ecutwfc = 80 Ry` and `ecutrho/ecutwfc = 4`.

Using the converged value of `ecutwfc`, **k**-point mesh convergence was carried out with increasingly dense grids. The x- and y-dimensions were kept equivalent to reflect the shape of the unit cell, and the z-dimension was held at 1, as there is a large vacuum region in this direction of approximately 50 Å to maintain integrity of the monolayer.

The results of this convergence test are displayed in Figure 4.1, where a $12 \times 12 \times 1$ grid provides convergence of the Fermi energy within 0.02 eV. The total system energy had converged long before this point, as can be seen in Figure 4.1. While convergence of the Fermi energy to within a threshold of 0.02 eV was reached with a grid of $12 \times 12 \times 1$, the computational cost was low for this set of calculations. As such, we proceeded here with a denser **k**-point mesh of $20 \times 20 \times 1$ to keep in line with the other TMDs discussed shortly, although this was not strictly necessary to do so.

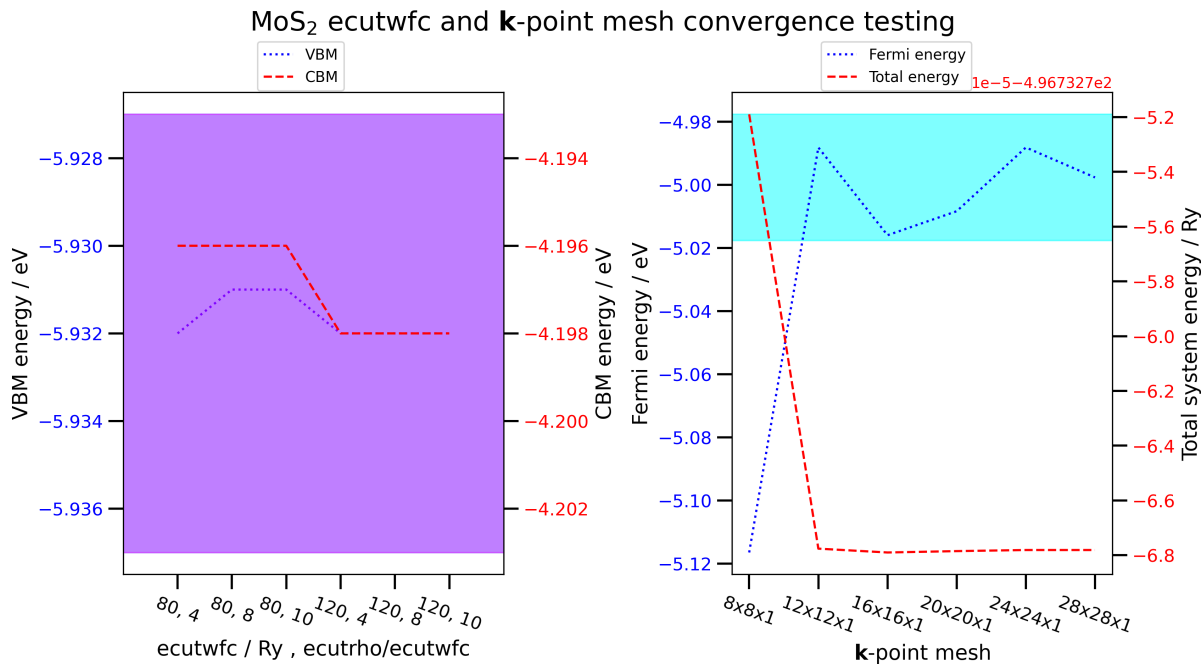


Figure 4.1: The results of `ecutwfc` (left) and `k`-point (right) convergence testing for MoS₂. VBM energy (left) and Fermi energy (right) are represented by blue dotted lines, and CBM energy (left) and total energy (right) are represented by red dashed lines. Convergence was achieved with `ecutwfc` = 80 Ry, `ecutrho/ecutwfc` = 4, and a `k`-point mesh of 12 × 12 × 1. The VBM and CBM values (left) are scaled the same, but represented within different energy ranges. The cyan and magenta bars (left) represent the convergence thresholds for VBM and CBM values, respectively, and the cyan bar (right) represents the convergence threshold for the Fermi energy, all centred on the value from the most expensive and accurate calculation. In the left image these bars overlap significantly, resulting in the single purple bar. Also note that the bars are of height twice the convergence threshold i.e. extend from the most accurate value by the threshold in both positive and negative directions.

HSE

Using geometry from previous DFT calculations (with converged parameters), and an `ecutwfc` previously determined, HSE `scf` calculations were carried out with successively denser Fock meshes. The results of this are displayed in Figure 4.2. Convergence was demonstrated following the results from using a 6 × 6 × 1 Fock mesh. Due to the cost associated with hybrid calculations, we did not investigate finer `k`-point grids, and simply used a 6 × 6 × 1 `k`-point mesh, with the intention to increase it in line with the `q`-point mesh if needed.

Notably for MoS₂, there was a requirement to increase `ecutfock` beyond the typical value of `ecutfock` = `ecutrho` = 4 × `ecutwfc` due to numerical instability that can

arise from exact calculations on the particular software used here. The solution was to increase `ecutfock` from 320 Ry to 400 Ry, and so we increased the other energy cut-offs proportionally (`ecutwfc` = 100 Ry, `ecutrho` = 400 Ry).

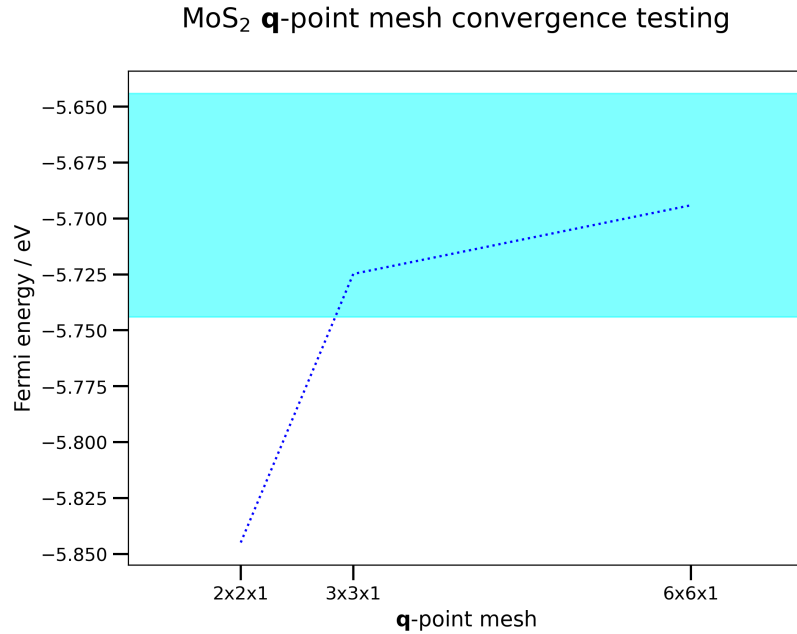


Figure 4.2: Convergence testing results for MoS₂, using the HSE functional. Convergence was achieved with a **q**-point mesh of $3 \times 3 \times 1$, but a calculation with $6 \times 6 \times 1$ had to be performed to demonstrate this. As such, the results from the more accurate mesh of $6 \times 6 \times 1$ were used. The convergence threshold is again represented by a cyan bar, centered on the most expensive and accurate result.

4.2.2 MoSe₂

DFT

The same procedure as for MoS₂ was performed, with resulting parameters of `ecutwfc` = 100 Ry, and `ecutrho/ecutwfc` = 4. Using these energy cut-off values, the **k**-point mesh was converged to a grid of $20 \times 20 \times 1$. This is the reason (along with WS₂) that MoS₂ and WSe₂ use denser grids than otherwise necessary. The results of the test are displayed in Figure 4.3. Again, the total system energy is shown for completeness, but converged long before the Fermi energy.

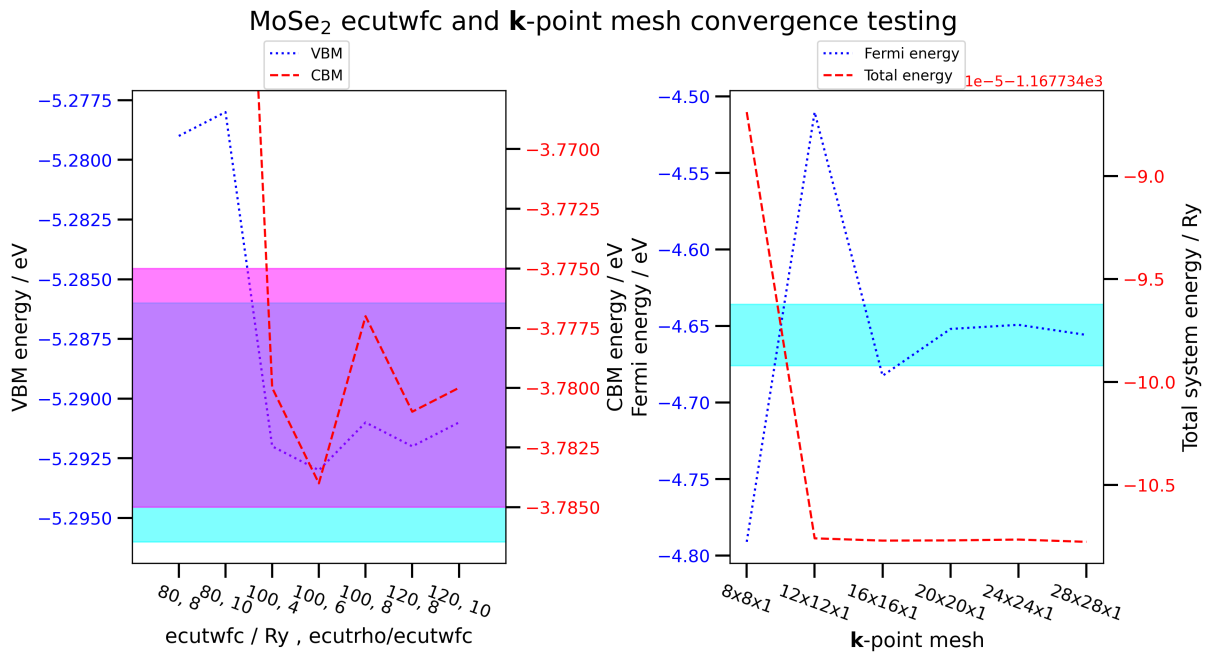


Figure 4.3: The results of `ecutwfc` and `ecutrho` convergence testing (left) and `k`-point mesh (right) for MoSe₂. VBM and CBM energies are shown with a blue dotted line and a red dashed line, respectively (left), and Fermi energy and total energy similarly (right). VBM and CBM energy thresholds are marked by a cyan and magenta bar, respectively (left), and the Fermi energy threshold likewise in cyan (right).

HSE

Convergence testing of the Fock mesh followed the same procedure as for MoS₂, but a `q`-point mesh of $2 \times 2 \times 1$ would have been appropriate (and so the next mesh of $3 \times 3 \times 1$ would have been used). However, (incorrectly) anticipating the need for a more dense mesh, a further calculation with a $6 \times 6 \times 1$ mesh was performed as part of the calculation batch. As such, we used the results from this more accurate calculation. This is shown in Figure 4.4.

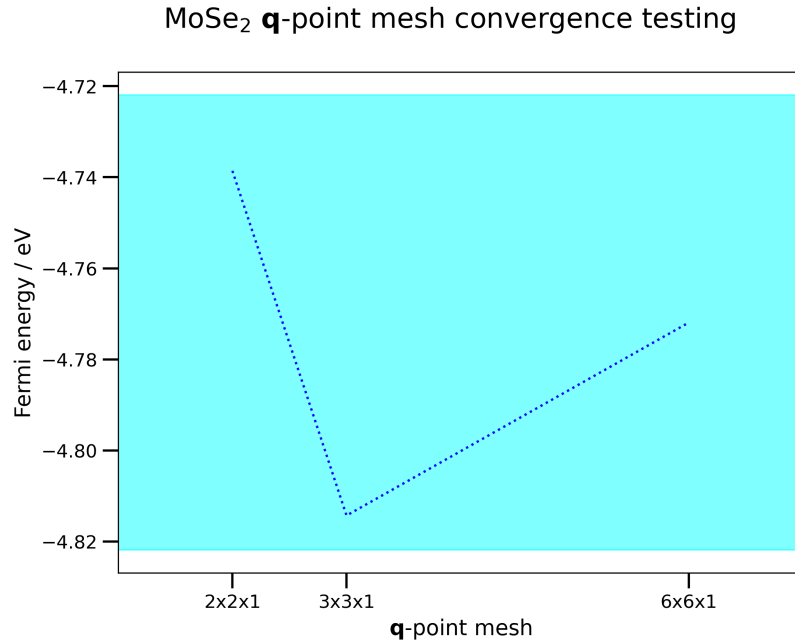


Figure 4.4: Convergence testing results for MoSe₂, using the HSE functional. Convergence was achieved with a **q**-point mesh of $2 \times 2 \times 1$ as shown by the threshold (cyan bar), but a calculation with $3 \times 3 \times 1$ had to be performed to demonstrate this, and the batch included a mesh of $6 \times 6 \times 1$; we use the denser mesh going forward.

4.2.3 WS₂

DFT

Convergence testing in the established manner for WS₂ resulted in `ecutwfc` = 80 Ry, `ecutrho/ecutwfc` = 4, and a **k**-point mesh of $20 \times 20 \times 1$. The results of the convergence test for DFT are displayed in Figure 4.5.

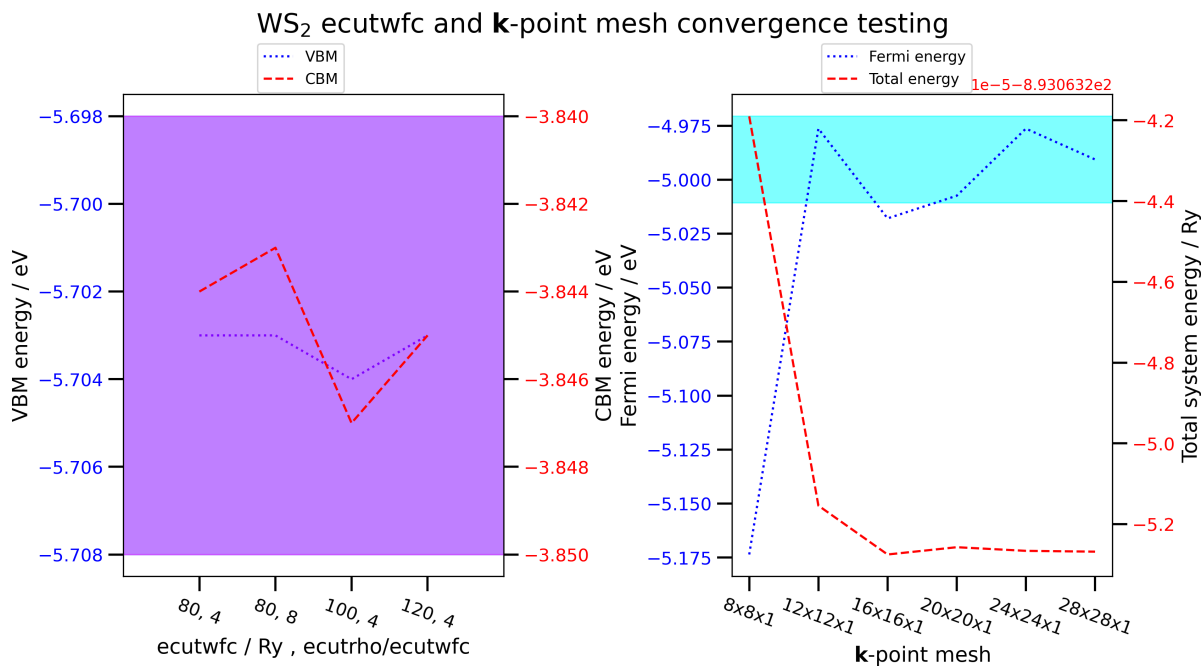


Figure 4.5: The results of energy cut-off (left) and \mathbf{k} -point mesh (right) convergence testing for WS₂. VBM and CBM values (left) are represented by blue dotted and red dashed lines, with their thresholds represented by cyan and magenta bars, respectively. Fermi energy and total energy (right) are represented by blue dotted and red dashed lines, respectively, and the Fermi energy threshold is the cyan bar.

HSE

The \mathbf{q} -point mesh convergence test results are displayed in Figure 4.6. Similarly to MoSe₂, a mesh of $2 \times 2 \times 1$ would have sufficed, but a more accurate mesh of $6 \times 6 \times 1$ was performed as part of the calculation batch anyway. As such, we elected to use the denser mesh going forward.

In the same manner as for MoS₂, there was a requirement to increase `ecutfock` beyond the typical value of `ecutfock = ecutrho = 4 × ecutwfc`. We again increased `ecutfock` from 320 Ry to 400 Ry, and increased the other energy cut-offs proportionally (`ecutwfc = 100 Ry`, `ecutrho = 400 Ry`).

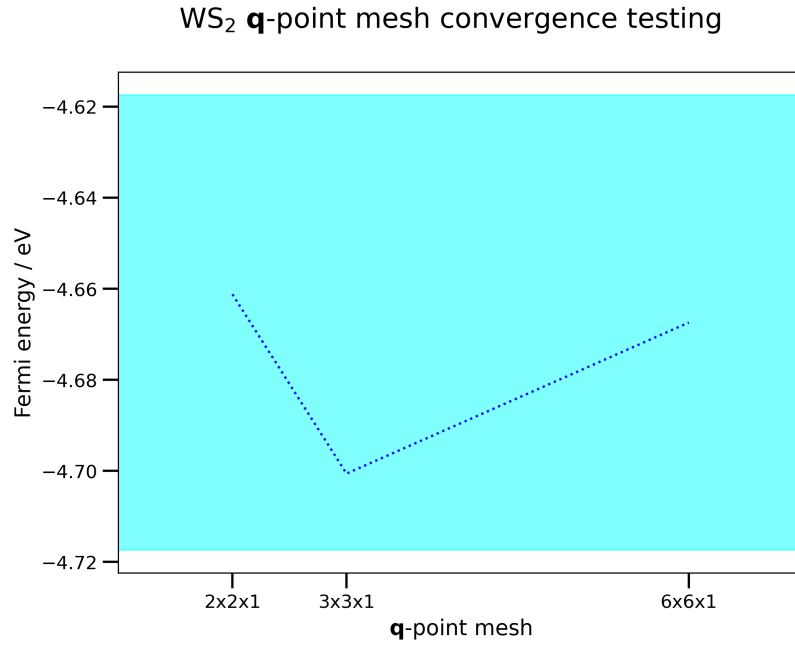


Figure 4.6: Convergence testing results for WS₂, using the HSE functional. Convergence was achieved with a \mathbf{q} -point mesh of $2 \times 2 \times 1$, as shown by the threshold (cyan bar), but a calculation with $3 \times 3 \times 1$ had to be performed to demonstrate this. As a $6 \times 6 \times 1$ mesh was investigated as a part of the calculation batch anyway, the results from this were used.

4.2.4 WSe₂

DFT

Convergence testing of WSe₂ parameters demonstrated a need for `ecutwfc` = 120 Ry, `ecutwfc/ecutrho` = 4, and a \mathbf{k} -point mesh of $16 \times 16 \times 1$. In keeping with the other TMDs above, a mesh of $20 \times 20 \times 1$ was instead selected. The results of the convergence test are displayed in Figure 4.7.

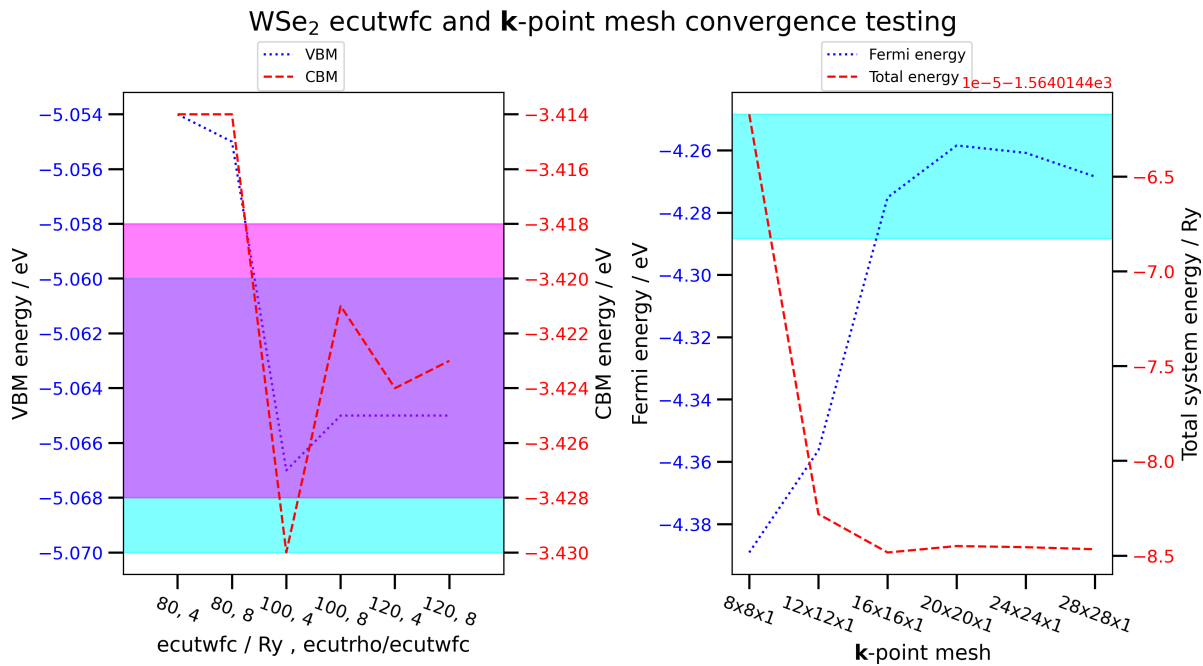


Figure 4.7: The results of convergence testing for WSe₂. The left panel displays the results of the energy cut-off convergence test, with the VBM energies as the blue dotted line and their threshold the cyan bar, and CBM energies the red dashed line with their threshold as the magenta bar. The right panel displays the results of the **k**-point mesh convergence test, with the Fermi energy and its threshold represented by the blue dotted line and cyan bar, respectively, and the total energy represented by the red dashed line.

HSE

Convergence testing results for the **q**-point mesh is shown in Figure 4.8, and again required only a $2 \times 2 \times 1$ mesh, but a calculation using a $6 \times 6 \times 1$ mesh was performed as a part of the batch. We used this more accurate mesh for our analysis.

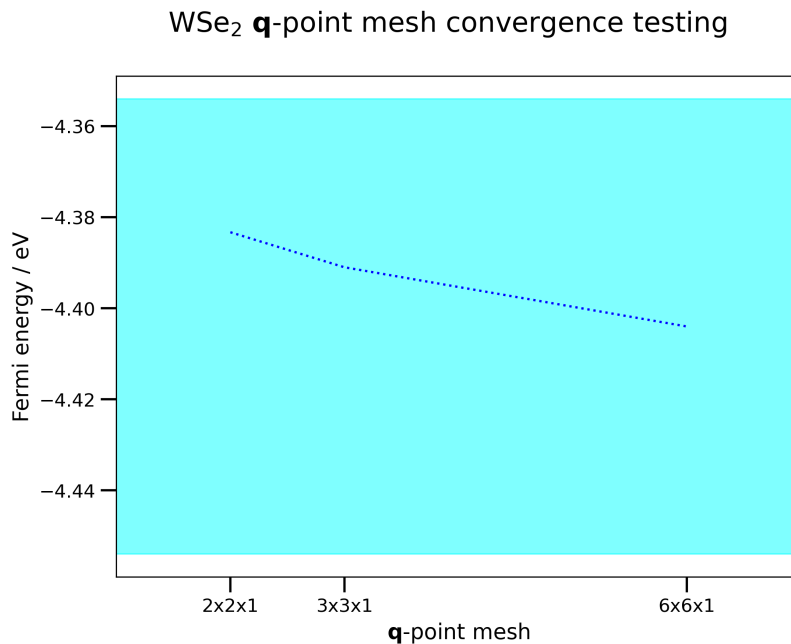


Figure 4.8: Convergence testing results for WSe_2 , using the HSE functional. As before, convergence was achieved with a \mathbf{q} -point mesh of $2 \times 2 \times 1$, as shown by the threshold (cyan bar), but a calculation with $3 \times 3 \times 1$ had to be performed to demonstrate this.

4.2.5 Pentacene

We did not perform convergence testing for the \mathbf{k} -point mesh for pentacene, as it is molecular and in a large cell. As such, we used Γ -point calculations throughout (a \mathbf{k} -point mesh of $1 \times 1 \times 1$). This is also true for the Fock mesh.

Convergence testing for the energy cut-off parameters is shown in Figure 4.9, where the parameters converged immediately. We were able to proceed with `ecutwfc` = 80 Ry, and `ecutrho/ecutwfc` = 4, but for early testing had already used `ecutwfc/ecutrho` = 5. This small discrepancy will not affect final computational output, as shown by the convergence test. For heterostructure calculations later in the project, the energy cut-offs used are those determined by the TMD, as those values will always suffice for the pentacene molecule.

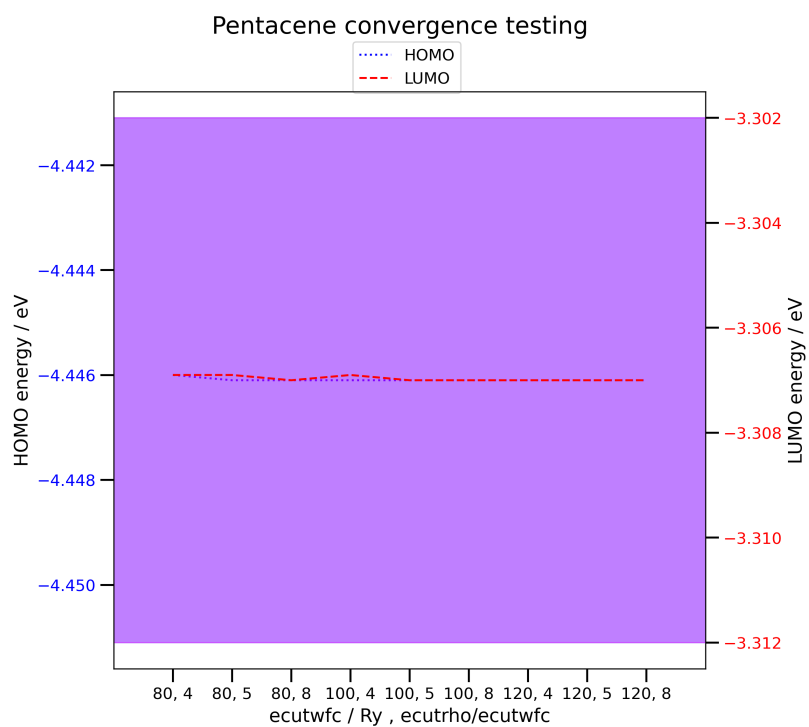


Figure 4.9: The results of `ecutwfc` convergence testing for pentacene, with the VBM energies as the blue dotted line and their threshold the cyan bar, and CBM energies the red dashed line with their threshold as the magenta bar. These threshold bars again overlap, resulting in the appearance of a single purple bar.

4.3 Geometry

Using the newly converged parameters, geometry optimization was carried out. First, a `vc-relax` calculation was performed with a hexagonal primitive crystal system (except for pentacene which, as the project’s adsorbate, has cell parameters dependent on its underlying substrate). This calculation allows for a relaxation of the cell parameter a , with $b = a$, and c determined by the introduced vacuum region and fixed. The vectors of the cell parameters in Cartesian coordinates, then, are $\mathbf{v}_1 = a(1, 0, 0)$, $\mathbf{v}_2 = a\left(-\frac{1}{2}, \frac{\sqrt{3}}{2}, 0\right)$, and $\mathbf{v}_3 = a\left(0, 0, \frac{c}{a}\right)$. The self-consistent DFT calculation minimizes the total energy and forces with respect to the atomic positions and cell parameters. Following convergence between self-consistent steps, the atomic position and cell parameter outputs are fed in to a `relax` calculation that re-minimizes the energy with respect to the atomic positions, but now with fixed cell parameters. The reason for this additional step is that the plane wave basis set is generated at the beginning of a calculation, and depends on the cell parameters. As the cell parameters change over the course of the `vc-relax` calculation, and the plane wave basis set is not updated, the atomic positions are determined by a plane wave basis set that is appropriate for the starting cell parameters, not the output cell parameters. By fixing the cell parameters during the `relax` calculation, the plane wave basis set is appropriate for the unit cell throughout, and this provides a slightly improved output of atomic positions within the cell.

Table 4.1: A comparison of geometry from the existing literature. XRD and ARXPS are experimental measurements, the others are theoretical results.

TMD	$a/\text{\AA}$	$d_{TM-Ch}/\text{\AA}$	$\Theta_{Ch-TM-Ch}$	$d_{Ch-Ch}/\text{\AA}$	Data
MoS ₂					
	3.18	2.42	82.30°	3.13	PBE [95]
	3.19	2.41	80.73°	3.13	PBE [96]
	3.20	2.42	80.69°	3.13	PW91 [97]
		2.41	82.31°	3.13	PW91 [98]
	3.16				XRD [†] [99]
	3.16				ARXPS [100]
	3.22	2.406			XRD, XAS [101]
	3.160	2.41	82.50°	3.19	XRD [†] [102]
MoSe ₂					
	3.319	2.524		3.288	PBE [103]
	3.32	2.54	82.11°	3.34	PBE [104]
	3.32				PBE [105]
	3.288	2.49	80.82°	3.23	XRD [†] [102]
	3.28				XRD [†] [106]
	3.27	2.528			XRD, XAS [101]
WS ₂					
	3.18	2.42	81.01°	3.14	PBE [104]
	3.185				PBE [107]
	3.185 [‡]	2.41	80.8°	3.13	PBE [108]
	3.154				XRD [†] [102]
	3.154				XRD [†] [109]
	3.23	2.417			XRD, XAS [101]
WSe ₂					
	3.32	2.55	82.43°	3.35	PBE [104]
	3.316				PBE [110]
	3.324				PBE [107]
	3.323				PW91 [110]
	3.286				XRD [†] [102]
	3.280				XRD [†] [111]
	3.287	2.532*			XRD [†] [112]
	3.290				XRD [†] [113]

[†] Data are from bulk or thin film samples.

[‡] A supercell approach was used, so the reported values here are adjusted to be the equivalent of a single unit cell.

* Multiple bond lengths at varying temperatures are given; the reported value above is that at 300K.

Table 4.2: A comparison of our calculated geometry results for monolayer TMD crystals, from DFT using the PBE functional, with (SOC) and without (nSOC) spin-orbit coupling, as well as the difference between the two (Δ).

TMD	$a/\text{\AA}$	$d_{TM-Ch}/\text{\AA}$	$\Theta_{Ch-TM-Ch}$	$d_{Ch-Ch}/\text{\AA}$
MoS ₂				
nSOC	3.1675	2.4083	81.139°	3.1314
SOC	3.1665	2.4069	81.147°	3.1310
Δ	0.0010	0.0014	0.008	0.0004
MoSe ₂				
nSOC	3.2979	2.5353	82.645°	3.3481
SOC	3.2975	2.5356	82.676°	3.3496
Δ	0.0004	0.0003	0.031°	0.0015
WS ₂				
nSOC	3.1721	2.4135	81.283°	3.1440
SOC	3.1721	2.4139	81.304°	3.1452
Δ	0.0000	0.0004	0.021°	0.0012
WSe ₂				
nSOC	3.2926	2.5398	83.082°	3.3685
SOC	3.2926	2.5398	83.082°	3.3685
Δ	0.0000	0.0000	0.000	0.0000

A number of existing experimental literature values we have provided in Table 4.1 are from bulk or thin film samples. For further comparison, we performed geometry optimization on bulk (2H, see Figure 1.1) TMDs, although these systems were not considered further in the project. Our computational details were the same as for monolayer systems, except for the \mathbf{k} -point mesh (using a $20 \times 20 \times 5$ mesh to account for the new cell parameter, c) and the updated structure to include repeating bilayers without a vacuum layer. The results of these calculations are displayed in Table 4.3, which are in keeping with the experimental values for cell parameters a (c) for bulk TMDs of 3.16 Å (12.32 Å), 3.28 Å (12.90 Å), 3.15 Å (12.36 Å), and 3.28 Å (12.95 Å) for MoS₂, MoSe₂, WS₂ and WSe₂, respectively [99, 102, 106, 109, 111]. The cell parameters a for our bulk calculations are all similar to those determined from our monolayer calculations.

Table 4.3: Calculated geometry results for bulk 2H TMD crystals, from DFT using the PBE functional, without (nSOC) spin-orbit coupling. The given c parameter is for one bilayer i.e. the cell maintaining the 2H relationship.

TMD	$a/\text{\AA}$	$c/\text{\AA}$
MoS ₂	3.1686	12.4913
MoSe ₂	3.2978	13.1608
WS ₂	3.1717	12.5601
WSe ₂	3.2918	13.1594

4.3.1 MoS₂

The structural parameters of monolayer MoS₂, without considering spin-orbit coupling, are displayed in Figure 4.10. Our lattice parameter result of $a = 3.1675 \text{ \AA}$ is similar to previous theoretical results that also use the PBE functional and monolayer structure, as are the Mo-S bond lengths, d_{Mo-S} , of 2.4083 \AA the S-Mo-S bond angle, Θ_{S-Mo-S} , of 81.139° , and layer thickness (S-S distance), d_{S-S} , of 3.1314 \AA . Comparisons can be made with the results from the literature in Table 4.1. Our results are also very close to experimental values for the lattice parameter, a , measured to be 3.16 by both X-ray powder diffraction (XRD) and angle-resolved X-ray photoemission spectroscopy (ARXPS).

If we consider spin-orbit coupling, the parameters are instead $a = 3.1665 \text{ \AA}$, $d_{Mo-S} = 2.4069 \text{ \AA}$, $\Theta_{S-Mo-S} = 81.147^\circ$, and $d_{S-S} = 3.1310 \text{ \AA}$, which are similar to those without spin-orbit coupling. A comparison of geometry results can be seen in Table 4.2. The geometry results from `vc-relax` and `relax` calculations that consider spin-orbit coupling are used for electronic structure calculations that also consider spin-orbit coupling. Later calculations (Chapters 5 and 6) that involve the supercell approach did not consider spin-orbit coupling (due to computational cost), and so use the previous geometry results without spin-orbit coupling to produce the supercell.

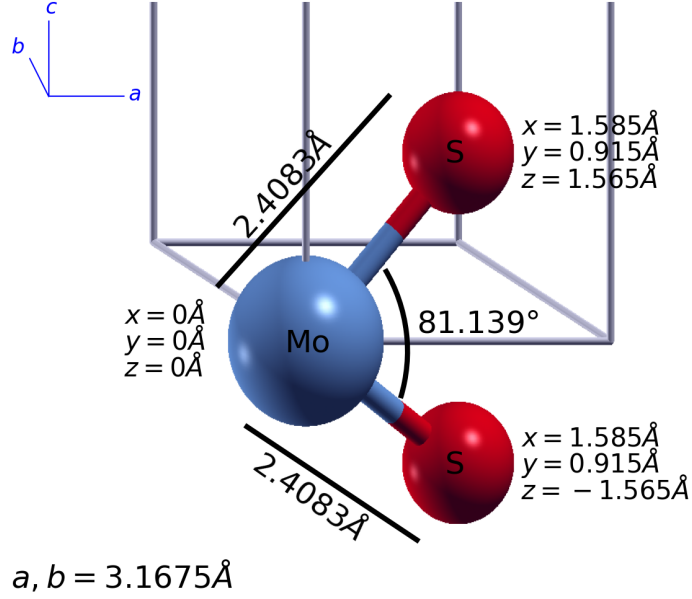


Figure 4.10: MoS₂ molecule following variable cell relaxation without spin-orbit coupling. Bond lengths, bond angle, atomic positions and the lattice parameter a are displayed. 1H monolayer TMDs are within the rhombohedral lattice system (trigonal crystal system), where the cell parameter $a = b$, and in principle c is also required to define the system, but here we set c to be large in order to create a vacuum region and ensure no interaction between layers.

4.3.2 MoSe₂

The MoSe₂ monolayer, without spin-orbit coupling, was found to have a lattice parameter of $a = 3.2979 \text{ \AA}$, an Se-Mo-Se bond angle of $\Theta_{Se-Mo-Se} = 82.645^\circ$, an Mo-Se bond length of $d_{Mo-Se} = 2.5353 \text{ \AA}$, and a layer thickness of $d_{Se-Se} = 3.3481 \text{ \AA}$. These can be compared to the literature values in Table 4.1, showing that our results are close to experimental results, and broadly agree with previous theoretical calculations. Our results are demonstrated in Figure 4.11.

Considering spin-orbit coupling, there are again small changes in geometry. The lattice parameter becomes $a = 3.2975 \text{ \AA}$, the Mo-Se bond length $d_{Mo-Se} = 2.5356 \text{ \AA}$, the Se-Mo-Se bond angle $\Theta_{Se-Mo-Se} = 82.676^\circ$, and the layer thickness $d_{Se-Se} = 3.3496 \text{ \AA}$, again displayed in Figure 4.2.

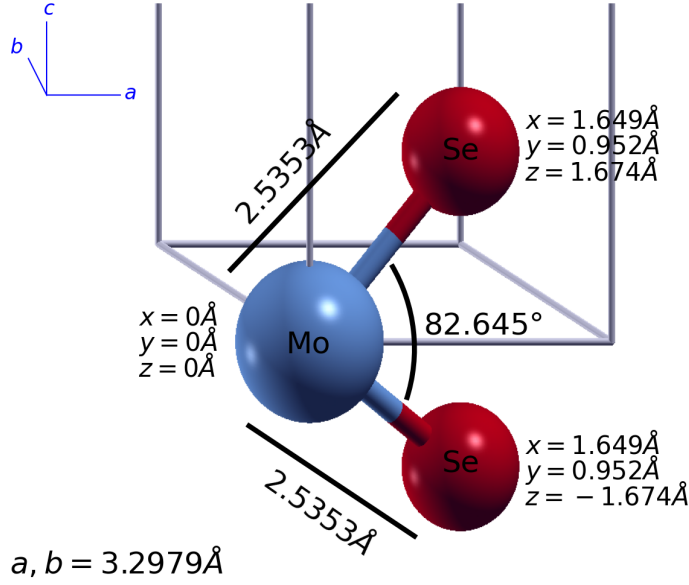


Figure 4.11: MoSe₂ molecule following variable cell relaxation without spin-orbit coupling. Bond lengths, bond angle, atomic positions and the lattice parameter a are displayed. 1H monolayer TMDs are within the rhombohedral lattice system (trigonal crystal system), where the cell parameter $a = b$, and in principle c is also required to define the system, but here we set c to be large in order to create a vacuum region and ensure no interaction between layers.

4.3.3 WS₂

The WS₂ monolayer, without spin-orbit coupling, was found to have a lattice parameter of $a = 3.1721\text{ \AA}$, a W-S bond length of $d_{W-S} = 2.4135\text{ \AA}$, an S-W-S bond angle of $\Theta_{S-Mo-S} = 81.283^\circ$, and a layer thickness of $d_{S-S} = 3.1440\text{ \AA}$. These can be compared to the literature values in Table 4.1, showing that our results are again similar to experimental results, and agree closely with previous theoretical calculations. Our results are demonstrated in Figure 4.12.

When considering spin-orbit coupling, small changes in geometry are again observed, but unlike for the molybdenum crystals, the lattice parameter is unchanged. The W-S bond length becomes $d_{W-S} = 2.5356\text{ \AA}$, the S-W-S bond angle becomes $\Theta_{S-Mo-S} = 82.676^\circ$, and the layer thickness becomes $d_{S-S} = 3.3496\text{ \AA}$. A comparison is made in Table 4.2.

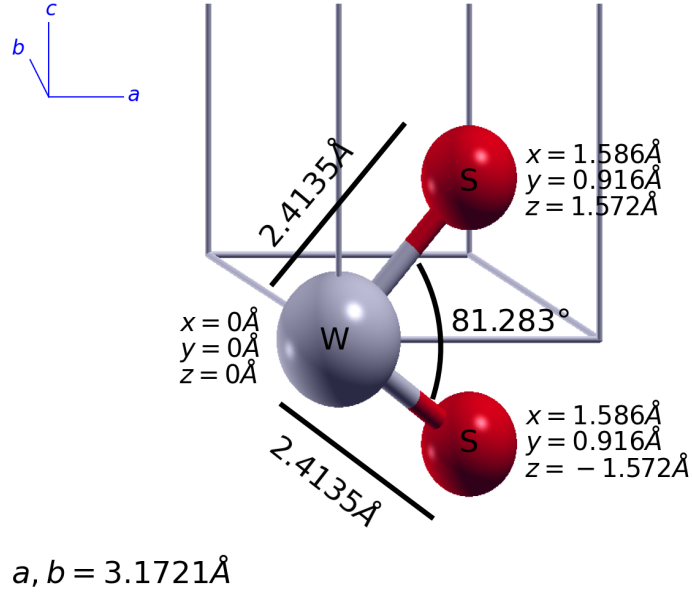


Figure 4.12: WS_2 molecule following variable cell relaxation without spin-orbit coupling. Bond lengths, bond angle, atomic positions and the lattice parameter a are displayed. 1H monolayer TMDs are within the rhombohedral lattice system (trigonal crystal system), where the cell parameter $a = b$, and in principle c is also required to define the system, but here we set c to be large in order to create a vacuum region and ensure no interaction between layers.

4.3.4 WSe_2

The WSe_2 monolayer, without spin-orbit coupling, was found to have a lattice parameter of $a = 3.2926 \text{ \AA}$, an Se-W-Se bond angle of $\Theta_{S-Mo-S} = 83.082^\circ$, an W-Se bond length of $d_{W-Se} = 2.5398 \text{ \AA}$, and a layer thickness of $d_{Se-Se} = 3.3685 \text{ \AA}$. These can be compared to the literature values in Table 4.1. Our results are close to experimental results, and agree with previous theoretical calculations, although in this case there is lacking information on the details of the structure, with existing literature mostly reporting just the lattice parameter. Our results are demonstrated in Figure 4.13.

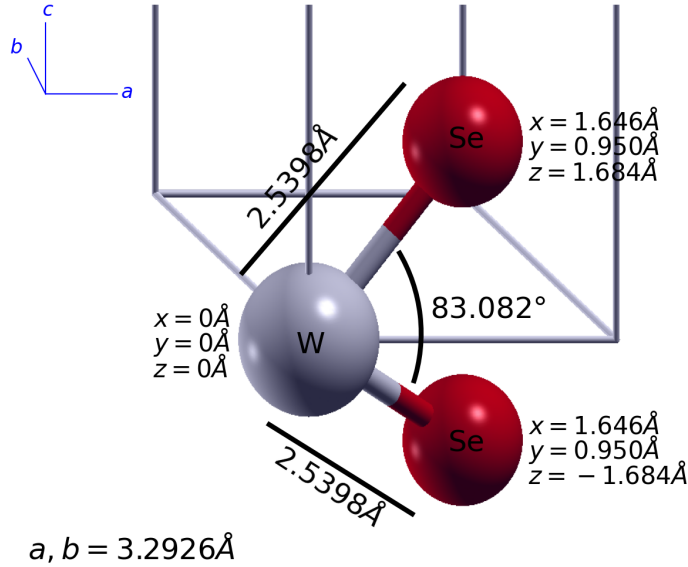


Figure 4.13: WSe₂ molecule following variable cell relaxation without spin-orbit coupling. Bond lengths, bond angle, atomic positions and the lattice parameter a are displayed. 1H monolayer TMDs are within the rhombohedral lattice system (trigonal crystal system), where the cell parameter $a = b$, and in principle c is also required to define the system, but here we set c to be large in order to create a vacuum region and ensure no interaction between layers.

In the case of WSe₂, performing geometry optimization while considering spin-orbit coupling results in no change compared to that without.

4.3.5 Pentacene

Being molecular, pentacene's geometry optimization is treated differently. We construct a cell with lattice parameters that ensures each molecule is isolated from its neighbours, and do not allow this cell to change (i.e. we do not perform the `vc-relax` calculation, only `relax`). Experimental work will often include lattice parameters as they must examine crystals of pentacene, but we do not. Our lattice parameters were chosen, not determined, such that molecular separation was over 30 Å in all directions in order to ensure there was no interaction between molecules. This was achieved with a cubic supercell of side length 48 Å. Performing geometry optimization with spin-orbit coupling considered did not change the molecular structure compared to excluding it, as may be expected of a molecule comprised of small atoms. Due to hardware limitations causing difficulty with HSE calculations with such large vacuum regions, we also considered a smaller cubic

supercell of side length 32 Å; this was confirmed to be large enough to maintain isolation between molecules (discussed in subsection 4.4.6), but this was only introduced later on when the need became apparent.

We also considered low concentration pentacene, where the molecules are considered in a repeating cell defined by the size of a 7×4 molecule sheet of underlying TMD substrate: $a = 22.19$ Å and $b = 12.68$ Å. The cell parameters are thus chosen as this is the size of the heterostructure supercells used later in the project. Similarly, we also considered a cell defined by the size of a 6×3 molecule sheet of underlying TMD substrate, with parameters $a = 19.02$ Å and $b = 9.51$ Å. This is for the high concentration pentacene heterostructures. We independently optimized the geometry of the molecule, but here report only the results of well-isolated pentacene, that being the system of interest at this stage; the investigation of pentacene in smaller cells is in order to decouple the effects of the substrate on the molecule from effects between molecules when in heterostructures, and will be discussed in later chapters (Chapters 5 and 6). We did, however, use the corresponding geometry of pentacene for the calculation of electronic structure within smaller cells.

These different concentrations of pentacene may be referred to as PEN_{iso} for the 48 Å cubic supercell, $\text{PEN}_{\text{small-iso}}$ for the 32 Å cubic supercell, $\text{PEN}_{7 \times 4}$ for the supercell defined by a 7×4 TMD substrate layer (low concentration pentacene), and $\text{PEN}_{6 \times 3}$ for the supercell defined by a 6×3 TMD substrate layer (high concentration pentacene).

Both experimental values and our own calculation show that the molecule's C-C bond lengths vary, and are symmetric across the length and width of the molecule. As such, we display the bond lengths on one side of Figure 4.14a, and bond angles on the other. Our calculations agree with previous experimental measurements via X-ray diffraction [114]. The experimental values are shown in in Figure 4.14b for comparison.

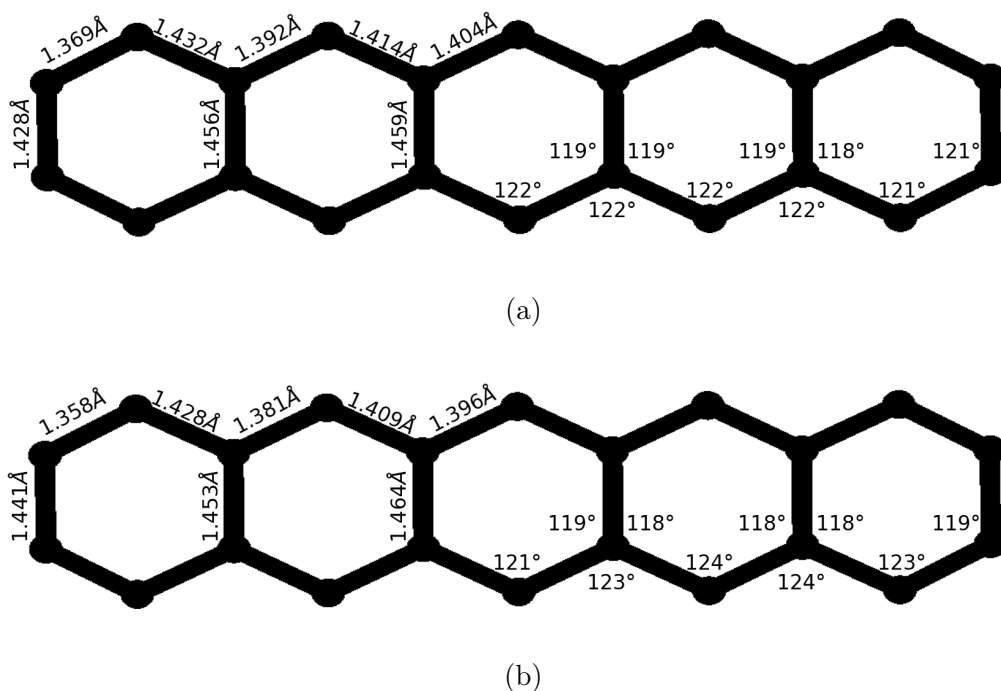


Figure 4.14: (a) Our calculated values for C-C bond lengths and C-C-C bond angles in the isolated pentacene molecule. Hydrogen atoms are not shown. The molecule is symmetric across the middle of its length and width for both bond lengths and angles. (b) Experimental values from XRD [114] for average C-C bond lengths and C-C-C bond angles of pentacene molecules in thin crystals. Hydrogen atoms are not shown. The molecule is symmetric across the middle of its length and width for both bond lengths and angles.

We found the total molecule dimensions in the x-y plane to be $14.1443 \text{ \AA} \times 5.0028 \text{ \AA}$, compared to $14.21 \text{ \AA} \times 5.04 \text{ \AA}$, from existing PBE DFT calculations in the literature [115]. That work used a similarly isolating cell, with dimensions of 50 \AA , and additionally found the C-H bond lengths to be uniform at 1.10 \AA , whereas we found them to be non-uniform, slightly longer towards the middle of the molecule's length: the middle carbon ring's C-H bonds were 1.0925 \AA , whereas the rings at the end of the molecule's length had C-H bond lengths of 1.0903 \AA . These values are all very close, and in agreement with each other.

Our calculations resulted in a mean deviation of the atomic positions from the molecular plane of 0.49 m\AA , with the largest deviation being 1.02 m\AA . This is comparable to the literature value for maximum deviation of 0.67 m\AA [115], agreeing with the finding that the molecule is essentially planar.

4.4 Electronic structure

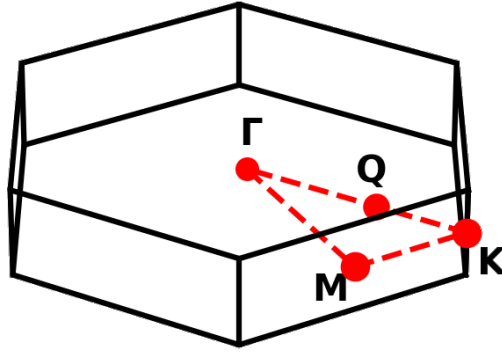


Figure 4.15: The first Brillouin zone of a hexagonal lattice, with the sampling path between high-symmetry points used for the band structure of our TMDs marked in red.

With the structure of the systems determined, the next stage of obtaining the electronic structure using DFT was to perform `scf` calculations. These provide information on electronic energies, with the theory behind the calculation being discussed in Section 3.1. This is enough to get information on total system energy and Fermi energy, where the vacuum energy is set to 0 (as it will be throughout). The frontier orbital energies can also be extracted, but with limited information on the underlying band structure. Following this, `nscf` calculations were performed on finer \mathbf{k} -point grids to improve accuracy. The `bands` calculation can then be performed with a defined path through \mathbf{k} -space over which to assess band energy, which gives us the full band structure following some post-processing with `bands.x`. The path through \mathbf{k} -space that we chose captures important critical points in the hexagonal Brillouin zone (Γ - M - K - Γ), and is displayed in Figure 4.15. This choice of path also naturally passes through the Q critical point. To calculate the density of states, we then run the post-processing codes `dos.x` and can also subsequently run `projwfc.x` for projection of the density of states on to orthogonalized atomic wavefunctions. This process is laid out in Figure 3.8.

For the electronic structure using the HSE functional, however, the workflow is slightly different (see Figure 3.9). The `scf` calculation is still performed, using hybrid-specific parameters such as the Fock mesh. This is enough to obtain total system energy. For pentacene, being molecular and assessed using only Γ -point calculations, the Fermi

energy and frontier orbital energies can additionally be extracted. To continue to the full band structure (and frontier orbital energies for the TMDs), however, we used Wannier interpolation to populate the required fine grid, the theory of which is discussed in subsection 3.3.1. This is because non-self consistent field calculations (notably `nscf` and `bands`) within the `PWscf` package are not compatible with hybrid functionals. Additionally, density of states is not implemented for hybrid functionals, and so we only produced the band structures with HSE. Table 4.4 is a summary of our results for the band gaps of the investigated systems, and Table 4.5 provides an overview of band gap values from the theoretical and experimental literature.

Table 4.4: The band gaps of the monolayer TMDs and pentacene in different concentrations for different levels of theory. PBE-nSOC and PBE-SOC are the PBE functional without and with consideration of spin-orbit coupling, respectively, and HSE calculations are always performed with consideration of spin-orbit coupling.

System	E_G / eV		
	$E_G(\text{PBE-nSOC})$	$E_G(\text{PBE-SOC})$	$E_G(\text{HSE})$
PEN _{iso}	1.142	1.139	
PEN _{small-iso}	1.139	1.139	1.616
PEN _{7×4}	1.139	1.139	1.596
PEN _{6×3}	1.140	1.142	1.581
MoS ₂	1.733	1.660	2.089
MoSe ₂	1.513	1.407	1.792
WS ₂	1.859	1.606	2.080
WSe ₂	1.645	1.291	1.801

Table 4.5: A comparison of experimental and theoretical band gap energies for our materials. If the peaks from PL measurements are wide, we have given a range.

TMD	E_G / eV	Data	
MoS ₂	1.79 [‡]	PW91	[116]
	1.67	PBE	[96]
	2.13	HSE06	[96]
	1.9	PL	[23]
	1.9	PL	[22]
	1.85	PL	[24]
	1.82	PL	[21]
MoSe ₂	1.444	PBE	[104]
	1.47	PBE	[117]
	1.95	HSE06	[118]
	2.33 [‡]	G_0W_0	[119]
	1.53	PL	[25]
	1.625	PL	[26]
	2.18	STS	[120]
WS ₂	1.6	LDA	[121]
	1.424	optB86b-vdW	[122]
	1.819	PBE	[104]
	1.9	PBE	[117]
	1.94-1.99	PL	[27]
	2.01 [†]	PL	[123]
WSe ₂	1.27 [‡]	LDA	[124]
	1.548	PBE	[104]
	1.7	PBE	[117]
	1.65	PL	[28]
Pentacene	1.1	PBE	[115]
	1.1	PBE	[125]
	1.97 [†]	AS	[126]
	1.97 [†]	AS	[127]
	1.85 [†]	AS	[128]

[†] Few-layer TMD or thin film pentacene.

[‡] Theoretical work that considered spin-orbit coupling.

Previous theoretical work with the PBE functional demonstrates that all the TMDs used in this project have Γ - Q band gaps when in bulk, which transition to direct at K when in monolayer. All but MoS₂ maintain their indirect Γ - Q gaps all the way to bilayer, only changing in character at monolayer. MoS₂ is still a direct gap semiconductor only in monolayer, but the bilayer gap is Γ - K instead [20].

4.4.1 MoS₂

DFT

The density of states, alongside the band structure for monolayer MoS₂, using DFT without spin-orbit coupling, is presented in Figure 4.16. The greatest contribution to the conduction bands are molybdenum d-orbitals, as may be expected. Their contribution is also the most significant one at the highest energy valence bands, with sulfur s-orbitals contributing more as energy decreases. The frontier orbitals were found to be at -4.20 eV for the conduction band minimum (CBM) and -5.94 eV for the valence band maximum (VBM), resulting in a band gap of 1.73 eV. This is a direct band gap at the high-symmetry (critical) point \mathbf{K} : both the CBM and VBM occur at \mathbf{K} . Our result is similar to other generalized gradient approximation (GGA) calculations (see Table 4.5), but is an underestimation of the experimental band gap. The direct character, however, agrees with experiment [21–24].

We can see that the indirect band gap is between the \mathbf{K} and \mathbf{Q} critical points for the VBM and CBM, respectively (and is larger than the direct band gap, with lowest conduction band energy at the \mathbf{Q} point being -3.99 eV). Bulk MoS₂ has a smaller indirect band gap than its direct band gap, between $\mathbf{\Gamma}$ (VBM) and \mathbf{Q} (CBM) critical points [116, 129], with the CBM reducing in energy around the \mathbf{Q} point with the increase in interlayer interaction [130] found in bulk and many-layer systems. Similarly, the top-most valence band decreases in energy at the $\mathbf{\Gamma}$ point with decreasing layers, whereas the direct gap at \mathbf{K} changes little [24].

MoS₂ band structure and pDOS, nSOC

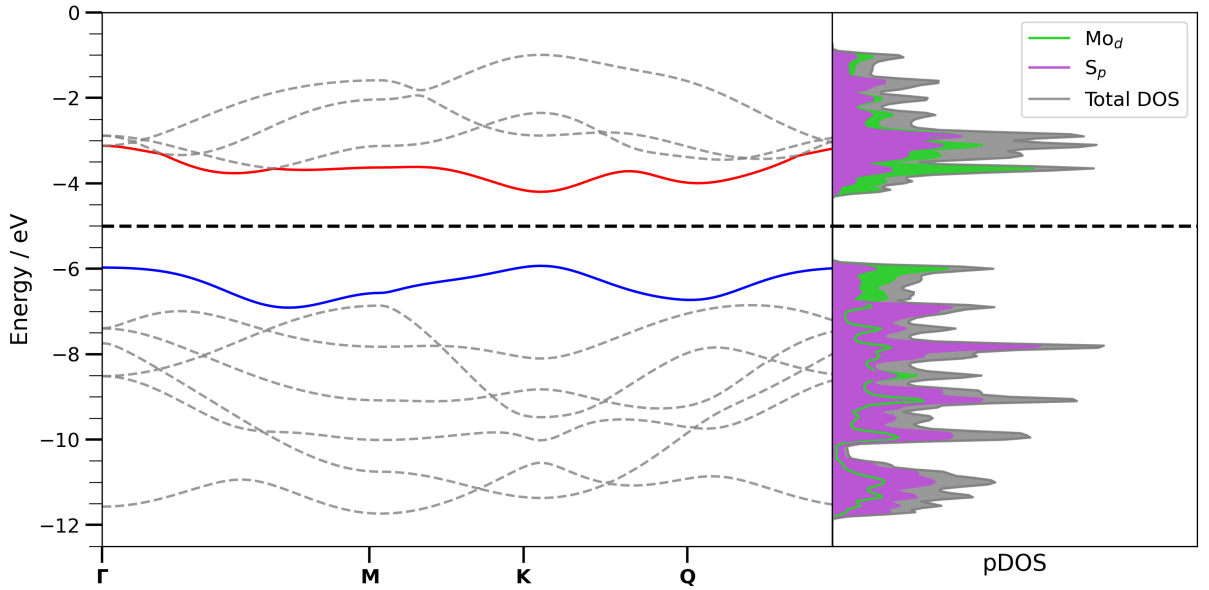


Figure 4.16: The projected density of states and band structure of monolayer MoS₂, without considering spin-orbit coupling, using DFT. The Fermi energy is represented by a black dashed line. There are very minor contributions to the density of states from lower energy orbitals within the displayed energy range (not shown).

When considering spin-orbit coupling, we see frontier orbital energies of -5.83 eV for the VBM and -4.17 eV for the CBM, resulting in a band gap of 1.66 eV. These values represent a small increase of 0.03 eV in the CBM, and an increase in the VBM of 0.10 eV, for a decrease in E_G of 0.07 eV. This is expected from spin-orbit coupling induced band splitting, much more notable in the valence bands: the top-most valence band is split by 147 meV at **K**, and the lowest conduction band is only split by 3 meV. This pattern is noted in the literature [116], and is similar to reported values for bulk MoS₂ both using PBE functionals and experimental measurement using angle-resolved photoemission spectroscopy (ARPES) [131], as well as monolayer values from photoluminescence measurements [24]. The band structure and pDOS of monolayer MoS₂ with consideration of spin-orbit coupling is displayed in Figure 4.17. Band splitting is clearly visible in the top-most valence band around the **K** critical point. The changes in the density of states from consideration of spin-orbit coupling are minor, and arise from the described changes in energies above.

MoS₂ band structure and pDOS, SOC

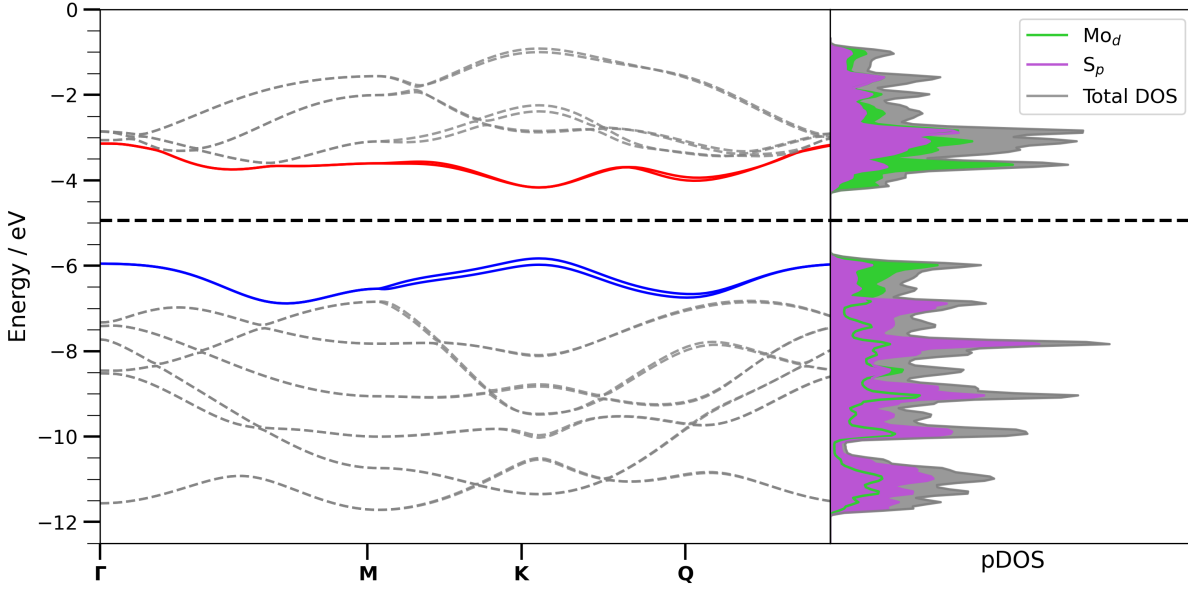


Figure 4.17: The projected density of states and band structure of monolayer MoS₂, considering spin-orbit coupling, using DFT. The Fermi energy is represented by a black dashed line. There are very minor contributions to the density of states from lower energy orbitals within the displayed energy range (not shown).

HSE

Using the hybrid HSE functional, we performed an `scf` calculation followed by Wannier interpolation on to a finer grid, and then extracted the band structure using post-processing from the `wannier90` tool. HSE calculations were with spin-orbit coupling considered. This is displayed in Figure 4.18, with a direct comparison to the DFT-only results in Figure 4.19. For all bands, the effect of HSE is to move them energetically further from the Fermi energy, with the exception of the lowest conduction band around the **K** critical point, where HSE predicts a slightly lower energy. The VBM decreases by 0.45 eV to -6.28 eV compared to DFT only with spin-orbit coupling. The CBM is calculated as -4.42 eV, and so also decreases, but only by 0.02 eV. This results in a calculated band gap of 2.09 eV, which is much closer to experimental values for the system (see Table 4.5) than our DFT results, and comfortably in line with previous HSE calculations. Band splitting of 189 meV and 19 meV occurs around the VBM and CBM, respectively. The basic structure remains unchanged, with a maintained direct band gap at the **K** critical point and an indirect band gap at **K** – **Q**, which is greater than the

direct band gap.

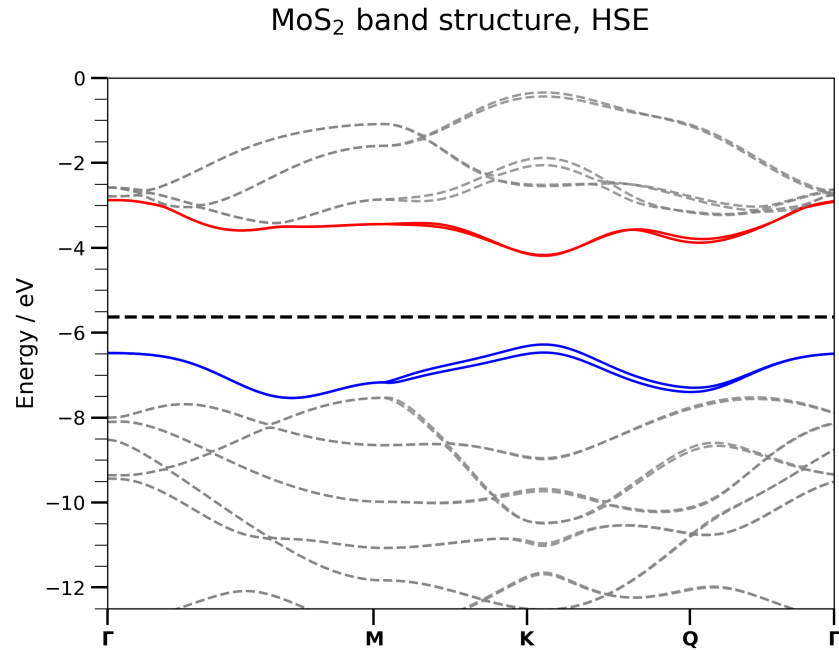


Figure 4.18: The band structure of MoS₂, calculated using the HSE hybrid functional, with spin-orbit coupling. The Fermi energy is denoted by the dashed black line.

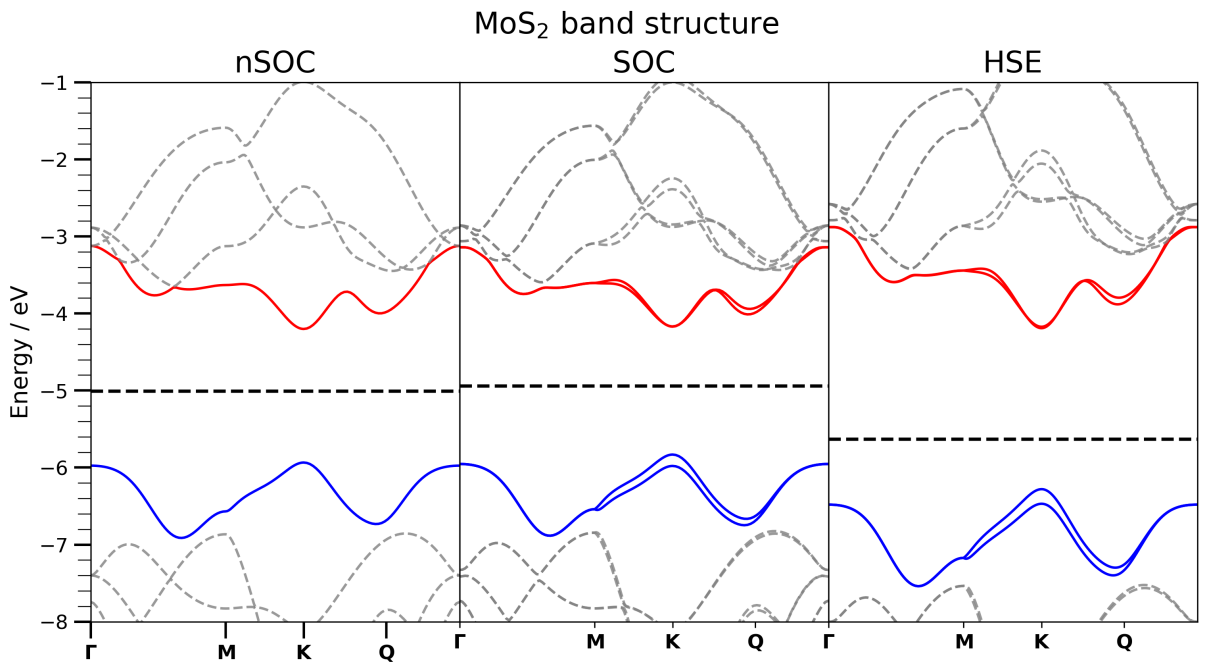


Figure 4.19: A comparison between DFT and HSE band structures of MoS₂: DFT without considering spin-orbit coupling (left), DFT considering spin-orbit coupling (middle), and HSE considering spin-orbit coupling (right). The Fermi energies are plotted as the dashed black lines, and the vacuum energy is set to 0.

4.4.2 MoSe₂

DFT

The density of states and bands structure of MoSe₂, without considering spin-orbit coupling, is displayed in Figure 4.20. As was the case for MoS₂, the largest contribution to the conduction bands are Mo d-orbitals, which are also the most important contribution to the top-most valence band, with selenium s-orbitals contributing more with decreasing energy. Selenium d-orbitals do not play an electronic role near the Fermi energy, being lower in energy than their respective shell's p-orbitals, as expected. The VBM was at -5.29 eV and the CBM at -3.78 eV, resulting in a band gap of 1.51 eV. This is broadly in line with experiment (see Table 4.5), although still represents an underestimation of the band gap. The band structure is reminiscent of MoS₂, with a direct band gap at **K**, and a slightly larger indirect band gap to **Q** in the conduction band.

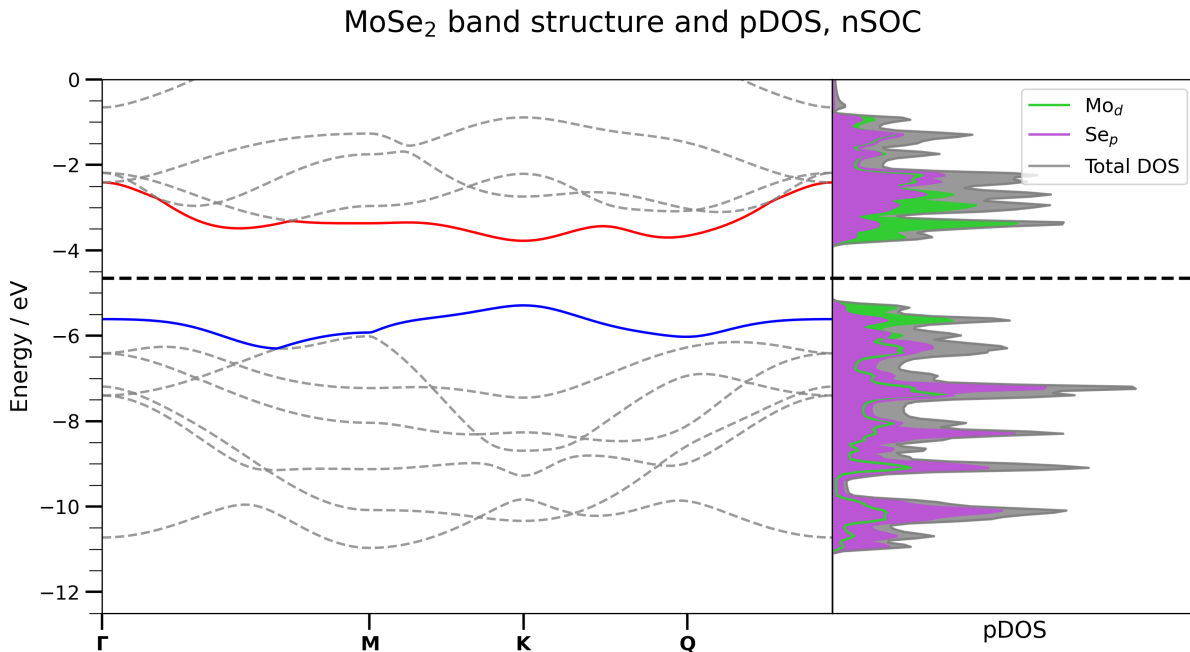


Figure 4.20: The projected density of states and band structure of monolayer MoSe₂, without considering spin-orbit coupling, using DFT. The Fermi energy is represented by a black dashed line. There are very minor contributions to the density of states from lower energy orbitals within the displayed energy range (not shown).

When considering spin-orbit coupling, the frontier orbital energies were -5.19 eV and -3.78 eV (VBM and CBM, respectively), resulting in a band gap of 1.41 eV, which was

still found to be direct at \mathbf{K} . These results represent an increase in the the VBM of 0.10 eV, a negligible decrease in the CBM, and a decrease in the band gap of 0.11 eV. The valence band experiences splitting of 185 meV at the \mathbf{K} point, and the conduction band was split by 21 meV. The valence band splitting is consistent with previously reported splitting of 180 meV from ARPES results [132], as well as with 183 meV from theoretical results [133]. The band structure for MoSe₂, along with density of states, from DFT with spin-orbit coupling is displayed in Figure 4.21. The density of states is very similar to that without spin-orbit coupling.

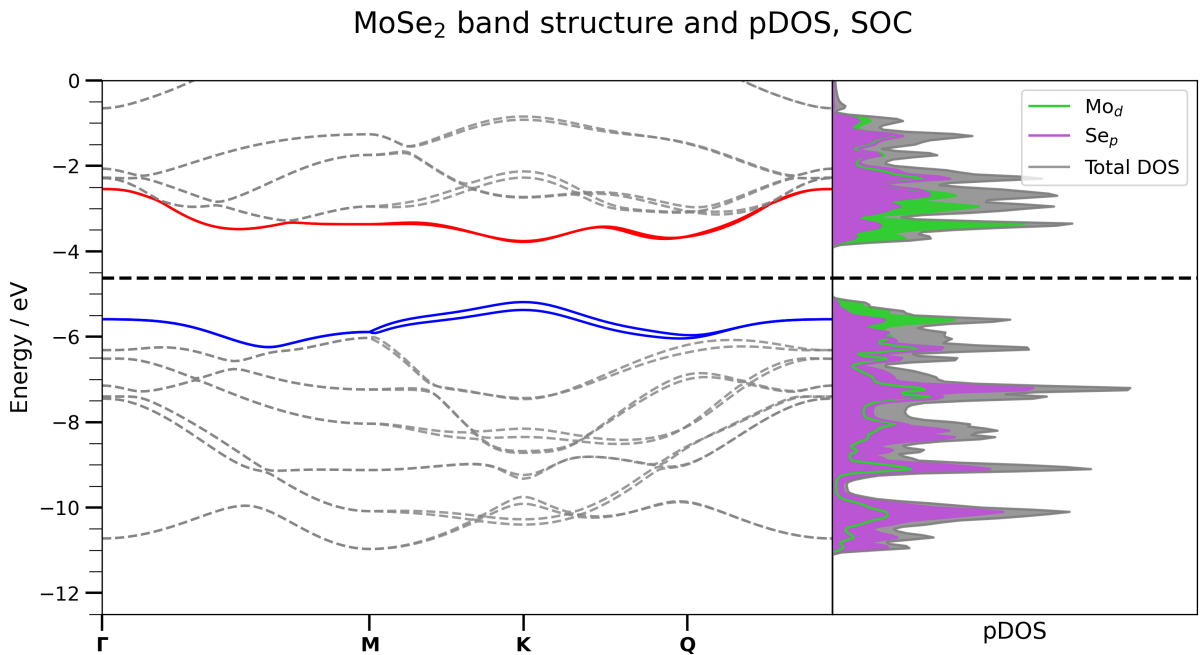


Figure 4.21: The projected density of states and band structure of monolayer MoSe₂, considering spin-orbit coupling, using DFT. The Fermi energy is represented by a black dashed line. There are very minor contributions to the density of states from lower energy orbitals within the displayed energy range (not shown).

HSE

Our HSE calculations for monolayer MoSe₂ yield a VBM of -5.71 eV at the \mathbf{K} point and a CBM of -3.92 eV at the \mathbf{K} point, for a correction to the frontier orbital energies of 0.52 eV and 0.14 eV (VBM and CBM, respectively), and a direct $\mathbf{K-K}$ band gap of 1.79 eV. The HSE band structure is displayed in Figure 4.22. Hybridising DFT calculations with exact exchange has the effect of decreasing the band energies across the whole Brillouin zone,

with more of an effect on valence bands. These results are close to previous theoretical predictions using HSE (see Table 4.5), but the band gap value is further from experimental results than is our results from DFT only. Band gap character is unchanged, VBM splitting is much larger than the DFT value at 258 meV at the \mathbf{K} point, and CBM splitting is also increased, at 48 meV.

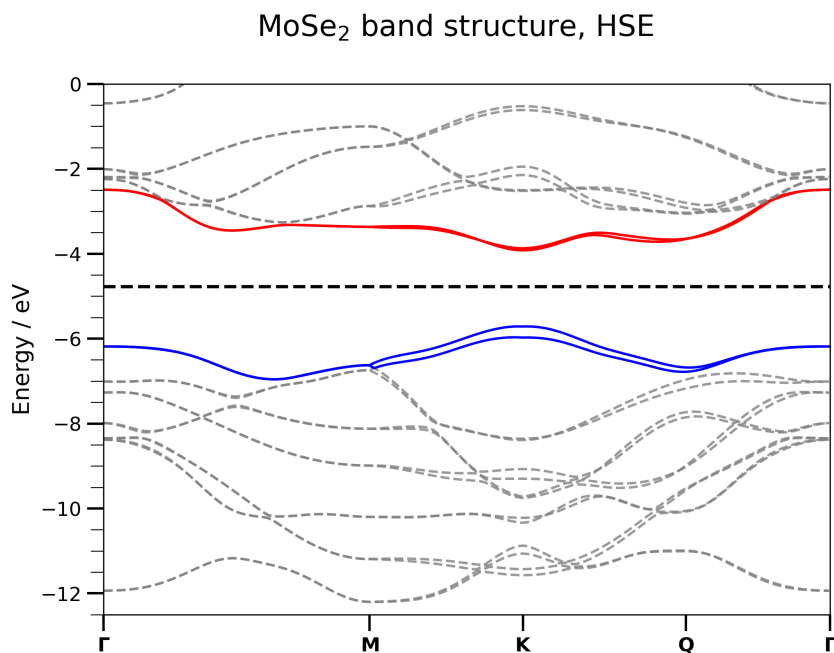


Figure 4.22: The band structure of MoSe₂, calculated using the HSE hybrid functional, with spin-orbit coupling. The Fermi energy is denoted by the dashed black line.

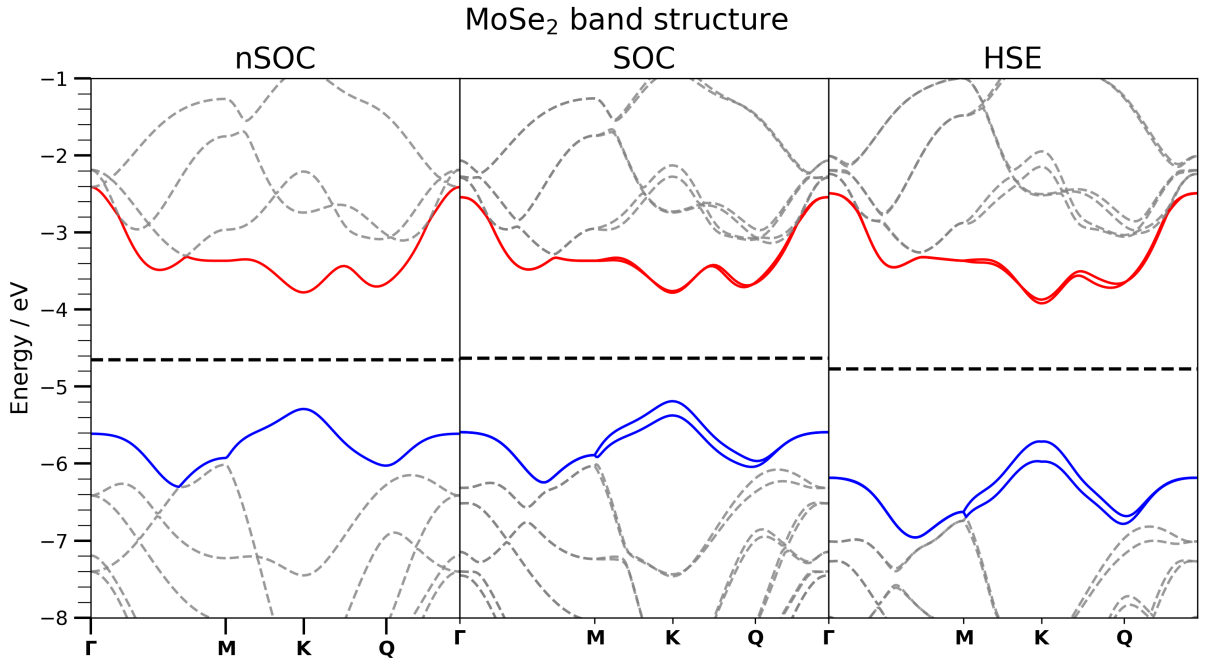


Figure 4.23: A comparison between DFT and HSE band structures of MoSe₂: DFT without considering spin-orbit coupling (left), DFT considering spin-orbit coupling (middle), and HSE considering spin-orbit coupling (right). The Fermi energies are plotted as the dashed black lines, and the vacuum energy is set to 0.

4.4.3 WS₂

DFT

WS₂ again follows suit, with the transition metal d-orbitals, now tungsten's, playing a major role around the Fermi energy, with the chalcogen p-orbitals becoming more important in the valence bands with decreasing energy. We see another direct band gap of 1.86 eV at the **K** critical point, between the VBM of -5.70 eV and the CBM of -3.84 eV. The band gap is similar to previous theoretical work (see Table 4.5), and is an underestimation of experimental results. There is again a **Q**-valley in the lowest conduction band, in keeping with the indirect (Γ -**Q**) to direct band gap transition found between bulk and monolayer WS₂. The band structure and density of states without spin-orbit coupling is displayed in Figure 4.24.

WS₂ band structure and pDOS, nSOC

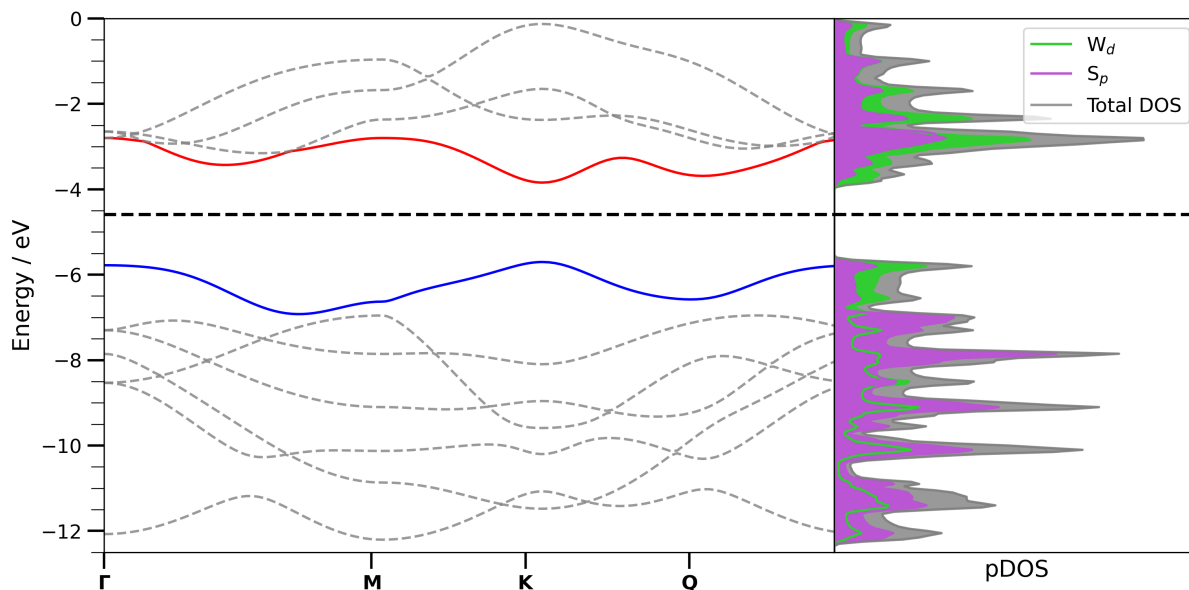


Figure 4.24: The projected density of states and band structure of monolayer WS₂, without considering spin-orbit coupling, using DFT. The Fermi energy is represented by a black dashed line. There are very minor contributions to the density of states from lower energy orbitals within the displayed energy range (not shown).

Our DFT calculations that consider spin-orbit coupling gave a band gap of 1.61 eV, a VBM at the **K** critical point of -5.51 eV and a CBM at the same point of -3.90 eV: a decrease of 0.25 eV, increase of 0.20 eV, and a small decrease of 0.06 eV, respectively, compared to DFT without spin-orbit coupling. Notably, the lowest conduction band at the **Q** point has an energy of -3.88 eV, resulting in an indirect band gap of -1.63 eV, only 23 meV larger than the direct band gap. This comes about from the large spin splitting experienced by the conduction bands around the **Q** point, a feature that was of much lesser magnitude in the molybdenum systems. The spin splitting at the VBM was large, at 426 meV, explaining the magnitude of the decrease in the band gap between DFT results without and with spin-orbit coupling, and a much more modest 32 meV at the CBM, more in keeping with what was seen with the molybdenum systems. The conduction band at the **Q** point, however, experienced splitting of 274 meV, which is an order of magnitude higher than that at the **K** point. The VBM splitting is in keeping with previous DFT literature [133,134], with the small splitting of the CBM and the large splitting of the lowest conduction band at the **Q** point also agreeing with existing DFT

results [134], the latter of which was reported as 0.33 eV. The density of states is, again, not appreciably different from the case without spin-orbit coupling. The density of states and band structure for DFT with spin-orbit coupling of WS₂ is displayed in Figure 4.25.

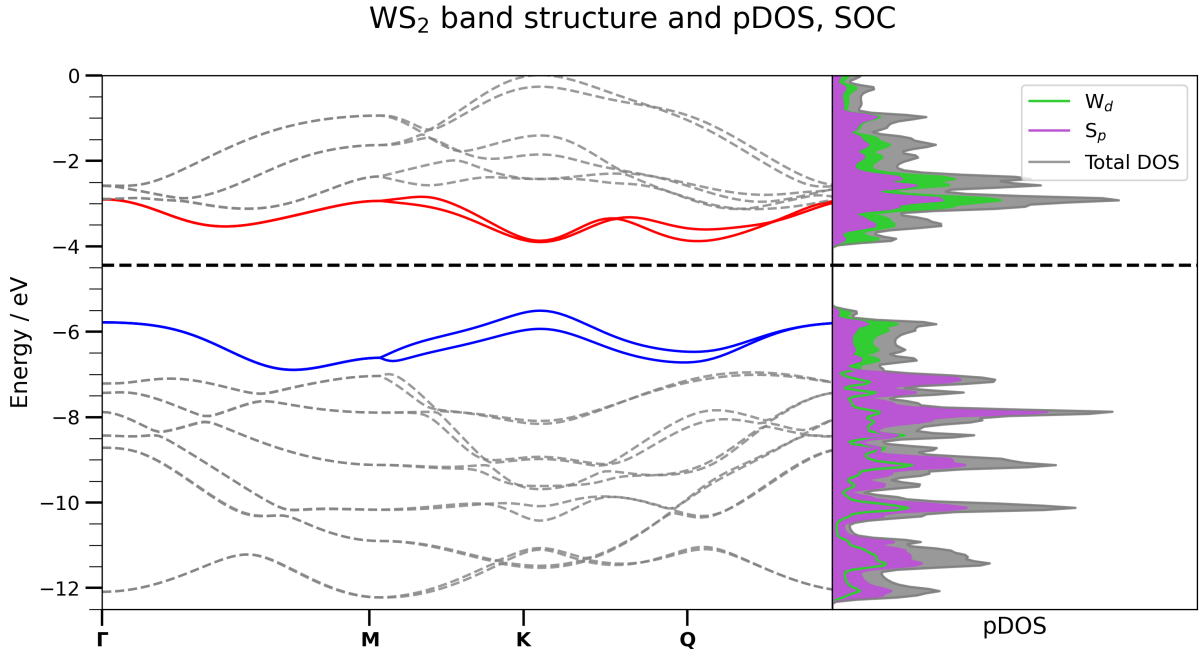


Figure 4.25: The projected density of states and band structure of monolayer WS₂, considering spin-orbit coupling, using DFT. The Fermi energy is represented by a black dashed line. There are very minor contributions to the density of states from lower energy orbitals within the displayed energy range (not shown).

HSE

The band structure calculations using HSE for WS₂, shown in Figure 4.26, report a VBM of -5.85 eV, a CBM of -3.77 eV (both at the **K** point), and so a direct band gap of 2.08 eV. This is in exceptional agreement with photoluminescence investigations (see Table 4.5). The changes in these energies between DFT and HSE (both with spin-orbit coupling) are an increase in the band gap of 0.47 eV, a decrease in the VBM of 0.34 eV, and an increase in the CBM of 0.13 eV: both frontier bands move away from the Fermi energy, opening up the band gap. The lowest conduction band has energy at the **Q** point of -3.65 eV. The spin splitting in the VBM was 496 meV and in the CBM it was only 2 meV. At the **Q** point, however, the splitting in the lowest conduction band was 287 meV, all fairly similar to the values obtained from DFT.

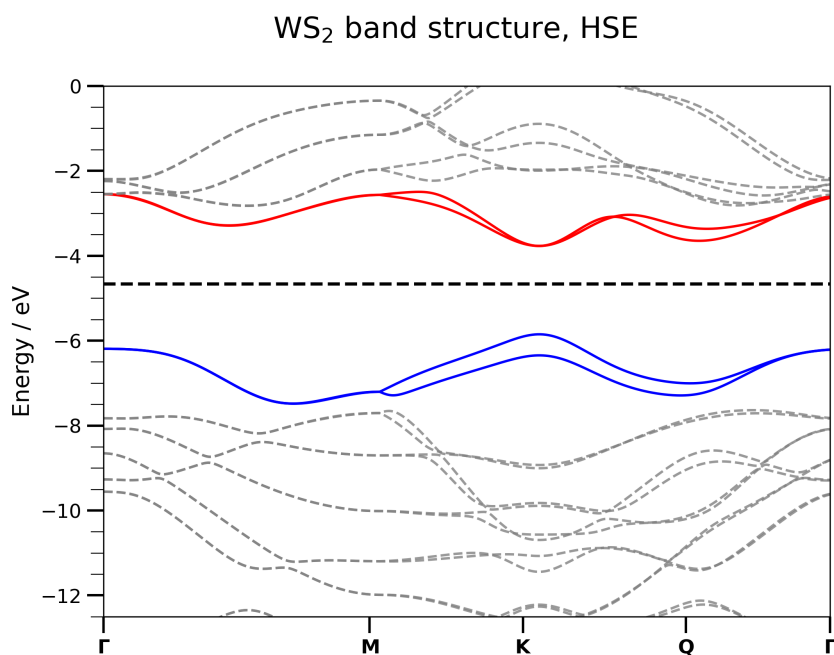


Figure 4.26: The band structure of WS_2 , calculated using the HSE hybrid functional, with spin-orbit coupling. The Fermi energy is denoted by the dashed black line.

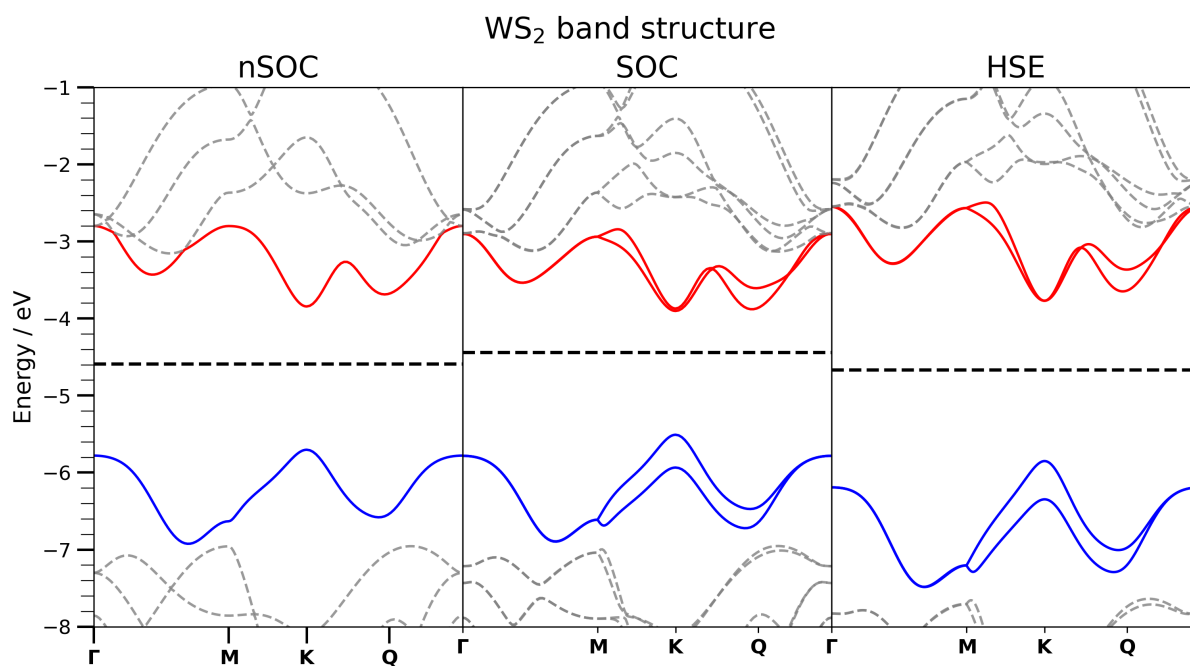


Figure 4.27: A comparison between DFT and HSE band structures of WS_2 : DFT without considering spin-orbit coupling (left), DFT considering spin-orbit coupling (middle), and HSE considering spin-orbit coupling (right). The Fermi energies are plotted as the dashed black lines, and the vacuum energy is set to 0.

4.4.4 WSe₂

DFT

The VBM was found to be -5.06 eV for WSe₂ using DFT without considering spin-orbit coupling, with a CBM of -3.42 eV and a direct band gap at the **K** point of 1.65 eV. This is very similar to photoluminescence results (see Table 4.5), as well as existing theoretical literature. There is a **Q** valley almost as deep as that at **K** in the lowest conduction band, with minimum energy -3.41 eV, only 5 meV higher than that at the **K** point. The proximity in energy of the local minima in the lowest conduction band around the **K** and **Q** points is documented in existing literature [135–137], with at least one experimental investigation using STS implying band gap near-degeneracy [138], and an indirect band gap in monolayer WSe₂, with the **K-Q** gap being 2.12 ± 0.06 eV and the direct gap at **K** being 2.20 ± 0.10 eV, as well as findings of an indirect **K-Q** band gap in monolayer WSe₂ [136, 137].

The density of states (shown in Figure 4.28 alongside the bands structure, without spin-orbit coupling) once again demonstrates the major contribution to the bands nearest the Fermi energy is from the transition metal’s d-orbitals, with increasing contributions from selenium p-orbitals with decreasing energy in the valence bands. As in MoSe₂, the selenium d-orbitals play an insignificant role near the band gap.

WSe₂ band structure and pDOS, nSOC

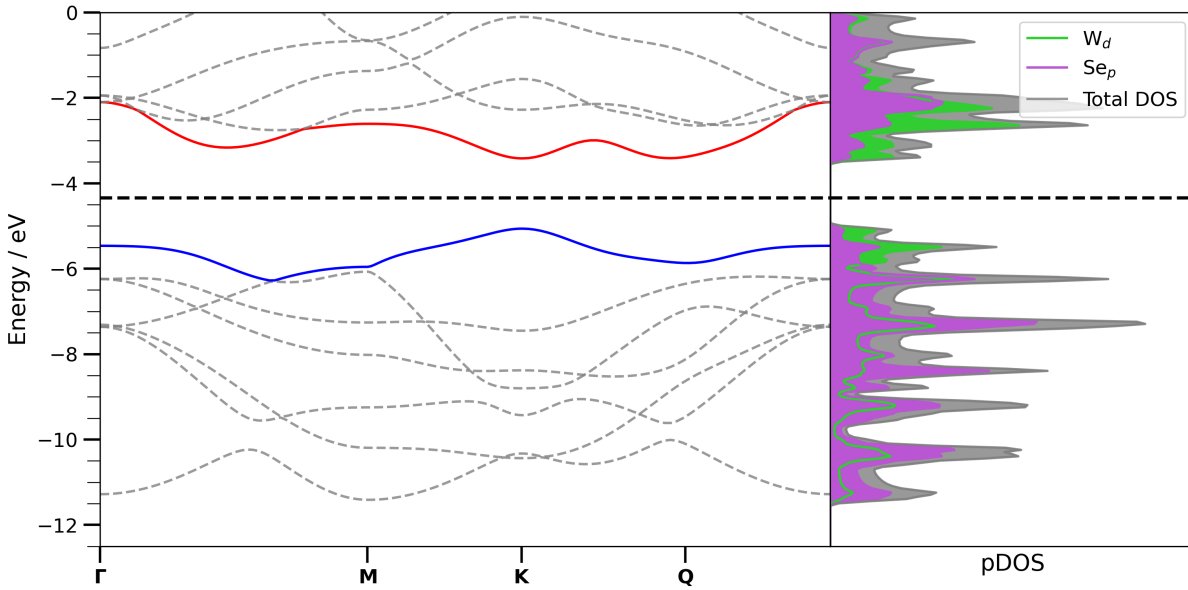


Figure 4.28: The projected density of states and band structure of monolayer WSe₂, without considering spin-orbit coupling, using DFT. The Fermi energy is represented by a black dashed line. There are very minor contributions to the density of states from lower energy orbitals within the displayed energy range (not shown).

Performing DFT calculations with spin-orbit coupling resulted in a VBM at the **K** critical point of -4.82 eV, and a CBM of -3.53 eV, but at the **Q** point: an indirect band gap in monolayer WSe₂. The energy of the lowest conduction band at the **K** point is -3.46 eV, and so the difference in local minima in the lowest conduction band at the **Q** and **K** points is only 66 meV. By considering spin-orbit coupling, the VBM increases by 0.25 eV, and the lowest conduction band energy at the **K** point (the CBM without spin-orbit coupling) increases by 0.04 eV. The band gap differs by 0.35 eV between the two calculations (with and without spin-orbit coupling). The spin splitting in the lowest conduction band at the **Q** point has been reported to be approximately 0.2 eV (via scanning tunnelling spectroscopy) [139], with our result here being in agreement at a CBM splitting of 226 meV. The splitting of the lowest conduction band at the **K** point is only 43 meV and splitting of the VBM is 457 meV, both similar to our DFT results for WS₂, and in keeping with previous PBE results [136]. The density of states is inappreciably different from that without spin-orbit coupling, and is displayed alongside the band structure in Figure 4.29.

WSe₂ band structure and pDOS, SOC

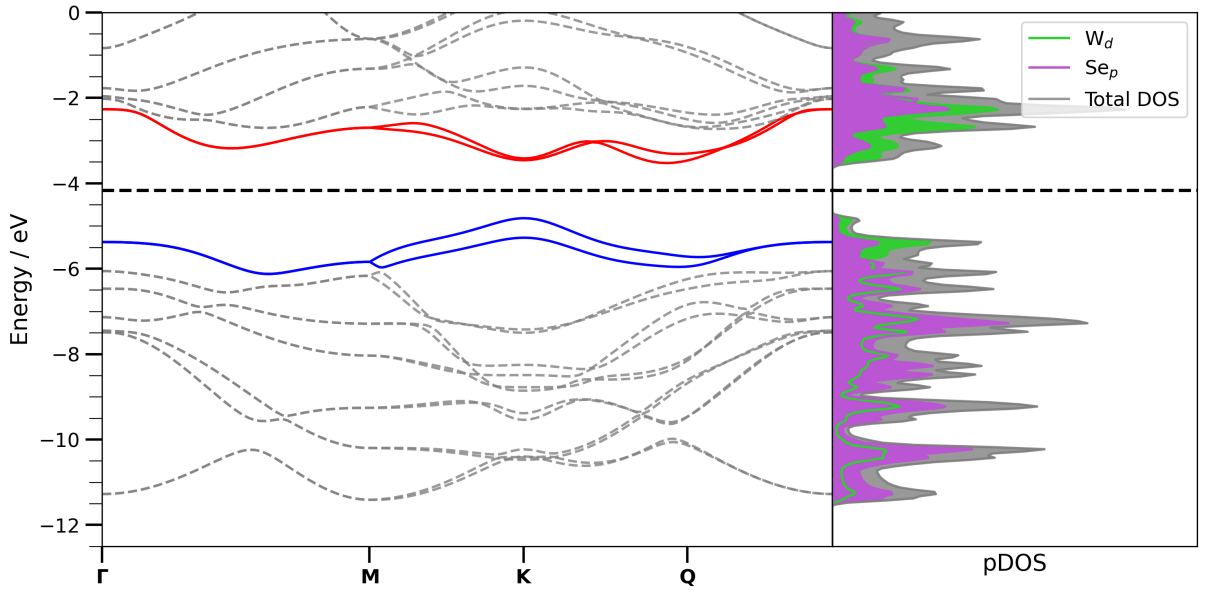


Figure 4.29: The projected density of states and band structure of monolayer WSe₂, considering spin-orbit coupling, using DFT. The Fermi energy is represented by a black dashed line. There are very minor contributions to the density of states from lower energy orbitals within the displayed energy range (not shown).

HSE

HSE calculations provide the band structure displayed in Figure 4.30, where the VBM was -5.29 eV at the **K** critical point, the CBM was -3.49 eV also at **K**, and so the band gap is direct at 1.80 eV. The lowest conduction band **Q** valley is close to that at **K**, with an energy of -3.48 eV: a difference of only 17 meV and behavior observed previously [139]. Band splitting is again small in the lowest conduction band at the **K** point (the CBM by HSE), at 4 meV, and large at the **Q** point, 225 meV. The VBM splitting was found to be 567 meV, in keeping with previously reported valence band maxima splitting using the HSE functional (586 meV) [136]. The band structure as compared to that from DFT is displayed in Figure 4.31, where the correction from hybridisation to that of PBE with spin-orbit coupling is to decrease the VBM by 0.48 eV, increase the CBM by 0.04 eV and move it to the the **K** critical point, recovering the direct band gap gap, for a total effect on the band gap of increasing it by 0.51 eV.

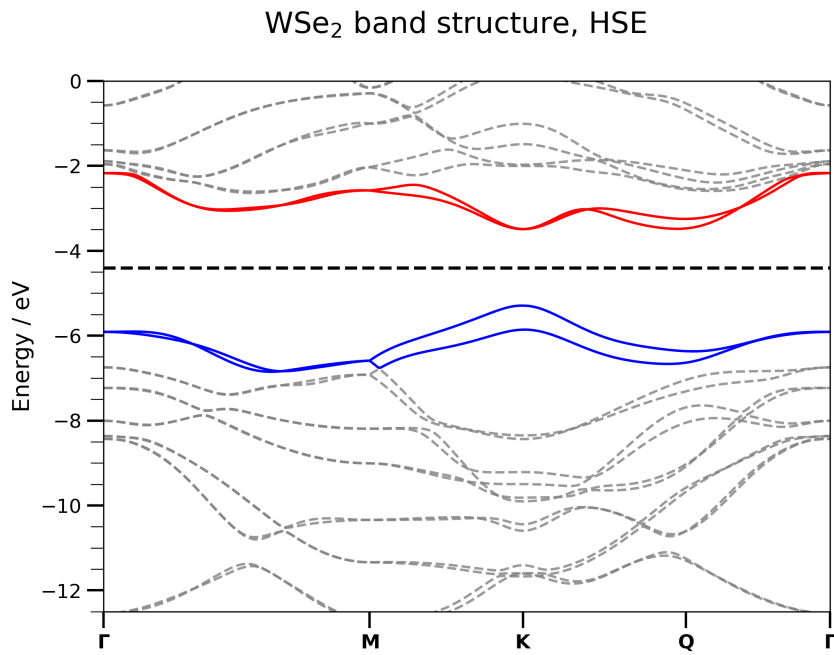


Figure 4.30: The band structure of WSe₂, calculated using the HSE hybrid functional, with spin-orbit coupling. The Fermi energy is denoted by the dashed black line.

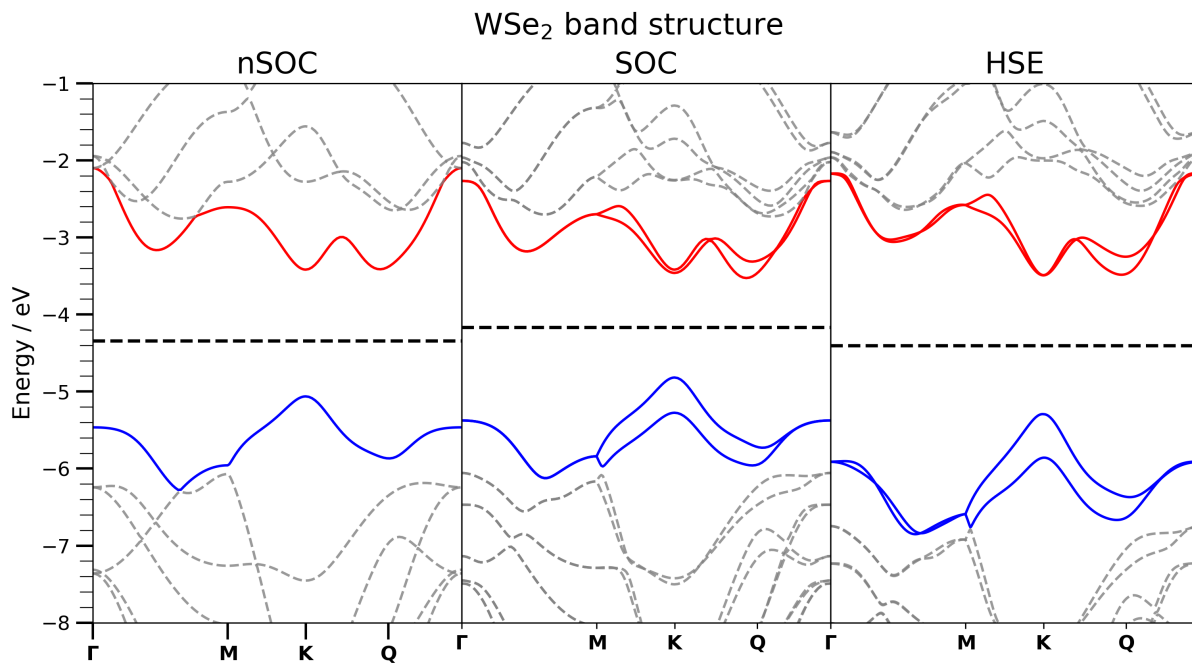


Figure 4.31: A comparison between DFT and HSE band structures of WSe₂: DFT without considering spin-orbit coupling (left), DFT considering spin-orbit coupling (middle), and HSE considering spin-orbit coupling (right). The Fermi energies are plotted as the dashed black lines, and the vacuum energy is set to 0.

4.4.5 Pentacene

Being molecular, pentacene does not inherently have a true band structure: periodicity is required for this. This is the reason for the use of the terms highest occupied molecular orbital (HOMO) and lowest unoccupied molecular orbital (LUMO), in lieu of the similar VBM and CBM that are discussed in the context of the periodic TMDs. We have constructed a repeating system in order to perform our calculations, but intentionally introduced vacuum into the cell in order to maintain isolation. As a result, we do not present the band structure of pentacene: only the frontier orbitals and density of states. This is also the case for pentacene in concentrations consistent with our later supercell approach.

DFT

We performed three sets of calculations for pentacene, each with different cell parameters. We considered isolated pentacene, with a large vacuum region in all directions to prevent interaction between molecules, low concentration pentacene in a cell defined by an underlying TMD substrate mesh of 7×4 molecules, and high concentration pentacene, in a cell defined by a 6×3 molecule substrate. These choices are in keeping with the concentrations considered later in the project, using a supercell approach for the pentacene-TMD heterostructures.

For isolated pentacene, without spin-orbit coupling, we found the HOMO energy to be -4.45 eV and a LUMO of -3.31 eV. This gives a band gap of 1.14 eV. The density of states is displayed in the left panel of Figure 4.32, and we can see that the contributions closest to the Fermi energy are from carbon p-orbitals. Hydrogen s-orbitals have contribution further from the band gap, with more significant contributions at lower energies (not shown). However, there are some permitted hydrogen s-orbital states above the band gap, amongst the highest energy bound states.

Considering spin-orbit coupling results in no change to the frontier orbital energies; a HOMO energy of -4.45 eV and LUMO of -3.31 eV. These values are in agreement with previous theoretical work (see Table 4.5), and are unchanged by the effect of spin-orbit

coupling, resulting in the same band gap of 1.14 eV: spin-orbit coupling has a smaller effect on smaller atoms. The density of states is displayed in the right panel of Figure 4.32, where there is no change from spin-orbit coupling. Our DFT calculations have, however, greatly underestimated the band gap compared to that found from absorption spectra, which predicts a band gap closer to 2 eV (see Table 4.5).

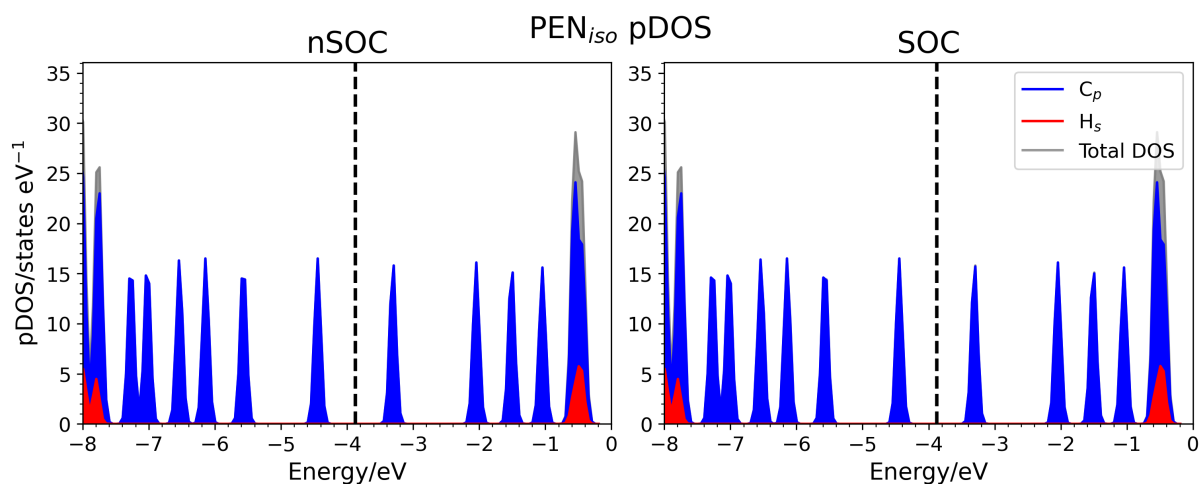


Figure 4.32: The pDOS of isolated pentacene without (left) and with (right) consideration of spin-orbit coupling. There is no significant distinction between the two cases, as expected of small atom systems.

For low concentration (7×4) pentacene, without spin-orbit coupling, the HOMO was -4.55 eV, and the was LUMO -3.41 eV, giving a band gap of 1.14 eV. The density of states shows a significant broadening of the permitted hydrogen-s orbital energies above the band gap, as well as showing the tuning evident from the reported values of the HOMO and LUMO when compared to the isolated system: the positions of both the HOMO and LUMO have decreased by 105 meV. This broadening is expected to result from the Gaussian smearing used in our calculations, rather than true band dispersion arising from molecule-molecule interaction. The effect is observable in the isolated case also, and is the cause for the peaks having appreciable, non-infinitesimal width in the first place. The density of states is displayed in the left panel of Figure 4.33.

Considering spin-orbit coupling for low concentration pentacene, we see frontier orbitals of -4.55 eV and -3.41 eV (HOMO and LUMO, respectively): a negligible change from the case without spin-orbit coupling, for the same band gap of 1.14 eV. Likewise,

the density of states is unchanged (right panel of Figure 4.33).

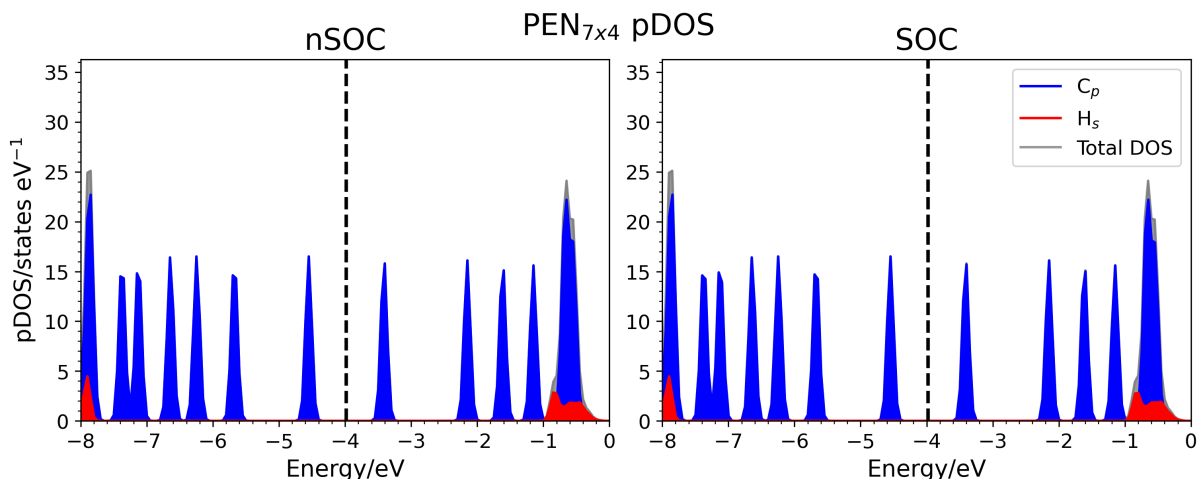


Figure 4.33: The pDOS of low concentration pentacene (one molecule in a 7×4 cell) without (left) and with (right) consideration of spin-orbit coupling. There is no significant distinction between the two cases, as expected of small atom systems.

Finally, we investigated high concentration (6×3) pentacene, and the results without considering spin-orbit coupling are a HOMO energy of -4.68 eV, and a LUMO energy of -3.54 eV, giving a band gap of 1.14 eV. With spin-orbit coupling, these values are instead -4.66 eV and -3.52 eV (HOMO energy and LUMO energy, respectively). These give a band gap of 1.14 eV. The frontier orbital energies have again shifted energetically down by 130 meV and 129 meV (HOMO and LUMO respectively) with further increasing concentration in the case of no spin-orbit coupling, and so the band gap remains approximately the same width. When considering spin-orbit coupling, the shifts in frontier orbital energies are 110 meV and 107 meV (HOMO and LUMO, respectively) instead, for a similarly negligible change in band gap width. The density of states is displayed in Figure 4.34, and reveals no significant difference from that of the low concentration pentacene case, excepting the slight change in energies and further broadening of hydrogen-s orbitals.

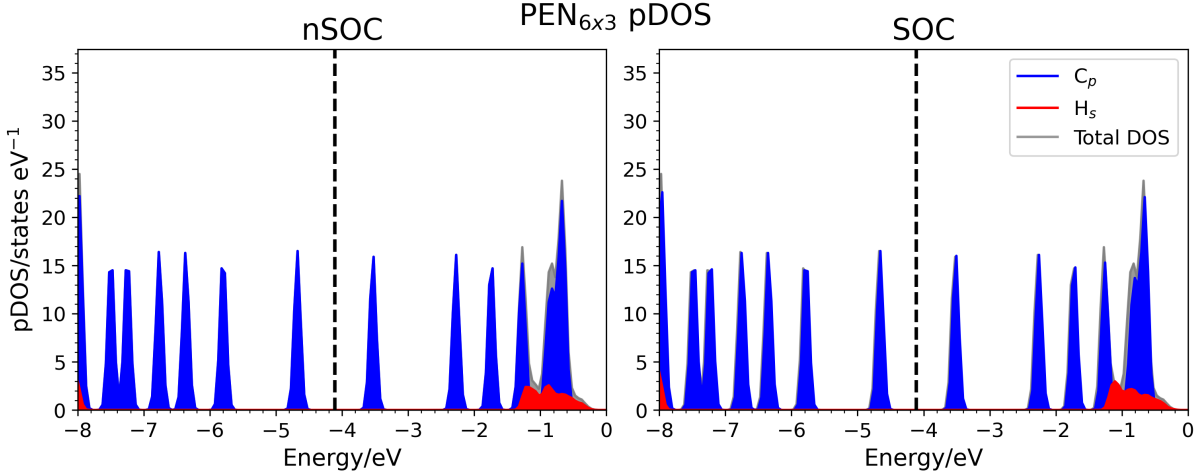


Figure 4.34: The pDOS of high concentration pentacene (one molecule in a 6×3 cell) without (left) and with (right) consideration of spin-orbit coupling. There is no significant distinction between the two cases, as expected of small atom systems.

Table 4.6: The Fermi energy and energy of the HOMO and LUMO for pentacene in different cells.

System	Fermi energy/eV	HOMO/eV	LUMO/eV	E_G /eV
Isolated pentacene				
nSOC	-3.88	-4.46	-3.32	1.14
SOC	-3.88	-4.45	-3.31	1.14
HSE [†]	-3.88	-4.70	-3.09	1.62
Low concentration (7×4 cell) pentacene				
nSOC	-3.98	-4.55	-3.41	1.14
SOC	-3.98	-4.55	-3.41	1.14
HSE	-3.98	-4.80	-3.20	1.60
High concentration (6×3 cell) pentacene				
nSOC	-4.11	-4.68	-3.54	1.14
SOC	-4.09	-4.66	-3.52	1.14
HSE	-4.12	-4.93	-3.35	1.58

[†] Isolated pentacene results for the HSE functional are from the smaller 32 \AA cubic cell.

Comparing low concentration pentacene to well-isolated pentacene, we see that there is no change in the band gap, but it is tuned to a lower energy with increasing concentration. This is demonstrated again by comparing high concentration pentacene to the low concentration results. Going forward with our investigation into heterostructures, this change in energetic position may have effects on the band alignment between layers, as the heterostructures necessarily do not have isolated pentacene. This band gap

modification can be easily appreciated in Table 4.6.

HSE

Due to hardware limitations, we were unable to successfully complete HSE calculations on the isolated pentacene within the cubic supercell of side 48 Å. By reducing the size of the vacuum region by using a cubic supercell of side 32 Å, we were then able to perform the HSE calculation. We also performed DFT calculations with and without spin-orbit coupling to confirm that this smaller cell maintained molecular isolation. As there was only a change in frontier orbital energies of 9 meV between the two (see Figure 2.12 and Table 4.7), we conclude that the smaller cell is sufficient for isolation. For isolated pentacene then, in the smaller 32 Å cubic supercell, the HOMO energy was calculated to be -4.70 eV and the LUMO energy -3.09 eV. This gives a band gap of 1.62 eV. This value is now much improved compared to our DFT results, more closely reflecting experiment (but still an underestimate, see Table 4.5).

For low concentration (7×4 cell) pentacene, the HOMO energy calculated by our HSE calculation was -4.80 eV, and a LUMO of -3.20 eV, for a band gap of 1.60 eV. Compared with the isolated pentacene HSE results, this represents a band gap tuning of 20 meV due to a reduction in HOMO and LUMO energies of 0.09 eV and 0.11 eV, respectively.

For high concentration (6×3 cell) pentacene, the HOMO energy was -4.93 eV and a LUMO of -3.35 eV. This results in a band gap of 1.58 eV. The band gap tuning between the two concentrations of interacting pentacene i.e. pentacene in 6×3 and 7×4 cells was 15 meV.

We again see that the effect of increasing concentration is a decrease in the energetic position of the band gap i.e. reduction in the frontier orbital energies. We saw a larger shift in frontier orbital position between low and high concentration regimes with the HSE functional than we did DFT only: a shift of approximately 0.15 eV in frontier orbital energies between pentacene in the 7×4 and 6×3 cells with HSE, but a smaller shift going from isolated to 7×4 pentacene. The total shift from isolated to 6×3 regimes is very similar, at approximately 0.22 eV for the HOMO energies, 0.26 eV for the LUMO

energy with HSE, and 0.21 eV (with spin-orbit coupling) or 0.23 eV (without spin-orbit coupling) for the LUMO energies with DFT. Overall, both frontier orbitals are decreased in energy with increasing concentration, the HOMO dropping from -4.70 eV to -4.93 eV between isolated and high concentration regimes, and the LUMO likewise drops from -3.09 eV to -3.35 eV, as displayed in Table 4.6. This changes the energetic position of the band gap relative to the TMD band gaps, potentially changing the band alignment between the two, and the band gap structure of any resulting heterostructures. This is discussed in the following subsection.

4.4.6 Band alignment

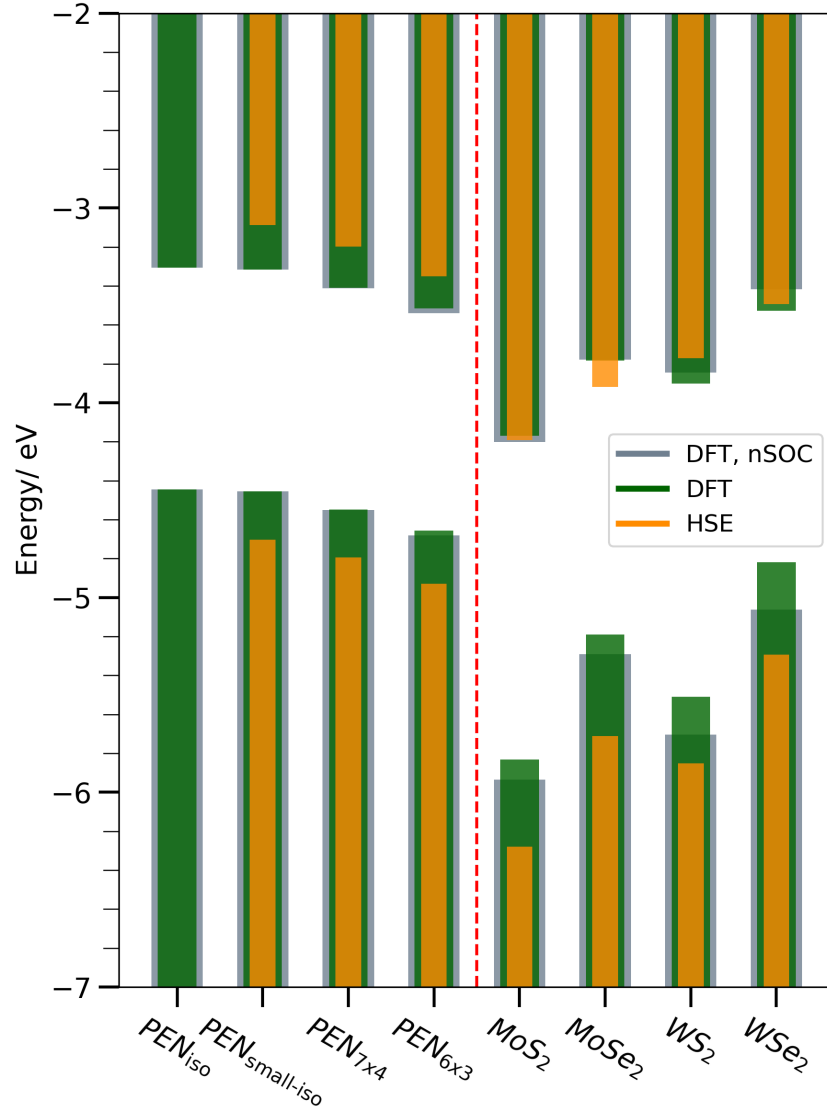


Figure 4.35: Band alignment between the three concentrations of pentacene (well isolated, pentacene in a 7×4 supercell, and pentacene in a 6×3 supercell; there are two results for well isolated pentacene due to the cost of hybrid calculations, as discussed in subsection 4.4.5) and the four considered monolayer TMDs. The vertical dashed red line separates the pentacene results from those of the TMDs. Displayed values are from calculations involving pentacene or the TMD only, not heterostructures.

The preferred band alignment of materials in heterostructure for photovoltaics, photodetectors and field effect transistors is Type II (see Section 2.3), as this alignment prevents immediate exciton recombination by allowing for confinement in different materials. Type I heterostructures may find use in devices that desire fast recombination times, such as LEDs, and Type III may find use in devices that operate on tunnelling

effects.

Table 4.7: A summary of frontier orbital energies (HOMOs and LUMOs, or VBMs and CBMs) as calculated with the three levels of theory for the monolayer TMDs and pentacene across different concentrations: isolated, isolated in a smaller cubic cell of side length 32 Å, low concentration and high concentration (PEN_{iso}, PEN_{small-iso}, PEN_{7×4} and PEN_{6×3}, respectively). The three levels of theory are DFT (PBE) without and with spin-orbit coupling (nSOC and SOC, respectively), and HSE.)

	VBM or HOMO/eV	CBM or LUMO/eV
PBE-nSOC		
PEN _{iso}	-4.45	-3.31
PEN _{small-iso}	-4.46	-3.32
PEN _{7×4}	-4.55	-3.41
PEN _{6×3}	-4.68	-3.54
MoS ₂	-5.94	-4.20
MoSe ₂	-5.29	-3.78
WS ₂	-5.70	-3.84
WSe ₂	-5.06	-3.42
PBE-SOC		
PEN _{iso}	-4.45	-3.31
PEN _{small-iso}	-4.46	-3.32
PEN _{7×4}	-4.55	-3.41
PEN _{6×3}	-4.66	-3.52
MoS ₂	-5.83	-4.17
MoSe ₂	-5.19	-3.78
WS ₂	-5.51	-3.90
WSe ₂	-4.82	-3.53
HSE		
PEN _{small-iso}	-4.70	-3.09
PEN _{7×4}	-4.80	-3.20
PEN _{6×3}	-4.93	-3.35
MoS ₂	-6.28	-4.19
MoSe ₂	-5.71	-3.92
WS ₂	-5.85	-3.77
WSe ₂	-5.29	-3.49

Figure 4.35 displays the band alignment between different concentrations of pentacene and monolayer TMDs, and Table 4.7 contains the relevant frontier orbital energies. We found that pentacene’s band gap only changes slightly with changing concentration, but its frontier orbitals decrease in energy. Isolated pentacene forms a Type II band gap with all four TMDs, regardless of which level of theory we used. This was maintained as we increased pentacene concentration, with the exception of non-isolated pentacene and WSe₂ when we used DFT without spin-orbit coupling. In this case, the CBM of WSe₂ was

-3.42 eV and the LUMO of pentacene in the 6×3 cell was -3.52 eV: a difference of 98 meV, where WSe₂'s CBM was the higher of the two, resulting in a Type I band alignment i.e. the band gap of WSe₂ totally encompasses that of high concentration pentacene. This effect was almost apparent with pentacene in the 7×4 cell, where pentacene's LUMO in this case was -3.41 eV: a difference of only 6 meV. This is, however, not the case for our DFT calculations with spin-orbit coupling or HSE calculations, which both predict a Type II heterojunction for both concentrations. There may be some band gap tuning from molecule-substrate interactions that are as of yet unaccounted for, as thus far the comparison is between independent systems, not the systems in heterostructure.

Chapter 5

Low concentration pentacene heterostructures

Publication relating to this chapter [140]:

E. Black, P. Kratzer, and J. M. Morbec, "Interaction between pentacene molecules and monolayer transition metal dichalcogenides," *Physical Chemistry Chemical Physics*, vol. 25, no. 43, pp. 29444-29450, 2023.

With information on the electronic structure of the TMDs and pentacene in the concentrations it will experience in heterostructure, we proceeded to construct heterostructures from the materials (see Figure 1.2). In this chapter, we only looked at the low concentration pentacene regime; high concentration pentacene was investigated and compared later. Additionally, we did not perform calculations with spin-orbit coupling, nor did we perform any hybrid calculations. The latter would be far too expensive, and was only performed on the smaller systems of the preceding chapter. We showed previously that spin-orbit coupling splits the VBM in TMDs, and has little effect on the CBM or pentacene. We discuss the consequences of only performing calculations without spin-orbit coupling in Section 5.2, but in summary we would only expect an

important effect in the PEN/WSe₂ heterostructure. Using optimized geometry, we extended the TMD cells into supercells that were 7 TMD molecular units by 4 TMD molecular units, remaining monolayer. To each of these supercells we then added a single flat-lying molecule of pentacene, with geometry defined by the isolated pentacene’s optimization, orientated length-ways with the long axis of the underlying TMD substrate, a layer separation of approximately $d = 3 \text{ \AA}$, and the middle ring of pentacene located over one of five adsorption sites (see Figure 5.1). Pentacene concentrations resulting from this made up the low concentration regime, with one pentacene molecule per 244 \AA^2 for PEN/MoS₂ and PEN/WS₂, 264 \AA^2 for PEN/MoSe₂, and 263 \AA^2 for PEN/WSe₂. The supercells were put through `relax` calculations, allowing the pentacene to find its heterostructure geometry, as well as increase or decrease its separation from the TMD layers, move along the surface of the TMD substrate layers, and rotate. Each TMD, therefore, had five heterostructures constructed with flat-lying pentacene: one for each adsorption site. Initially, we considered additional heterostructures where pentacene lay vertically on the substrate (Figure 5.2) when performing preliminary calculations on 6×3 TMD supercells. We found that these were highly energetically unfavorable, in keeping with findings from existing experimental [141] and theoretical [142] literature, where pentacene molecules are flat-lying on monolayer MoS₂, and so vertically adsorbed pentacene was not investigated in the low concentration pentacene (7×4 TMD supercell) regime.

Each adsorption site is defined by the position of the central ring of pentacene relative to the underlying substrate. The adsorption sites are displayed in Figure 5.1, and are as follows:

- Bridge-A: the central ring of pentacene lies over a transition metal-chalcogen bond that is perpendicular to the long axis of the substrate plane, Figure 5.1a
- Bridge-B: the central ring of pentacene lies over a transition metal-chalcogen bond that is not perpendicular to the long axis of the substrate plane, Figure 5.1b
- Hollow: the central ring of pentacene is over the gap created by the hexagonal

structure of the monolayer, Figure 5.1c

- Top-TM: the central ring of pentacene lies over a transition metal atom, Figure 5.1d
- Top-Ch: the central ring of pentacene lies over a chalcogen atom, Figure 5.1e

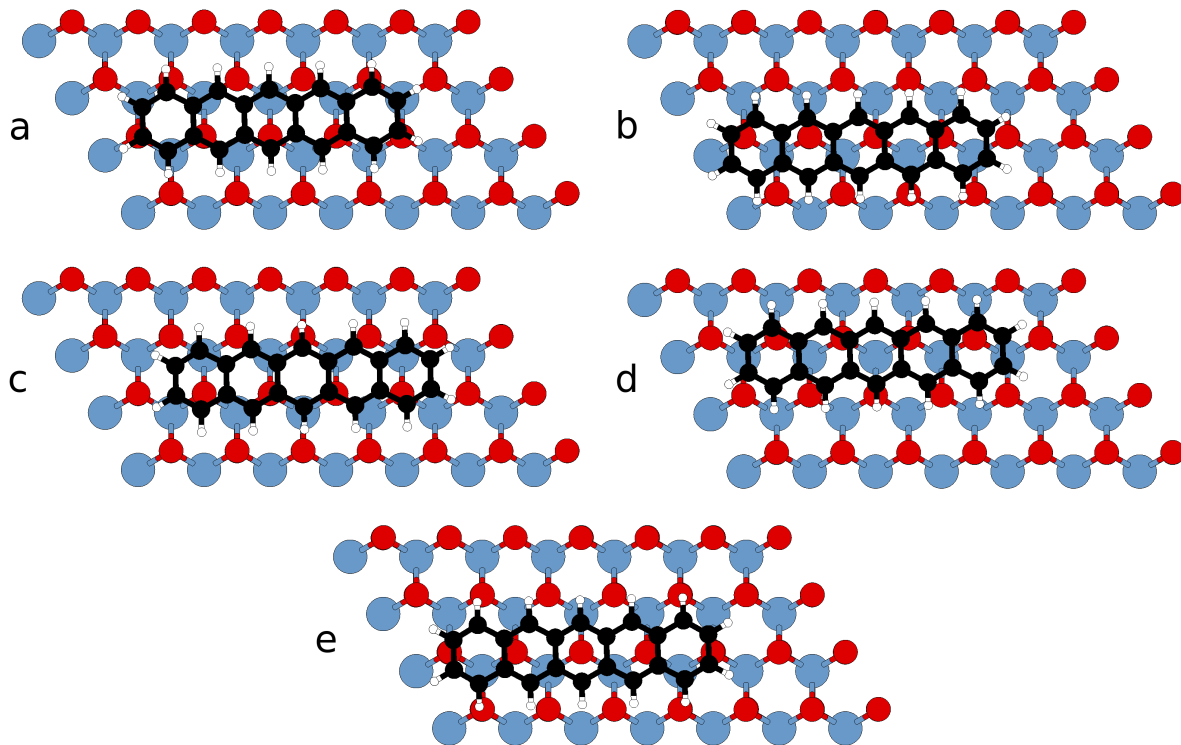


Figure 5.1: Top-down views of the heterostructure supercells, showing pentacene’s adsorption sites on a 7×4 TMD substrate. (a) the Bridge-A site, (b) the Bridge-B site, (c) the Hollow site, (d) the Top-TM site, and (e) the Top-Ch site. Pentacene’s carbon atoms and hydrogen atoms are black and white, respectively, with transition metals in blue and chalcogens in red.

The computational details of heterostructure calculations differ from those of the materials out of heterostructure. We use the energy cut-offs determined by the respective TMD, as these values were larger for the TMDs than for pentacene in the previous chapter. The \mathbf{k} -point mesh used for the single molecular unit cells would result in significant computational cost if applied to the much larger heterostructures, and so a mesh of $3 \times 6 \times 1$ was employed in cases of PEN/TMD heterostructures. This approximately maintains the density of sampling of the supercell between x- and y-directions. Other considerations, such as the functional and pseudopotentials were the same. For the high

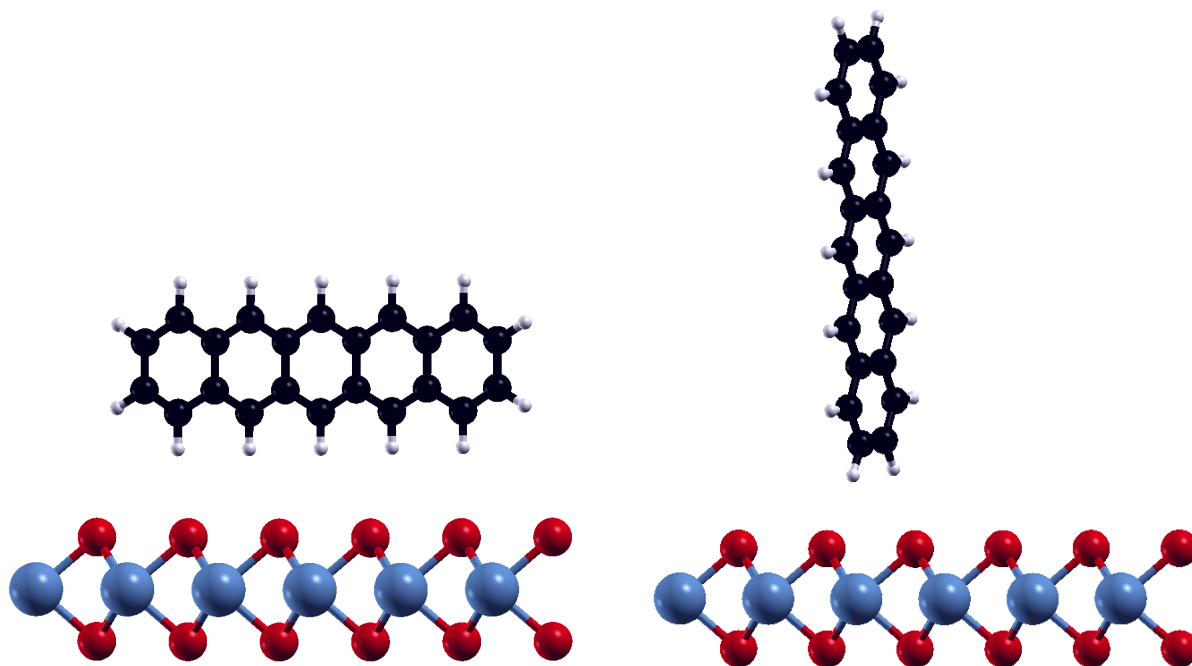


Figure 5.2: Side views of pentacene adsorbed vertically on to a TMD substrate. These adsorption schemes were investigated in preliminary calculations using a 6×3 TMD supercell, and were highly energetically unfavorable, and so were not included in our analysis of low concentration pentacene adsorption.

molecular concentration and rotated molecule heterostructures in the following chapter, we use the same parameters as here.

5.1 The heterostructures

Starting with structural information from previously optimized geometry for the materials, we created our heterostructures and performed `relax` calculations in order to find the optimized heterostructure geometry. Following this, the minimum molecule-molecule distance for pentacene molecules across periodic boundary conditions was approximately 6.2 Å for both sulfur systems (pentacene-MoS₂ and pentacene-WS₂ heterostructures), and approximately 6.5 Å for selenium systems (pentacene-MoSe₂ and pentacene-WSe₂ heterostructures). From these `relax` calculations, we were able to compare the total system energies of different binding sites of the same substrate. The binding site with the lowest total energy was the most favorable one, and had its electronic properties investigated further. The comparison of total energy of different binding sites is equivalent to a comparison of adsorption energy between heterostructures with the same TMD, as the materials are the same between compared systems. We found that for all TMDs the most favorable pentacene binding site was Top-Ch i.e. where the middle ring of pentacene lies over a sulfur atom or a selenium atom, depending on the TMD. The difference in total energy of each adsorption site from the total energy of the most favorable adsorption site for that TMD substrate is given in Table 5.1.

Table 5.1: The difference in total energy, in eV, between adsorption sites of pentacene-TMD heterostructures with low concentration pentacene and their most favorable adsorption site.

Heterostructure	Bridge-A	Bridge-B	Hollow	Top-TM	Top-Ch
PEN/MoS ₂	0.079	0.003	0.049	0.046	0.000
PEN/MoSe ₂	0.072	0.002	0.038	0.035	0.000
PEN/WS ₂	0.083	0.002	0.053	0.055	0.000
PEN/WSe ₂	0.075	0.006	0.024	0.056	0.000

For all substrates, the second most favorable site was Bridge-B, with a difference of only 2 to 6 meV. This implies significant mobility between Top-Ch and Bridge-B sites, with the least favorable site of Bridge-A still only being 72 to 83 meV less favorable than Top-Ch; this indicated high molecular mobility in all heterostructures, which has been demonstrated experimentally in MoS₂ [141]. The more favorable adsorption sites

of Top-Ch and Bridge-B have a large number of pentacene’s carbon atoms located over hollow sites, instead of over the top of chalcogen atoms as is more frequently the case for the other sites. This reduces steric repulsion between carbons and TMD chalcogens, increasing energetic favorability, as we found.

Layer separation, that between the center of mass of pentacene and the average z -position of the top-most plane of chalcogen atoms, was found to be the smallest for the most favorable TOP-Ch adsorption site, for all TMDs. This was 3.309 Å for MoS₂, 3.400 Å for MoSe₂, 3.297 Å for WS₂, and 3.378 Å for WSe₂. We saw that the selenium systems have their pentacene bind at a larger distance than for sulfur systems, explained by the larger van der Waals radius of the selenium atom (1.90 Å [143]) compared to a sulfur atom (1.73 Å [143]), a result observed in TMD heterostructures with other organic molecules [144]. Differences in layer separation between different adsorption sites for the same TMD substrate can again be explained by steric repulsion between carbons and chalcogens. The layer separations for each heterostructure are displayed in Table 5.2.

Table 5.2: Layer separation, d , in Å, of 7×4 PEN/TMD heterostructures, defined as the distance between the center of mass of pentacene and the average z -coordinate of the top-most chalcogens of the underlying TMD substrate.

Heterostructure	Bridge-A	Bridge-B	Hollow	Top-TM	Top-Ch
PEN/MoS ₂	3.397	3.334	3.395	3.392	3.309
PEN/MoSe ₂	3.475	3.415	3.463	3.459	3.400
PEN/WS ₂	3.389	3.328	3.374	3.375	3.297
PEN/WSe ₂	3.468	3.410	3.447	3.480	3.378

The pentacene molecule remains flat-lying for all systems, with no significant twisting and very minor deformation. With the exception of layer separation, pentacene remained at approximately the same position as it began before the `relax` calculations i.e. the initial atomic positions used for adsorption sites were all stable positions.

Further investigation was performed on only the most favorable binding sites, which is Top-Ch for all TMD substrates. From this point forward, remaining reference and discussion about the heterostructures within this chapter are understood to be those heterostructures with the Top-Ch adsorption site, unless otherwise explicitly outlined.

Comparing the geometry of the relaxed heterostructures to that of the relaxed

materials out of heterostructure, we observed some small deformation in the pentacene molecule. There was a mean atomic deviation from the molecular plane of isolated pentacene’s atoms of 0.49 mÅ, with the largest atomic deviation being 1.02 mÅ (see Section 4.3). For pentacene within the PEN/MoS₂ heterostructure, we observed a mean atomic deviation of 40 mÅ, with a maximum atomic deviation of 111 mÅ, occurring at the middle of the molecule. Pentacene within PEN/MoSe₂ had a mean atomic deviation of 33 mÅ with a maximum of 89 mÅ, also at the middle of the molecule. For the PEN/WS₂ heterostructure, we observed a very similar change in structure, with a mean atomic deviation from the molecular plane of 42 mÅ, and a maximum atomic deviation of 122 mÅ, again at the middle of the molecule. The PEN/WSe₂ heterostructure did not behave differently, with a mean atomic deviation of 33 mÅ and a maximum of 92 mÅ, again occurring at the middle of the pentacene molecule. Carbon-carbon bond lengths in pentacene changed by approximately 0.1% with the formation of heterostructure, regardless of the substrate, and the substrate itself experienced similar bond length changes of less than 0.1% as a result of the addition of pentacene. The bond lengths between transition metal atoms and adjacent chalcogen atoms become position-dependent with the addition of pentacene, with those bonds directly below the pentacene molecule undergoing the largest contraction (3.7 mÅ, 4.5 mÅ, 4.3 mÅ, and 6.4 mÅ for heterostructures with MoS₂, MoSe₂, WS₂ and WSe₂, respectively) and the bonds nearby these shortened bonds (but no longer directly underneath the pentacene molecule) undergoing some lengthening in order to maintain a fixed supercell volume: the largest bond lengthening observed was 4.7 mÅ, 3.3 mÅ, 4.1 mÅ, and 1.6 mÅ for heterostructures with MoS₂, MoSe₂, WS₂ and WSe₂, respectively.

We additionally examined the contribution to the adsorption energy (E_{ads}), by comparing E_{ads} of the pentacene-TMD heterostructure calculated with the PBE functional and Grimme’s DFT-D3 van der Waals correction to E_{ads} of the same heterostructure calculated with only the PBE functional (i.e. without contributions from van der Waals forces). E_{ads} is defined as the difference between the total energy of the heterostructure ($E_{\text{PEN/TMD}}$) and the combined total energies of the relaxed geometries of isolated

pentacene ($E_{\text{PEN}}^{\text{iso-relax}}$) and the 7×4 substrate layer without pentacene ($E_{\text{TMD}}^{\text{relax}}$):

$$E_{\text{ads}} = E_{\text{PEN/TMD}} - E_{\text{TMD}}^{\text{relax}} - E_{\text{PEN}}^{\text{iso-relax}}. \quad (5.1)$$

The adsorption energies of the favorable adsorption sites for each TMD heterostructure (all Top-Ch) are displayed in Table 5.3, alongside the layer separation. We can see that the overwhelming contribution to the adsorption energies is vdW interaction: E_{ads} are reduced by an order of magnitude with the absence of van der Waals contribution, as well as observe a greater layer separation, measured in the usual way, without van der Waals forces. The effect of van der Waals interactions on layer separation is to decrease it by approximately 0.65 Å for molybdenum systems, and by approximately 0.75 Å for tungsten systems.

Table 5.3: E_{ads} and layer separation, d , of the 7×4 heterostructures with pentacene in the Top-Ch adsorption site calculated with and without consideration of van der Waals interactions.

Heterostructure	PBE + vdW		PBE only	
	E_{ads}/eV	$d/\text{Å}$	E_{ads}/eV	$d/\text{Å}$
PEN/MoS ₂	-1.389	3.309	-0.100	3.988
PEN/MoSe ₂	-1.424	3.400	-0.101	4.020
PEN/WS ₂	-1.434	3.297	-0.097	4.049
PEN/WSe ₂	-1.458	3.378	-0.099	4.147

In a similar manner, we also investigated the contributions to the adsorption energy from molecule-molecule ($E_{\text{PEN}}^{\text{int}}$) and molecule-substrate ($E_{\text{PEN}}^{\text{TMD}}$) interactions, and molecule and substrate deformation effects ($E_{\text{PEN}}^{\text{def}}$ and $E_{\text{TMD}}^{\text{def}}$, respectively). These contributions were calculated by considering pentacene and the TMD substrate in an environment that eliminates other contributions, and comparing the resultant total energies to those from environments that include only the particular contribution of interest.

Molecule-molecule interactions are those between a pentacene molecule and other pentacene molecules from supercells across the periodic boundary, and so was calculated as the difference between the total energy of pentacene in its adsorbed geometry (that from `relax` calculations of the heterostructure), but isolated from the substrate and

other pentacene molecules by placing it in a large cubic cell of lateral dimensions 48 Å, $E_{\text{PEN}}^{\text{iso-adsgeom}}$, and the total energy of pentacene in its adsorbed geometry in the heterostructure supercell, but without the substrate, $E_{\text{PEN}}^{\text{scell-adsgeom}}$:

$$E_{\text{PEN}}^{\text{int}} = E_{\text{PEN}}^{\text{scell-adsgeom}} - E_{\text{PEN}}^{\text{iso-adsgeom}} . \quad (5.2)$$

Molecule-substrate interactions are those between a pentacene molecule and the underlying substrate, calculated as the difference between the total energy of the whole heterostructure, $E_{\text{PEN/TMD}}$, and the combined total energies of the TMD and pentacene, both in their adsorbed geometry and heterostructure supercell, but each without the other material ($E_{\text{TMD}}^{\text{adsgeom}}$ and the same $E_{\text{PEN}}^{\text{scell-adsgeom}}$ as above, respectively):

$$E_{\text{PEN}}^{\text{TMD}} = E_{\text{PEN/TMD}} - E_{\text{TMD}}^{\text{adsgeom}} - E_{\text{PEN}}^{\text{scell-adsgeom}} . \quad (5.3)$$

Deformation effects are those caused by changes in geometry from formation of the heterostructure, and so for pentacene this is the difference in total energy of isolated pentacene in its relaxed geometry, $E_{\text{PEN}}^{\text{iso-relax}}$, and isolated pentacene in its adsorbed geometry from the heterostructure. For the TMDs, the deformation energy is the difference in total energies between the TMD in its adsorbed geometry, but without pentacene, and the TMD in its geometry without pentacene ($E_{\text{TMD}}^{\text{relax}}$):

$$E_{\text{PEN}}^{\text{def}} = E_{\text{PEN}}^{\text{iso-adsgeom}} - E_{\text{PEN}}^{\text{iso-relax}} \quad (5.4)$$

$$E_{\text{TMD}}^{\text{def}} = E_{\text{TMD}}^{\text{adsgeom}} - E_{\text{TMD}}^{\text{relax}} . \quad (5.5)$$

The results of these calculations are given in Table 5.4, where we can see that the overwhelming majority of contribution comes from molecule-substrate interaction, which is to be expected as this is the contribution that is defined by the van der Waals interaction between the materials. Molecule-substrate interaction is of the order of 1 meV, and deformation energies are also small, in keeping with our observation that there was only a small change between adsorbed and isolated geometries.

Table 5.4: Contributions to the adsorption energy of 7×4 heterostructures in their favorable adsorption site from molecule-molecule, molecule-substrate, molecule deformation and substrate deformation effects, in eV. Molecule-substrate interaction is consistently the largest contribution across all systems.

	PEN/MoS ₂	PEN/MoSe ₂	PEN/WS ₂	PEN/WSe ₂
molecule-molecule interaction	-0.004	-0.003	-0.004	-0.003
molecule-substrate interaction	-1.402	-1.423	-1.340	-1.452
molecule deformation	0.005	-0.007	-0.003	-0.007
substrate deformation	0.012	0.008	-0.088	0.004

5.2 Electronic properties

5.2.1 Density of states

We also investigated the electronic properties of our heterostructures with pentacene in the Top-Ch adsorption site. We calculated the density of states of the heterostructures, the results of which are displayed in Figure 5.3. We found that in all cases the HOMO of pentacene is located within the band gap of the TMD substrate, and is closer to the TMD's VBM in the selenide systems. Using the density of states calculation results, the differences between pentacene's HOMO and the TMD's VBM were calculated to be 1.10 eV for PEN/MoS₂, 0.55 eV for PEN/MoSe₂, 0.95 eV for PEN/WS₂ and 0.30 eV for PEN/WSe₂. As the frontier orbital energies were taken from density of states calculations instead of bands calculations, which were performed with an energy bin of 0.05 eV, there is a loss of precision compared to previous discussions of frontier orbitals.

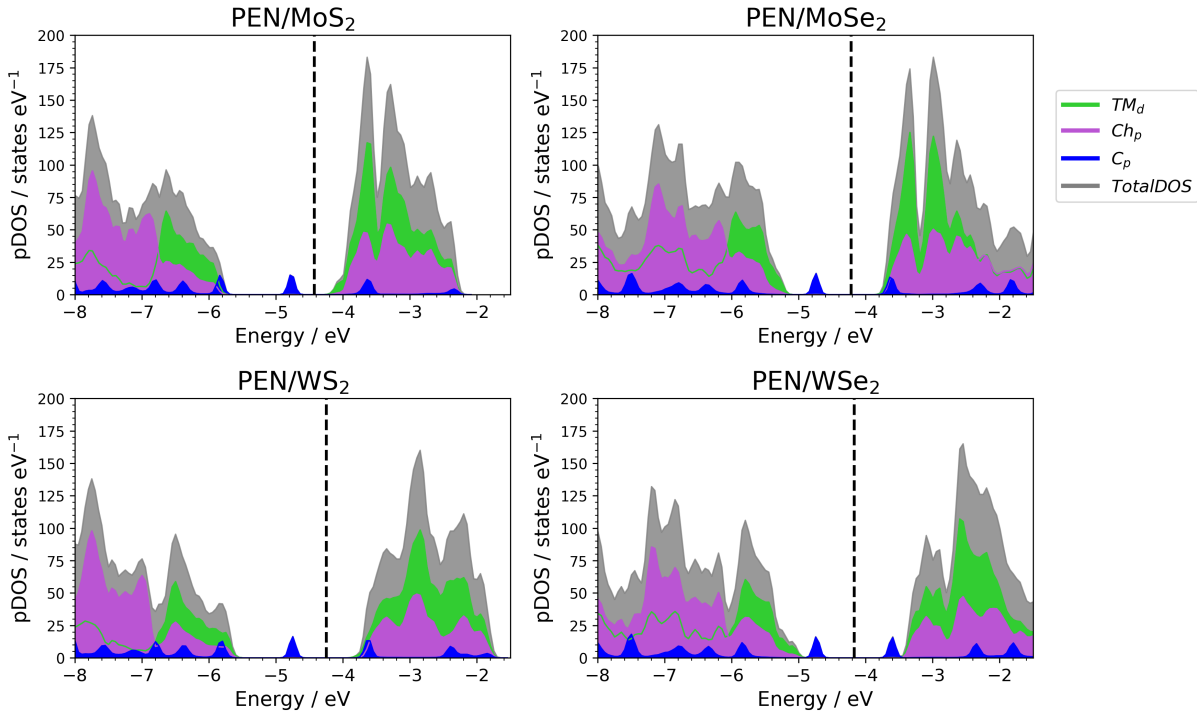


Figure 5.3: The density of states of 7×4 PEN/TMD heterostructures, with the Fermi energy given by the vertical back dashed line.

We notice also that pentacene's LUMO is close to the TMD's CBM in all cases except PEN/MoS₂, where there is a difference of 0.4 eV, providing a robust type-II band

alignment. Also forming a type-II heterojunction are PEN/MoSe₂ and PEN/WS₂, with differences between the CBM and LUMO of 0.05 eV and 0.10 eV, respectively. The PEN/WSe₂ heterostructure, however, possesses a type-I heterojunction, with the TMD’s band gap straddling the pentacene’s. The frontier orbital energies and their comparisons are displayed in Table 5.5, where it can be seen that the LUMO-CBM value for PEN/WSe₂ is negative (at -0.25 eV) i.e. the LUMO is lower than the CBM, and the band alignment is of straddling type.

Table 5.5: Frontier orbital energies and their difference, in eV, of 7×4 PEN/TMD heterostructures. All heterostructures except PEN/WSe₂ form type-II heterojunctions. The values presented here are from density of states calculations, and so have a precision only of 0.05 eV. Previous frontier orbital energies have been from materials not in heterostructure, and so **bands** calculations were performed for this purpose.

Heterostructure	PEN		TMD		Δ	
	HOMO	LUMO	VBM	CBM	HOMO-VBM	LUMO-CBM
PEN/MoS ₂	-4.70	-3.80	-5.80	-4.20	1.10	0.40
PEN/MoSe ₂	-4.65	-3.75	-5.20	-3.80	0.55	0.05
PEN/WS ₂	-4.65	-3.75	-5.60	-3.85	0.95	0.10
PEN/WSe ₂	-4.65	-3.70	-4.95	-3.45	0.30	-0.25

Previously, we determined that the band alignment between pentacene and WSe₂ outside of heterostructure is of type-II. As such, we investigated the effect on the density of states of molecule-molecule and molecule-substrate interactions for PEN/WSe₂. We did so by calculating the density of states of pentacene within a cell of size defined by the PEN/WSe₂ heterostructure (which would suffer from molecule-molecule interactions but not molecule-substrate interactions), and comparing the results to the density of states of the pentacene in the heterostructure (which undergoes molecule-molecule and molecule-substrate interactions) and also well-isolated pentacene (which undergoes the effects of neither interaction). The extracted frontier orbitals from **scf** calculations are given in Table 5.6, and a comparison of the density of states is displayed in Figure 5.4. Importantly, we are only able to use the **scf** results for the frontier orbitals of pentacene within the PEN/WSe₂ heterostructure because it forms a type-I heterojunction: we can only extract the whole system’s frontier orbitals. With the other heterostructures we would instead be extracting the TMD’s CBM, not pentacene’s LUMO, which would give different values

(although we expect the same pattern, as seen in the accompanying Figure 5.4).

Table 5.6: HOMO and LUMO positions of pentacene in a well-isolated environment (PEN_{iso}), in a 7×4 supercell without a substrate ($\text{PEN}_{7 \times 4}$), and in the PEN/WSe_2 heterostructure ($\text{PEN}_{\text{PEN}/\text{WSe}_2}$). Values are in eV, and are extracted from scf calculations as in Chapter 4, resulting in higher precision.

System	HOMO	LUMO
PEN_{iso}	-4.446	-3.307
$\text{PEN}_{7 \times 4}$	-4.551	-3.412
$\text{PEN}_{\text{PEN}/\text{WSe}_2}$	-4.752	-3.662

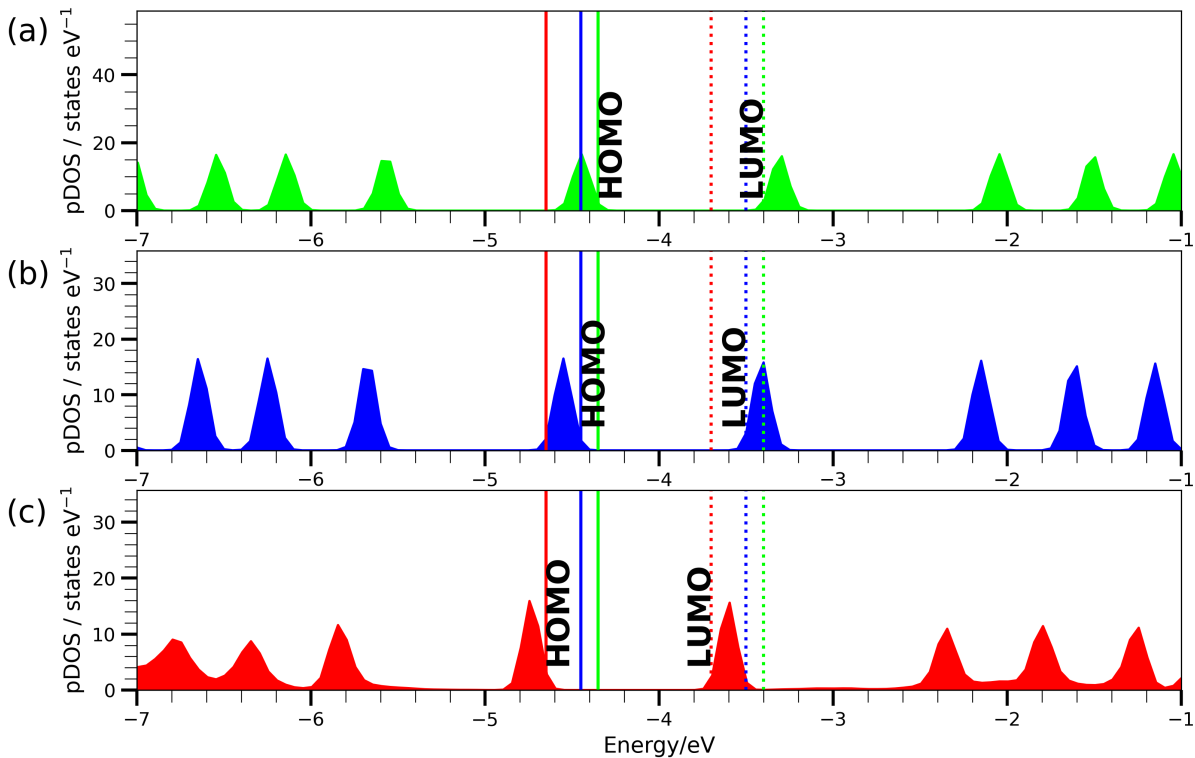


Figure 5.4: The total density of states of pentacene in three different environments with their HOMO and LUMO energies labelled and marked on all three subplots with solid and dashed colored lines, respectively: (a) well-isolated pentacene in green, (b) pentacene in a cell defined by the 7×4 PEN/WSe_2 heterostructure, but without the TMD, in blue, and (c) pentacene in the PEN/WSe_2 heterostructure in red. It is clear that the frontier orbitals decrease in energy with both an increase in concentration and adsorption.

We can see from Table 5.6 that there is decrease in both the HOMO and LUMO energies of 105 meV from bringing the pentacene molecules closer together, but without the substrate; this is therefore the effect of molecule-molecule interaction. Comparing to values from pentacene in the PEN/WSe_2 heterostructure, we see a further decrease in the HOMO and LUMO energies of 201 eV and 250 meV, respectively; this is the contribution

of molecule-substrate interactions. The contribution from molecule-molecule interaction is almost enough to result in a change from type-II to type-I band alignment, resulting in only a 6 meV difference between pentacene’s LUMO and the TMD’s CBM, with molecule-substrate interactions enhancing this effect and comfortably shifting the band alignment to type-I. It is important to note, however, that there exist small differences in calculated frontier orbital energies between `scf` and density of states calculations, in part because of the energy step size for density of states calculations being larger, as well as smearing effects to form a continuum. As such, we additionally compared the frontier orbital energies of pentacene as determined by density of states calculations, and see the same broad pattern: both molecule-molecule and molecule-substrate interactions act to decrease the HOMO and LUMO energies, by approximately 0.10 eV and then 0.20 eV each in combination. These values are displayed in Table 5.7.

Table 5.7: HOMO and LUMO positions of pentacene in a well-isolated environment (PEN_{iso}), in a 7×4 supercell without a substrate ($\text{PEN}_{7 \times 4}$), and in the PEN/WSe_2 heterostructure ($\text{PEN}_{\text{PEN}/\text{WSe}_2}$). Values are in eV, and are extracted from density of states calculations.

System	HOMO	LUMO
PEN_{iso}	-4.35	-3.40
$\text{PEN}_{7 \times 4}$	-4.45	-3.50
$\text{PEN}_{\text{PEN}/\text{WSe}_2}$	-4.65	-3.70

Band alignment was determined in Chapter 4 by frontier orbital energies from `scf` and `bands` calculations, but the density of states calculation results can differ slightly from these, so we present in Figure 5.5a the density of states of well-isolated pentacene superimposed on that of monolayer WSe_2 out of heterostructure; we see clearly that pentacene’s HOMO sits in the WSe_2 band gap, while pentacene’s LUMO is above the TMD’s CBM, showing a type-II band alignment for the materials out of heterostructure. Figure 5.5b displays the density of states of pentacene in a 7×4 supercell, superimposed on the same WSe_2 density of states. We can see there that pentacene’s LUMO appears to be almost degenerate with the TMD’s CBM: indeed the CBM of WSe_2 out of heterostructure was calculated as -3.45 eV from these density of states calculations, while the previously discussed LUMO was -3.50 eV. As mentioned above, the more

precise `scf` results predicted a Type-II band alignment between pentacene in the 7×4 supercell and WSe_2 , but only by 6 meV.

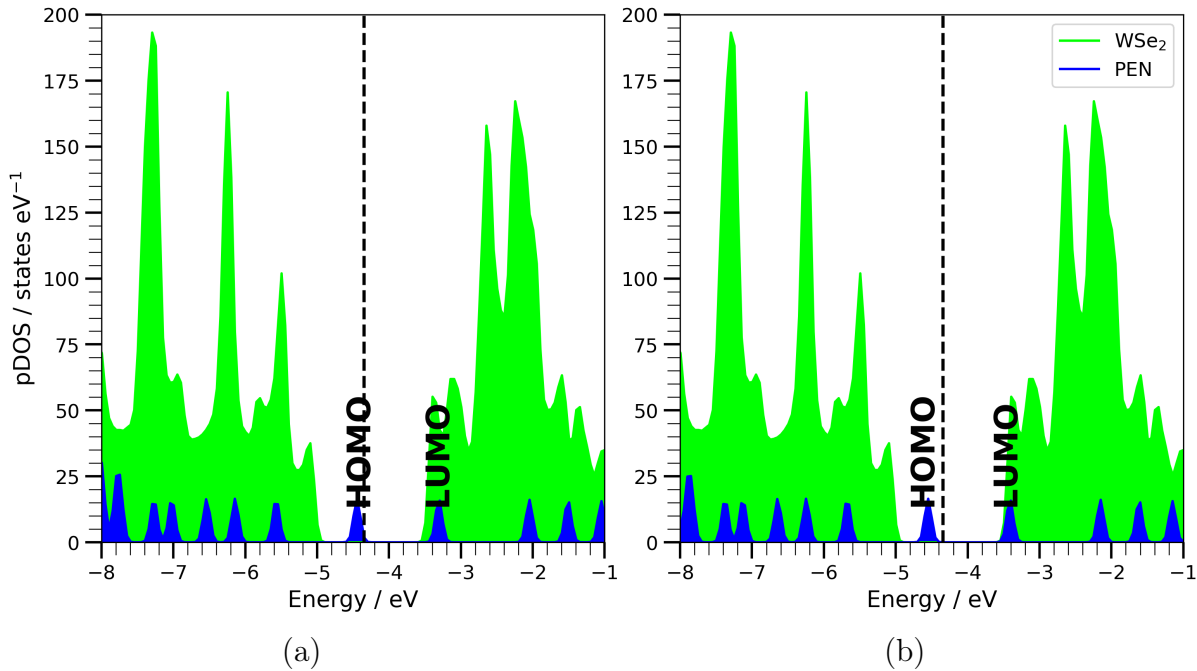


Figure 5.5: (a) The density of states of well-isolated pentacene (blue) and that of WSe_2 (green), presented to demonstrate type-II band alignment of the materials outside of heterostructure when using frontier orbital energies from density of states calculations, for comparison with those from the heterostructure. Pentacene’s HOMO and LUMO, as well as the TMD’s VBM and CBM, are labelled. (b) The density of states of pentacene in a 7×4 supercell (blue) and that of WSe_2 , demonstrating that pentacene’s LUMO and the TMD’s CBM are effectively overlapping. The Fermi energy of the TMD is shown as dashed black lines.

In the other three heterostructures, similar shifts were observed in pentacene’s HOMO and LUMO. We cannot provide the comparison from `scf` calculations due to the issue mentioned above: extracting pentacene’s LUMO is not feasible, as the frontier orbital above the band gap of the heterostructure is the TMD’s CBM. Therefore, we can only make the comparison from density of states data. Such a comparison can be made between the HOMO and LUMO values for well-isolated pentacene and pentacene in the 7×4 supercell without a substrate from Table 5.7, and those for pentacene in heterostructure from Table 5.5. We see that forming a heterostructure with MoS_2 decreases pentacene’s HOMO by 0.25 eV and the LUMO by 0.30 eV. For MoSe_2 and WS_2 , these effects are slightly smaller, both decreasing by 0.20 eV and 0.25 eV for the HOMO and LUMO energies, respectively. This is the same decrease in HOMO as with WSe_2 , but a slightly

large decrease in LUMO than for WSe₂. With the smallest effect occurring in the PEN/WSe₂ heterostructure, it is only because of how close the band alignment was between isolated systems that we see the type-I band alignment in this heterostructure.

We did not perform these calculations with spin-orbit coupling, the justification being that pentacene is broadly unaffected by spin-orbit coupling, and the effect on the TMDs was already described. In the case of molybdenum systems, spin-orbit coupling increases the VBM by approximately 0.1 eV, while pentacene’s HOMO is more than 0.5 eV above the VBM, so we expect no effect on band alignment here. The CBM of MoS₂ is similarly safely removed from pentacene’s LUMO. While the CBM of MoSe₂ is fairly close to pentacene’s LUMO in heterostructure, the effect of spin-orbit coupling on the CBM of MoSe₂ is only 4 meV, and so there is no expected effect on band alignment for PEN/MoSe₂ either. The tungsten systems are more affected by spin-orbit coupling, however. WS₂ has a VBM that is increased by 0.195 eV by spin-orbit coupling, but has almost a 1 eV difference between the TMD’s VBM and pentacene’s HOMO in heterostructure, so the effect is not felt by the band alignment. Similarly, the CBM and LUMO are separated by a large enough energy that spin-orbit coupling is not expected to change the type of heterojunction. The PEN/WSe₂ heterostructure, however, may be affected by spin-orbit coupling. The VBM is increased by 0.245 eV, almost enough to bring the VBM past pentacene’s HOMO. The CBM is increased by 0.044 eV, worsening the effect from molecule-molecule and molecule-substrate interactions, to further push pentacene’s LUMO below the CBM of WSe₂. In this case, the effect of spin-orbit may be to recover the type-II band alignment, but with a reversed direction i.e. it is pentacene’s LUMO, and not HOMO, that could sit in the TMD band gap.

5.2.2 Charge transfer and work function

We then examined the charge transfer of the heterostructures by calculating the charge density (`scf` calculations do this, and we used a post-processing script, `pp.x`, to extract plottable data) of pentacene in the 7×4 supercell and the TMD without pentacene, then subtracting these from the charge density of the complete heterostructure. This

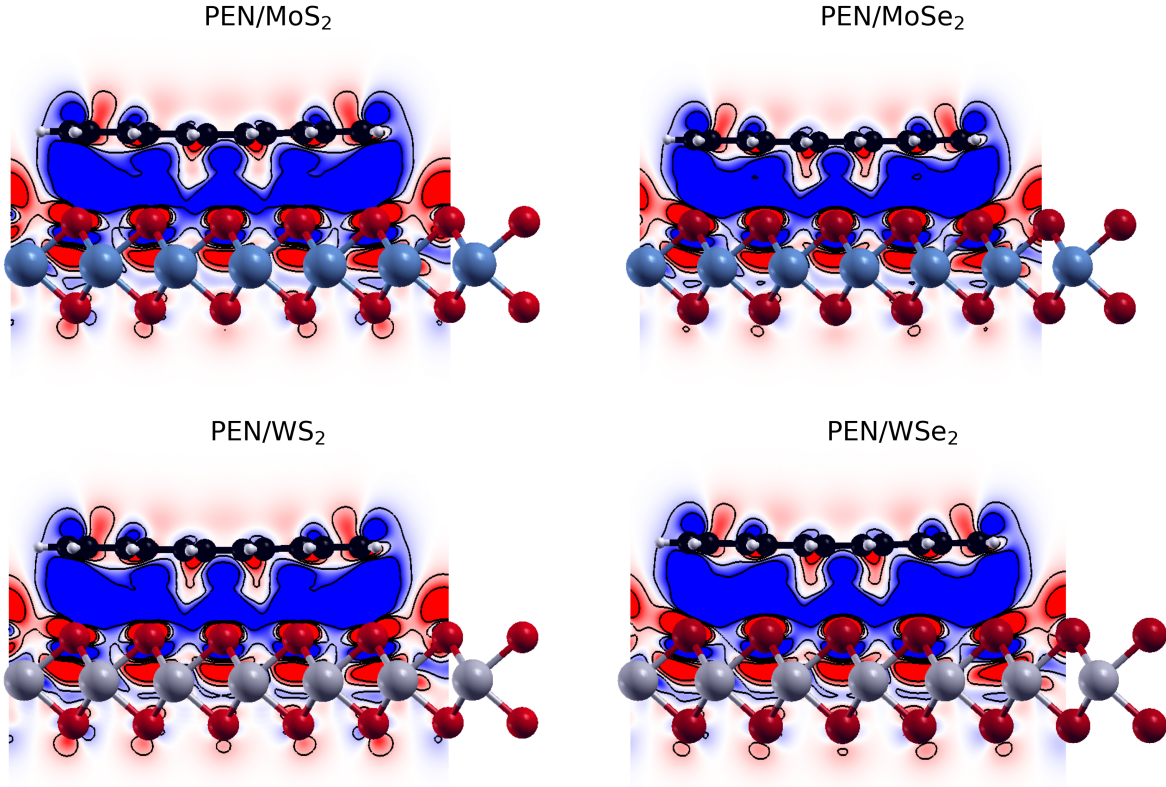


Figure 5.6: The difference in charge density between the 7×4 PEN/TMD heterostructures and the materials in a heterostructure cell without their counterpart, plotted on a plane perpendicular to the plane of pentacene and that of the TMD monolayer, aligned along the long axis of pentacene. Regions of charge accumulation and depletion are displayed in red and blue, respectively.

is displayed in Figure 5.6, where we see accumulation of charge around the top-most chalcogen atoms and the pentacene molecule, with a depletion of charge in the region between layers; this is typical of Pauli repulsion.

In order to quantitatively assess the change in charge distribution we integrated the difference in charge density along the x-y plane to obtain the plane-averaged differential charge density, $\Delta\rho(z)$:

$$\Delta\rho(z) = \int_{xy} \Delta\rho(x, y, z) \delta x \delta y , \quad (5.6)$$

where the integral is over the entire x-y plane and $\Delta\rho(x, y, z)$ is the differential charge density at the point (x, y, z) ,

$$\Delta\rho(x, y, z) = \rho_{\text{PEN/TMD}}(x, y, z) - \rho_{\text{PEN}}(x, y, z) - \rho_{\text{TMD}}(x, y, z) . \quad (5.7)$$

The cumulative charge difference through the heterostructure, $\Delta Q(z)$, can then be calculated as

$$\Delta Q(z) = \int_{-\infty}^z \Delta \rho(z') \delta z' . \quad (5.8)$$

The results of this analysis are displayed in Figure 5.7, where we see that the change in charge distribution between pentacene and the TMDs is between 0.011 and 0.013 electrons per supercell (the maximum cumulative charge difference), corresponding to between 4×10^{-4} and 5×10^{-4} electrons per chalcogen atom (of the top plane of chalcogen atoms), or between 3.6×10^{11} and 4.7×10^{11} electrons per square centimeter.

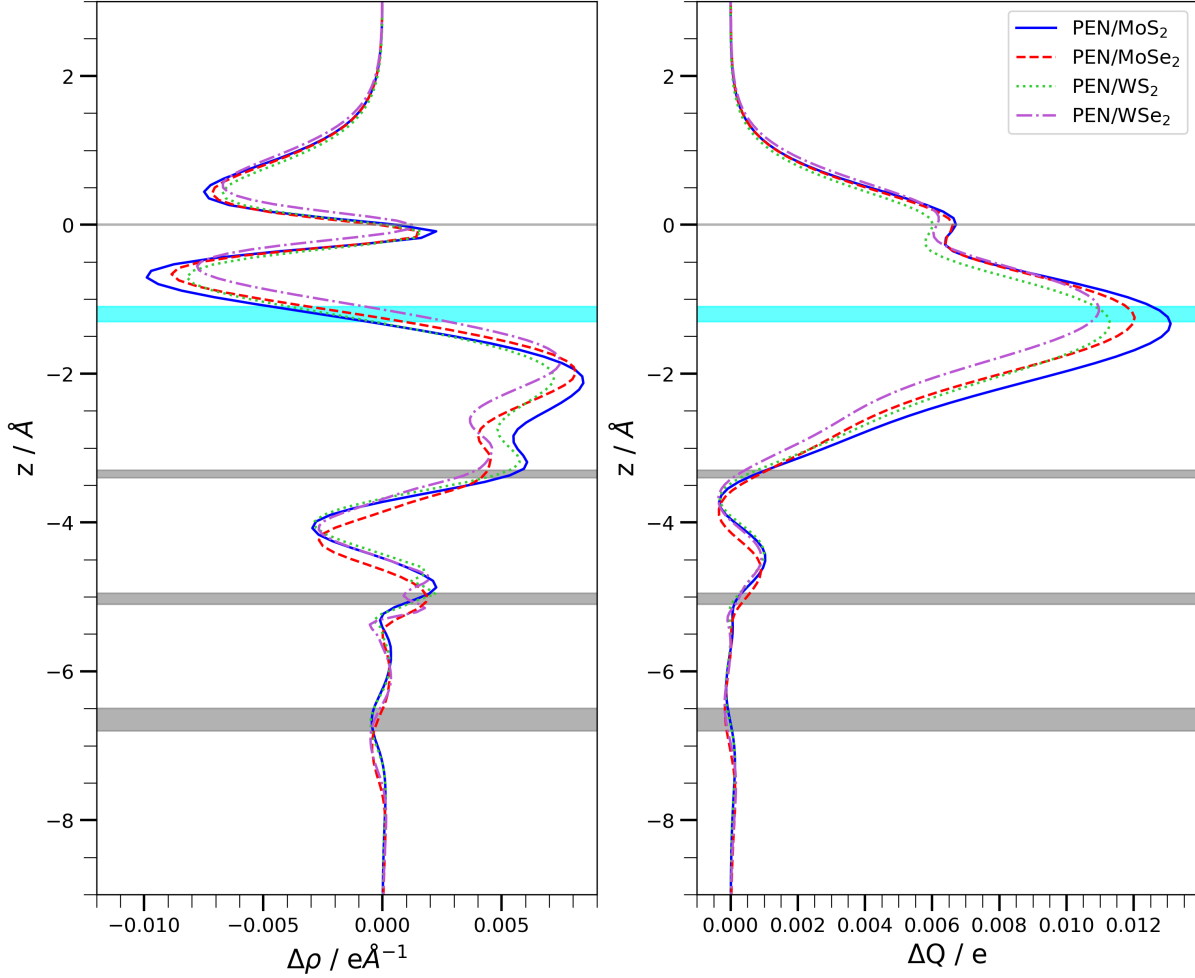


Figure 5.7: (a) The plane-averaged differential charge density, $\Delta\rho(z)$ (Equation 5.6) of the four 7×4 PEN/TMD heterostructures. (b) The cumulative change in charge distribution, $\Delta Q(z)$ (Equation 5.8) of the four PEN/TMD heterostructures. The horizontal gray bands represent the position of heterostructure atomic planes. In order from the top of the image: pentacene, the top chalcogen plane of the TMD substrate, the transition metal plane of the TMD substrate, and the bottom chalcogen plane of the TMD substrate. The bands representing the transition metal and chalcogen positions are wider than that for the molecular plane due to variation between TMDs. The cyan band represents the position of the heterostructure interface.

For the PEN/MoS₂ heterostructure, we calculated a change in charge distribution of 0.013 electrons per supercell, which is low compared to previous results on similar systems (although the same order of magnitude); flat-lying pentacene adsorbed on a hexagonal MoS₂ monolayer with a substrate size of 7×4 molecules per supercell (i.e. the same concentration we investigated here) has had charge transfer calculated as 0.066 electrons per supercell [142]. However, this value is from calculations using the HSE06 functional and Grimme’s DFT-D2 van der Waals correction [51]: an improvement in exchange-

correlation functional, but a less accurate treatment of van der Waals interactions. Additionally, this work did not appear to consider adsorption site favorability, and used a site between what we have called Top-TM and hollow. These differences in methodology may account for the differences in results. This work also investigated the equivalent heterostructure with 1T-MoS₂, finding the charge transfer to be approximately 7 times greater than the hexagonal monolayer case. There are charge transfer values of between 0.10 and 0.013 electrons per sulfur atom reported for Ti₃C₃ and Ti₃C₂F₂, respectively, adsorbed on 1T-MoS₂ [145], much larger than what we have found for pentacene on 1H monolayers, and there is a dearth in the literature for the other TMDs with adsorbed pentacene in a manner similar to the structures we investigated here.

We have not distinguished between cases of charge polarization resulting from heterostructure formation and true charge transfer i.e. we did not adequately define the geometry of the interfacial surface between heterostructure layers, nor ‘track’ the origin and final destination of individual electrons by e.g. partitioning our charge density grid into Bader volumes and assessing the energetic cost of adding and removing electrons to the volumes. We cannot, therefore, consider our results here to be robustly a case of charge transfer, and polarization seems more likely. Given that our heterostructures are either of Type-I or Type-II band alignment, for true charge transfer to occur then an electron must first be excited into the conduction band where migration becomes possible. As these are ground state calculations we conclude that this is not a case of charge transfer, but rather is indeed a case of polarization.

Additionally, our integrations over charge densities were performed on a grid and our results were small in magnitude. By performing the calculations over a finer grid it is possible that we would efface our low magnitude results and so find that they are only due to numerical error. The character of our charge redistribution curve (Figure 5.7) i.e. the physical positions within the cell that we see local maxima and minima in the differential charge density, would imply that numerical error alone is not responsible for our results, however.

Finally, we calculated the reduction in work function (see Table 5.8) due to absorption

of the pentacene molecule, where the work function, ϕ , is calculated as

$$\phi = \epsilon_0 - \epsilon_F , \quad (5.9)$$

where ϵ_0 is the energy in vacuum, set automatically as the zero reference by the computational suite (accurate as long as the integrity of the monolayer is maintained) i.e. $\epsilon_0 = 0$, and ϵ_F is the Fermi energy (see subsection 2.4.1). We can see from Figure 5.3 that the reduction comes primarily from the introduction of permitted states within the band gap from pentacene’s HOMO, increasing the Fermi energy. The change in work function being smaller in selenium systems compared to their sulfur counterparts agrees with this observation, as the difference in pentacene’s HOMO energy to the underlying TMD’s VBM energy is greater in the sulfur systems than in the selenium systems. Similarly, the difference in pentacene’s HOMO and the TMD’s VBM is greater in molybdenum systems than tungsten, and so the change in work function from pentacene adsorption is greater in molybdenum systems than the corresponding tungsten systems. As expected, then, the MoS₂ heterostructure sees the largest change in work function, and WSe₂ the smallest.

Table 5.8: Work function of the TMDs and their 7 × 4 PEN/TMD heterostructures, as well as the change in work function due to pentacene adsorption, $\Delta\phi = \phi_{\text{TMD}} - \phi_{\text{PEN/TMD}}$.

TMD	$\phi_{\text{TMD}}/\text{eV}$	$\phi_{\text{PEN/TMD}}/\text{eV}$	$\Delta\phi/\text{eV}$
MoS ₂	5.01	4.42	0.59
MoSe ₂	4.65	4.21	0.44
WS ₂	4.59	4.25	0.34
WSe ₂	4.35	4.17	0.18

Chapter 6

The effect of molecular concentration and rotation on PEN/TMD heterostructures

Publication relating to this chapter [146]:

E. Black and J. M. Morbec, "Effect of molecular rotation and concentration on the adsorption of pentacene molecules on two-dimensional monolayer transition metal dichalcogenides," *Electronic Structure*, vol. 6, no. 2, p. 025008, 2024.

As we have investigated favorable adsorption sites for pentacene molecules on 7×4 -molecule TMD substrate layers and the electronic properties of the resultant heterostructures, we then looked at the effect of pentacene concentration within similar heterostructures. By constructing supercells of 6×3 -molecule TMD substrate layers and introducing a pentacene molecule to the cell, we created PEN/TMD heterostructures with higher pentacene concentration than in Chapter 5. We performed the same analysis on these high concentration pentacene structures as before by identifying the heterostructure with the most favorable molecular adsorption site for each TMD layer

and then calculating their electronic properties. As mentioned previously, here we also initially considered a vertical adsorption site for high concentration pentacene; we did so early in the project, where high concentration pentacene is the smaller and less computationally expensive supercell structure, and determined that the vertical adsorption of pentacene is extremely unfavorable: of the order of 1 eV less favorable than the most favorable flat-lying adsorption site in both PEN/MoS₂ and PEN/MoSe₂. As such, vertically adsorbed pentacene was not investigated further.

Additionally, while molecular pentacene has been determined to remain flat-lying on substrates (by us and in existing literature [141, 147]), there is limited literature on the alignment of pentacene with an underlying TMD substrate and how that may affect the electronic properties. So far, we have only considered pentacene with its long axis aligned with that of the long axis of the underlying substrate. This results in an alignment where the pentacene long axis is perpendicular to the plane of some transition metal-chalcogen bonds within the hexagonal pattern. By rotating pentacene by 30°, we align the long axis of pentacene such that it is instead parallel to some of these bond planes. A rotation of 60° results in the same alignment between any one particular pentacene molecule and the underlying substrate due to the rotational symmetry of the substrate layer, but changes the relationship of the molecule with surrounding molecules due to the asymmetric nature of the supercells' dimensions. 90° rotation provides the same relationship between between a given molecule and the substrate as does 30°, but similarly changes the molecule-molecule distances. These three angles of rotation were investigated around the previously determined favorable adsorption sites and compared to the unrotated, or 0°, heterostructures, for both concentrations of pentacene.

6.1 Investigating pentacene concentration

We controlled pentacene concentration by changing the number of molecular units that were within a supercell of the underlying substrate. Previously, our substrate layers were made up of 28 molecular units of TMD, in a 7×4 supercell. This gave us low concentration pentacene, and corresponded to one pentacene molecule per 244 \AA^2 for MoS_2 and WS_2 heterostructures, 264 \AA^2 for PEN/MoSe_2 , and 263 \AA^2 for PEN/WSe_2 . By reducing the number of molecular units of TMD per supercell to 18 (dimensions of 6×3 molecular units), pentacene molecules were closer to their neighbours across periodic cell boundaries. This was the high concentration pentacene regime, with concentration of one pentacene molecule per 157 \AA^2 for MoS_2 and WS_2 , 170 \AA^2 for MoSe_2 , and 169 \AA^2 for WSe_2 . The underlying TMD substrates for each concentration regime are compared in Figure 6.1.

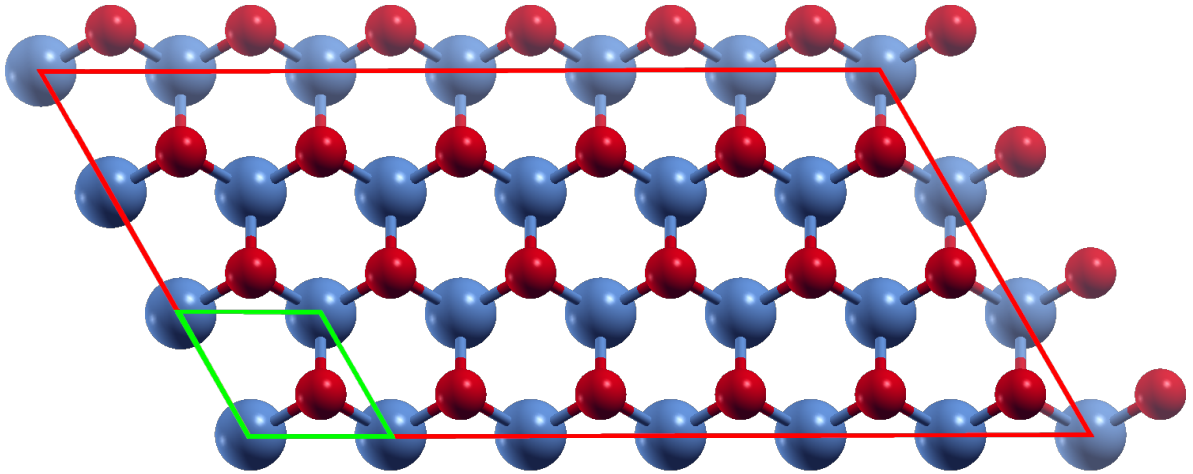


Figure 6.1: Ball and stick representation of the underlying monolayer TMD substrate. The extent of the figure in its entirety is the substrate for a 7×4 supercell, with the 6×3 equivalent enclosed by the red quadrilateral (showing the limits of the 6×3 supercells), and a single molecular unit, representing the unit cell of a pristine monolayer TMD, is enclosed within the green quadrilateral.

6.1.1 High concentration pentacene heterostructures: structure

After optimizing the geometry of the 6×3 supercell heterostructures, we found that the molecule-molecule separation across periodic boundary conditions was approximately 3.4 \AA for sulfur systems, and 3.7 \AA for selenium systems. We considered the same adsorption sites as in Chapter 5, those being Bridge-A, Bridge-B, Hollow, Top-TM and Top-Ch

(see Figure 5.1). As mentioned above, we additionally considered a heterostructure with vertically adsorbed pentacene (see Figure 5.2) that was shortly abandoned. Following relaxation of the heterostructures, we found that the Top-TM site for pentacene-MoS₂ was unstable: the `relax` calculation for this heterostructure showed that pentacene is most favorable in an adsorption site between Top-TM and Hollow, the result of which is shown in Figure 6.2. When it came to rotation of the pentacene molecule, discussed later in this chapter, we investigated both the relaxed intermediate site as well as the pre-relaxation Top-TM site where we did not permit the molecule to move along the substrate surface. We found even after rotation that the heterostructures with a pre-relaxed Top-TM adsorption site were less favorable than those with the intermediate adsorption sites, where we had still allowed the rotated structure to further relax. Therefore, we shall refer to the intermediate site obtained following `relax` calculations here as ‘Top-TM’, with the structures where the adsorption site was forced to remain at ‘true’ Top-TM referred to as ‘true’ Top-TM. This was not a concern for any other heterostructure, as the rest were stable: only PEN/MoS₂, and then only in the high concentration pentacene case.

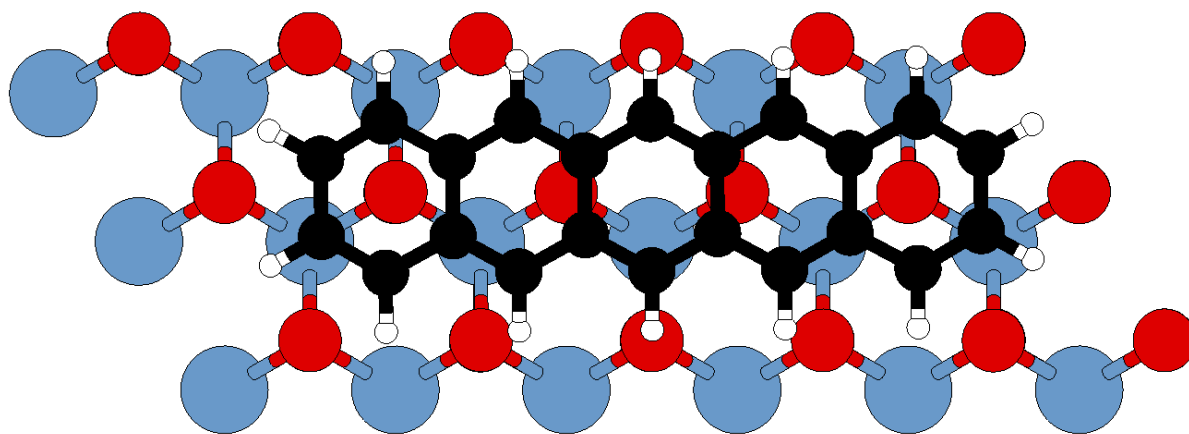


Figure 6.2: The intermediate adsorption site resulting from relaxation of pentacene adsorbed on 6×3 MoS₂, starting geometric relaxation in the Top-TM site.

Unlike the 7×4 case, the most favorable adsorption site depended on the heterostructure. By calculating the total energy of each heterostructure with different adsorption sites, we determined the energetic favorability of the various adsorption sites; this comparison is equivalent to comparing adsorption energy between heterostructures

with the same TMD. Pentacene-MoS₂ was found to be most favorable in the Top-TM site, which as discussed above found stability in an intermediate adsorption site. The next-most favorable site was Bridge-B, with a total energy 48 meV higher than that of Top-TM. The difference between Top-TM and the least favorable adsorption site was 143 meV. The PEN/MoSe₂ heterostructure favored the Bridge-B adsorption site, but this was closely contended by Top-Ch (the most favorable in the low concentration pentacene case), with a difference between the two of only 5 meV. 89 meV separated the most from the least favorable adsorption site, indicating high molecular mobility. Similarly, the pentacene-WSe₂ heterostructure was mobile between Top-Ch and Bridge-B with a difference in total energy of 12 meV, but in this case it was Top-Ch that had the lowest total energy. The least favorable site here was 87 meV less favorable than Top-Ch, implying good mobility across the entire surface of the TMD substrate, similar to MoSe₂ systems. The lowest molecular mobility was found in the PEN/WSe₂ heterostructure, with a difference between the most favorable adsorption site, Bridge-A, and the next most favorable, Bridge-B, to be 137 meV, almost as large as the differential across all adsorption sites in the PEN/MoS₂ systems. The difference in total energies between the most and least favorable flat-lying sites for pentacene-WSe₂ heterostructures was found to be 188 meV. The differences in total energies of the various adsorption sites for high concentration pentacene systems compared to the most favorable sites are displayed in Table 6.1. The pentacene molecule remains flat-lying for all systems, with only minor deformation.

Table 6.1: The difference in total energy, in eV, between adsorption sites of pentacene-TMD heterostructures with high concentration pentacene and their most favorable adsorption site.

Heterostructure	Bridge-A	Bridge-B	Hollow	Top-TM	Top-Ch
PEN/MoS ₂	0.143	0.048	0.098	0.000	0.054
PEN/MoSe ₂	0.089	0.000	0.050	0.060	0.005
PEN/WSe ₂	0.087	0.011	0.061	0.062	0.000
PEN/WSe ₂	0.000	0.137	0.186	0.187	0.140

Layer separation, d , was found to not be the smallest for the most favorable adsorption site, in contrast to the case with 7×4 heterostructures. The pentacene-MoS₂

heterostructure did have a smaller layer separation in its most favorable adsorption site, at 3.297 Å, but both PEN/MoSe₂ and PEN/WS₂ heterostructures had their smallest layer separation in their second-most favorable site, Top-Ch and Bridge-B, respectively. Their most favorable adsorption sites, Bridge-B and Top-Ch, respectively, were the second closest-binding systems. We noted that the values between both the total energy and the layer separation in both cases for both TMDs are very close: only 5 meV and 11 meV, and 8 mÅ and 1 mÅ, respectively. PEN/WSe₂ interestingly has its largest layer separation with pentacene in its most favorable adsorption site, Bridge-A. The closest binding adsorption sites here are Bridge-B and Top-Ch, as in PEN/MoSe₂ and PEN/WS₂, and we notice that all heterostructures have the greatest layer separation with the Bridge-A adsorption site. In keeping with what we saw with the high concentration pentacene heterostructures, there were larger binding distances observed in selenium systems than in sulfur, again explained by the large van der Waals radii of the respective chalcogen atoms. The layer separations for each heterostructure are displayed in Table 6.2.

Table 6.2: Layer separation, d , in Å, of 6×3 PEN/TMD heterostructures, defined as the distance between the center of mass of pentacene and the average z-coordinate of the top-most chalcogens of the underlying TMD substrate.

Heterostructure	Bridge-A	Bridge-B	Hollow	Top-TM	Top-Ch
PEN/MoS ₂	3.421	3.342	3.397	3.297	3.346
PEN/MoSe ₂	3.482	3.425	3.477	3.480	3.417
PEN/WS ₂	3.412	3.320	3.402	3.401	3.321
PEN/WSe ₂	3.480	3.410	3.468	3.464	3.416

As with the high concentration regime, we continued our calculations and analysis only on the most favorable adsorption sites, with the exception of briefly revisiting the ‘true’ Top-TM adsorption site for PEN/MoS₂ when we investigated rotated pentacene.

By examining the relaxed heterostructure geometry and comparing it to the relaxed geometry of the TMDs and pentacene out of heterostructure, we observed some minor deformation of the pentacene molecule. We recall that isolated pentacene had a mean atomic deviation from the molecular plane of 0.49 mÅ, with the largest atomic deviation being 1.02 mÅ (see Section 4.3). As for the case of high concentration pentacene

systems, we saw more deviation from the molecular plane than in the case of isolated pentacene, and with their maximum deviation occurring near, but not necessarily at, the middle of the molecule: there is some very minor twisting noted. Pentacene within the PEN/MoS₂ heterostructure saw a mean atomic deviation of 60 mÅ, and a maximum atomic deviation of 118 mÅ on one side of the middle carbon ring, the PEN/MoSe₂ heterostructure saw a mean atomic deviation of 41 mÅ and a maximum of 111 mÅ at one of the second from middle carbon rings, PEN/WS₂ had a mean atomic deviation of 38 mÅ and a maximum of 105 mÅ in the middle of the molecule, and PEN/WSe₂ had a mean atomic deviation of 26 mÅ and a maximum of 67 mÅ between one of the outer carbon rings and the next one in. Pentacene’s carbon-carbon bond lengths were again negligibly changed, by less than 0.1%, with the formation of the heterostructures. The transition metal-chalcogen bond lengths underwent position-dependent change, with the largest contraction (3.6 mÅ, 4.1 mÅ, 3.9 mÅ, and 4.8 mÅ in PEN/MoS₂, PEN/MoSe₂, PEN/WS₂, and PEN/WSe₂ heterostructures, respectively) occurring underneath the pentacene molecule and the largest bond lengthening (2.3 mÅ, 2.9 mÅ, 3.5 mÅ, and 2.4 mÅ in PEN/MoS₂, PEN/MoSe₂, PEN/WS₂, and PEN/WSe₂ heterostructures, respectively) observed in bonds near those most contracted, but no longer underneath the pentacene.

The adsorption energies, E_{ads} (Equation 5.1), of the favorable heterostructures are shown in Table 6.3. The differences between total energies of different binding sites from Table 6.1 apply to adsorption energies as well, as the different adsorption sites for the same TMD share the same energies of their materials out of heterostructure, but the absolute value of total and adsorption energies will differ.

Table 6.3: Adsorption energy, E_{ads} and layer separation, d , of the 6×3 heterostructures with pentacene in the most favorable adsorption site.

Heterostructure	Adsorption Site	E_{ads}/eV	$d/\text{Å}$
PEN/MoS ₂	Top-TM	-1.461	3.297
PEN/MoSe ₂	Bridge-B	-1.437	3.425
PEN/WS ₂	Top-Ch	-1.454	3.321
PEN/WSe ₂	Bridge-A	-1.606	3.480

Unlike in the 7×4 case, we did not perform calculations here without van der Waals corrections, as we showed previously that the adsorption energy due to van der Waals was many times large than that without; there is no reason to expect any difference here (or indeed later), and the level of interest in any slight differences beyond that discussed in the context of molecule-substrate interactions is not worth the computational cost of additional large heterostructure calculations.

We additionally calculated the contributions to adsorption energy from molecule-molecule and molecule-substrate interactions, and molecule and substrate deformation effects, as described in Section 5.1 and defined by Equations 5.2-5.5. The results of these calculations are given in Table 6.4, where we see that the major contribution is molecule-substrate interaction. This is expected, given that this includes van der Waals interactions. Deformation effects are small, but molecule-molecule interactions are an order of magnitude larger than deformation effects, as well as molecule-molecule interactions in the low concentration pentacene calculations (see Table 5.4), which is, again, expected given the decreased distance between molecules.

Table 6.4: Contributions to the adsorption energy of 6×3 heterostructures in their favorable adsorption site from molecule-molecule, molecule-substrate, molecule deformation and substrate deformation effects, in eV. Molecule-substrate interaction is consistently the largest contribution across all systems.

	PEN/MoS ₂	PEN/MoSe ₂	PEN/WS ₂	PEN/WSe ₂
molecule-molecule interaction	-0.059	-0.038	-0.056	-0.038
molecule-substrate interaction	-1.398	-1.400	-1.374	-1.422
molecule deformation	-0.009	-0.005	-0.009	-0.007
substrate deformation	0.002	0.002	0.003	-0.005

6.1.2 High concentration pentacene heterostructures: electronic properties

Density of states

The density of states was calculated for each heterostructure in its most favorable geometry, the results of which are displayed in Figure 6.3. In all cases, pentacene’s HOMO is located within the TMD band gap, closer to the TMD’s VBM in the cases of

the selenide systems. The differences between pentacene's HOMO and the TMD's VBM, determined with the density of states calculations, were 1.05 eV, 0.50 eV, 0.90 eV, and 0.25 eV, for PEN/MoS₂, PEN/MoSe₂, PEN/WS₂, and PEN/WSe₂, respectively.

Pentacene's LUMO is close to the TMD's CBM, excepting the case of the PEN/MoS₂ system, which maintains a robust Type-II heterojunction with a difference between the pentacene's LUMO and the CBM of MoS₂ of 0.30 eV. PEN/WS₂ is predicted to have a Type-II band alignment, but close: a difference between LUMO and CBM of only 0.05 eV. PEN/WSe₂ forms a Type-I heterojunction, where pentacene's LUMO is 0.35 eV below the CBM of WSe₂. In the case of PEN/MoSe₂, however, there was no difference between LUMO and CBM to the precision of our density of states calculation. These values are presented in Table 6.5.

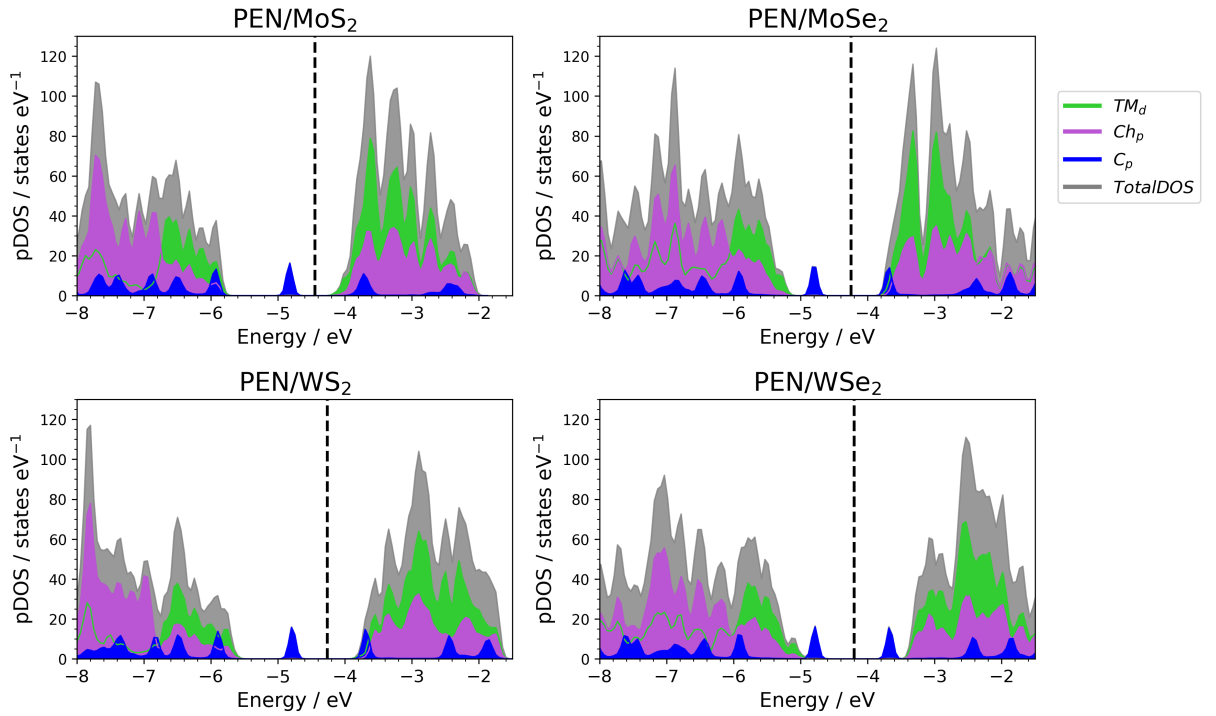


Figure 6.3: The density of states of 6×3 PEN/TMD heterostructures, with the Fermi energies given by the vertical black dashed line.

Table 6.5: Frontier orbital energies and their difference, Δ , in eV, of 6×3 PEN/TMD heterostructures. The values presented here are from density of states calculations, and so have a precision only of 0.05 eV. As in the case of the 7×4 heterostructures, PEN/WSe₂ is in a Type-I band alignment. However, with high concentration pentacene, PEN/MoSe₂ now potentially forms a Type-I heterojunction as well.

Heterostructure	PEN		TMD		Δ	
	HOMO	LUMO	VBM	CBM	HOMO-VBM	LUMO-CBM
PEN/MoS ₂	-4.70	-3.85	-5.75	-4.15	1.05	0.30
PEN/MoSe ₂	-4.65	-3.75	-5.15	-3.75	0.50	0.00
PEN/WS ₂	-4.70	-3.80	-5.60	-3.85	0.90	0.05
PEN/WSe ₂	-4.70	-3.80	-4.95	-3.45	0.25	-0.35

The band alignment of MoSe₂ and pentacene out of heterostructure, but with a molecular concentration consistent with the 6×3 heterostructures, was determined in Chapter 4 to be of Type-II. Here, however, we could not distinguish between Type-I and Type-II within the precision of our density of states calculations. The higher precision *scf* calculations do not map frontier orbital energies on to molecular orbitals, and so we cannot tell what the band alignment is from there. As such, we repeated the density of states calculations with a smaller energy bin, 0.01 eV, in order to determine the band alignment. The frontier orbitals from this calculation were a TMD CBM of -3.77 eV and a pentacene LUMO of -3.81 eV, resulting in a Type-I heterojunction. Knowing now which orbital the *scf* calculation energies belonged to, we then determined the contributions of molecule-molecule and molecule-substrate interactions to the change in frontier orbital energies seen when bringing pentacene into high concentration heterostructure with MoSe₂.

Table 6.6: HOMO and LUMO positions of pentacene in a well-isolated environment (PEN_{iso}), in a 6×3 supercell without a substrate (PEN_{6 \times 3}), and in the PEN/MoSe₂ and PEN/WSe₂ heterostructures (PEN_{PEN/TMD}). Values are in eV, and are either extracted from *scf* calculations as in Chapter 4, resulting in higher precision, or are extracted from density of states (pDOS) calculations (reporting the values for PEN_{PEN/WSe₂} using the 0.05 eV bin for consistency).

System	<i>scf</i>		pDOS	
	HOMO	LUMO	HOMO	LUMO
PEN _{iso}	-4.446	-3.307	-4.35	-3.40
PEN _{6\times3}	-4.681	-3.541	-4.55	-3.60
PEN _{PEN/MoSe₂}	-4.799	-3.687	-4.65	-3.75
PEN _{PEN/WSe₂}	-4.788	-3.669	-4.70	-3.80

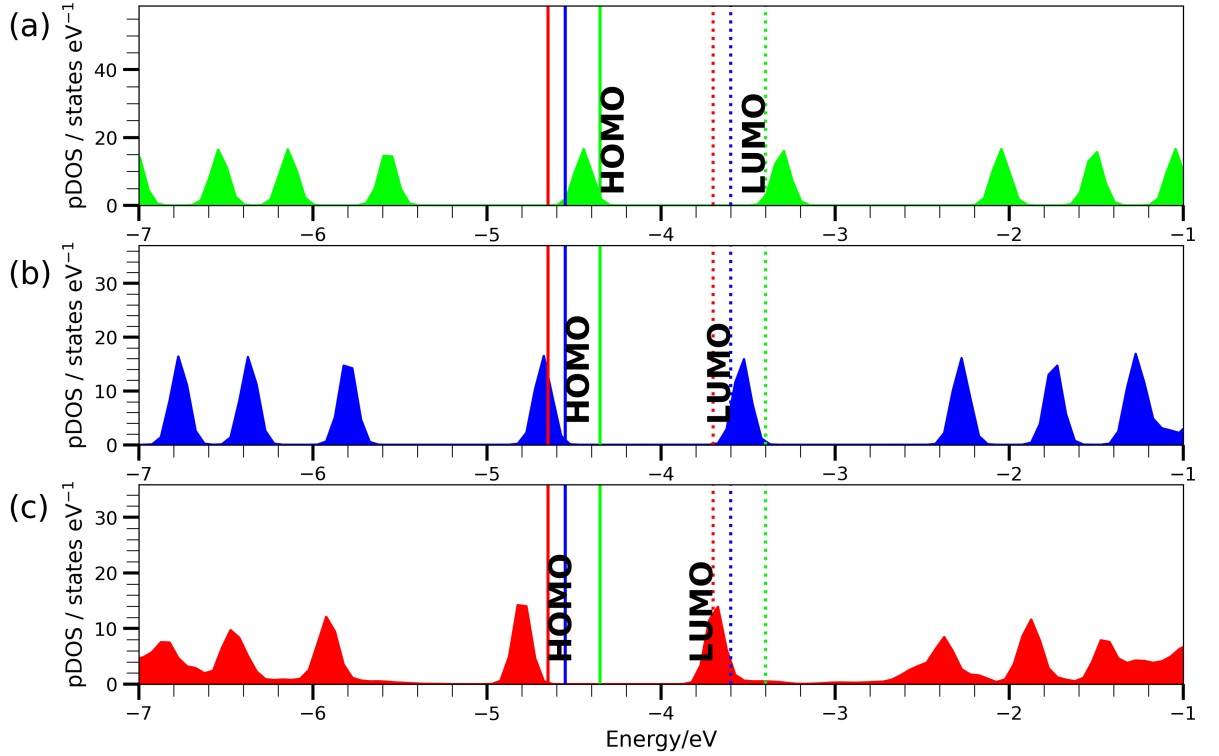


Figure 6.4: The total density of states of pentacene in three different environments with their HOMO and LUMO energies labelled and marked on all three subplots with solid and dashed colored lines, respectively: (a) well-isolated pentacene in green, (b) pentacene in a cell defined by the 6×3 PEN/MoSe₂ heterostructure, but without the TMD (and geometrically optimized in this cell, without the TMD), in blue, and (c) pentacene in the PEN/MoSe₂ heterostructure in red. It is clear that the frontier orbitals decrease in energy with both an increase in concentration and adsorption.

We see from Table 6.6 that bringing isolated pentacene into a concentration consistent with the PEN/MoSe₂ heterostructure (but without the TMD) results in a decrease of both HOMO and LUMO energies of 235 meV and 234 meV, respectively. This represents the effect of molecule-molecule interactions on the frontier orbitals. There is a further decrease in the HOMO upon adsorption on the MoSe₂ substrate of 118 meV, and a decrease of 146 meV in the LUMO. These are the molecule-substrate interaction contributions. We can see this effect in Figure 6.4. Both are required to result in a transition from Type-II to Type-I band alignment (as would be expected, given that the 7×4 system remained Type-II; molecule-substrate interaction there was not sufficient). We additionally compared the frontier orbital energies of these systems as determined by density of states calculations, the results of which are presented in Table 6.6, where we observe the same effect. Molecule-molecule interactions act on both frontier orbitals to decrease them by 0.20 eV, and

molecule-substrate interactions further decrease them by 0.10 eV and 0.15 eV for the HOMO and LUMO, respectively.

Frontier orbital energies used to predict band alignment in Chapter 4 were calculated with `scf` and `bands` calculations, which differ slightly from results obtained from density of states calculations. As such, we present in Figure 6.5a the density of states of well-isolated pentacene and MoSe₂ out of heterostructure, showing a predicted staggered band gap alignment. Figure 6.5b displays the density of states of pentacene in a 6×3 supercell, without the TMD, superimposed on the same MoSe₂ data. These calculations, that do not take into account molecule-substrate interactions, but the latter of which did consider molecule-molecule interactions, predicted a staggered gap. Only with the addition of molecule-substrate interactions was the tuning of frontier orbital energies enough to change the band alignment.

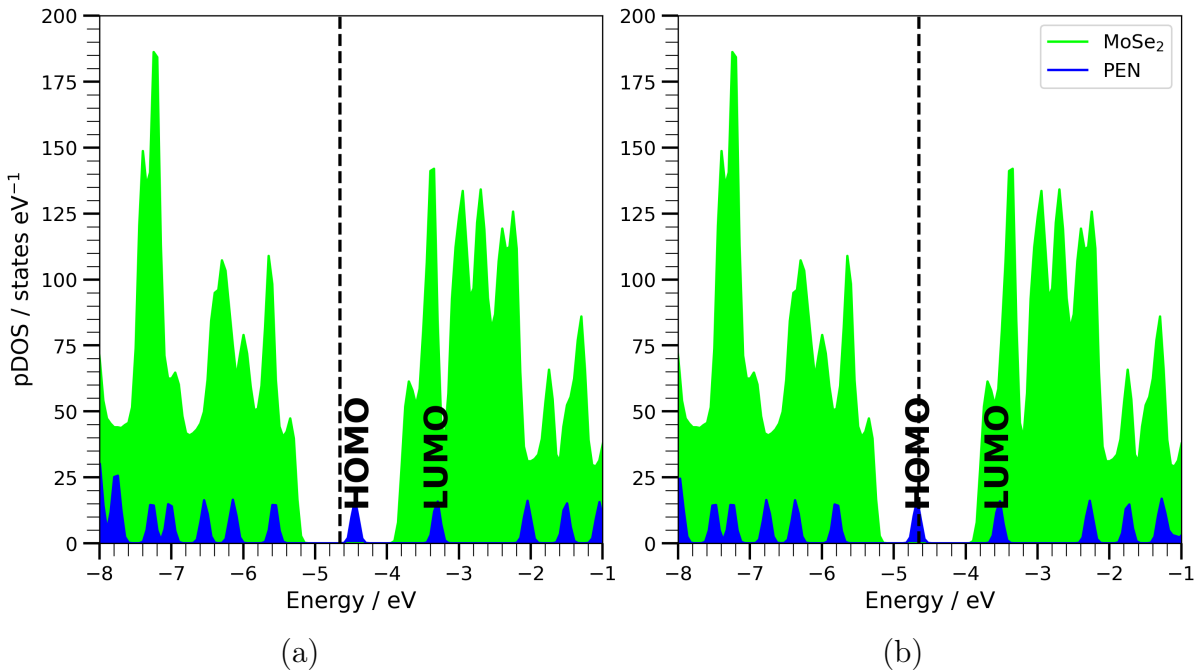


Figure 6.5: (a) The density of states of well-isolated pentacene (blue) and that of MoSe₂ (green), presented to demonstrate type-II band alignment of the materials outside of heterostructure when using frontier orbital energies from density of states calculations, for comparison with those from the heterostructure. Pentacene’s HOMO and LUMO, as well as the TMD’s VBM and CBM, are labelled. (b) The density of states of pentacene in a 6×3 supercell without the substrate (blue) and that of MoSe₂, demonstrating that pentacene’s LUMO and the TMD’s CBM are effectively overlapping. The molecule-molecule interaction effects on the orbitals is not enough to cause a band alignment type transition, but the additional molecule substrate effects were.

As we saw that PEN/WSe₂ formed a Type-II heterojunction when in the low concentration regime due to molecule-molecule and molecule-substrate effects, it was reasonable to assume that with increased concentration, and so increased molecule-molecule interaction, this alignment would be maintained in the 6×3 system. This was the case, as can be seen in Figure 6.3, where the pentacene frontier orbitals are completely straddled by the TMD frontier orbitals. Isolated pentacene was predicted to have Type-II band alignment with WSe₂ in Chapter 4, but did not consider the effects that come with heterostructure formation. Density of states calculations (see Table 6.6) show that molecule-molecule interactions move pentacene's HOMO and LUMO energetically lower by 0.20 eV, and molecule-substrate interactions have the same effect again, by 0.15 eV for the HOMO and 0.20 eV for the LUMO. The combination of the two is enough for a Type-II to Type-I band alignment transition. Because of the straddling gap, we can use `scf` calculation values for a more precise discussion, with values also given in Table 6.6. The molecule-molecule effects are discussed above in the context of the MoSe₂ heterostructure, and are independent of the TMD. Molecule-substrate interaction results in a further decrease in the HOMO energy of 107 meV, and the LUMO of 128 meV. These are both within 20 meV of the changes seen from heterostructure formation with MoSe₂. We can see these changes in Figure 6.6, which demonstrates the changes in frontier orbital energies of pentacene as it is brought into the high concentration regime, and then heterostructure with WSe₂.

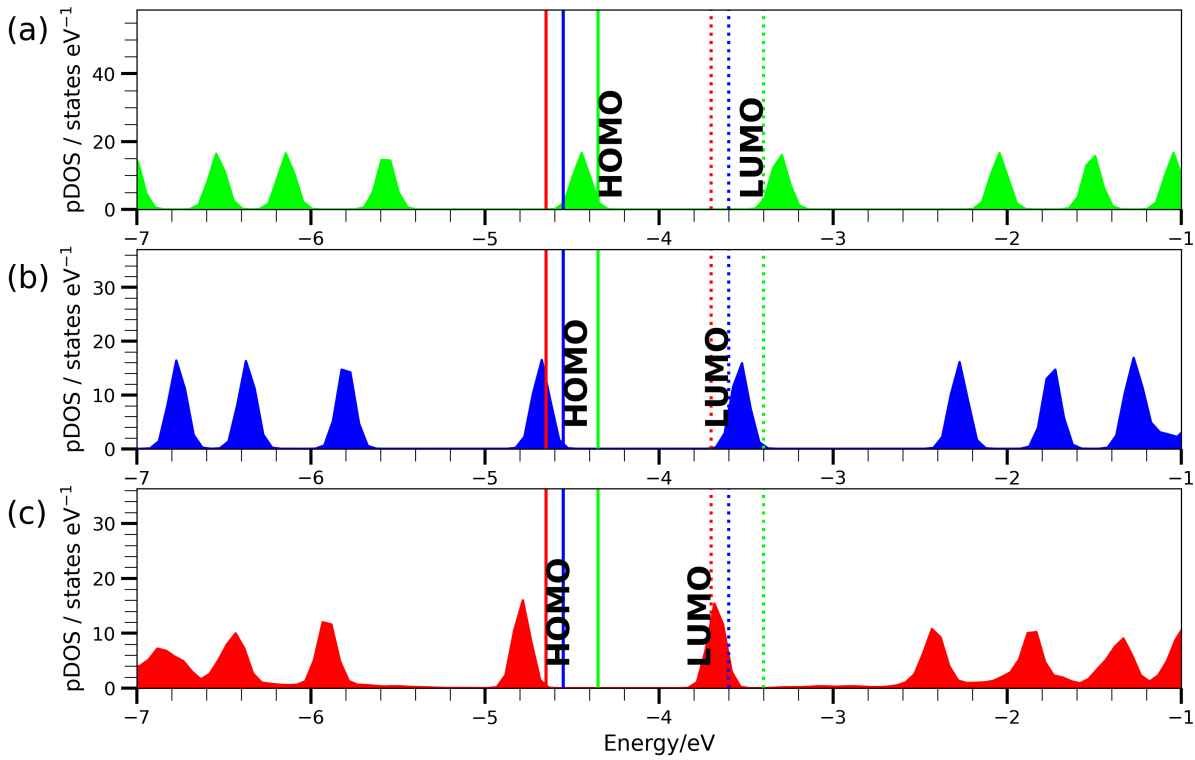


Figure 6.6: The total density of states of pentacene in three different environments with their HOMO and LUMO energies labelled and marked on all three subplots with solid and dashed colored lines, respectively: (a) well-isolated pentacene in green, (b) pentacene in a cell defined by the 6×3 PEN/WSe₂ heterostructure, but without the TMD, in blue, and (c) pentacene in the PEN/WSe₂ heterostructure in red. It is clear that the frontier orbitals decrease in energy with both an increase in concentration and adsorption.

Work function

The reduction in work function, ϕ (Equation 5.9), of the TMDs due to adsorption of high concentration pentacene was calculated as described in subsection 5.2.2, with results displayed in Table 6.7. The introduction of permitted pentacene orbitals into the TMD band gap results in an increase in the Fermi energy, reducing the work function. The change in work function being more pronounced in sulfur systems agrees with this observation, where the selenium systems with the smaller difference between pentacene's HOMO and the TMD's VBM (see Table 6.5) experience a smaller change in work function.

Table 6.7: Work function of the TMDs and their 6×3 PEN/TMD heterostructures, as well as the change in work function due to pentacene adsorption, $\Delta\phi = \phi_{\text{TMD}} - \phi_{\text{PEN/TMD}}$.

TMD	$\phi_{\text{TMD}}/\text{eV}$	$\phi_{\text{PEN/TMD}}/\text{eV}$	$\Delta\phi/\text{eV}$
MoS ₂	5.01	4.45	0.56
MoSe ₂	4.65	4.25	0.40
WS ₂	4.59	4.26	0.33
WSe ₂	4.35	4.20	0.15

We did not perform charge transfer calculations on the high pentacene concentration heterostructures, as we have already shown the position within the heterostructures that charge transfer (likely polarization rather than true charge transfer, see subsection 5.2.2) occurs, and noted no significant difference between choice of TMD beyond that expected due to electron density.

6.1.3 Comparison of pentacene concentrations

Structural favorability

Compared to the 7×4 heterostructures of Chapter 5, the pentacene molecules in the high concentration regime are approximately 3.2 \AA closer to each other across the periodic boundaries, and 64% the concentration by area.

With increased concentration to the 6×3 supercell comes changes to the most favorable adsorption site. All PEN/TMD systems with low concentration pentacene were most favorable with the adsorbed molecule in the Top-Ch site. We see PEN/MoS₂ express much less mobility in its molecular adsorption site with increased concentration of pentacene, and the Top-TM site become unstable; this site relaxes to an intermediate site between Top-TM and Hollow, which is the most favorable adsorption site. High concentration PEN/WSe₂ also expresses a marked decrease in pentacene’s mobility across the TMD surface, being most favorable in the Bridge-A adsorption site. PEN/MoSe₂ is again most favorable in a different adsorption site (Bridge-B) compared to the low concentration pentacene case, but retains its mobility, and PEN/WS₂ is most favorable in the same site as in the 7×4 supercell, and comparably mobile. A summary of this is given in Table 6.8. We believe these effects to be due to increased molecule-molecule interactions,

which exaggerate effects from differences in the lattice parameters between TMDs. These difference in lattice parameters affect a difference in the spatial relationship between pentacene’s carbon rings and the underlying chalcogens. This difference is minor, given that all the TMDs are broadly similar in structure: they form a hexagonal lattice with similar lattice parameters, where chalcogens form the adsorption surface at a similar distance from the transition metal atoms deeper in the TMD later. In the absence of strong molecule-molecule interactions these differences are not significant enough to influence the preferred adsorption site. However, in the high concentration regime, where we would expect steeper energetic barriers to surround stable adsorption sites, they are. This results in a variation in adsorption sites, compared to the consistent Top-Ch site found in the 7×4 systems. Thus, molecular mobility was reduced, with adjacent pentacene’s acting to constrain the positions which were found favorable. The 7×4 systems demonstrated a difference in E_{ads} between most and next-most favorable adsorption sites of between 2 meV and 6 meV, and a difference between most and least favorable of between 24 meV to 83 meV. The 6×3 systems, however, had a much larger range of differences: between 5 meV and 137 meV for the differences between most and next-most favorable adsorption sites, and between 87 meV and 188 meV for the difference between most and least favorable adsorption site. As expected from lower molecule-molecule interaction, the molecular mobility within the 7×4 heterostructures is greater.

Table 6.8: A structural comparison of PEN/TMD heterostructures of the two concentration regimes investigated. Adsorption site mobility is the range of difference in energy of the most favorable adsorption site and the others.

	PEN/MoS ₂	PEN/MoSe ₂	PEN/WS ₂	PEN/WSe ₂
7×4 , low concentration				
Adsorption Site	Top-Ch	Top-Ch	Top-Ch	Top-Ch
Adsorption Site Mobility/eV	3 - 79	2 - 72	2 - 83	6 - 75
Adsorption Energy/eV	-1.39	-1.42	-1.43	-1.46
$d/\text{\AA}$	3.31	3.40	3.30	3.38
Minimum molecule-molecule distance/ \AA	6.2	6.5	6.2	6.5
6×3 , high concentration				
Adsorption Site	Top-TM	Bridge-B	Top-Ch	Bridge-A
Adsorption Site Mobility/eV	48 - 143	5 - 89	11 - 87	137 - 187
Adsorption Energy/eV	-1.46	-1.44	-1.45	-1.61
$d/\text{\AA}$	3.30	3.42	3.32	3.48
Minimum molecule-molecule distance/ \AA	3.4	3.7	3.4	3.7

This difference in mobility between molecular concentrations is seen prominently in PEN/MoS₂, which has the smallest lattice parameter, the shortest transition metal-chalcogen bonding, and the shortest distance in the z-direction between the transition metal atoms and the adsorption surface (increasing their effect on pentacene), resulting in the second lowest mobility between adsorption sites. However, it is PEN/WSe₂ which has the lowest mobility between adsorption sites. We expect PEN/WSe₂ to exhibit the strongest binding between layers of any TMD, given that the majority of the adsorption effect is due to van der Waals forces, and WSe₂ contains the largest atoms of the TMDs investigated. We saw that this was indeed the case, and with increased molecular concentration we saw an increased layer separation, d , but also an increased binding strength (when comparing the unrotated systems across concentrations); the high concentration regime investigated here was not high enough to completely saturate the adsorption sites (after which one would expect a decrease in binding strength).

A direct comparison of E_{ads} for each PEN/TMD pair in different molecular concentrations is difficult, as they favored different adsorption sites. However, the general trend is that the 6×3 systems have lower adsorption energy, indicating stronger binding, but with a larger layer separation (see Table 6.8). As the substrate is not saturated in either concentration regime, the increased adsorption strength in the high concentration regime is due to effectively the same van der Waals effect on each pentacene molecule across concentrations, but more pentacene molecules per TMD unit, and so increased van der Waals interaction per TMD unit in the high concentration case. Additionally, molecule-molecule interactions assist in binding, a claim supported by the larger magnitude of molecule-molecule interactions seen in the 6×3 supercell systems. The van der Waals force response curve minima (see Figure 2.14) becomes shifted to higher distances, but is increased in depth.

The differences in layer separation between high and low concentration regimes are 12 mÅ for PEN/MoS₂, 25 mÅ for PEN/MoSe₂, 24 mÅ for PEN/WS₂, and a large 102 mÅ for PEN/WSe₂. The discrepancy between PEN/WSe₂ and the other systems is due to the differences in layer separation within the 6×3 systems, with the 7×4 all being fairly

similar. For 6×3 PEN/WSe₂, the most favorable adsorption site was Bridge-A, which was the site with the largest layer separation for all the TMDs. This explains why there is such a difference within the WSe₂ systems.

During our calculation and previous discussions of adsorption energies, we were able to determine the respective contributions from various effects: molecule-molecule and molecule-substrate interactions, as well as molecule and substrate deformations. To a limited extent we can discuss changes in the electronic structure of heterostructures arising from varying molecular concentration and rotation in this way as well, which we do so in the remainder of this subsection.

Molecule-substrate interaction effects

The interaction between the adsorbed pentacene molecule and the TMD layer of the supercell includes the van der Waals interaction, as well as competing electrostatic repulsion. With changing pentacene concentration the magnitude of these effects is altered. A summary of the contribution of molecule-substrate interactions to E_{ads} across the two concentration regimes, as well as the difference between them, is presented in Table 6.9.

Table 6.9: The contributions to E_{ads} of molecule-substrate interactions, in eV, in unrotated heterostructures across the concentration regimes, as well as their difference. A positive difference represents a more positive (oppositional) contribution with an increase in concentration.

Heterostructure	7×4	6×3	Δ
PEN/MoS ₂	-1.402	-1.398	0.004
PEN/MoSe ₂	-1.423	-1.400	0.023
PEN/WS ₂	-1.340	-1.347	-0.007
PEN/WSe ₂	-1.452	-1.422	0.030

We see that the effect of increasing molecular concentration is to decrease the contribution of molecule-substrate interactions to the adsorption energy in selenium systems by a few tens of meV. Sulfur systems experience a much smaller modulation of these effects by an order of magnitude. In PEN/WS₂ this change is a small increase in contribution. The relative change with increasing concentration is effectively negligible

in all heterostructures.

We can also consider the contribution of the molecule-substrate interaction on changes in frontier orbital energies in a similar manner to that outlined in Section 5.1, but with density of states calculations. In this case, however, the effects were small and only to a precision of 0.05 eV (being determined from our density of states calculations), so we did not uncouple the molecule-substrate effects from deformation effects. We have seen previously that molecule-substrate effects are always much larger than those due to material deformation (Tables 5.4 and 6.4 for 7×4 and 6×3 systems, respectively), and so differentiation between the two would be effaced by the precision limit.

The effect of increasing molecular concentration on the molecule-substrate interaction contribution to pentacene’s frontier orbital energies is presented in Table 6.10, where we see that the molybdenum systems are affected slightly more than the tungsten, and the HOMO more or the same as the LUMO. All effects due to increased concentration are either zero within our precision limit, or act to decrease the effect of the molecule-substrate interaction on frontier orbital energy.

Table 6.10: The effect on pentacene’s frontier orbitals from molecule-substrate interactions and material deformation, in eV, in heterostructures across both concentration regimes (a negative value represents a decrease in orbital energy due to these effects) and the modulation of these effects due to increasing concentration. Deformation effects are a smaller contribution to E_{ads} than molecule-substrate interaction effects.

Heterostructure	7×4		6×3		Δ	
	HOMO	LUMO	HOMO	LUMO	HOMO	LUMO
PEN/MoS ₂	-0.25	-0.30	-0.15	-0.25	0.10	0.05
PEN/MoSe ₂	-0.20	-0.25	-0.10	-0.15	0.10	0.10
PEN/WS ₂	-0.20	-0.25	-0.15	-0.20	0.05	0.05
PEN/WSe ₂	-0.20	-0.20	-0.15	-0.20	0.05	0.00

The effect of increasing molecular concentration of the same on TMD frontier orbital energies is presented in Table 6.31, where we see no effect on tungsten systems, and a small increase in the molecule-substrate interaction contribution to frontier orbital energies in molybdenum systems. A distinction along the lines of the transition metal is expected, as the frontier orbitals of the TMD are provided by molybdenum or tungsten d-orbitals.

Overall we see that the molecule-substrate interaction component of the effect of

increasing molecular concentration on frontier orbital energies is larger in pentacene than the TMDs, and larger in molybdenum systems.

Table 6.11: The effect on the TMD’s frontier orbitals from molecule-substrate interactions and material deformation, in eV, in heterostructures across both concentration regimes (a negative value represents a decrease in orbital energy due to these effects) and the modulation of these effects due to increasing concentration. Deformation effects are a smaller contribution to E_{ads} than molecule-substrate interaction effects.

Heterostructure	7×4		6×3		Δ	
	VBM	CBM	VBM	CBM	VBM	CBM
PEN/MoS ₂	0.10	0.00	0.15	0.05	0.05	0.05
PEN/MoSe ₂	0.10	0.00	0.15	0.05	0.05	0.05
PEN/WS ₂	0.10	0.00	0.10	0.00	0.00	0.00
PEN/WSe ₂	0.10	0.00	0.10	0.00	0.00	0.00

Molecule-molecule interaction effects

Molecule-molecule interactions, those between pentacene molecules across periodic cell boundaries, for both concentration regimes are displayed and compared in Table 6.12. We see that there is a significant relative increase in molecule-molecule interaction with increasing PEN concentration, acting to assist heterostructure binding; this is presumably due to decreased inter-molecular distances and increased van der Waals attraction. Additionally, the contributions in sulfur systems, with smaller inter-molecular distances than selenium systems, are of greater magnitude.

Table 6.12: The contributions to E_{ads} of molecule-molecule interactions, in meV, in heterostructures across the concentration regimes, as well as their difference. A positive difference represents a more positive (oppositional) contribution with an increase in concentration.

Heterostructure	7×4	6×3	Δ
PEN/MoS ₂	-4	-59	-55
PEN/MoSe ₂	-3	-38	-35
PEN/WS ₂	-4	-56	-51
PEN/WSe ₂	-3	-38	-35

Given that our investigation of frontier orbital energies comes primarily from density of states calculations with a precision of 0.05 eV, and we are interested here in excluding interactions involving the substrate, we did not gather frontier orbital data from pentacene

in supercells defined by each of the heterostructures’ lattice parameters. As the lattice parameters are all broadly similar, we instead evaluated pentacene in one supercell per concentration regime, representative of the lattice parameters from the 7×4 and 6×3 TMD substrates, and not separately for each TMD.

The effect of molecule-molecule interactions on frontier orbital energies, then, is the difference between the well isolated case and that of the molecule in a supercell representative of that in the 7×4 or 6×3 supercell. We did not consider pentacene in the adsorbed geometry here, only the relaxed geometry, different from the determination of the contribution to adsorption energy (Equation 5.2). The differences between the two methods are those introduced by molecular deformation, which is not only small, but broadly accounted for in the fact that we compare relaxed geometry in both the isolated and the concentration-specific superstructure cases. We expect any discrepancies to be effaced by our precision limit.

The effect of increased concentration on pentacene’s frontier orbitals due to molecule-molecule interactions is displayed in Table 6.13. We see that these effects are responsible for a change in HOMO and LUMO energies in the 7×4 supercell compared to the well isolated case of 0.10 eV, acting to decrease both energies, and a further change of the same amount between the 7×4 supercell and the 6×3 supercell.

Table 6.13: The effect on pentacene’s frontier orbitals from molecule-molecule interactions, in eV, across both concentration regimes (a negative value represents a decrease in orbital energy due to these effects) and the modulation of these effects due to increasing concentration.

Heterostructure	HOMO	LUMO
PEN _{7×4}	-0.10	-0.10
PEN _{6×3}	-0.20	-0.20
Δ	-0.10	-0.10

Molecular deformation due to heterostructure formation

By bringing pentacene into heterostructure with the TMDs, there is a change in structure that occurs. This is the molecular deformation, and with changed atomic position comes a change in electronic density profile. As such, deformation of the molecule (and the

substrate itself) can contribute to adsorption energy. We did not decouple deformation effects from molecule-substrate interaction effects for frontier orbital energies due to the relative magnitude of these effects, but we did so for adsorption energy contributions.

Table 6.14 shows the contribution of molecular deformation to adsorption energy for each heterostructure between pentacene concentration regimes, as well as their difference, representing the effect of increasing molecular concentration on the energetic contribution of molecular deformation to E_{ads} . We can see that with increasing concentration, molecular deformation becomes a larger contributor to the adsorption energy, except for PEN/WSe₂, where no effect is observed. There is a greater magnitude of change due to concentration increase in the molybdenum systems, although the effect throughout is small.

Table 6.14: The contributions to E_{ads} of molecule deformation effects, in meV, in heterostructures across the concentration regimes, as well as their difference. A positive difference represents a more positive (oppositional) contribution with an increase in concentration.

Heterostructure	7×4	6×3	Δ
PEN/MoS ₂	5	-9	-14
PEN/MoSe ₂	-7	-10	-3
PEN/WS ₂	-3	-9	-6
PEN/WSe ₂	-7	-7	0

We also investigated the atomic deviation of pentacene from its molecular plane, where we saw that well isolated pentacene was effectively flat lying, with a very slight bowling effect of approximate magnitude of 1 mÅ. There was no significant change from this structure when considering pentacene in a 7×4 or 6×3 supercell without the substrate. Only when introducing a substrate was there molecular deviation greater than a few mÅ. It should be noted that even in the most extreme case these deviations were approximately one tenth of an angstrom, so the molecule can still reasonably be considered flat lying with no significant twisting. The difference between the z-coordinates of pentacene atoms out of heterostructure are displayed in Figure 6.7, showing the nature of this small deviation from the molecular plane. We can see that isolated pentacene and pentacene in both the 7×4 and the 6×3 supercell, without the TMD, are very similar: the carbon rings sit

higher than the hydrogen atoms, forming an upside-down bowl shape. This is identical to the case where the carbon rings sit below the hydrogen atoms, as in the absence of a substrate there is no up or down reference.

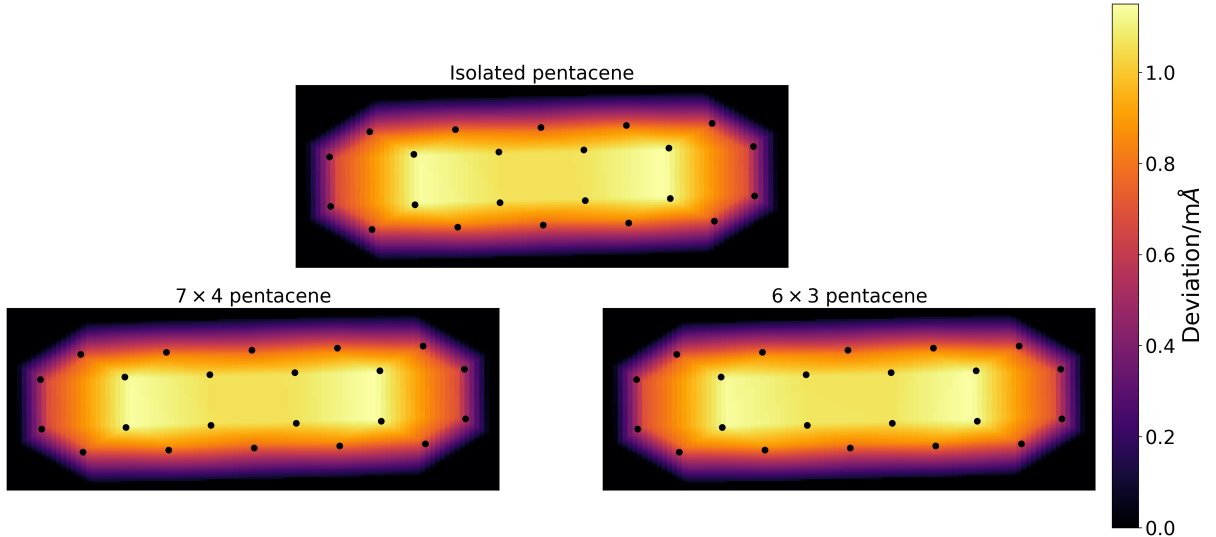


Figure 6.7: The deviation in z -coordinate of pentacene atoms from the minimum z -coordinate value of the atoms for well-isolated pentacene and pentacene in the 7×4 and 6×3 supercells without TMDs, shown as a heat map on the molecular plane. Circular black points mark the atomic positions of carbon atoms. Positions between atomic sites are interpolated for grid plotting. There is no large difference between the systems, all showing a mild bowling effect where the outer hydrogen atoms are offset from the carbon rings, which themselves are deflected from the position of the central ring. The scale here is very small: the maximum deviation from the molecular plane is only 1.02 mÅ.

When in heterostructure, however, we see two different effects occur depending on molecular concentration. These can be seen in Figure 6.8. In the low concentration regime, there is an increased deflection from the molecular plane, with an exaggeration of the bowl shape of isolated pentacene: the middle carbon ring is closer to the substrate than the outer rings or hydrogen atoms. Note the change in scale for the heat maps of Figures 6.7 and 6.8. In the high concentration regime the clear bowling effect was lost, with larger overall deviation but with effects that are dependent on the underlying substrate structure, although each heterostructure in this concentration regime was investigated in a different adsorption site. The exception was PEN/WS₂, which favored the same adsorption site as the 7×4 systems. When adsorbed on MoS₂, in the Top-TM site, there is some twisting of the pentacene. The central ring is higher on one side than the other,

with the deviation across that ring being greater than the outer rings. This is due to the Top-TM site here having shifted slightly to between Top-TM and Hollow, and a clear loss of symmetry in underlying substrate atom across the long axis of the pentacene molecule. With the MoSe₂ substrate, in the Bridge-B adsorption site, there is a similar lack of symmetry in underlying substrate atom across the long axis of pentacene, and there is again some minor twisting. In PEN/WSe₂, there was a slight reversal of the bowling effect that was seen in the 7 × 4 systems, with the central carbon ring sitting further from the underlying substrate than the hydrogen atoms, as well as some lateral warping.

When we instead investigated the atomic deviation of high concentration pentacene in the Top-Ch adsorption site, instead of whichever was most favorable, we saw that pentacene adopts the bowling effect seen in the low concentration regime. This confirms that the warping effects are due to the adsorption site rather than other TMD-specific interactions. The corresponding image can be seen in Appendix I. The bowling effect described is not well reported for pentacene in the literature, presumably due to the very small deviations from flat-lying geometry for isolated pentacene, but it has been noted in N-phenylenes which are broadly similar in structure [148].

We see that pentacene within molybdenum systems experienced more deformation in the higher concentration regime than the lower, with an increase in both the mean and the maximum values of atomic deviation from the molecular plane. Conversely, pentacene in heterostructure with the tungsten dichalcogenides experienced a decrease in mean and maximum atomic deviation. Appendix I contains a summary table of the mean and maximum atomic deviations from the molecular plane for each heterostructure, and a comparison of these across concentration regimes. However, where these deviations occur is not described by such data.

Substrate deformation due to heterostructure formation

Upon adsorption of pentacene, the underlying TMD undergoes slight deformation as well as the molecule. This deformation can again contribute to the adsorption energy and changes in frontier orbital energies, but we did not decouple the effect from the molecule-

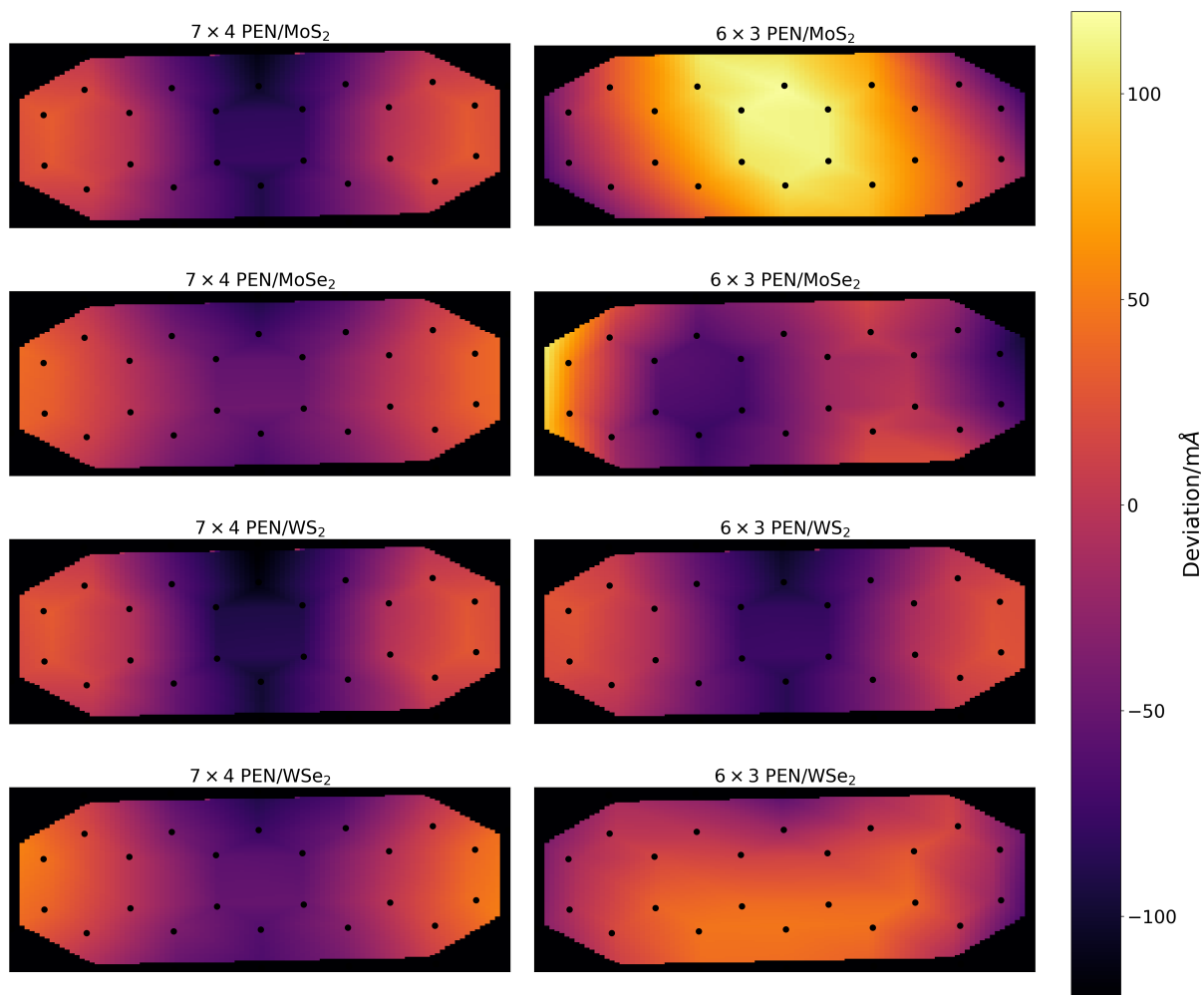


Figure 6.8: The deviation of pentacene atoms from the molecular plane for pentacene in heterostructure, shown as a heat map. Circular black points mark the atomic positions of carbon atoms. The 7×4 systems show a clear bowling effect, with the central carbon ring closer to the substrate than the outer hydrogen atoms by approximately 0.1 \AA . The effects noted in the high concentration regime are TMD-specific.

substrate interaction in the case of frontier orbital energies. TMD bond length changes were all small, and slightly larger in the 7×4 systems due to smaller layer separation.

Table 6.15 shows the contribution of substrate deformation to adsorption energy for each heterostructure between concentration regimes, as well as their difference, representing the effect of increasing molecular concentration on the energetic contribution of substrate deformation to E_{ads} . We see that PEN/WS₂ in the low concentration regime experiences quite a large contribution towards its adsorption energy from substrate deformation of 88 meV, acting to strengthen molecular adsorption. This may be due to the size of tungsten and the small layer separation, which was the closest binding out of all unrotated systems. The other heterostructures had substrate deformations that opposed pentacene adsorption. In the high concentration regime, PEN/WS₂ was now more in line with the other heterostructures. PEN/WSe₂ was the only one that strengthened adsorption, but in all cases the effect magnitude was small. As the heterostructures in the high concentration regime experienced a very small contribution to their adsorption energies from substrate deformation, the difference between concentration regimes was most extreme for PEN/WS₂. In the other systems, increased molecular concentration acted to change substrate deformation in such a way as to oppose pentacene adsorption less.

Table 6.15: The contributions to E_{ads} of substrate deformation effects, in meV, in PEN/TMD heterostructures across the concentration regimes, as well as their difference. A positive difference represents a more positive (oppositional) contribution with an increase in concentration.

Heterostructure	7×4	6×3	Δ
PEN/MoS ₂	12	2	-10
PEN/MoSe ₂	8	2	-6
PEN/WS ₂	-88	3	91
PEN/WSe ₂	4	-5	-9

A summary of transition metal-chalcogen bond length changes between TMDs in heterostructure and pristine TMDs is provided in Table 6.16, as well as the difference between effects across concentration regimes. Bond contraction was observed underneath the pentacene molecule, and subsequent lengthening necessarily occurred elsewhere to

maintain fixed cell parameters, with the maximum lengthening occurring near areas of bond contraction. The effect is consistently small throughout the structure.

Table 6.16: Changes in transition metal and upper layer chalcogen bond lengths from their lengths in TMDs without adsorbed pentacene, in mÅ, in unrotated heterostructures across the concentration regimes, as well as their difference.

Heterostructure	7×4	6×3	Δ
Maximum bond contraction			
PEN/MoS ₂	3.7	3.6	-0.1
PEN/MoSe ₂	4.5	4.1	-0.4
PEN/WS ₂	4.3	3.9	-0.4
PEN/WSe ₂	6.4	4.8	-1.6
Maximum bond lengthening			
PEN/MoS ₂	4.7	2.3	-2.4
PEN/MoSe ₂	3.3	2.9	-0.4
PEN/WS ₂	4.1	3.5	-0.6
PEN/WSe ₂	1.6	2.4	0.8

Work function

Finally, we looked at the change in work function, $\Delta\phi$, of TMDs due to the adsorption of pentacene. A comparison of this change between pentacene concentrations is given in Table 6.17, where we see that the effect of increasing pentacene concentration is to decrease the effect that pentacene adsorption has on the work function.

Table 6.17: The change in work function, $\Delta\phi$, of the TMD due to unrotated pentacene adsorption, in eV, across the concentration regimes, as well as their difference.

Heterostructure	7×4	6×3	Δ
PEN/MoS ₂	0.59	0.56	-0.03
PEN/MoSe ₂	0.44	0.40	-0.04
PEN/WS ₂	0.34	0.33	-0.01
PEN/WSe ₂	0.18	0.15	-0.03

6.2 Investigating pentacene rotation

The effect of adsorbate rotation was investigated by rotating the pentacene molecule about its center of mass in the plane of the monolayer substrate. This was done for each PEN/TMD system across both concentrations with the most favorable adsorption site. We considered counterclockwise rotation angles of 30° , 60° and 90° , resulting in systems with varying relationships to underlying TM-Ch bonds, as described at the beginning of this chapter. Following rotation, we performed `relax` calculations to optimize the new geometry. Rotated geometry, before relaxation, is displayed in Figure 6.9.

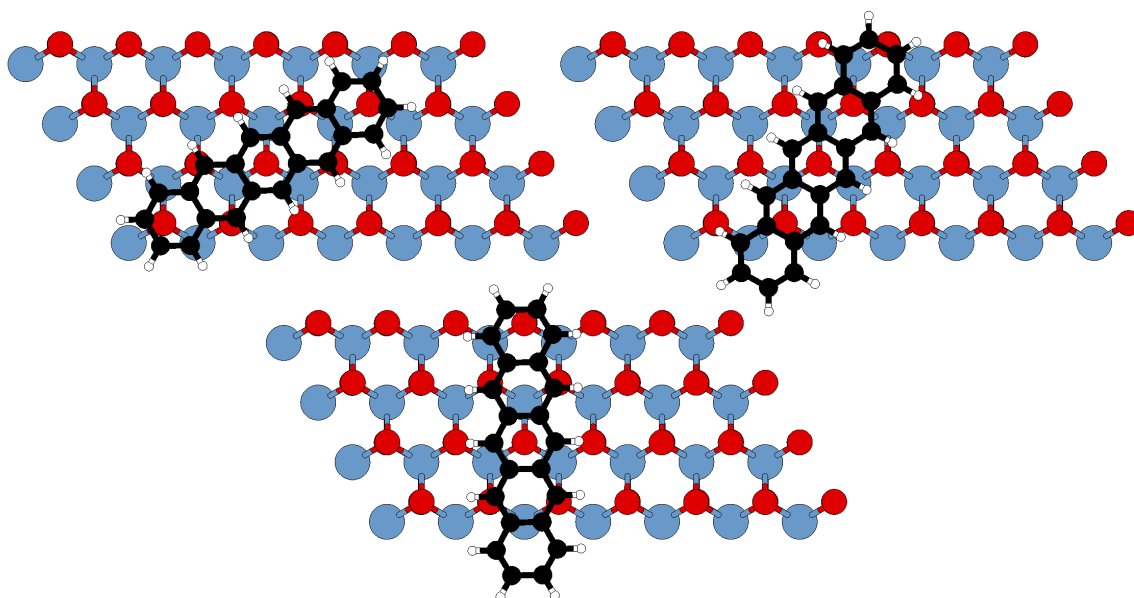


Figure 6.9: The rotation of pentacene, measured counterclockwise from the 0° case, being defined as pentacene's long axis being aligned with the supercell's x-axis (and therefore the underlying substrate). From top-left, clockwise: 30° , 60° , 90° . 30° and 90° angles share the same relationship between pentacene atoms underlying substrate atoms, but with different molecule-molecule spatial relationships across the periodic boundaries. The same is true for the angle of 60° and the unrotated case.

6.2.1 Low concentration pentacene heterostructures: structure

Within the 7×4 heterostructures, Top-Ch was found to be the most favorable adsorption site throughout. Using the relaxed geometry of these long-axis aligned systems (referred to here as 0° systems), we rotated the pentacene and again relaxed the resulting structures. All systems were stable under relaxation around their initial angles of rotation. The

minimum molecule-molecule distance for the 0° systems were previously determined to be 6.2 Å and 6.5 Å for sulfur and selenide systems, respectively. With 30° of rotation these distances were 5.2 Å and 6.0 Å for sulfur and selenide systems, 5.9 Å and 6.3 Å with 60° rotation for sulfur and selenide systems, and 1.9 Å and 2.5 Å with 90° sulfur and selenide systems. Rotate pentacene systems have only a small number of carbon atoms located over chalcogens on the substrate layer, so all rotation angles experience similar steric repulsion as do the unrotated systems.

We found that all four PEN/TMD systems were more energetically favorable at a rotation of 60° , where all but PEN/WSe₂ was next most favorable at 0° and least favorable at 30° . The differences in total system energies compared to the most favorable rotation angle are presented in Table 6.18. We found that layer separation was very similar between the most favorable rotation angle of 60° and the previously determined 0° systems. The layer separations of 60° systems were 3.309 Å, 3.400 Å, 3.296 Å, and 3.388 Å, for PEN/MoS₂, PEN/MoSe₂, PEN/WS₂ and PEN/WSe₂, respectively. The only differences between the layer separation of favorably rotated systems and the unrotated systems are in PEN/WS₂ and PEN/WSe₂, of a small 1 mÅ and 10 mÅ, respectively.

Table 6.18: The difference in total energy, in eV, between rotations of PEN/TMD heterostructures with low concentration pentacene and their most favorable rotation angle.

Heterostructure	0°	30°	60°	90°
PEN/MoS ₂	0.001	0.029	0.000	0.020
PEN/MoSe ₂	0.001	0.039	0.000	0.003
PEN/WS ₂	0.002	0.037	0.000	0.029
PEN/WSe ₂	0.355	0.045	0.000	0.011

The mobility between rotation angles is fairly high, again, excepting PEN/WSe₂, with differences between most and next most favorable angles being only 1 meV for the molybdenum systems and 2 meV for PEN/WS₂. The difference between most and least favorable angles is 29 meV for PEN/MoS₂, 39 meV for PEN/MoSe₂, and 37 meV for PEN/WS₂. PEN/WSe₂, however, is next most favorable with 90° rotation by 11 meV, and least favorable at 0° , by a large 355 meV. These values imply that, with the exception of PEN/WSe₂, the adsorbed molecule is mobile within its z-axis rotational degree of

freedom, with reduced mobility as it rotated from 0° to 30° , near which it finds a local minima (as all rotation angles we used as relaxation inputs were stable) in adsorption energy. Beyond this energy barrier lies another local minima around 60° of rotation, with yet another around 90° . We additionally note that, again excepting PEN/WSe₂, the adsorption energies of 0° and 60° are very similar, as are those of 30° and 90° . These angles of rotation naturally form pairs, where if considering a single molecule on and infinite underlying substrate, they are equivalent with to their counterpart: the only difference arises from the unequal spacing between molecules in the x- and y-directions that arises from our choice of supercell dimensions. The small discrepancies in energy, then, between 0° and 60° of 1-2 meV and between 30° and 60° of 9-36 meV are due to molecule-molecule interaction effects. The larger difference between 30° and 90° observed in PEN/MoSe₂ of 36 meV is due to the relative favorability of 90° of rotation in this system compared to the others: PEN/MoSe₂ has the largest supercell dimensions, and the largest molecule-molecule distance. We see also that a rotation of 90° in the PEN/WSe₂ heterostructure is relatively more favorable than in the sulfur systems due to the larger supercell and molecule-molecule separation.

The contributions to the adsorption energy of favorably rotated (60°) 7×4 systems from molecule-molecule interactions, molecule-substrate interactions, and molecule and substrate deformation effects were calculated in the same manner as described in Section 5.1, and are displayed in Table 6.19.

Table 6.19: Contributions to the adsorption energy of favorably rotated 7×4 heterostructures in their favorable adsorption site from molecule-molecule, molecule-substrate, molecule deformation and substrate deformation effects, in eV. Molecule-substrate interaction is consistently the largest contribution across all systems.

	PEN _{60°} /MoS ₂	PEN _{60°} /MoSe ₂	PEN _{60°} /WS ₂	PEN _{60°} /WSe ₂
molecule-molecule interaction	-0.005	-0.003	-0.005	-0.004
molecule-substrate interaction	-1.393	-1.422	-1.439	-1.461
molecule deformation	-0.007	-0.010	-0.006	-0.009
substrate deformation	0.006	0.001	0.100	-0.346

Expectedly, molecule-substrate interaction is the overwhelming majority contributor to adsorption energy in the rotated systems, as this includes the van der Waals interaction,

but we found that in tungsten systems the substrate deformation effects were only an order of magnitude smaller than molecule-substrate interaction effects. Substrate deformation effects contribute 346 meV to the adsorption energy in $\text{PEN}_{60^\circ}/\text{WSe}_2$, and in the case of $\text{PEN}_{60^\circ}/\text{WS}_2$, they oppose heterostructure formation by 100 meV. In the unrotated systems, heterostructures of the TMDs except WS_2 have substrate deformation effects that oppose heterostructure formation, but the effects are much smaller (see Table 5.4). Molecule-molecule interaction is similar to that of unrotated systems in the low concentration regime.

The atomic deviation of the pentacene molecule within rotated systems was again examined. We found a mean atomic deviation of 40 mÅ from the molecular plane within the $\text{PEN}_{60^\circ}/\text{MoS}_2$ heterostructure, with a maximum atomic deviation of 112 mÅ, occurring at the middle of the molecule. Pentacene within $\text{PEN}_{60^\circ}/\text{MoSe}_2$ had a mean atomic deviation of 34 mÅ with a maximum of 88 mÅ, also at the middle of the molecule. For the $\text{PEN}_{60^\circ}/\text{WS}_2$ heterostructure, we observed a very similar change in structure, with a mean atomic deviation from the molecular plane of 43 mÅ, and a maximum atomic deviation of 123 mÅ, again at the middle of the molecule. The $\text{PEN}_{60^\circ}/\text{WSe}_2$ heterostructure did not behave differently, with a mean atomic deviation of 41 mÅ and a maximum of 97 mÅ, again occurring at the middle of the pentacene molecule. These values are all very similar to the unrotated structures: within 1 mÅ except for $\text{PEN}_{60^\circ}/\text{WSe}_2$, which is within 8 mÅ. Carbon-carbon bond lengths in pentacene again barely changed, with differences of approximately 0.1% with the formation of heterostructure, regardless of the substrate, and the substrate itself experienced similar bond length changes of less than 0.1% as a result of the addition of pentacene.

We found the largest TM-Ch bond contraction to be 4.0 mÅ, 5.2 mÅ, 5.5 mÅ and 5.7 mÅ compared to the TMD out of heterostructure, an increase of 8%, 16%, 28% and a decrease of 10% compared to the contraction observed in the unrotated structures for $\text{PEN}_{60^\circ}/\text{MoS}_2$, $\text{PEN}_{60^\circ}/\text{MoSe}_2$, $\text{PEN}_{60^\circ}/\text{WS}_2$, and $\text{PEN}_{60^\circ}/\text{WSe}_2$ heterostructures, respectively. This again occurred underneath the pentacene molecule. Bond lengthening was observed in surrounding bonds, the maximum of which was 4.2 mÅ, 3.8 mÅ, 4.4

mÅ, and 0.9 mÅ for PEN_{60°}/MoS₂, PEN_{60°}/MoSe₂, PEN_{60°}/WS₂, and PEN_{60°}/WSe₂ heterostructures, respectively. This represents a decrease of 11% and 44% in the cases of PEN_{60°}/MoS₂ and PEN_{60°}/WSe₂, and an increase of 15% and 7% in the cases of PEN_{60°}/MoSe₂ and PEN_{60°}/WS₂.

6.2.2 Low concentration pentacene heterostructures: electronic properties

The favorably rotated low concentration pentacene systems then had their electronic properties investigated. The results of density of states calculations for these systems are displayed in Figure 6.10.

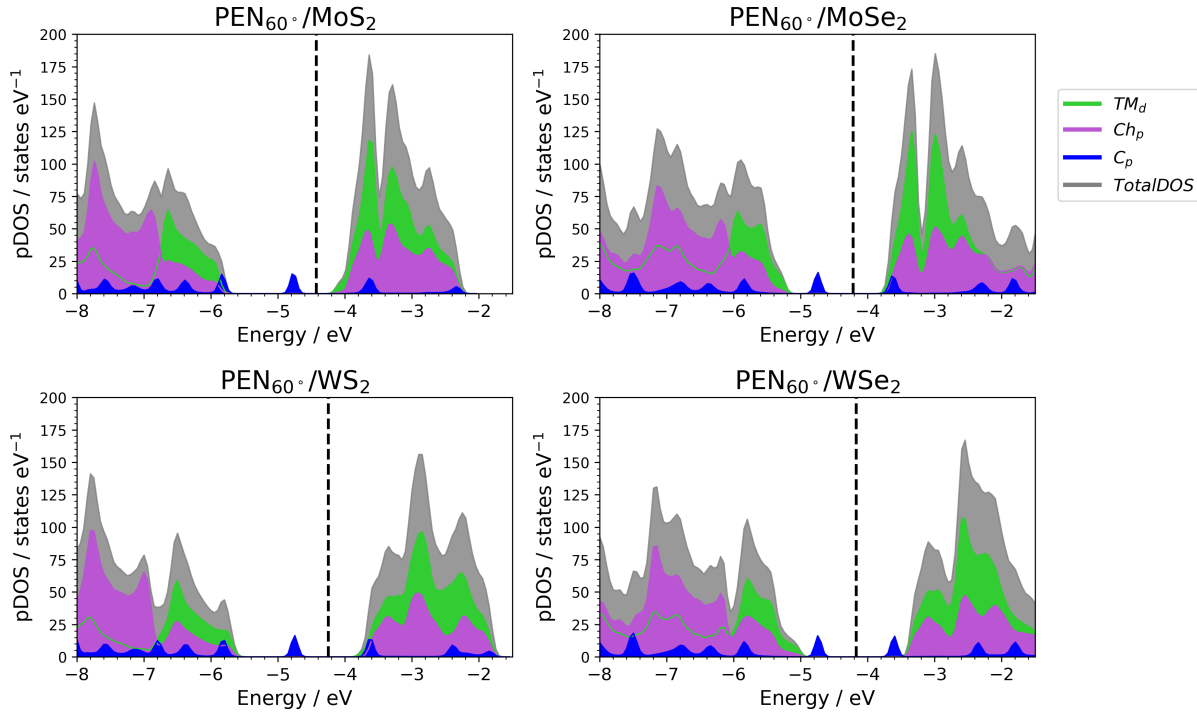


Figure 6.10: The density of states of favorably rotated 7×4 PEN/TMD heterostructures, with the Fermi energies given by the vertical black dashed line.

We saw no additional effects that would change band alignment between the density of states of unrotated and rotated systems, with comparable contributions from atomic orbitals, but we do note a second carbon p-orbital state within the TMD band gap of PEN_{60°}/MoS₂. In this heterostructure there are therefore two density of states peaks contributed by pentacene’s carbon atoms within the TMD band gap: the HOMO and

another orbital around -5.75 eV, whereas the TMD’s VBM is at -5.80 eV. This does not affect the band alignment, as both orbitals are occupied. We see again that pentacene’s HOMO sits further within the TMD band gap for the sulfur systems than the selenium systems, and pentacene’s LUMO is energetically higher than the TMD’s CBM in the case of all systems except $\text{PEN}_{60^\circ}/\text{WSe}_2$, which forms a Type-I heterostructure. The HOMO and LUMO energies of pentacene within these heterostructures, along with the TMD VBM and CBM energies are presented in Table 6.20.

Table 6.20: Frontier orbital energies and their difference, Δ , in eV, of favorably rotated 7×4 PEN/TMD heterostructures. The values presented here are from density of states calculations, and so have a precision only of 0.05 eV.

Heterostructure	PEN		TMD		Δ	
	HOMO	LUMO	VBM	CBM	HOMO-VBM	LUMO-CBM
$\text{PEN}_{60^\circ}/\text{MoS}_2$	-4.70	-3.80	-5.80	-4.20	1.10	0.40
$\text{PEN}_{60^\circ}/\text{MoSe}_2$	-4.65	-3.75	-5.20	-3.80	0.55	0.05
$\text{PEN}_{60^\circ}/\text{WS}_2$	-4.65	-3.75	-5.60	-3.80	0.95	0.05
$\text{PEN}_{60^\circ}/\text{WSe}_2$	-4.65	-3.70	-4.95	-3.45	0.30	-0.25

We again examined the work function of the heterostructures, and can calculate the reduction in work function, ϕ (Equation 5.9), of the TMDs due to formation of the heterostructures in the same manner as in subsection 5.2.2, with results displayed in Table 6.21.

Table 6.21: Work function of the TMDs and their favorably rotated 7×4 PEN/TMD heterostructures, as well as the change in work function due to pentacene adsorption in the rotated position, $\Delta\phi = \phi_{\text{TMD}} - \phi_{\text{PEN/TMD}}$.

TMD	$\phi_{\text{TMD}}/\text{eV}$	$\phi_{\text{PEN/TMD}}/\text{eV}$	$\Delta\phi/\text{eV}$
MoS_2	5.01	4.43	0.58
MoSe_2	4.65	4.21	0.44
WS_2	4.59	4.25	0.34
WSe_2	4.35	4.17	0.18

The introduction of permitted pentacene orbitals into the TMD band gap results in an increase in the Fermi energy, reducing the work function. The change in work function being more pronounced in sulfur systems agrees with this observation, where the selenium systems with the smaller difference between pentacene’s HOMO and the TMD’s VBM (see Table 6.20) experience a smaller change in work function.

6.2.3 High concentration pentacene heterostructures: structure

Within the 6×3 heterostructures, the favorability of adsorption site varied. We had previously found that PEN/MoS₂ is most favorable in the Top-TM site, PEN/MoSe₂ is most favorable in the Bridge-B site, PEN/WS₂ is most favorable in the Top-Ch site, and PEN/WSe₂ is most favorable in the Bridge-A site (see Table 6.1 and Table 6.8). We only considered rotation within the most favorable site for each heterostructure, where we rotated the pentacene molecule by 30°, 60°, and 90°, then relaxed the resulting structure. With the higher molecular concentration, the 90° rotation was unstable: PEN_{90°}/MoS₂ relaxed to a pentacene angle of rotation of 79°, PEN_{90°}/WS₂ to 70°, and both PEN_{90°}/MoSe₂ and PEN_{90°}/WSe₂ to 74°. We will continue to refer to the systems as having been rotated by 90°, but they did not remain there, in contrast to the 7×4 systems. 30° and 60° rotations were stable and remained at their rotation angles following geometry optimization.

With 30° of rotation, the minimum molecule-molecule distance was 2.3 Å in PEN_{30°}/MoS₂, 2.4 Å in PEN_{30°}/WS₂, and 3.0 Å in the selenide systems. 60° rotated pentacene resulted in minimum molecule-molecule distances of 3.2 Å, 3.5 Å, 3.1 Å, and 3.4 Å, for heterostructures of MoS₂, MoSe₂, WS₂, and WSe₂, respectively. 90° systems all had a minimum molecule-molecule distance of 2.3 Å, except PEN_{90°}/WSe₂, which was 2.2 Å.

We found that the molybdenum systems were more favorable unrotated. We had already investigated these structures, with the results reported in Section 6.1. Tungsten systems, however, were most favorable with a pentacene rotation angle of 60°, the same as in the low concentration regime. The differences in total system energies compared to the most favorable rotated system are presented in Table 6.22. The layer separations of the tungsten systems with 60° rotated pentacene were 3.322 Å and 3.462 Å, for WS₂ and WSe₂ systems, respectively. This gives a difference in layer separation between the unrotated and favorably rotated WS₂ systems of 2 mÅ, and a difference of 18 mÅ between the WSe₂ systems.

Table 6.22: The difference in total energy, in eV, between rotations of PEN/TMD heterostructures with high concentration pentacene and their most favorable rotation angle.

Heterostructure	0°	30°	60°	90°
PEN/MoS ₂	0.000	0.090	0.162	0.159
PEN/MoSe ₂	0.000	0.052	0.081	0.032
PEN/WS ₂	0.006	0.034	0.000	0.048
PEN/WSe ₂	0.076	0.045	0.000	0.015

The mobility between rotation angles was lower in the molybdenum systems, which preferred no rotation, than in the tungsten systems. PEN/MoS₂ is least mobile through rotation, with the next most favorable rotation angle of 30° being 90 meV less favorable than the unrotated case, and 60° being the least favorable, separated energetically by 162 meV. PEN/MoSe₂ is next most favorable at 90° of rotation (although following relaxation this angle is only 74°) with a difference between it and the most favorable unrotated case of 32 meV, and the least favorable 60° case differing by 81 meV. Only PEN/WS₂ has a difference between most and next most favorable rotation angle of the order of meV, but this is between 60° and 0°: these are closely related geometrically, as previously discussed at the beginning of this chapter, but are physically separated by the relatively unfavorable angles of 30° and 90°, the latter of which is least favorable and differs from the most favorable by 48 meV. PEN/WSe₂ is least favorable in the unrotated case, with a differential of 76 meV, and next most favorable at 90(74)° by 15 meV.

The contributions to the adsorption energy of favorably rotated 6×3 systems from molecule-molecule interactions, molecule-substrate interactions, and molecule and substrate deformation effects were calculated in the same manner as described in Section 5.1, and are displayed in Table 6.23.

Table 6.23: Contributions to the adsorption energy of favorably rotated 6×3 heterostructures in their favorable adsorption site from molecule-molecule, molecule-substrate, molecule deformation and substrate deformation effects, in eV. Molecule-substrate interaction is consistently the largest contribution across all systems.

	PEN _{60°} /WS ₂	PEN _{60°} /WSe ₂
molecule-molecule interaction	-0.065	-0.038
molecule-substrate interaction	-1.393	-1.422
molecule deformation	-0.009	-0.007
substrate deformation	0.003	-0.218

We see once again that molecule-substrate interactions are the largest contributor to the adsorption energy. In the high concentration rotated case, we see that molecule-molecule interactions take on a relatively large role, an order of magnitude larger than the low concentration rotated case (see Table 6.19), and similar to the high concentration unrotated case (see Table 6.4). Molecule deformation effects again play a larger role in the WSe₂ system, with a contribution of 218 meV.

The mean atomic deviation of pentacene from the molecular plane within the PEN_{60°}/WS₂ was found to be 39 mÅ with a maximum deviation of 94 mÅ at the center of the molecule. Pentacene within the PEN_{60°}/WSe₂ heterostructure experienced a mean atomic deviation of 20 mÅ and the maximum deviation was 50 mÅ, located on one side of one of the carbon rings next out from the central ring. This indicated some small amount of twisting. These values are similar to the unrotated case for high concentration pentacene. Carbon-carbon and carbon-hydrogen bond lengths are again effectively unchanged.

The largest TM-Ch bond contraction was again located underneath the pentacene molecule, and compared to the TMDs out of heterostructure was found to be 4.2 mÅ and 5.0 mÅ: an increase of 8% and 4% from the unrotated cases for PEN_{60°}/WS₂ and PEN_{60°}/WSe₂ heterostructures, respectively. Bond lengthening, observed at its maximum in nearby bonds again, was maximally 3.6 mÅ and 0.4 mÅ for PEN_{60°}/WS₂ and PEN_{60°}/WSe₂ heterostructures, respectively. This represents a change from the unrotated case of 3% for PEN_{60°}/WS₂. With very little bond lengthening anywhere in the PEN_{60°}/WSe₂ heterostructure, there is a decrease in maximum bond lengthening

between unrotated and favorably rotated 6×3 PEN/WSe₂ systems of 83%.

6.2.4 High concentration pentacene heterostructures: electronic properties

The 6×3 PEN_{60°}/WS₂ and PEN_{60°}/WSe₂ heterostructures then had their electronic properties investigated. Their density of states are displayed in Figure 6.11.

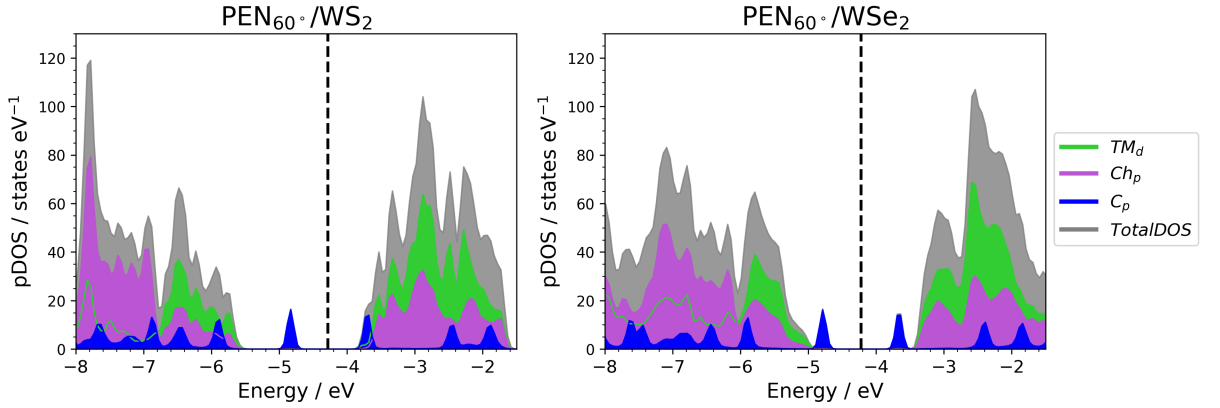


Figure 6.11: The density of states of favorably rotated 6×3 PEN/TMD heterostructures, with the Fermi energies given by the vertical black dashed line.

We saw no effects from the rotation of pentacene that change band alignment, and note broadly the same structure as before; the Fermi energy sits slightly energetically higher within the TMD band gap in the case of the sulfur system, as pentacene’s HOMO energy is further in to the gap. PEN_{60°}/WS₂ maintains its Type-II heterojunction, although is again close to a transition to Type-I as it is in the unrotated case, and indeed the low concentration case. PEN_{60°}/WSe₂ is a Type-I heterostructure, no different than the unrotated or high concentration cases. The frontier orbitals are displayed in Table 6.24.

Table 6.24: Frontier orbital energies and their difference, Δ , in eV, of favorably rotated 6×3 PEN/TMD heterostructures. The values presented here are from density of states calculations, and so have a precision only of 0.05 eV.

Heterostructure	PEN		TMD		Δ	
	HOMO	LUMO	VBM	CBM	HOMO-VBM	LUMO-CBM
PEN _{60°} /WS ₂	-4.75	-3.80	-5.60	-3.85	0.85	0.05
PEN _{60°} /WSe ₂	-4.70	-3.80	-5.00	-3.45	0.30	-0.35

The change in reduction in work function, ϕ (Equation 5.9), from heterostructure formation with rotated pentacene was again calculated as in subsection 5.2.2, with results displayed in Figure 6.25.

Table 6.25: Work function of the TMDs and their favorably rotated 6×3 PEN/TMD heterostructures, as well as the change in work function due to pentacene adsorption in the rotated position, $\Delta\phi = \phi_{\text{TMD}} - \phi_{\text{PEN/TMD}}$.

TMD	$\phi_{\text{TMD}}/\text{eV}$	$\phi_{\text{PEN/TMD}}/\text{eV}$	$\Delta\phi/\text{eV}$
WS ₂	4.59	4.28	0.31
WSe ₂	4.35	4.22	0.13

As has been the case for unrotated high concentration systems, the introduction of pentacene’s HOMO into the TMD band gap results in a reduction in the work function due to pentacene adsorption and subsequent increase in the Fermi energy.

6.2.5 Comparison of pentacene rotation angles

Structural favorability

Investigating the effects of rotation on adsorption energy and layer separation, we see from Table 6.26 that rotation only has a small effect on most systems. Rotational mobility is high, and the effect on layer separation of rotation of pentacene is minor. The exception is PEN/WSe₂ in the low concentration regime, where substrate deformation effects of a magnitude not seen in other systems result in a much more favorable heterostructure when pentacene is rotated by 60°. This was not observed in the unrotated case. Overall, the difference in adsorption energy between concentrations is relatively small, but when allowing for rotation PEN/WSe₂ greatly favors the low concentration regime. Within concentration regimes, rotating the pentacene molecule only greatly affects E_{ads} in the PEN/WSe₂ system.

Table 6.26: The adsorption energies, E_{ads} , and layer separations, d , of the heterostructures compared across pentacene angles of rotations, as well as the effect of rotation on these parameters.

Heterostructure	0°		60°		Δ	
	E_{ads}/eV	$d/\text{\AA}$	E_{ads}/eV	$d/\text{\AA}$	$E_{\text{ads}}/\text{meV}$	$d/\text{m\AA}$
7×4						
PEN/MoS ₂	-1.389	3.309	-1.390	3.309	-1	0
PEN/MoSe ₂	-1.424	3.400	-1.425	3.400	-1	0
PEN/WS ₂	-1.434	3.297	-1.436	3.296	-2	-1
PEN/WSe ₂	-1.458	3.378	-1.813	3.388	-355	10
6×3						
PEN/WS ₂	-1.454	3.321	-1.460	3.322	-6	1
PEN/WSe ₂	-1.606	3.480	-1.682	3.462	-76	-18

Within the low concentration regime, all PEN/TMD heterostructures favored a pentacene rotation angle of 60° , where adsorption energies decreased slightly between unrotated and PEN_{60°}/TMD systems, with differences of 1 meV, 1 meV and 2 meV for PEN/MoS₂, PEN/WSe₂, and PEN/WS₂, respectively. PEN/WSe₂ was notably more favorable through all rotation angles, with the most favorable again being 60° , with a difference in E_{ads} between that and the unrotated case of a much larger 355 meV. Differences in layer separation between the 0° and 60° systems were small, only noticed in the tungsten systems where they are 10 mÅ.

A summary of the structural properties of 7×4 heterostructures with unrotated and favorably rotated (60°) pentacene is given in Table 6.27. We can see that there are no large changes in any of the parameters, which is reflected in the minimal changes of the electronic properties.

Table 6.27: A structural comparison of PEN/TMD heterostructures of the 7×4 unrotated and 7×4 favorably rotated structures. All systems have pentacene in the Top-Ch adsorption site. Molecule-molecule interaction energies here are that which contributes to E_{ads} .

	PEN/MoS ₂	PEN/MoSe ₂	PEN/WS ₂	PEN/WSe ₂
0°				
Adsorption Energy (E_{ads} /eV)	-1.39	-1.42	-1.43	-1.46
$d/\text{\AA}$	3.31	3.40	3.30	3.38
Minimum molecule-molecule distance/ \AA	6.2	6.5	6.2	6.5
Molecule-molecule interaction/eV	-0.004	-0.003	-0.004	-0.003
60°				
Adsorption Energy/eV	-1.39	-1.42	-1.43	-1.81
$d/\text{\AA}$	3.31	3.40	3.30	3.39
Minimum molecule-molecule distance/ \AA	5.9	6.3	5.9	6.3
Molecule-molecule interaction/eV	-0.005	-0.003	-0.005	-0.004

Within the high concentration regime, molybdenum systems were most favorable at a molecular angle of 0°. Tungsten systems, in the same manner as for the 7×4 heterostructures, were most favorable with a pentacene angle of 60°. The differences in E_{ads} here are 6 meV and 76 meV for PEN/WS₂ and PEN/WSe₂, respectively.

A summary of the structural properties of 6×3 heterostructures with unrotated and favorably rotated (60°) pentacene is given in Table 6.28. We can see that there is a small decrease in the minimum molecule-molecule distances and a subsequent increase in molecule-molecule interaction contribution to the adsorption energy of the PEN/WS₂ heterostructures with rotation of pentacene.

Table 6.28: A structural comparison of PEN/TMD heterostructures of the 6×3 unrotated and 6×3 favorably rotated structures. Molecule-molecule interaction energies here are that which contributes to E_{ads} .

	PEN/WS ₂	PEN/WSe ₂
Adsorption site	Top-Ch	Bridge-A
0°		
Adsorption Energy (E_{ads} /eV)	-1.45	-1.61
$d/\text{\AA}$	3.32	3.48
Minimum molecule-molecule distance/ \AA	3.4	3.7
Molecule-molecule interaction/eV	-0.056	-0.038
60°		
Adsorption Energy/eV	-1.46	-1.68
$d/\text{\AA}$	3.32	3.46
Minimum molecule-molecule distance/ \AA	3.1	3.4
Molecule-molecule interaction/eV	-0.065	-0.038

In the low concentration case, pentacene rotation did not lead to changes in frontier orbital energies within the pentacene or TMDs, within the precision of our density of states calculations. The only change to pentacene’s frontier orbitals resulting from rotation within the high concentration regime was a decrease of the HOMO in PEN_{60°}/WS₂ of 0.05 eV compared to that of the unrotated case. This is not enough to cause band alignment changes: the HOMO-VBM alignment was consistently robust, and the LUMO-CBM alignment is where any changes may occur.

Molecule-substrate interaction effects

The effect of molecular rotation on the contribution of molecule-substrate interactions to the adsorption energy is displayed in Table 6.29, and mostly shows only a small change due to rotation. The PEN/WS₂ systems experience a larger change in effect of approximately 7% in the low concentration case, increasing in contribution to E_{ads}.

Table 6.29: The contributions to E_{ads} of molecule-substrate interactions, in eV, compared across pentacene rotation angles, as well as their difference. A positive difference represents a more positive (oppositional) contribution with rotation to 60°.

Heterostructure	0°	60°	Δ
7×4			
PEN/MoS ₂	-1.402	-1.393	0.009
PEN/MoSe ₂	-1.423	-1.422	0.001
PEN/WS ₂	-1.340	-1.439	-0.099
PEN/WSe ₂	-1.452	-1.461	-0.009
6×3			
PEN/WS ₂	-1.347	-1.393	-0.046
PEN/WSe ₂	-1.422	-1.422	0.000

Similarly, we can compare the effect of molecular rotation on frontier orbital energies. Tables 6.30 and 6.31 show the effect of molecular rotation on the molecule-substrate contribution to the pentacene and TMD frontier orbital energies, respectively. The effect of rotation on pentacene’s frontier orbitals is only noted in the high concentration systems, with a larger effect on the LUMO. The effect of rotation on the TMD frontier orbitals is zero within our precision for all but the CBM of 7×4 PEN/WS₂ and the VBM of 6×3 PEN/WSe₂, where it is instead of magnitude 0.05 eV.

Table 6.30: The effect on pentacene’s frontier orbitals from molecule-substrate interactions and material deformation, in eV, in heterostructures across angles of rotation for pentacene (a negative value represents a decrease in orbital energy due to these effects) and the modulation of these effects due to rotation. Deformation effects are a smaller contribution to E_{ads} than molecule-substrate interaction effects.

Heterostructure	0°		60°		Δ	
	HOMO	LUMO	HOMO	LUMO	HOMO	LUMO
7×4						
PEN/MoS ₂	-0.25	-0.30	-0.25	-0.30	0.00	0.00
PEN/MoSe ₂	-0.20	-0.25	-0.20	-0.25	0.00	0.00
PEN/WS ₂	-0.20	-0.25	-0.20	-0.25	0.00	0.00
PEN/WSe ₂	-0.20	-0.20	-0.20	-0.20	0.00	0.00
6×3						
PEN/WS ₂	-0.15	-0.20	-0.15	-0.15	0.00	0.05
PEN/WSe ₂	-0.15	-0.20	-0.10	-0.15	0.05	0.10

Table 6.31: The effect on the TMD’s frontier orbitals from molecule-substrate interactions and material deformation, in eV, in heterostructures across angles of rotation for pentacene (a negative value represents a decrease in orbital energy due to these effects) and the modulation of these effects due to rotation. Deformation effects are a smaller contribution to E_{ads} than molecule-substrate interaction effects.

Heterostructure	0°		60°		Δ	
	VBM	CBM	VBM	CBM	VBM	CBM
7×4						
PEN/MoS ₂	0.10	0.00	0.10	0.00	0.00	0.00
PEN/MoSe ₂	0.10	0.00	0.10	0.00	0.00	0.00
PEN/WS ₂	0.10	0.00	0.10	0.05	0.00	0.05
PEN/WSe ₂	0.10	0.00	0.10	0.00	0.00	0.00
6×3						
PEN/WS ₂	0.10	0.00	0.10	0.00	0.00	0.00
PEN/WSe ₂	0.10	0.00	0.05	0.00	-0.05	0.00

Overall we see that the molecule-substrate interaction component of the effect of molecular rotation on frontier orbital energies is negligible for most systems, with small effects on pentacene’s orbitals in the high concentration regime.

Molecule-molecule interaction effects

The effect of molecular rotation on molecule-molecule interaction effects is displayed in Table 6.32, where we see that molecular rotation in the low concentration regime affects

only a small change on the molecule-molecule interaction contribution to E_{ads} , which is of maximum magnitude 1 meV. In the high concentration regime, this contribution is increased in magnitude by 6 meV in the PEN/WS₂ heterostructure, with no change in the PEN/WSe₂ heterostructure.

Table 6.32: The contributions to E_{ads} of molecule-molecule interactions, in meV, compared across pentacene rotation angles, as well as their difference. A positive difference represents a more positive (oppositional) contribution with rotation to 60°.

Heterostructure	0°	60°	Δ
7×4			
PEN/MoS ₂	-4	-5	-1
PEN/MoSe ₂	-3	-3	0
PEN/WS ₂	-4	-5	-1
PEN/WSe ₂	-3	-4	-1
6×3			
PEN/WS ₂	-59	-65	-6
PEN/WSe ₂	-38	-38	0

Overall, we see that the effects of increasing concentration and molecular rotation on the contribution to E_{ads} from molecule-molecule interactions are relatively large, with increasing concentration increasing the contribution by an order of magnitude, but absolutely small when compared to the molecule-substrate interaction contribution.

Similarly, we can examine the effect of molecular rotation by comparing the rotated molecule to the unrotated molecule in a supercell of the same size. This is displayed in Table 6.33, where we can see that there are not significant enough changes in molecule-molecule interaction effects with molecular rotation in the low concentration regime to affect a change in frontier orbital energies, but in the high concentration case there are. This effect is to reduce both frontier orbital energies by 0.05 eV.

Table 6.33: The effect of molecular rotation on pentacene’s frontier orbitals from molecule-molecule interactions, in eV, in both concentration regimes (a negative value represents a decrease in orbital energy due to changes in these effects through rotation).

Heterostructure	0°		60°		Δ	
	HOMO	LUMO	HOMO	LUMO	HOMO	LUMO
PEN _{7×4}	-0.10	-0.10	-0.10	-0.10	0.00	0.00
PEN _{6×3}	-0.20	-0.20	-0.25	-0.25	-0.05	-0.05

Molecular deformation due to heterostructure formation

Changes in atomic deviation of pentacene from the molecular plane are fairly minor with rotation, with mean and maximum atomic deviations being similar, and the overall bowling effect being maintained. A heat map of atomic deviation for favorably rotated systems across both concentration regimes is displayed in Figure 6.12.

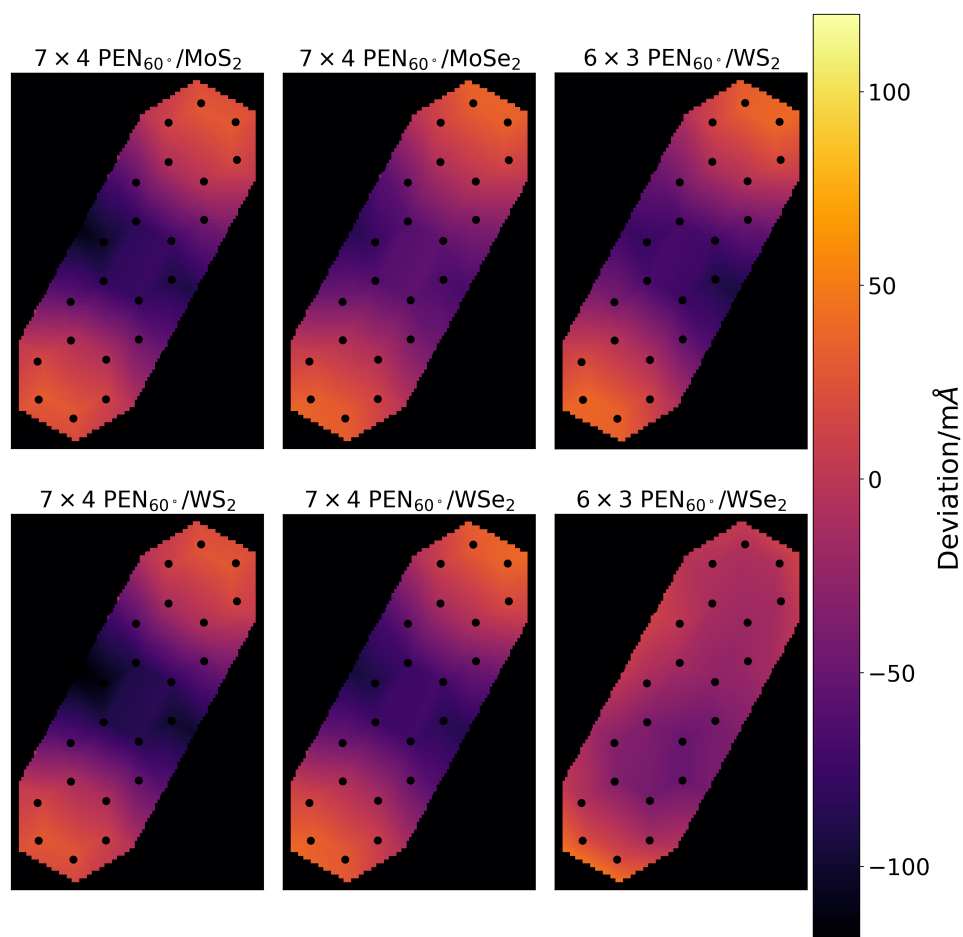


Figure 6.12: The deviation of pentacene atoms from the molecular plane for favorably rotated pentacene in heterostructure, shown as a heat map. Circular black points mark the atomic positions of carbon atoms. The 7×4 systems and $\text{PEN}_{60^\circ}/\text{WS}_2$ show a clear bowling effect, but of lesser magnitude than the unrotated 7×4 systems in Figure 6.8. There is some bowling, skewed from the center, in the high concentration $\text{PEN}_{60^\circ}/\text{WSe}_2$ heterostructure.

Changes in the atomic deviation of pentacene within the PEN/WS_2 heterostructure due to rotation lead to the bowling effect noted in all 7×4 heterostructures, whereas when unrotated we observed bowling in the opposite direction: the middle carbon ring was further from the substrate than the extremities. This is reversed with rotation of 60° .

PEN/WSe₂ had a similar magnitude of deviation between rotation angles, but moves closer to the bowl shape of the low concentration systems in the 60° case. This can be seen in Figure 6.12.

The effect of molecular rotation on the contribution of molecular deformation towards adsorption energies is displayed in Table 6.34. We see that the effect size is small throughout, being zero in the high pentacene concentration systems and at most only a modulation of 12 meV in the case of low molecular concentration PEN/MoS₂.

Table 6.34: The contributions to E_{ads} of molecule deformation, in meV, compared across pentacene rotation angles, as well as their difference. A positive difference represents a more positive (oppositional) contribution with rotation to 60°.

Heterostructure	0°	60°	Δ
<hr/>			
7 × 4			
PEN/MoS ₂	5	-7	-12
PEN/MoSe ₂	-7	-3	4
PEN/WS ₂	-3	-6	-3
PEN/WSe ₂	-7	-9	-2
<hr/>			
6 × 3			
PEN/WS ₂	-9	-9	0
PEN/WSe ₂	-7	-7	0
<hr/>			

When considering the effect of rotation, we noted that the 7 × 4 systems maintain their bowl shape upon rotation, with PEN/MoS₂ shown in Figure 6.13 as representative of the others, which can be found in Appendix I.

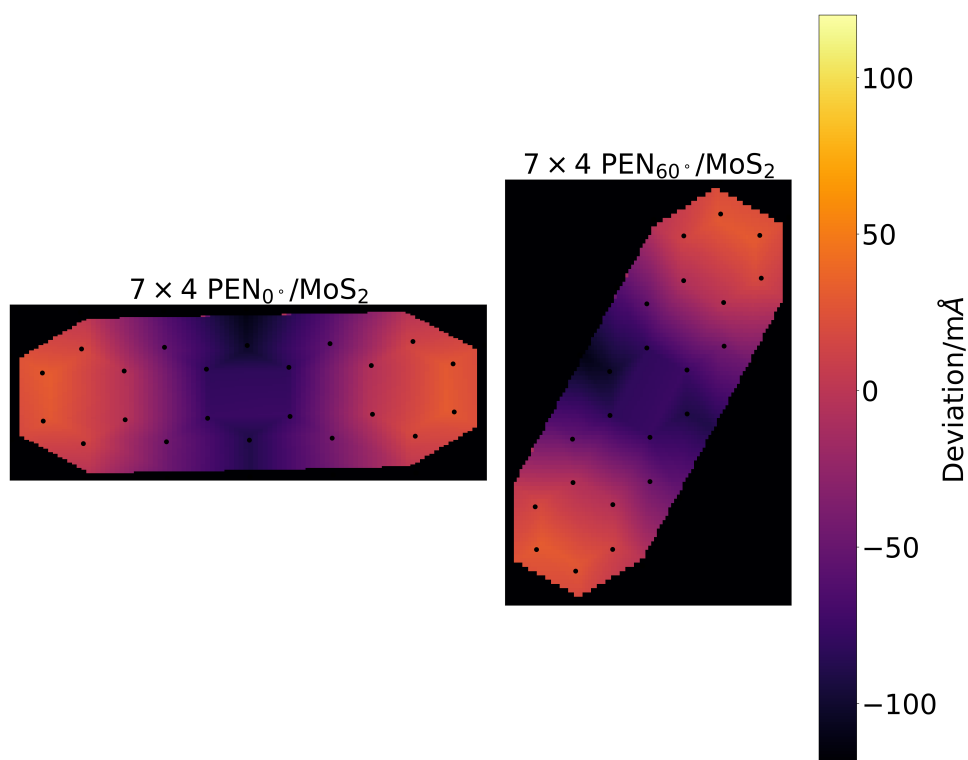


Figure 6.13: Heat maps of the atomic deviation from the molecular plane in the pentacene molecules of 7×4 PEN/MoS₂ heterostructures, with 0° and favorable (60°) rotation angles. We can see a bowling effect in both cases, with the central carbon ring being closer to the TMD substrate (a negative deviation from the molecular plane). This is broadly representative of all 7×4 systems, with only minor differences in the magnitude of deviation.

The high concentration PEN_{60°}/WS₂ system maintains the bowling effect (Figure 6.14), and the PEN_{60°}/WSe₂ system remains slightly twisted but closer in general to the bowled shape (Figure 6.15). We recall that PEN/WS₂ was most favorable in the Top-Ch adsorption site across both concentration regimes, which explains why it adopts the bowl shape noted in all 7×4 systems as discussed in subsection 6.1.3.

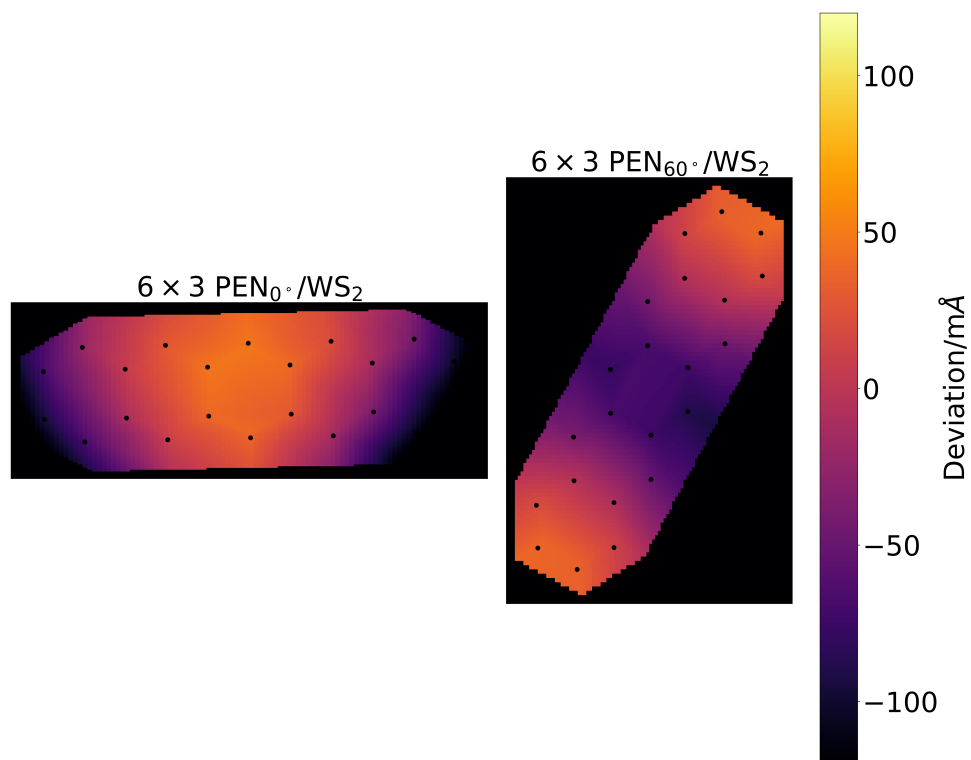


Figure 6.14: Heat maps of the atomic deviation from the molecular plane in the pentacene molecules of $6 \times 3 \text{ PEN} / \text{WS}_2$ heterostructures, with 0° and favorable (60°) rotation angles. The unrotated case shows a bowling effect, but inverted from that in the 7×4 systems, and the rotated case demonstrates the same bowl shape as 7×4 systems, but slightly less extreme. These are in the Top-Ch adsorption site, which was most favorable for high concentration PEN / WS_2 .

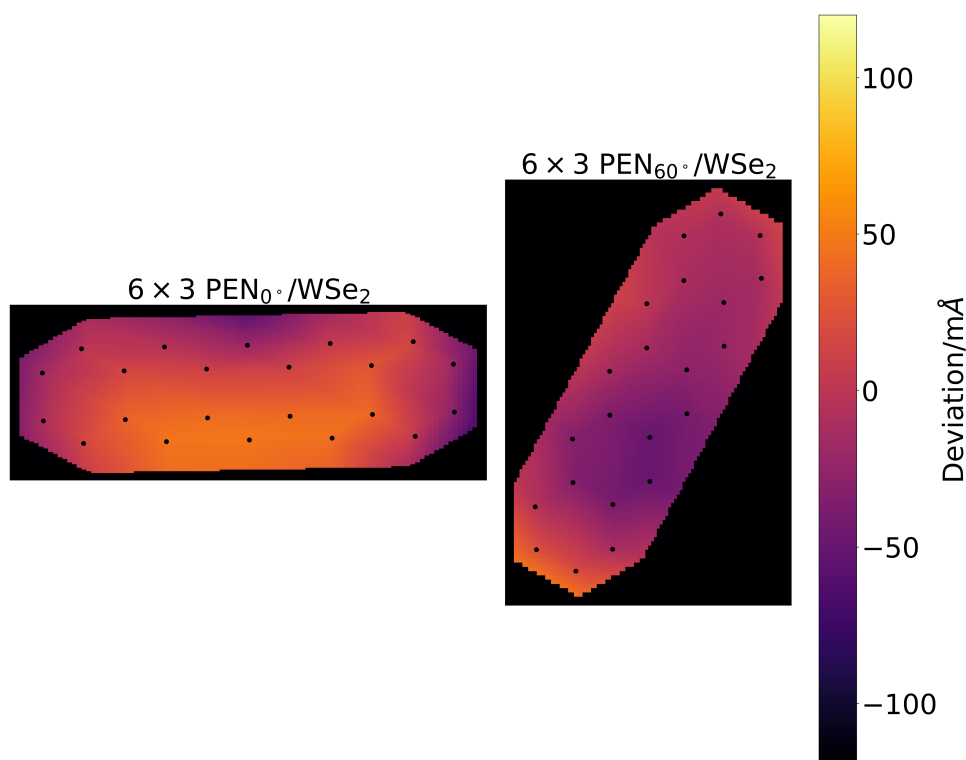


Figure 6.15: Heat maps of the atomic deviation from the molecular plane in the pentacene molecules of 6×3 PEN/WSe₂ heterostructures, with 0° and favorable (60°) rotation angles. The unrotated case shows a warping effect with one side of the pentacene lifting and twisting, and the rotated case demonstrates a movement towards the same bowl shape as 7×4 systems, but does not quite adopt it entirely. These are in the Bridge-A adsorption site, which was most favorable for high concentration PEN/WSe₂.

Substrate deformation due to heterostructure formation

Similarly looking at the effect of molecular rotation, we see differing effects between substrates and pentacene concentrations, presented in Table 6.35. The low concentration regime molybdenum systems see only small modulation of the substrate deformation contribution to E_{ads} due to molecular rotation, as does the high concentration PEN/WS₂ heterostructure. The low concentration tungsten systems, however, experience modulations of opposite effects. PEN/WS₂ substrate deformation, which greatly increased the strength of unrotated molecular adsorption, greatly opposes rotated adsorption, whereas PEN/WSe₂ was unremarkable in the unrotated case but very strongly assists in rotated molecular adsorption. It is this effect that leads to such strong adsorption in this system compared to the others. Similarly, high concentration rotated pentacene adsorption is assisted by WSe₂ deformation as well.

Table 6.35: The contributions to E_{ads} of substrate deformation, in meV, compared across pentacene rotation angles, as well as their difference. A positive difference represents a more positive (oppositional) contribution with rotation to 60° .

Heterostructure	0°	60°	Δ
7×4			
PEN/MoS ₂	12	6	-6
PEN/MoSe ₂	8	1	-7
PEN/WS ₂	-88	100	188
PEN/WSe ₂	4	-346	-350
6×3			
PEN/WS ₂	3	3	0
PEN/WSe ₂	-5	-218	-213

A summary of transition metal-chalcogen (upper layer) bond length changes between TMDs in heterostructure and pristine TMDs are provided in Table 6.36, for changes across rotation regimes. Bond contraction was observed underneath the pentacene molecule, and subsequent lengthening necessarily occurred elsewhere to maintain fixed cell parameters, with the maximum lengthening occurring near areas of bond contraction.

In the low concentration tungsten systems, which exhibited large changes in substrate deformation contributions to E_{ads} with molecular rotation and, in the case of PEN/WS₂, concentration, we see no outstanding distinction from the molybdenum systems. This is also true for high concentration PEN/WSe₂ upon rotation, with maximum bond length changes with rotation being only slightly larger than the other systems. It is important to note that, similarly to pentacene deviation data, the maximum values reported here do not capture the entire effect: the pattern of bond length changes, where they occur, and in what cardinal direction the corresponding atomic position deviations occur in are all important metrics.

Table 6.36: Changes in transition metal and upper layer chalcogen bond lengths from their lengths in TMDs without adsorbed pentacene, in mÅ, in heterostructures across pentacene rotation angles, as well as their difference.

Heterostructure	0°	60°	Δ
7×4			
Maximum bond contraction			
PEN/MoS ₂	3.7	4.0	0.3
PEN/MoSe ₂	4.5	5.2	0.7
PEN/WS ₂	4.3	5.5	1.2
PEN/WSe ₂	6.4	5.7	-0.7
Maximum bond lengthening			
PEN/MoS ₂	4.7	4.2	-0.5
PEN/MoSe ₂	3.3	3.8	0.5
PEN/WS ₂	4.1	4.4	0.3
PEN/WSe ₂	1.6	0.9	-0.7
6×3			
Maximum bond contraction			
PEN/WS ₂	3.9	4.2	0.3
PEN/WSe ₂	4.8	5.0	0.2
Maximum bond lengthening			
PEN/WS ₂	3.5	3.6	0.1
PEN/WSe ₂	2.4	0.4	-2.0

Work function

The effect of molecular rotation on the change in work function is presented in Table 6.37, where we see little or no effect in the low concentration regime, and an effect similar in magnitude to increasing concentration in the high concentration regime, which is also small.

Table 6.37: The change in work function, $\Delta\phi$, of the TMD due to pentacene adsorption, in eV, across rotation angles, as well as their difference.

Heterostructure	0°	60°	Δ
7×4			
PEN/MoS ₂	0.59	0.58	-0.01
PEN/MoSe ₂	0.44	0.44	0.00
PEN/WS ₂	0.34	0.34	0.00
PEN/WSe ₂	0.18	0.18	0.00
6×3			
PEN/WS ₂	0.33	0.31	-0.02
PEN/WSe ₂	0.15	0.13	-0.02

Chapter 7

Conclusion

In this project we have investigated the structural and electronic properties of van der Waals heterostructures comprised of pentacene in two different concentration regimes adsorbed on TMD substrates. We considered the effects of adsorption on the physical structure and density of states of the materials, and differences in these effects due to the concentration of pentacene and the rotation of pentacene with respect to the underlying substrate. Varying concentrations and rotation angles results in varying spatial relationships between pentacene and substrate, and pentacene and other pentacene molecules, leading to a change in heterostructure properties. We have attempted to identify which changes are due to which relationship.

Ultimately, we have shown that pentacene forms stable heterostructures with all four TMDs investigated, in both concentration regimes. Rotation of pentacene is also stable, but with varying favorability. As such, we expect laboratory samples to express multiple pentacene adsorption sites and rotation angles, but with some specific adsorption geometries being more common. The largest contribution to the adsorption energies is the molecule-substrate interaction, which would be expected as this includes van der Waals attraction. Molecule-molecule interactions are much more pronounced in the high concentration regime due to the closer approach of pentacene molecules to each other, and these act to increase adsorption energy. Substrate deformation plays a fairly large role in the selenium systems, and molecule deformation effects are consistently small. Nevertheless, we were able to describe small changes to pentacene's geometry due to

adsorption, although these were of such low magnitude that we would still consider pentacene to be effectively flat lying.

In terms of device creation, we have shown that a PEN/MoS₂ heterostructure forms a robust Type-II heterojunction in both concentration regimes, with low concentration PEN/MoSe₂ and PEN/WS₂ heterostructures also forming Type-II heterojunctions, but with a smaller difference between the TMD's CBM and pentacene LUMO in these cases. The effect of using HSE calculations is not expected to change this band alignment, instead acting to increase pentacene's LUMO by a larger amount than they should increase the TMD's CBM (in some cases decreasing the TMD's CBM). Low concentration PEN/WSe₂ is predicted to form a robust straddling (Type-I) heterojunction, with increasing pentacene concentration or rotation not changing orbital energies by enough to transition to Type-II. In the high concentration regime, we predict a small shift in frontier orbitals, acting to change the band alignment in favor of Type-I heterojunctions. There is enough of a change in the case of PEN/MoSe₂ to cause a concentration-dependent heterojunction transition from Type-II in the low concentration regime to Type-I in the high concentration regime. Molecule-molecule interactions are responsible for slight decreases in pentacene's LUMO, with an expectedly greater effect in the high concentration regime. In combination with the reduced molecule-substrate interactions that act to decrease the CBM of MoSe₂ in the high concentration regime, resulting in a higher CBM than in the low concentration regime, we see that the concentration-dependent heterojunction type transition in PEN/MoSe₂ is not due to only one effect.

7.1 Future projects within the materials group and investigations of interest

Over the course of this project, a few branching paths appeared as potential choices for how this investigation should develop. We chose those which seemed most interesting, but of course a single project does not encompass all work that may go on within a research group. Here we present a few suggestions for interesting future investigations (without claims as to the suitability of such work for a self-contained PhD project), that if performed here would have amounted only to excursus.

It seems clear that the most favorable molecular adsorption site is related to the spatial relationship between pentacene's carbon rings and underlying substrate structure, and we believe that the higher molecular concentration may exacerbate any 'phase differences' between successive carbon rings and their underlying substrate structure by increasing the depth of potential wells experienced by pentacene along the plane of the chalcogen surface; this results in something almost analogous to a lattice mismatch between carbon rings and TMD 'rings' that develops over the length of the pentacene molecule. If this is indeed the case, one may expect to see a change of adsorption site favorability with strain. Investigating variously strained heterostructures would allow calculations on systems of differing supercell sizes without being limited to integer numbers of molecular units as we were here.

While we considered a range of different substrates, we did not investigate any different adsorbates. Perfluoropentacene is a potential alternative to pentacene, where it forms similar thin films and has a similar band gap energy [149]. Also of interest may be other polycyclic aromatic hydrocarbons such as anthracene or tetracene, both organic semiconductors. Similarly, there are a wide variety of transition-metal dichalcogenides that were not investigated, but would not have been unreasonable to include if not for limitations of scope. Foremost amongst these is molybdenum ditelluride, MoTe_2 , an

indirect band gap semiconductor in bulk, which a transition to direct upon exfoliation to bi- or monolayer structure [150], the same as our TMDs here.

Something that was not feasible with the resources available to our project (but that might provide some entertainment to somebody with infinite computational resources at their disposal) is to perform our calculations using a higher level of theory or a higher level of control. This could be as simple as performing the heterostructure calculations with hybrid functionals, or using much larger supercells with multiple pentacene molecules in each one, allowing for a combination of binding sites and rotation angles. We do not believe that using a level of theory such as HSE would result in qualitatively different conclusions, but perhaps combinations of different sites and angles would. We did not entertain this idea for long.

A more reasonable suggestion may be to continue using DFT, but to investigate thin films of pentacene on monolayer and bilayer TMDs. Pentacene thin films condense to a herringbone structure, which can necessitate fairly large supercells in certain specific structures. These calculations would be laborious, but more in line with the structures that an experimentalist may be interested in, at least until they figure out how to create true van der Waals ‘Lego’ structures.

Appendix A

Central equation

The derivation of the central equation (Equation 2.30) begins with a wavefunction expressed as its Fourier series expansion of the sum of all allowed wavevectors, and the periodic potential, also expressed as a Fourier series of all allowed wavevectors with a periodicity of the lattice (see subsection 2.1.2):

$$\psi(\mathbf{r}) = \sum_{\mathbf{k}} C_{\mathbf{k}} e^{i\mathbf{k}\cdot\mathbf{r}} \quad (\text{A.1})$$

$$U_{\mathbf{r}} = \sum_{\mathbf{G}} U_{\mathbf{G}} e^{i\mathbf{G}\cdot\mathbf{r}} . \quad (\text{A.2})$$

The kinetic energy term of the time-independent Schrödinger equation (Equation 2.1) is

$$-\frac{\hbar^2}{2m} \nabla^2 \psi(\mathbf{r}) = \frac{\hbar^2}{2m} \sum_{\mathbf{k}} k^2 C_{\mathbf{k}} e^{i\mathbf{k}\cdot\mathbf{r}} , \quad (\text{A.3})$$

and the potential energy term is

$$U(\mathbf{r})\psi(\mathbf{r}) = \left(\sum_{\mathbf{G}} U_{\mathbf{G}} e^{i\mathbf{G}\cdot\mathbf{r}} \right) \psi(\mathbf{r}) = \sum_{\mathbf{G}} \sum_{\mathbf{k}} U_{\mathbf{G}} C_{\mathbf{k}} e^{i(\mathbf{k}+\mathbf{G})\cdot\mathbf{r}} . \quad (\text{A.4})$$

As the sums over \mathbf{k} are infinite and as \mathbf{G} is a reciprocal lattice vector, we can substitute in $\mathbf{w}' = (\mathbf{k} + \mathbf{G})$, where summation over \mathbf{w}' is the same as summation over \mathbf{k} :

$$U(\mathbf{r})\psi(\mathbf{r}) = \sum_{\mathbf{G}} \sum_{\mathbf{w}'} U_{\mathbf{G}} C_{\mathbf{w}'-\mathbf{G}} e^{i\mathbf{w}'\cdot\mathbf{r}} . \quad (\text{A.5})$$

We are free to make the substitution $\mathbf{k} = \mathbf{w}'$ using the same reasoning:

$$U(\mathbf{r})\psi(\mathbf{r}) = \sum_{\mathbf{G}} \sum_{\mathbf{k}} U_{\mathbf{G}} C_{\mathbf{k}-\mathbf{G}} e^{i\mathbf{k}\cdot\mathbf{r}} , \quad (\text{A.6})$$

and so the time-independent Schrödinger equation is then

$$\frac{\hbar^2}{2m} \sum_{\mathbf{k}} k^2 C_{\mathbf{k}} e^{i\mathbf{k}\cdot\mathbf{r}} + \sum_{\mathbf{G}} \sum_{\mathbf{k}} U_{\mathbf{G}} C_{\mathbf{k}-\mathbf{G}} e^{i\mathbf{k}\cdot\mathbf{r}} - E \sum_{\mathbf{k}} C_{\mathbf{k}} e^{i\mathbf{k}\cdot\mathbf{r}} = 0 . \quad (\text{A.7})$$

As the Born-von Karman boundary condition requires, the plane waves $e^{i\mathbf{k}\cdot\mathbf{r}}$ are an orthogonal set. We multiply our Schrödinger equation by $e^{-i\mathbf{w}'\cdot\mathbf{r}}$ and integrate over the unit cell, where \mathbf{w}' is a wavevector belonging to the set of \mathbf{k} wavevectors:

$$\begin{aligned} \frac{\hbar^2}{2m} \int_{\text{cell}} \sum_{\mathbf{k}} k^2 C_{\mathbf{k}} e^{i\mathbf{k}\cdot\mathbf{r}} e^{-i\mathbf{k}\cdot\mathbf{r}} d\mathbf{r} + \int_{\text{cell}} \sum_{\mathbf{G}} \sum_{\mathbf{k}} U_{\mathbf{G}} C_{\mathbf{k}-\mathbf{G}} e^{i\mathbf{k}\cdot\mathbf{r}} e^{-i\mathbf{k}\cdot\mathbf{r}} d\mathbf{r} \\ - E \int_{\text{cell}} \sum_{\mathbf{k}} C_{\mathbf{k}} e^{i\mathbf{k}\cdot\mathbf{r}} e^{-i\mathbf{k}\cdot\mathbf{r}} d\mathbf{r} = 0 . \end{aligned} \quad (\text{A.8})$$

Due to the orthogonality of our vectors, their inner products evaluate to either 0 or a volume constant which can be divided out, so is set to 1 here:

$$\int_{\text{cell}} e^{i\mathbf{k}\cdot\mathbf{r}} e^{-i\mathbf{w}'\cdot\mathbf{r}} d\mathbf{r} = \begin{cases} 1, & \mathbf{k} = \mathbf{w}' \\ 0, & \mathbf{k} \neq \mathbf{w}' \end{cases} . \quad (\text{A.9})$$

As such, the sums over \mathbf{k} only count the terms where $\mathbf{k} = \mathbf{w}'$, and we now have

$$\frac{\hbar^2}{2m} k^2 C_{\mathbf{k}} + \sum_{\mathbf{G}} U_{\mathbf{G}} C_{\mathbf{k}-\mathbf{G}} - E C_{\mathbf{k}} = 0 . \quad (\text{A.10})$$

Gathering terms and making the substitution for $\lambda_{\mathbf{k}}$, we arrive at the central equation (Equation 2.30),

$$(\lambda_{\mathbf{k}} - E) C_{\mathbf{k}} + \sum_{\mathbf{G}} U_{\mathbf{G}} C_{\mathbf{k}-\mathbf{G}} = 0 , \quad (\text{A.11})$$

where

$$\lambda_{\mathbf{k}} = \frac{\hbar^2 k^2}{2m} . \quad (\text{A.12})$$

For some uses, this is better displayed in an equivalent form, where we make the notational substitution $\mathbf{G} \rightarrow \mathbf{G}'$,

$$(\lambda_{\mathbf{k}} - E) C_{\mathbf{k}} + \sum_{\mathbf{G}'} U_{\mathbf{G}'} C_{\mathbf{k}-\mathbf{G}'} = 0 \quad (\text{A.13})$$

and then let $\mathbf{k} = \mathbf{k}' - \mathbf{G}$:

$$(\lambda_{\mathbf{k}'-\mathbf{G}} - E) C_{\mathbf{k}'-\mathbf{G}} + \sum_{\mathbf{G}'} U_{\mathbf{G}'} C_{\mathbf{k}'-\mathbf{G}-\mathbf{G}'} = 0 . \quad (\text{A.14})$$

We make the variable substitution $\mathbf{G}' \rightarrow \mathbf{G}' - \mathbf{G}$, and note that as both \mathbf{G} and \mathbf{G}' are reciprocal lattice vectors, a sum over the difference between them is the same as the sum over either of them:

$$(\lambda_{\mathbf{k}'-\mathbf{G}} - E) C_{\mathbf{k}'-\mathbf{G}} + \sum_{\mathbf{G}'} U_{\mathbf{G}'-\mathbf{G}} C_{\mathbf{k}'-\mathbf{G}} = 0 , \quad (\text{A.15})$$

and finally the notational substitution of $\mathbf{k}' \rightarrow \mathbf{k}$ produces the variation of the central equation that we use in Section 2.2,

$$(\lambda_{\mathbf{k}-\mathbf{G}} - E) C_{\mathbf{k}-\mathbf{G}} + \sum_{\mathbf{G}'} U_{\mathbf{G}'-\mathbf{G}} C_{\mathbf{k}-\mathbf{G}} = 0 . \quad (\text{A.16})$$

Appendix B

Bloch electron velocity

Consider electrons in a system as described in subsection 2.1.2, in which subsection we claimed that the Bloch theorem predicts a non-vanishing mean electronic velocity in the periodic lattice. Here we will demonstrate the reasoning for this claim. If the system is perturbed by some potential, V , the eigenvalues of the Hamiltonian $H = H_0 + V$, where the unperturbed Hamiltonian has eigenvalues ϵ_n^0 , are

$$\epsilon_n = \epsilon_n^0 + \langle \psi | V | \psi \rangle + \dots \quad (\text{B.1})$$

We only need consider the first-order term here, as we will consider the first derivative with respect to k of $\epsilon_n(\mathbf{k})$. The Taylor expansion of $\epsilon_n(\mathbf{k} + \mathbf{q})$, up to the linear term in \mathbf{q} and centered on \mathbf{k} and with \mathbf{q} being our small perturbation, is

$$\epsilon_n(\mathbf{k} + \mathbf{q}) = \epsilon_n(\mathbf{k}) + \sum_i \frac{\delta \epsilon_n}{\delta k_i} q_i + \dots \quad (\text{B.2})$$

By applying the (unperturbed) Hamiltonian to a Bloch wavefunction, we can simplify it to exclude the exponential term and only consider the periodic function, $u_{n\mathbf{k}}$:

$$\begin{aligned}
H\psi &= \epsilon\psi = -\frac{\hbar^2}{2m}\nabla^2\psi + U\psi = -\frac{\hbar^2}{2m}e^{i\mathbf{k}\cdot\mathbf{r}}u_{n\mathbf{k}} + U\psi \\
&= -\frac{\hbar^2}{2m}\left[\nabla\cdot(i\mathbf{k}e^{i\mathbf{k}\cdot\mathbf{r}}u_{n\mathbf{k}}) + e^{i\mathbf{k}\cdot\mathbf{r}}\nabla u_{n\mathbf{k}}\right] + Ue^{i\mathbf{k}\cdot\mathbf{r}}u_{n\mathbf{k}} \\
&= -\frac{\hbar^2}{2m}\left[-k^2e^{i\mathbf{k}\cdot\mathbf{r}}u_{n\mathbf{k}} + 2i\mathbf{k}e^{i\mathbf{k}\cdot\mathbf{r}}\nabla u_{n\mathbf{k}} + e^{i\mathbf{k}\cdot\mathbf{r}}\nabla^2 u_{n\mathbf{k}}\right] + Uu_{n\mathbf{k}} \\
&= e^{i\mathbf{k}\cdot\mathbf{r}}\left[\frac{\hbar^2}{2m}(\nabla^2 - 2i\mathbf{k}\cdot\nabla + k^2) + U\right]\cdot u_{n\mathbf{k}} = e^{i\mathbf{k}\cdot\mathbf{r}}\left[\frac{\hbar^2}{2m}(\mathbf{k} - i\nabla)^2 + U\right]\cdot u_{n\mathbf{k}}.
\end{aligned} \tag{B.3}$$

Dividing by $e^{i\mathbf{k}\cdot\mathbf{r}}$ allows us to extract a simplified Hamiltonian in \mathbf{k} for use on Bloch systems;

$$H_{\mathbf{k}}u_{n\mathbf{k}} = \epsilon_n(\mathbf{k})u_{n\mathbf{k}} = \left[\frac{\hbar^2}{2m}(\mathbf{k} - i\nabla)^2 + U\right]\cdot u_{n\mathbf{k}} \tag{B.4}$$

and therefore

$$H_{\mathbf{k}} = \frac{\hbar^2}{2m}[(\mathbf{k} - i\nabla)^2 + U]. \tag{B.5}$$

As $\epsilon_n(\mathbf{k})$ is an eigenvalue of $H_{\mathbf{k}}$, our perturbed energy from before, $\epsilon_n(\mathbf{k} + \mathbf{q})$, must be an eigenvalue of $H_{\mathbf{k}+\mathbf{q}}$:

$$\begin{aligned}
H_{\mathbf{k}+\mathbf{q}} &= \frac{\hbar^2}{2m}[(\mathbf{k} + \mathbf{q} - i\nabla)^2 + U] \\
&= \frac{\hbar^2}{2m}(-\nabla^2 - 2i\mathbf{k}\cdot\nabla + k^2 + q^2 - 2i\mathbf{q}\cdot\nabla + 2\mathbf{k}\cdot\mathbf{q}) + U \\
&= \frac{\hbar^2}{2m}(-\nabla^2 - 2i\mathbf{k}\cdot\nabla + k^2) + U + \frac{\hbar^2}{2m}(q^2 - 2i\mathbf{q}\cdot\nabla + 2\mathbf{k}\cdot\mathbf{q}) \\
&= H_{\mathbf{k}} + \frac{\hbar^2}{2m}(q^2 - 2i\mathbf{q}\cdot\nabla + 2\mathbf{k}\cdot\mathbf{q}) = H_{\mathbf{k}} + \frac{\hbar^2}{m}\mathbf{q}\cdot(\mathbf{k} - i\nabla) + \frac{\hbar^2 q^2}{2m}.
\end{aligned} \tag{B.6}$$

This is of the form $H = H_0 + V$, where $V = \frac{\hbar^2}{m}\mathbf{q}\cdot(\mathbf{k} - i\nabla) + \frac{\hbar^2 q^2}{2m}$. As such, we can substitute this in to the first-order term of our perturbed energy eigenvalue, where we only need the the term linear in \mathbf{q} . This expression is equal to the linear term in \mathbf{q} of the Taylor expansion of $\epsilon_n(\mathbf{k} + \mathbf{q})$ and is represented as a sum over all elements of \mathbf{q} :

$$\sum_i \frac{\delta \epsilon_n}{\delta k_i} q_i = \sum_i \langle \psi | V_i | \psi \rangle = \sum_i \int_{\text{cell}} u_{n\mathbf{k}}^* \frac{\hbar^2}{m} (\mathbf{k} - i\nabla) q_i u_{n\mathbf{k}} d\mathbf{r} . \quad (\text{B.7})$$

The integration is over the space that $u_{n\mathbf{k}}$ is normalized over, we construct the functions such that this is the primitive cell. As the dependence of V on \mathbf{q} has been represented as a scalar sum over q_i , $i \in \mathbb{Z}$, we can divide by q_i , eliminate the summation and express in terms of $\psi_{n\mathbf{k}}$ through Bloch's theorem (Equation 2.33):

$$\begin{aligned} \frac{\delta \epsilon_n}{\delta \mathbf{k}} &= \int_{\text{cell}} u_{n\mathbf{k}}^* \frac{\hbar^2}{m} (\mathbf{k} - i\nabla) u_{n\mathbf{k}} d\mathbf{r} = \frac{\hbar^2}{m} \int_{\text{cell}} e^{i\mathbf{k}\cdot\mathbf{r}} \psi_{n\mathbf{k}}^* (\mathbf{k} - i\nabla) e^{-i\mathbf{k}\cdot\mathbf{r}} \psi_{n\mathbf{k}} d\mathbf{r} \\ &= \frac{\hbar^2}{m} \int_{\text{cell}} e^{i\mathbf{k}\cdot\mathbf{r}} \psi_{n\mathbf{k}}^* [\mathbf{k} e^{-i\mathbf{k}\cdot\mathbf{r}} \psi_{n\mathbf{k}} - i\nabla e^{-i\mathbf{k}\cdot\mathbf{r}} \psi_{n\mathbf{k}}] d\mathbf{r} \\ &= \frac{\hbar^2}{m} \int_{\text{cell}} e^{i\mathbf{k}\cdot\mathbf{r}} \psi_{n\mathbf{k}}^* [\mathbf{k} e^{-i\mathbf{k}\cdot\mathbf{r}} \psi_{n\mathbf{k}} + i^2 \mathbf{k} e^{-i\mathbf{k}\cdot\mathbf{r}} \psi_{n\mathbf{k}} - i e^{-i\mathbf{k}\cdot\mathbf{r}} \nabla \psi_{n\mathbf{k}}] d\mathbf{r} \\ &= \frac{\hbar^2}{m} \int_{\text{cell}} e^{i\mathbf{k}\cdot\mathbf{r}} e^{-i\mathbf{k}\cdot\mathbf{r}} \psi_{n\mathbf{k}}^* (-i\nabla) \psi_{n\mathbf{k}} d\mathbf{r} . \end{aligned} \quad (\text{B.8})$$

By rearranging some factors we can show the equivalence of the expectation value of the velocity, where the momentum operator is $\mathbf{p} = -i\hbar\nabla$ and the velocity operator is $\mathbf{v} = \frac{\mathbf{p}}{m}$:

$$\begin{aligned} \frac{1}{\hbar} \frac{\delta \epsilon_n}{\delta \mathbf{k}} &= \int_{\text{cell}} \psi_{n\mathbf{k}}^* \left(-\frac{i\hbar}{m} \nabla \right) \psi_{n\mathbf{k}} d\mathbf{r} \\ &= \langle \psi_{n\mathbf{k}} | -\frac{i\hbar}{m} \nabla | \psi_{n\mathbf{k}} \rangle = \langle \psi_{n\mathbf{k}} | \frac{\mathbf{p}}{m} | \psi_{n\mathbf{k}} \rangle = \langle \psi_{n\mathbf{k}} | \mathbf{v} | \psi_{n\mathbf{k}} \rangle . \end{aligned} \quad (\text{B.9})$$

Therefore, the expectation value of the velocity of a Bloch electron, interpreted as the mean group velocity of an electronic wave packet within the semiclassical model, is

$$\mathbf{v}_n(\mathbf{k}) = \frac{1}{\hbar} \frac{\delta \epsilon_n(\mathbf{k})}{\delta \mathbf{k}} . \quad (\text{B.10})$$

Appendix C

Semiclassical equations of motion

The semiclassical equations of motion of a Bloch electron are two equations that use the electronic wave behaviour of the Drude-Sommerfeld theory and apply it to behaviour in classically treated electromagnetic fields. There are limitations to this, which are discussed in the subsection 2.1.3, and this treatment requires the modelling of the electrons as wave packets: maintaining their wave behaviour for the purposes of interaction with the small scale periodic field from the lattice ions, and introducing particle properties such as a partially defined position.

The first semiclassical equation of motion is that which is stated in subsection 2.1.2 and derived in Appendix B for the velocity of a Bloch electron, and here has the interpretation that the electronic velocity is the wave packet's group velocity,

$$\dot{\mathbf{r}} = \mathbf{v}_n(\mathbf{k}) = \frac{1}{\hbar} \frac{\delta \epsilon_n(\mathbf{k})}{\delta \mathbf{k}} . \quad (\text{C.1})$$

The second semiclassical equation of motion is the rate of change of a Bloch electron's crystal momentum, and is an analogy to the Lorentz force for a semiclassical Bloch system:

$$\hbar \dot{\mathbf{k}} = -e \left[\mathbf{E}(\mathbf{r}, t) + \frac{1}{c} \dot{\mathbf{r}}_n(\mathbf{k}) \times \mathbf{H}(\mathbf{r}, t) \right] . \quad (\text{C.2})$$

Crystal momentum changes only in response to external fields and is unaffected by the periodic field of the ionic lattice, whereas the real electronic momentum, \mathbf{p} , responds to both external and periodic potentials. The rate of change in true momentum due to only the periodic potential is $\frac{\delta}{\delta t} (\mathbf{p} - \hbar\mathbf{k})$.

Appendix D

Vanishing current contribution of filled bands

$\epsilon(\mathbf{k})$ is periodic over the Brillouin zone, i.e. $\epsilon(\mathbf{k}) = \epsilon(\mathbf{k} + \mathbf{G})$. Integration of this function is closed if performed over the Brillouin zone, and the integration of its gradient is equivalent to

$$\int_{\text{BZ}} \frac{\delta}{\delta \mathbf{k}} \epsilon(\mathbf{k}) \delta \mathbf{k} = \int_{\mathbf{k}}^{\mathbf{k}+\mathbf{G}} \frac{\delta}{\delta \mathbf{k}} \epsilon(\mathbf{k}) \delta \mathbf{k} . \quad (\text{D.1})$$

$\frac{\delta}{\delta \mathbf{k}} \epsilon(\mathbf{k})$ represents the rate of change with varying \mathbf{k} in $\epsilon(\mathbf{k})$, the integral over which then represents the net change in $\epsilon(\mathbf{k})$ over the limits of the integral:

$$\int_{\mathbf{k}}^{\mathbf{k}+\mathbf{G}} \frac{\delta}{\delta \mathbf{k}} \epsilon(\mathbf{k}) \delta \mathbf{k} = [\epsilon(\mathbf{k})]_{\mathbf{k}}^{\mathbf{k}+\mathbf{G}} = \epsilon(\mathbf{k} + \mathbf{G}) - \epsilon(\mathbf{k}) = 0 . \quad (\text{D.2})$$

Therefore, our equation for the contribution of a filled band towards electric current density within the semiclassical model is (see subsection 2.1.3)

$$\mathbf{j} = -e \int_{\text{BZ}} \frac{1}{4\pi^3 \hbar} \frac{\delta \epsilon(\mathbf{k})}{\delta \mathbf{k}} \delta \mathbf{k} = -e \frac{1}{4\pi^3 \hbar} \int_{\text{BZ}} \frac{\delta \epsilon(\mathbf{k})}{\delta \mathbf{k}} \delta \mathbf{k} = 0 . \quad (\text{D.3})$$

Considering now the contribution towards \mathbf{j}_ϵ , and that $\frac{\delta}{\delta \mathbf{k}} \epsilon^2(\mathbf{k}) = 2\epsilon(\mathbf{k}) \frac{\delta \epsilon(\mathbf{k})}{\delta \mathbf{k}}$ by the chain rule of calculus, we have

$$\mathbf{j}_\epsilon = \int_{\text{BZ}} \frac{1}{4\pi^3 \hbar} \epsilon(\mathbf{k}) \frac{\delta \epsilon(\mathbf{k})}{\delta \mathbf{k}} \delta \mathbf{k} = \frac{1}{8\pi^3 \hbar} \int_{\text{BZ}} \frac{\delta}{\delta \mathbf{k}} \epsilon^2(\mathbf{k}) \delta \mathbf{k} . \quad (\text{D.4})$$

The integral of the gradient is still the net change, but this time in $\epsilon^2(\mathbf{k})$, over the integral limits. A function periodic in \mathbf{k} is still periodic over the same boundary when squared, and so similarly to the above case of the electric current density, we can show that the contribution towards \mathbf{j}_ϵ of a semiclassical filled band is zero:

$$\mathbf{j}_\epsilon = \frac{1}{8\pi^3 \hbar} \int_{\text{BZ}} \frac{\delta}{\delta \mathbf{k}} \epsilon^2(\mathbf{k}) \delta \mathbf{k} = \frac{1}{8\pi^3 \hbar} \int_{\mathbf{k}}^{\mathbf{k}+\mathbf{G}} \frac{\delta}{\delta \mathbf{k}} \epsilon^2(\mathbf{k}) \delta \mathbf{k} = \frac{1}{8\pi^3 \hbar} [\epsilon^2(\mathbf{k})]_{\mathbf{k}}^{\mathbf{k}+\mathbf{G}} = 0 . \quad (\text{D.5})$$

Appendix E

Spin-orbit coupling

Spin-orbit coupling, or the spin-orbit interaction, is an important effect in the context of energy bands, discussed in subsection 2.2.3. This appendix provides detail on how the the perturbation to the Hamiltonian from spin-orbit coupling, H_{SO} , is derived. H_{SO} is a sum of the Larmor interaction energy and the Thomas interaction energy. The Larmor interaction energy is the energy associated with Larmor precession, the precession of a magnetic moment in a magnetic field, \mathbf{B} ,

$$H_L = -\boldsymbol{\mu} \cdot \mathbf{B} , \quad (\text{E.1})$$

where $\boldsymbol{\mu}$ is the magnetic dipole moment. For an electron undergoing spin-orbit coupling, the magnetic moment is its spin magnetic moment, $\boldsymbol{\mu}_s$,

$$\boldsymbol{\mu} = \boldsymbol{\mu}_s = -g_s \mu_B \frac{\mathbf{S}}{\hbar} , \quad (\text{E.2})$$

where \mathbf{S} is the spin angular momentum, μ_B is the Bohr magneton, and g_s is the electron spin g-factor (a proportionality constant). The magnetic field felt by the electron in its own frame is

$$\mathbf{B} = -\frac{\mathbf{v} \times \mathbf{E}}{c^2} = -\frac{1}{m_e c^2} \frac{\mathbf{p} \times \mathbf{r} |E|}{r} , \quad (\text{E.3})$$

where \mathbf{v} is the electronic velocity through an electric field \mathbf{E} , which results in momentum $\mathbf{p} = m_e \mathbf{v}$. We have taken advantage of the radial nature of the electric field with respect to the ion, $\mathbf{E} = \frac{|E|\mathbf{r}}{r}$ where \mathbf{r} is the displacement of the electron from the ion. As $|E| = \frac{1}{e} \frac{\delta U}{\delta r}$, where U is the potential energy of the electron, and the angular momentum of the electron is $\mathbf{L} = \mathbf{r} \times \mathbf{p}$, we have that

$$\mathbf{B} = \frac{1}{rm_e e c^2} \frac{\delta U(\mathbf{r})}{\delta r} \mathbf{L}, \quad (\text{E.4})$$

as given in subsection 2.2.3. So, the Larmor interaction energy is

$$H_L = -\boldsymbol{\mu}_s \cdot \mathbf{B} = g_s \mu_B \frac{\mathbf{S}}{\hbar} \cdot \frac{1}{rm_e e c^2} \frac{\delta U(\mathbf{r})}{\delta r} \mathbf{L} = \frac{g_s \mu_B}{\hbar r m_e e c^2} \frac{\delta U(\mathbf{r})}{\delta r} \mathbf{L} \cdot \mathbf{S}. \quad (\text{E.5})$$

The Thomas interaction energy, H_T , is the energy change associated with the relativistic correction of Thomas precession of angular velocity $\boldsymbol{\omega}_T$, whereby a particle moving in a curved trajectory experiences precession of its reference frame. The precession of reference frame includes precession of spin axis in the observer's frame,

$$H_T = \boldsymbol{\omega}_T \cdot \mathbf{S}. \quad (\text{E.6})$$

The spin axis precesses with an angular velocity of

$$\boldsymbol{\omega}_T = \frac{1}{c^2} \frac{\gamma^2}{\gamma + 1} \mathbf{a} \times \mathbf{v}, \quad (\text{E.7})$$

where γ is the Lorentz factor, which in the non-relativistic limit of $v \ll c$ is

$$\lim_{\gamma \rightarrow 1} \boldsymbol{\omega}_T = \frac{1}{2c^2} \mathbf{a} \times \mathbf{v} = -\frac{1}{2c^2} \mathbf{v} \times \mathbf{a}. \quad (\text{E.8})$$

As our electron is a charged particle in an electric field, we can describe its acceleration, \mathbf{a} , in terms of \mathbf{E} and make the same substitution as we did for Larmor precession for

radial fields:

$$\boldsymbol{\omega}_T = -\frac{1}{2c^2} \mathbf{v} \times \left(\frac{e\mathbf{E}}{m_e} \right) = -\frac{1}{2c^2 m_e} \mathbf{v} \times \left(-\frac{\mathbf{r}}{r} \frac{\delta U(\mathbf{r})}{\delta r} \right) = -\frac{\mathbf{r} \times \mathbf{v}}{2c^2 r m_e} \frac{\delta U(\mathbf{r})}{\delta r} . \quad (\text{E.9})$$

Substituting in $\mathbf{L} = \mathbf{r} \times \mathbf{p} = m_e \mathbf{r} \times \mathbf{v}$ and the Bohr magneton, $\mu_B = \frac{e\hbar}{2m_e}$, we get

$$\boldsymbol{\omega}_T = -\frac{\mu_B}{\hbar m_e e c^2 r} \frac{\delta U}{\delta r} \mathbf{L} , \quad (\text{E.10})$$

and therefore

$$H_T = -\frac{\mu_B}{\hbar m_e e c^2 r} \frac{\delta U}{\delta r} \mathbf{L} \cdot \mathbf{S} . \quad (\text{E.11})$$

Our total spin-orbit energy correction is then

$$H_{SO} = H_L + H_T = \mu_B \frac{g_s - 1}{r \hbar m_e e c^2} \frac{\delta U(\mathbf{r})}{\delta r} \mathbf{L} \cdot \mathbf{S} . \quad (\text{E.12})$$

Finally, consider the total angular momentum, $\mathbf{J} = \mathbf{L} + \mathbf{S}$ we have

$$\mathbf{J} \cdot \mathbf{J} = \mathbf{J}^2 = \mathbf{L}^2 + \mathbf{S}^2 + 2\mathbf{L} \cdot \mathbf{S} , \quad (\text{E.13})$$

and therefore

$$\mathbf{L} \cdot \mathbf{S} = \frac{1}{2} (\mathbf{J}^2 - \mathbf{L}^2 - \mathbf{S}^2) . \quad (\text{E.14})$$

As $\mathbf{J}^2 = \hbar^2 j(j+1)$, where $j = |l \pm s|$, $\mathbf{L}^2 = \hbar^2 l(l+1)$ and $\mathbf{S}^2 = \hbar^2 s(s+1)$, we can say that

$$\mathbf{L} \cdot \mathbf{S} = \frac{\hbar^2}{2} (j(j+1) - l(l+1) - s(s+1)) , \quad (\text{E.15})$$

as required for subsection 2.2.3.

Appendix F

Scattering

In subsection 3.2.2, it is shown that the first energy derivative of the logarithmic derivative $D_l(\epsilon, r_{\text{cut}})$ is the same between wavefunctions that match at and beyond r_{cut} if they are norm-conserving with respect to each other. This results in the same change in energy states between wavefunctions when perturbed by scattering potentials i.e. when placed in a poly-atomic system.

Here we consider a spherical scattering potential, where $V = 0$ beyond $r = r_{\text{cut}}$. The wavefunction of an electron travelling in this potential is a superposition of an incoming plane wave and an outgoing scattered spherical wave, as in Figure F.1. The well-known radial Schrödinger equation can be simplified by substituting for the reduced radial solution, $u_l(r) = rA_l(r)$, such that it reduces to

$$\left[\frac{\delta^2}{\delta r^2} - V + \epsilon - \frac{l(l+1)}{r^2} \right] u_l(r) = 0 . \quad (\text{F.1})$$

Beyond r_{cut} , $V(r) = 0$, and the equation has solutions

$$u_l(r) = C_{1,l} r j_l(kr) + C_{2,l} r n_l(kr) , \quad (\text{F.2})$$

where $j_l(kr)$ and $n_l(kr)$ are the spherical Bessel and spherical Neumann functions,

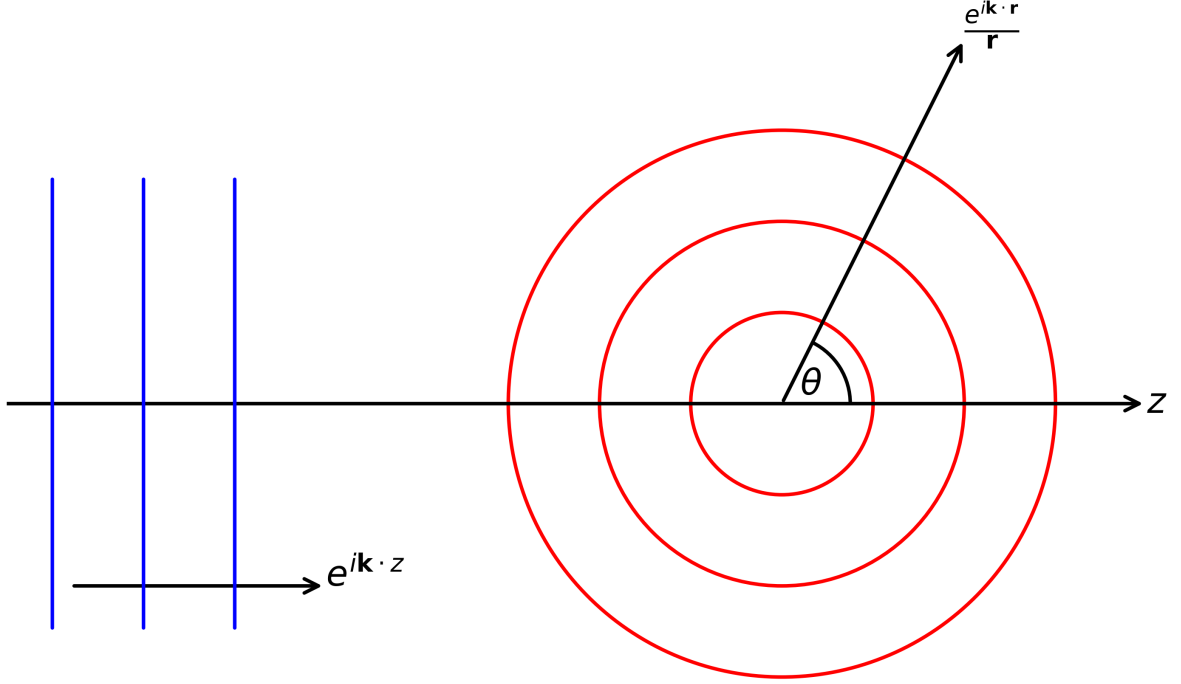


Figure F.1: An incoming plane wave (blue) along some Cartesian direction z , scattering at angle θ , with an outgoing scattered spherical wave of form $\frac{e^{ik \cdot r}}{r}$ (red).

respectively:

$$j_l(kr) = (-kr)^l \left(\frac{1}{kr} \frac{\delta}{\delta kr} \right)^l \frac{\sin kr}{kr} \quad (\text{F.3})$$

$$n_l(kr) = -(-kr)^l \left(\frac{1}{kr} \frac{\delta}{\delta kr} \right)^l \frac{\cos kr}{kr}, \quad (\text{F.4})$$

and the usual

$$k = \frac{\sqrt{2m\epsilon}}{\hbar}. \quad (\text{F.5})$$

We introduce this in terms of the Hankel functions,

$$h_l^{(1)(kr)} = j_l(kr) + in_l(kr) \quad (\text{F.6})$$

and

$$h_l^{(2)}(kr) = j_l(kr) - in_l(kr), \quad (\text{F.7})$$

in order to condense our reduced solution:

$$u_l(r) = C_l^{(1)} r h_l^{(1)}(kr) + C_l^{(2)} r h_l^{(2)}(kr) . \quad (\text{F.8})$$

We can re-express this in terms of the ratio of the coefficients $C_l^{(1)}$ and $C_l^{(2)}$. As the coefficients are the amplitudes of the respective waves, their ratio is the phase difference between them, as shown below for two arbitrary phase-dependent wave amplitudes, A and B :

$$A = |A|e^{i\phi_A} , \quad B = |B|e^{i\phi_B} \quad (\text{F.9})$$

$$\frac{A}{B} = \frac{|A|}{|B|} e^{i(\phi_A - \phi_B)} \quad (\text{F.10})$$

$$= C_{AB} e^{i\eta} , \quad (\text{F.11})$$

where C_{AB} is a real constant and η is the phase difference between waves. As such, our coefficient ratio for those in $u_l(r)$ is

$$\frac{C_l^{(1)}}{C_l^{(2)}} = e^{2i\eta} , \quad (\text{F.12})$$

where we have dropped the resultant real coefficient (as it has no effect on later discussion, serving only to take up more space in equations, so it may as well be 1) and represented the phase shift as $2\eta_l$ to be in keeping with the convention of scattering theory (this also does not change our final conclusion for our purposes). $\eta_l(\epsilon)$ is a function ϵ , but we will not notate this explicitly. We now represent $u_l(r)$ as

$$\begin{aligned} u_l(r) &= C_l^{(2)} \left[e^{2i\eta} r h_l^{(1)}(kr) + r h_l^{(2)}(kr) \right] \\ &= C_l^{(2)} r e^{i\eta} \left[e^{i\eta} (j_l(kr) + in_l(kr)) + e^{-i\eta} (j_l(kr) - in_l(kr)) \right] \\ &= C_l^{(2)} r e^{i\eta} \left[(\cos \eta + i \sin \eta) (j_l(kr) + in_l(kr)) + (\cos \eta - i \sin \eta) (j_l(kr) - in_l(kr)) \right] \\ &= 2C_l^{(2)} r e^{i\eta} \left[j_l(kr) \cos \eta - n_l(kr) \sin \eta \right] \end{aligned} \quad (\text{F.13})$$

Consider again our logarithmic derivative from subsection 3.2.2, $D_l(\epsilon, r_{\text{cut}})$, (Equation 3.117) which here is

$$D_l(\epsilon, r) = r \frac{u_l'(r)}{u_l(r)}, \quad (\text{F.14})$$

where a prime denotes differentiation with respect to r . We take the derivative of $u_l(r)$,

$$u_l'(r) = 2C_l^{(2)} r e^{i\eta} [kr j_l'(kr) \cos \eta + j_l(kr) \cos \eta - rn_l'(kr) \sin \eta - n_l(kr) \sin \eta], \quad (\text{F.15})$$

and solve for $D_l(\epsilon, r)$:

$$D_l(\epsilon, r) = r \frac{2C_l^{(2)} r e^{i\eta}}{2C_l^{(2)} r e^{i\eta}} \left[\frac{j_l(kr) \cos \eta - n_l(kr) \sin \eta}{r j_l(kr) \cos \eta - r n_l(kr) \sin \eta} + \frac{kr j_l'(kr) \cos \eta - kr n_l'(kr) \sin \eta}{r j_l(kr) \cos \eta - r n_l(kr) \sin \eta} \right], \quad (\text{F.16})$$

which at $r = r_{\text{cut}}$ is

$$D_l(\epsilon, r_{\text{cut}}) = 1 + kr_{\text{cut}} \left[\frac{j_l'(kr_{\text{cut}}) \cos \eta - n_l'(kr_{\text{cut}}) \sin \eta}{j_l(kr_{\text{cut}}) \cos \eta - n_l(kr_{\text{cut}}) \sin \eta} \right]. \quad (\text{F.17})$$

Dropping the variable dependence notation to reduce clutter (remembering that the Bessel and Neumann functions act on kr_{cut}), this can be rearranged as

$$(D_l - 1)(j_l \cos \eta - n_l \sin \eta) = kr_{\text{cut}} j_l' \cos \eta - kr_{\text{cut}} n_l' \sin \eta, \quad (\text{F.18})$$

and so

$$\begin{aligned} (D_l - 1)(j_l \cot \eta - n_l) &= kr_{\text{cut}} j_l' \cot \eta - kr_{\text{cut}} n_l' \\ kr_{\text{cut}} j_l' \cot \eta - (D_l - 1) j_l \cot \eta &= kr_{\text{cut}} n_l' - (D_l - 1) n_l, \end{aligned} \quad (\text{F.19})$$

resulting in

$$\cot \eta = \frac{kr_{\text{cut}} n_l' - (D_l - 1) n_l}{kr_{\text{cut}} j_l' - (D_l - 1) j_l}. \quad (\text{F.20})$$

We see then that when considering the scattering process for electrons described by the pseudopotentials from subsection 3.2.2, the phase shift depends only on parameters that agree between the pseudo- and all-electron wavefunctions and the logarithmic derivative, $D_l(\epsilon, r)$. As a result, if the first energy derivative of $D_l(\epsilon, r)$ agrees between pseudo- and all-electron wavefunctions, the phase shift experienced in a scattering process (interaction with an external potential) will be identical. This means that they undergo the same scattering process, and so any resultant energy shift will be the same.

Appendix G

Derivative discontinuity

In subsection 3.1.1, we stated that a drawback of DFT is the underestimation of band gap energies. This is due to the derivative discontinuity of energy with respect to number of electrons, as discussed here.

Consider the energy of a system with N electrons; adding an electron will change the energy of the system, depending on the starting electronic configuration. Removing an electron will likewise result in a change in energy. Treating this system as an ensemble, Perdew et al. [151] show that by letting N take non-integer values, $N = M + \omega$, where M is an integer and $0 \leq \omega \leq 1$, the lowest average energy of a system of $M + \omega$ electrons is a statistical mixture of integer electron systems, with coefficients in ω being respective probabilities,

$$E = (1 - \omega) E_M + \omega E_{M+1} . \quad (\text{G.1})$$

The curve of E against N , then, is a continuous series of straight line segments, each between integer values of N . While this function is continuous, its gradient is not; the gradient is discontinuous at integers of N , as in Figure G.1.

Specific physical meaning is attached to the gradient: the ionization energy, $I(N)$, which is the energy required to remove an electron, and the electron affinity, $A(N)$, which is the energy required to add an electron, are the negative of the gradient $\frac{\delta E}{\delta N}$ between $N - 1$ and N , and N and $N + 1$, respectively. These energies are also related

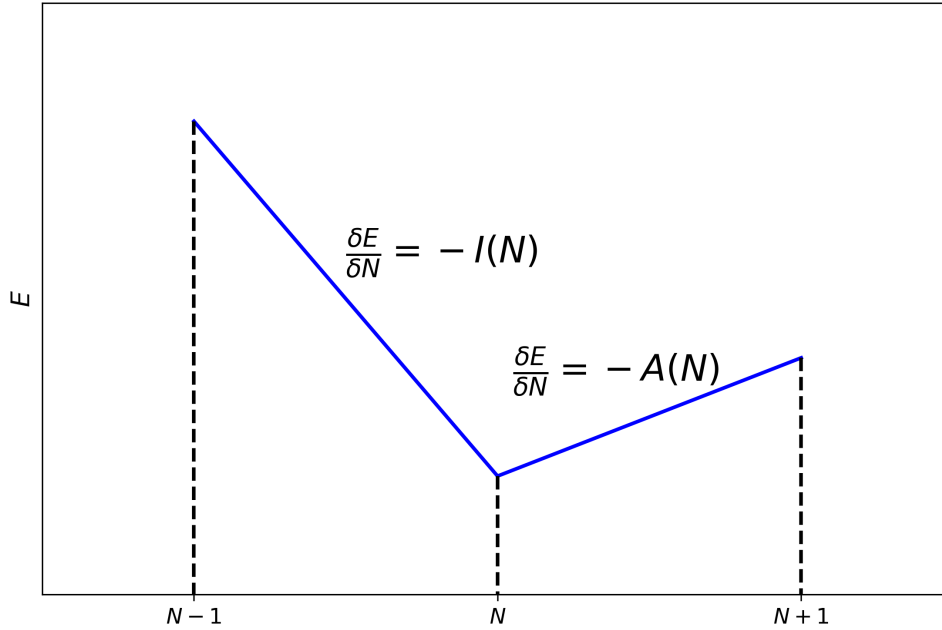


Figure G.1: A schematic representation of a system's energy with $N - 1$, N and $N + 1$ electrons. Fraction electron counts are found through linear interpolation between integer points, which results in a discontinuity in $\frac{\delta E}{\delta N}$ across integer values of N .

to the band structure, where the true fundamental band gap is $I - A$. The Kohn-Sham band gap, however, is just the difference in the energy between the lowest unoccupied molecular orbital (LUMO) and the highest occupied molecular orbital (HOMO), i.e. the energy difference of the system at integer values of N , $E_N - E_{N+1}$.

The discrepancy between the DFT band gap and the true fundamental band gap, then, arises from this discontinuity; as we move through integer values of N , the discontinuity acts as an addition of a constant to the gradient. This must be only a constant, as a variable value would result in non-unique potentials defining a density, which is disallowed by the Hohenberg-Kohn theorem. The DFT band gap is

$$E_G^{(\text{DFT})} = \epsilon_{N+1} - \epsilon_N = E_{\text{LUMO}} - E_{\text{HOMO}} . \quad (\text{G.2})$$

In an infinite crystal, the addition of one extra electron affects the density by an infinitesimal amount, δ , associated with an infinitesimal change in the effective potential, with a constant which may appear as the electron number increases through an integer.

So, for positive δ ,

$$I(N) = -\epsilon_N(N - \delta) \quad , \quad A(N) = -\epsilon_{N+1}(N + \delta) \quad , \quad (\text{G.3})$$

where ϵ_N are orbital energies. So, given that an increase through integer N (by adding the infinitesimal change δ), can result in our modification by positive constant C ,

$$A(N) = -\epsilon_{N+1}(N + \delta) = -[\epsilon_{N+1}(N - \delta) + C] \quad , \quad (\text{G.4})$$

we have the true fundamental band gap of

$$\begin{aligned} E_G^{(\text{true})} &= I(N) - A(N) = \epsilon_{N+1}(N - \delta) - \epsilon_N(N - \delta) + C \\ &= \epsilon_{N+1}(N) - \epsilon_N(N) + C = E_{\text{LUMO}} - E_{\text{HOMO}} + C \quad , \end{aligned} \quad (\text{G.5})$$

i.e.

$$E_G^{(\text{DFT})} = E_G^{(\text{true})} - C \quad . \quad (\text{G.6})$$

With C being a positive constant, we find that the Kohn-Sham DFT band gap is an underestimation of the true fundamental band gap, due to the derivative discontinuity through integer electron numbers of energy against electron number.

Appendix H

Minimizing the Kohn-Sham energy functional

In order to minimize the Kohn-Sham energy functional in subsection 3.1.1, we used the method of Lagrange multipliers. We began with the variational equation, Equation 3.17, and ended with the Kohn-Sham equations, Equation 3.24. This process is outlined more fully here.

Beginning with the variational equation,

$$\frac{\delta E_{KS}}{\delta \psi_i^*} = \frac{\delta T_S}{\delta \psi_i^*} + \frac{\delta n}{\delta \psi_i^*} V_{\text{eff}}(\mathbf{r}) , \quad (\text{H.1})$$

and the constraint of minimization,

$$\langle \psi_i | \psi_j \rangle = \delta_{ij} , \quad (\text{H.2})$$

we define a set of constraint functions,

$$g_{ij} = 0 = \langle \psi_i | \psi_j \rangle - \delta_{ij} . \quad (\text{H.3})$$

Our objective function is just the derivative of the Kohn-Sham energy functional with

respect to ψ_i^* , and so the derivative of the Lagrangian is

$$\frac{\delta \mathcal{L}}{\delta \psi_i^*} = \frac{\delta E_{KS}}{\delta \psi_i^*} - \sum_{i,j} \lambda_{ij} \frac{\delta g_{ij}}{\delta \psi_i^*} = 0 , \quad (\text{H.4})$$

with λ_{ij} being the set of undetermined (Lagrange) multipliers. We substitute in equivalencies from Equations 3.18 - 3.21 (subsection 3.1.1) to get

$$-\frac{1}{2} \nabla^2 \psi_i(\mathbf{r}) + V_{\text{eff}}(\mathbf{r}) \psi_i(\mathbf{r}) - \sum_{i,j} \lambda_{ij} \frac{\delta g_{ij}}{\delta \psi_i^*} = 0 , \quad (\text{H.5})$$

which we can rearrange for

$$\left(-\frac{1}{2} \nabla^2 + V_{\text{eff}}(\mathbf{r}) \right) \psi_i(\mathbf{r}) = \sum_j \lambda_{ij} \psi_j(\mathbf{r}) . \quad (\text{H.6})$$

Multiplying by $\psi_j^*(\mathbf{r})$ we get

$$\sum_j \lambda_{ij} \psi_j^*(\mathbf{r}) \psi_j(\mathbf{r}) = \psi_j^*(\mathbf{r}) \left(-\frac{1}{2} \nabla^2 + V_{\text{eff}}(\mathbf{r}) \right) \psi_i(\mathbf{r}) , \quad (\text{H.7})$$

which we can integrate with respect to \mathbf{r} for

$$\lambda_{ij} \langle \psi_j | \psi_j \rangle = \langle \psi_j^* | \mathcal{H}_{KS} | \psi_i \rangle , \quad (\text{H.8})$$

and therefore

$$\therefore \lambda_{ij} = \delta_{ij} \epsilon_j \quad (\text{H.9})$$

for non-degenerate systems. Substituting this in to Equation H.6, and removing the summation as contributions are only non-zero when $i = j$, we are left with

$$\left(-\frac{1}{2} \nabla^2 + V_{\text{eff}}(\mathbf{r}) \right) \psi_i(\mathbf{r}) = \epsilon_i \psi_i(\mathbf{r}) , \quad (\text{H.10})$$

which is Equation 3.24 through the definition of the Kohn-Sham Hamiltonian, Equation

3.9.

Appendix I

Pentacene's atomic deviation from the molecular plane

In subsection 6.1.3, we compared the atomic deviation of pentacene's atoms from the molecular plane in heterostructures with their favorable binding sites in the high concentration regime. The effects seen were varied (see Figure 6.8), but when we performed the same analysis using heterostructures with the Top-Ch adsorption site, regardless of favorability, we recovered the bowling effect seen in the low concentration regime. The results of this are displayed in Figure I.1.

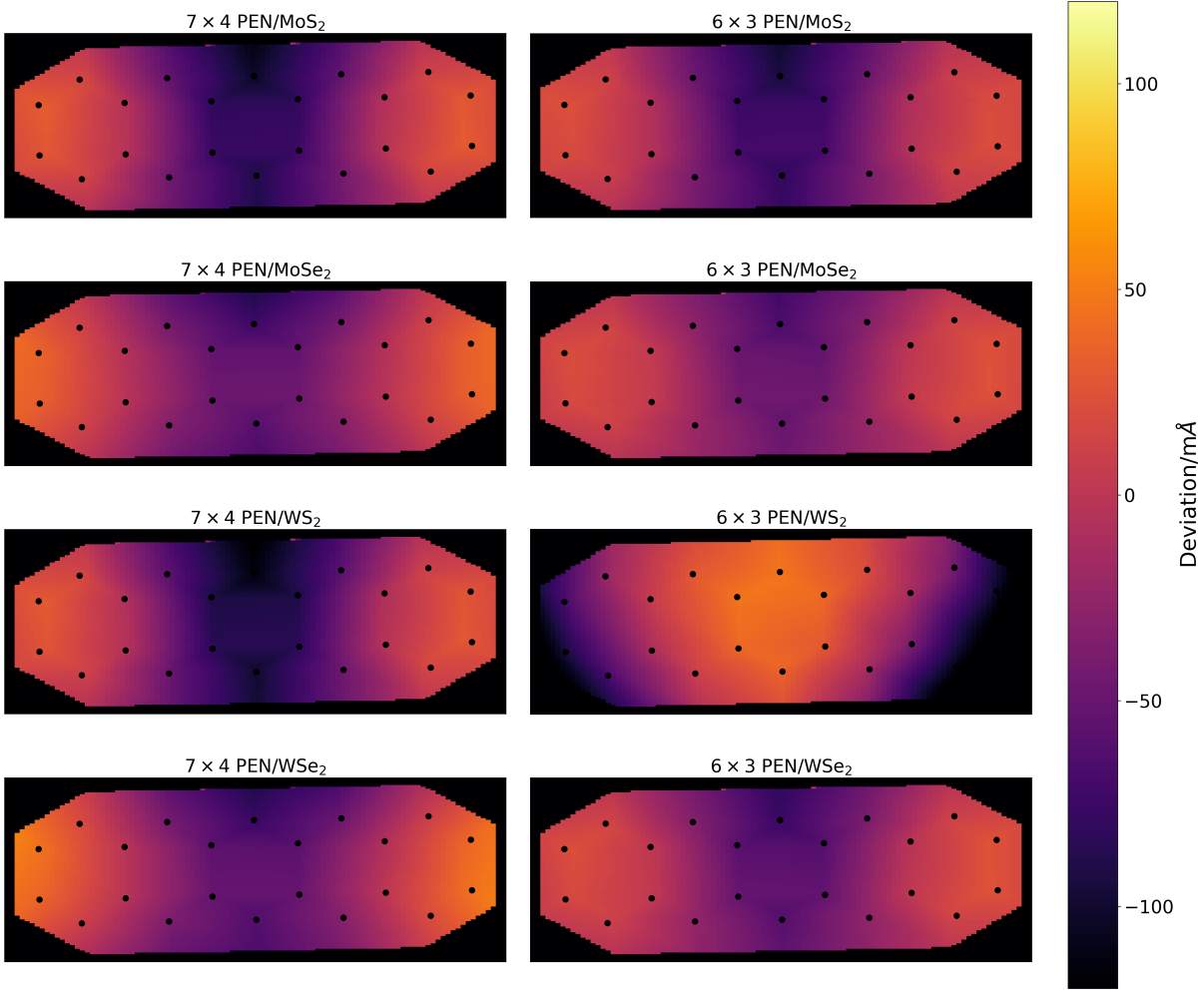


Figure I.1: The deviation of pentacene atoms from the molecular plane for both low (7×4) and high (6×3) concentration pentacene in heterostructure with the Top-Ch adsorption site, shown as a heat map. Circular black points mark the atomic positions of carbon atoms. The systems show a clear bowling effect, in contrast to the effects noted in the high concentration regime with favorable adsorption sites, which are TMD-specific.

Table I.1 displays the mean and maximum values of the atomic deviation from the molecular plane, δz , for each heterostructure, without rotation, across both concentration regimes, as well as their difference.

Table I.1: Atomic deviation from the molecular plane of unrotated pentacene in the different concentration regimes, in mÅ.

Heterostructure	7×4		6×3		Δ	
	Mean δz	Maximum δz	Mean δz	Maximum δ	Mean δz	Maximum δ
PEN/MoS ₂	40	111	60	118	20	7
PEN/MoSe ₂	33	89	41	111	8	22
PEN/WS ₂	42	122	38	105	-4	-17
PEN/WSe ₂	33	92	26	67	-7	-25

Additionally, in Section 6.2.5, we presented Figure 6.13, a heat map of the atomic deviation for pentacene in heterostructure with MoS₂, in the low concentration regime, comparing the unrotated and favorably rotated systems. This graphic is representative of the heterostructures with other TMDs in the same concentration, and here we present the equivalent graphics for PEN/MoSe₂ (Figure I.2), PEN/WS₂ (Figure I.3), and PEN/WSe₂ (Figure I.4).

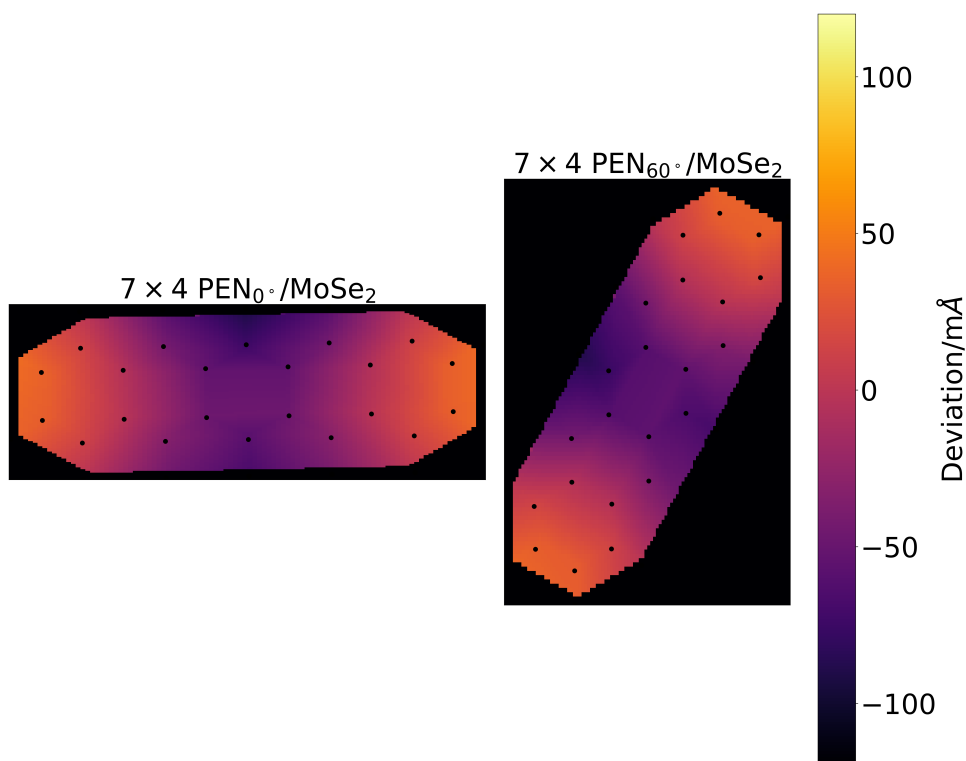


Figure I.2: Heat maps of the atomic deviation from the molecular plane in the pentacene molecules of 7×4 PEN/MoSe₂ heterostructures, with 0° and favorable (60°) rotation angles. We can see a bowling effect in both cases, with the central carbon ring being closer to the TMD substrate (a negative deviation from the molecular plane).

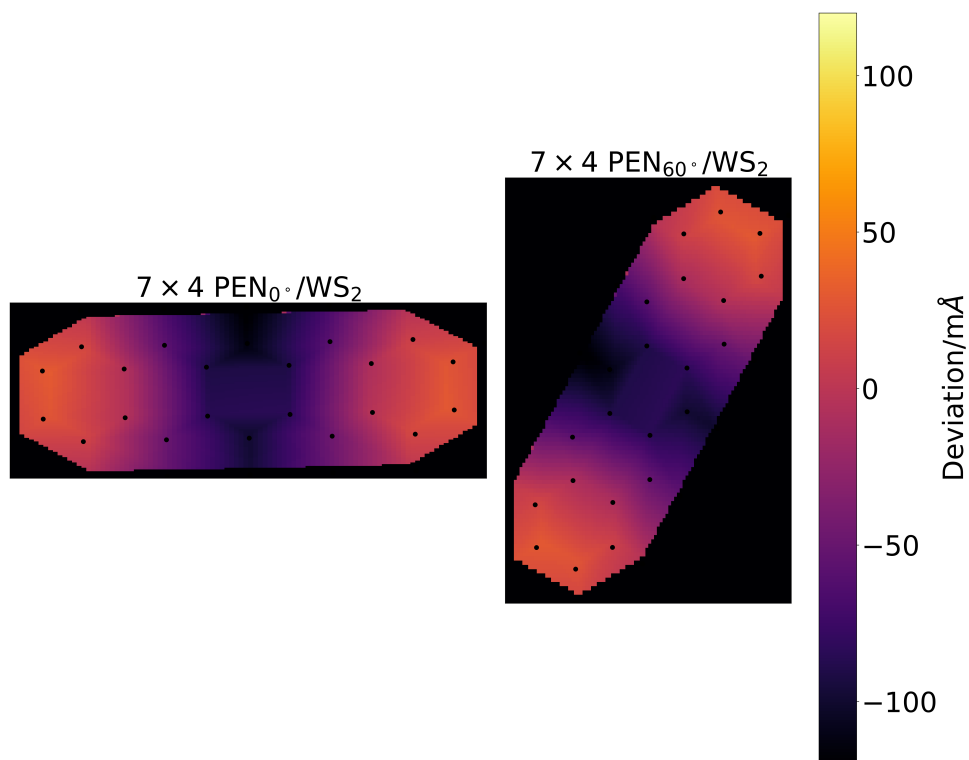


Figure I.3: Heat maps of the atomic deviation from the molecular plane in the pentacene molecules of 7×4 PEN/ WS_2 heterostructures, with 0° and favorable (60°) rotation angles. We can see a bowling effect in both cases, with the central carbon ring being closer to the TMD substrate (a negative deviation from the molecular plane).

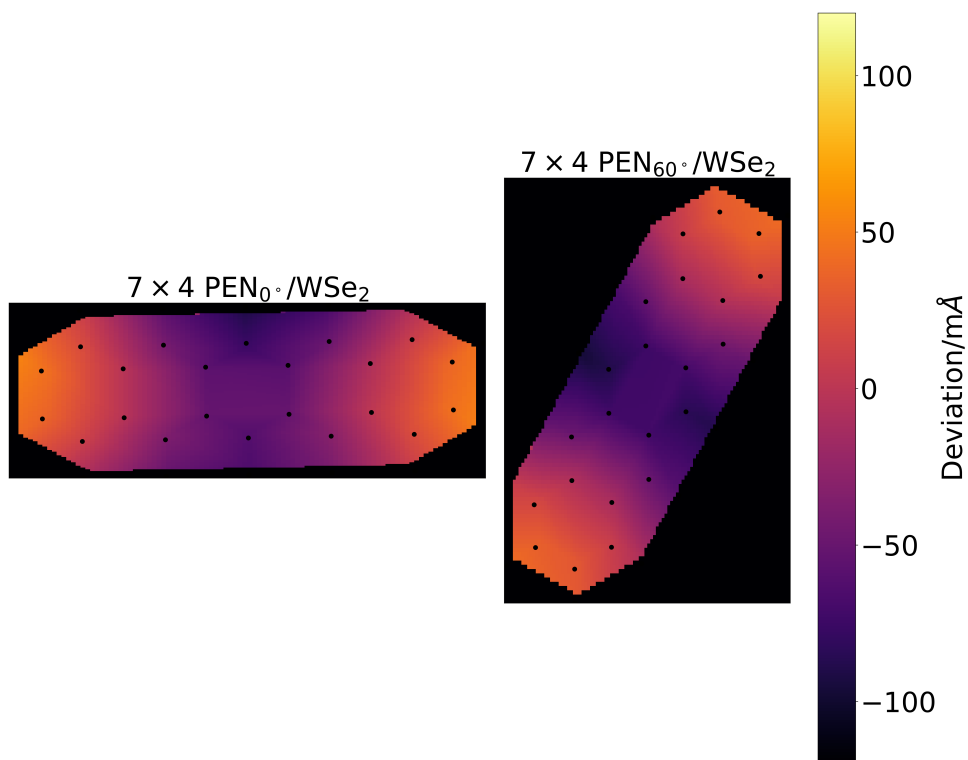


Figure I.4: Heat maps of the atomic deviation from the molecular plane in the pentacene molecules of 7×4 PEN/WSe₂ heterostructures, with 0° and favorable (60°) rotation angles. We can see a bowling effect in both cases, with the central carbon ring being closer to the TMD substrate (a negative deviation from the molecular plane). This is broadly representative of all 7×4 systems, with only minor differences in the magnitude of deviation.

Bibliography

- [1] R. Dong and I. Kuljanishvili, “Progress in fabrication of transition metal dichalcogenides heterostructure systems,” *Journal of Vacuum Science & Technology B*, vol. 35, no. 3, 2017.
- [2] Y. Liu, N. O. Weiss, X. Duan, H.-C. Cheng, Y. Huang, and X. Duan, “Van der Waals heterostructures and devices,” *Nature Reviews Materials*, vol. 1, no. 9, pp. 1–17, 2016.
- [3] W. Zhao, R. M. Ribeiro, and G. Eda, “Electronic structure and optical signatures of semiconducting transition metal dichalcogenide nanosheets,” *Accounts of Chemical Research*, vol. 48, no. 1, pp. 91–99, 2015.
- [4] R. Kumar, I. Verzhbitskiy, and G. Eda, “Strong optical absorption and photocarrier relaxation in 2-D semiconductors,” *IEEE Journal of Quantum Electronics*, vol. 51, no. 10, pp. 1–6, 2015.
- [5] J. Wong, D. Jariwala, G. Tagliabue, K. Tat, A. R. Davoyan, M. C. Sherrott, and H. A. Atwater, “High photovoltaic quantum efficiency in ultrathin van der Waals heterostructures,” *ACS Nano*, vol. 11, no. 7, pp. 7230–7240, 2017.
- [6] F. Withers, O. Del Pozo-Zamudio, A. Mishchenko, A. P. Rooney, A. Gholinia, K. Watanabe, T. Taniguchi, S. J. Haigh, A. Geim, A. Tartakovskii, *et al.*, “Light-emitting diodes by band-structure engineering in van der Waals heterostructures,” *Nature Materials*, vol. 14, no. 3, pp. 301–306, 2015.

- [7] S. Wi, H. Kim, M. Chen, H. Nam, L. J. Guo, E. Meyhofer, and X. Liang, “Enhancement of photovoltaic response in multilayer MoS₂ induced by plasma doping,” *ACS Nano*, vol. 8, no. 5, pp. 5270–5281, 2014.
- [8] W. Liu, J. Kang, D. Sarkar, Y. Khatami, D. Jena, and K. Banerjee, “Role of metal contacts in designing high-performance monolayer n-type WSe₂ field effect transistors,” *Nano Letters*, vol. 13, no. 5, pp. 1983–1990, 2013.
- [9] J. H. Park, S. Vishwanath, S. Wolf, K. Zhang, I. Kwak, M. Edmonds, M. Breedem, X. Liu, M. Dobrowolska, J. Furdyna, *et al.*, “Selective chemical response of transition metal dichalcogenides and metal dichalcogenides in ambient conditions,” *ACS Applied Materials & Interfaces*, vol. 9, no. 34, pp. 29255–29264, 2017.
- [10] S.-L. Li, K. Tsukagoshi, E. Orgiu, and P. Samorì, “Charge transport and mobility engineering in two-dimensional transition metal chalcogenide semiconductors,” *Chemical Society Reviews*, vol. 45, no. 1, pp. 118–151, 2016.
- [11] Y. Jiang, S. Chen, W. Zheng, B. Zheng, and A. Pan, “Interlayer exciton formation, relaxation, and transport in TMD van der Waals heterostructures,” *Light: Science & Applications*, vol. 10, no. 1, p. 72, 2021.
- [12] S. Joseph, J. Mohan, S. Lakshmy, S. Thomas, B. Chakraborty, S. Thomas, and N. Kalarikkal, “A review of the synthesis, properties, and applications of 2D transition metal dichalcogenides and their heterostructures,” *Materials Chemistry and Physics*, vol. 297, p. 127332, 2023.
- [13] S. Bettis Homan, V. K. Sangwan, I. Balla, H. Bergeron, E. A. Weiss, and M. C. Hersam, “Ultrafast exciton dissociation and long-lived charge separation in a photovoltaic pentacene–MoS₂ van der Waals heterojunction,” *Nano Letters*, vol. 17, no. 1, pp. 164–169, 2017.
- [14] J. Wang, Z. Ji, G. Yang, X. Chuai, F. Liu, Z. Zhou, C. Lu, W. Wei, X. Shi, J. Niu, *et al.*, “Charge transfer within the F4TCNQ–MoS₂ van der Waals interface: toward

- electrical properties tuning and gas sensing application,” *Advanced Functional Materials*, vol. 28, no. 51, p. 1806244, 2018.
- [15] Y. L. Huang, Y. J. Zheng, Z. Song, D. Chi, A. T. Wee, and S. Y. Quek, “The organic–2D transition metal dichalcogenide heterointerface,” *Chemical Society Reviews*, vol. 47, no. 9, pp. 3241–3264, 2018.
- [16] M. Chhowalla, H. S. Shin, G. Eda, L.-J. Li, K. P. Loh, and H. Zhang, “The chemistry of two-dimensional layered transition metal dichalcogenide nanosheets,” *Nature Chemistry*, vol. 5, no. 4, pp. 263–275, 2013.
- [17] P. Cheng, K. Sun, and Y. H. Hu, “Mechanically-induced reverse phase transformation of MoS₂ from stable 2H to metastable 1T and its memristive behavior,” *RSC Advances*, vol. 6, no. 70, pp. 65691–65697, 2016.
- [18] B. Han and Y. H. Hu, “MoS₂ as a co-catalyst for photocatalytic hydrogen production from water,” *Energy Science & Engineering*, vol. 4, no. 5, pp. 285–304, 2016.
- [19] G. Eda, H. Yamaguchi, D. Voiry, T. Fujita, M. Chen, and M. Chhowalla, “Photoluminescence from chemically exfoliated MoS₂,” *Nano Letters*, vol. 11, no. 12, pp. 5111–5116, 2011.
- [20] L. Ortenzi, L. Pietronero, and E. Cappelluti, “Zero-point motion and direct-indirect band-gap crossover in layered transition-metal dichalcogenides,” *Physical Review B*, vol. 98, no. 19, p. 195313, 2018.
- [21] H. J. Conley, B. Wang, J. I. Ziegler, R. F. Haglund Jr, S. T. Pantelides, and K. I. Bolotin, “Bandgap engineering of strained monolayer and bilayer MoS₂,” *Nano Letters*, vol. 13, no. 8, pp. 3626–3630, 2013.
- [22] R. Sundaram, M. Engel, A. Lombardo, R. Krupke, A. Ferrari, P. Avouris, and M. Steiner, “Electroluminescence in single layer MoS₂,” *Nano Letters*, vol. 13, no. 4, pp. 1416–1421, 2013.

- [23] K. F. Mak, C. Lee, J. Hone, J. Shan, and T. F. Heinz, “Atomically thin MoS₂: a new direct-gap semiconductor,” *Physical Review Letters*, vol. 105, no. 13, p. 136805, 2010.
- [24] A. Splendiani, L. Sun, Y. Zhang, T. Li, J. Kim, C.-Y. Chim, G. Galli, and F. Wang, “Emerging photoluminescence in monolayer MoS₂,” *Nano Letters*, vol. 10, no. 4, pp. 1271–1275, 2010.
- [25] H.-V. Han, A.-Y. Lu, L.-S. Lu, J.-K. Huang, H. Li, C.-L. Hsu, Y.-C. Lin, M.-H. Chiu, K. Suenaga, C.-W. Chu, *et al.*, “Photoluminescence enhancement and structure repairing of monolayer MoSe₂ by hydrohalic acid treatment,” *ACS Nano*, vol. 10, no. 1, pp. 1454–1461, 2016.
- [26] G. Kioseoglou, A. T. Hanbicki, M. Currie, A. L. Friedman, and B. T. Jonker, “Optical polarization and intervalley scattering in single layers of MoS₂ and MoSe₂,” *Scientific Reports*, vol. 6, no. 1, p. 25041, 2016.
- [27] H. R. Gutiérrez, N. Perea-López, A. L. Elías, A. Berkdemir, B. Wang, R. Lv, F. López-Urías, V. H. Crespi, H. Terrones, and M. Terrones, “Extraordinary room-temperature photoluminescence in triangular WS₂ monolayers,” *Nano Letters*, vol. 13, no. 8, pp. 3447–3454, 2013.
- [28] P. Tonndorf, R. Schmidt, P. Böttger, X. Zhang, J. Börner, A. Liebig, M. Albrecht, C. Kloc, O. Gordan, D. R. Zahn, *et al.*, “Photoluminescence emission and Raman response of monolayer MoS₂, MoSe₂, and WSe₂,” *Optics Express*, vol. 21, no. 4, pp. 4908–4916, 2013.
- [29] H. S. Lee, S.-W. Min, Y.-G. Chang, M. K. Park, T. Nam, H. Kim, J. H. Kim, S. Ryu, and S. Im, “MoS₂ nanosheet phototransistors with thickness-modulated optical energy gap,” *Nano Letters*, vol. 12, no. 7, pp. 3695–3700, 2012.
- [30] N. R. Pradhan, D. Rhodes, Y. Xin, S. Memaran, L. Bhaskaran, M. Siddiq, S. Hill, P. M. Ajayan, and L. Balicas, “Ambipolar molybdenum diselenide field-effect

- transistors: field-effect and Hall mobilities,” *ACS Nano*, vol. 8, no. 8, pp. 7923–7929, 2014.
- [31] D. Ovchinnikov, A. Allain, Y.-S. Huang, D. Dumcenco, and A. Kis, “Electrical transport properties of single-layer WS₂,” *ACS Nano*, vol. 8, no. 8, pp. 8174–8181, 2014.
- [32] J.-K. Huang, J. Pu, C.-L. Hsu, M.-H. Chiu, Z.-Y. Juang, Y.-H. Chang, W.-H. Chang, Y. Iwasa, T. Takenobu, and L.-J. Li, “Large-area synthesis of highly crystalline WSe₂ monolayers and device applications,” *ACS Nano*, vol. 8, no. 1, pp. 923–930, 2014.
- [33] H. Kleemann, C. Schuenemann, A. A. Zakhidov, M. Riede, B. Lüssem, and K. Leo, “Structural phase transition in pentacene caused by molecular doping and its effect on charge carrier mobility,” *Organic Electronics*, vol. 13, no. 1, pp. 58–65, 2012.
- [34] D. J. Gundlach, Y.-Y. Lin, T. N. Jackson, S. Nelson, and D. Schlom, “Pentacene organic thin-film transistors-molecular ordering and mobility,” *IEEE Electron Device Letters*, vol. 18, no. 3, pp. 87–89, 1997.
- [35] H. Klauk, D. J. Gundlach, and T. N. Jackson, “Fast organic thin-film transistor circuits,” *IEEE Electron Device Letters*, vol. 20, no. 6, pp. 289–291, 1999.
- [36] A. Brown, A. Pomp, D. M. de Leeuw, D. Klaassen, E. Havinga, P. Herwig, and K. Müllen, “Precursor route pentacene metal-insulator-semiconductor field-effect transistors,” *Journal of Applied Physics*, vol. 79, no. 4, pp. 2136–2138, 1996.
- [37] D. Jariwala, S. L. Howell, K.-S. Chen, J. Kang, V. K. Sangwan, S. A. Filippone, R. Turrisi, T. J. Marks, L. J. Lauhon, and M. C. Hersam, “Hybrid, gate-tunable, van der Waals p–n heterojunctions from pentacene and MoS₂,” *Nano Letters*, vol. 16, no. 1, pp. 497–503, 2016.
- [38] H. Im and S. Kim, “Effectively enhanced broadband phototransistors based on multilayer WSe₂/pentacene,” *Advanced Electronic Materials*, vol. 7, no. 5, p. 2100003, 2021.

- [39] T. Zhu, L. Yuan, Y. Zhao, M. Zhou, Y. Wan, J. Mei, and L. Huang, “Highly mobile charge-transfer excitons in two-dimensional WS₂/tetracene heterostructures,” *Science Advances*, vol. 4, no. 1, p. eaao3104, 2018.
- [40] J.-W. Qiao, M.-S. Niu, Z.-C. Wen, X.-K. Yang, Z.-H. Chen, Y.-X. Wang, L. Feng, W. Qin, and X.-T. Hao, “Efficient photoluminescence enhancement and tunable photocarrier transfer in vertical 2D organic–inorganic heterostructure by energy funneling,” *2D Materials*, vol. 8, no. 2, p. 025026, 2021.
- [41] M. R. Habib, W. Wang, A. Khan, Y. Khan, S. M. Obaidulla, X. Pi, and M. Xu, “Theoretical study of interfacial and electronic properties of transition metal dichalcogenides and organic molecules based van der Waals heterostructures,” *Advanced Theory and Simulations*, vol. 3, no. 6, p. 2000045, 2020.
- [42] P. A. Markeev, E. Najafidehaghani, G. F. Samu, K. Sarosi, S. B. Kalkan, Z. Gan, A. George, V. Reisner, K. Mogyorosi, V. Chikan, *et al.*, “Exciton dynamics in MoS₂-pentacene and WSe₂-pentacene heterojunctions,” *ACS Nano*, vol. 16, no. 10, pp. 16668–16676, 2022.
- [43] J. P. Perdew, K. Burke, and M. Ernzerhof, “Generalized gradient approximation made simple,” *Physical Review Letters*, vol. 77, no. 18, p. 3865, 1996.
- [44] P. E. Blöchl, “Projector augmented-wave method,” *Physical Review B*, vol. 50, no. 24, p. 17953, 1994.
- [45] H. J. Monkhorst and J. D. Pack, “Special points for Brillouin-zone integrations,” *Physical Review B*, vol. 13, no. 12, p. 5188, 1976.
- [46] P. Giannozzi, S. Baroni, N. Bonini, M. Calandra, R. Car, C. Cavazzoni, D. Ceresoli, G. L. Chiarotti, M. Cococcioni, I. Dabo, *et al.*, “Quantum ESPRESSO: a modular and open-source software project for quantum simulations of materials,” *Journal of Physics: Condensed Matter*, vol. 21, no. 39, p. 395502, 2009.
- [47] P. Giannozzi, O. Andreussi, T. Brumme, O. Bunau, M. B. Nardelli, M. Calandra, R. Car, C. Cavazzoni, D. Ceresoli, M. Cococcioni, *et al.*, “Advanced capabilities for

- materials modelling with Quantum ESPRESSO,” *Journal of Physics: Condensed Matter*, vol. 29, no. 46, p. 465901, 2017.
- [48] P. Borlido, T. Aull, A. W. Huran, F. Tran, M. A. Marques, and S. Botti, “Large-scale benchmark of exchange–correlation functionals for the determination of electronic band gaps of solids,” *Journal of Chemical Theory and Computation*, vol. 15, no. 9, pp. 5069–5079, 2019.
- [49] M. Buhl, C. Reimann, D. A. Pantazis, T. Bredow, and F. Neese, “Geometries of third-row transition-metal complexes from density-functional theory,” *Journal of Chemical Theory and Computation*, vol. 4, no. 9, pp. 1449–1459, 2008.
- [50] J. Tao, L.-H. Ye, and Y. Duan, “Exchange-correlation energies of atoms from efficient density functionals: influence of the electron density,” *Journal of Physics B: Atomic, Molecular and Optical Physics*, vol. 50, no. 24, p. 245004, 2017.
- [51] S. Grimme, “Semiempirical GGA-type density functional constructed with a long-range dispersion correction,” *Journal of Computational Chemistry*, vol. 27, no. 15, pp. 1787–1799, 2006.
- [52] M. Kim, W. J. Kim, E. K. Lee, S. Lebegue, and H. Kim, “Recent development of atom-pairwise van der Waals corrections for density functional theory: From molecules to solids,” *International Journal of Quantum Chemistry*, vol. 116, no. 8, pp. 598–607, 2016.
- [53] J. Heyd, G. E. Scuseria, and M. Ernzerhof, “Hybrid functionals based on a screened Coulomb potential,” *The Journal of Chemical Physics*, vol. 118, no. 18, pp. 8207–8215, 2003. *Erratum*. [93].
- [54] Y.-i. Matsushita, K. Nakamura, and A. Oshiyama, “Comparative study of hybrid functionals applied to structural and electronic properties of semiconductors and insulators,” *Physical Review B*, vol. 84, no. 7, p. 075205, 2011.

- [55] P. Drude, “Zur Elektronentheorie der Metalle; II. Teil. Galvanomagnetische und thermomagnetische Effecte,” *Annalen der Physik*, vol. 308, no. 11, pp. 369–402, 1900.
- [56] J. J. Thomson, “XL. cathode rays,” *The London, Edinburgh, and Dublin Philosophical Magazine and Journal of Science*, vol. 44, no. 269, pp. 293–316, 1897.
- [57] A. Sommerfeld, “Zur Elektronentheorie der Metalle,” *Naturwissenschaften*, vol. 15, no. 41, pp. 825–832, 1927.
- [58] W. Heisenberg, “Über den anschaulichen Inhalt der quantentheoretischen Kinematik und Mechanik,” *Zeitschrift für Physik*, vol. 43, no. 3-4, pp. 172–198, 1927.
- [59] F. Bloch, “Über die Quantenmechanik der Elektronen in Kristallgittern,” *Zeitschrift für Physik*, vol. 52, no. 7-8, pp. 555–600, 1929.
- [60] J. Liouville, “Note sur la théorie de la variation des constantes arbitraires,” *Journal de Mathématiques Pures et Appliquées*, vol. 3, pp. 342–349, 1838.
- [61] J. W. Gibbs, “On the fundamental formula of statistical mechanics, with applications to astronomy and thermodynamics,” in *Proceedings of the American Association for the Advancement of Science*, pp. 57–58, 1884.
- [62] D. D. Scherer and B. M. Andersen, “Spin-orbit coupling and magnetic anisotropy in iron-based superconductors,” *Physical Review Letters*, vol. 121, no. 3, p. 037205, 2018.
- [63] H. Jansen, “Magnetic anisotropy in density-functional theory,” *Physical Review B*, vol. 59, no. 7, p. 4699, 1999.
- [64] K. Premasiri and X. P. Gao, “Tuning spin-orbit coupling in 2D materials for spintronics: a topical review,” *Journal of Physics: Condensed Matter*, vol. 31, no. 19, p. 193001, 2019.

- [65] S. Grimme, J. Antony, S. Ehrlich, and H. Krieg, “A consistent and accurate ab initio parametrization of density functional dispersion correction (DFT-D) for the 94 elements H-Pu,” *The Journal of Chemical Physics*, vol. 132, no. 15, 2010.
- [66] F. London, “Zur Theorie und Systematik der Molekularkräfte,” *Zeitschrift für Physik*, vol. 63, no. 3, pp. 245–279, 1930.
- [67] F. London, “The general theory of molecular forces,” *Transactions of the Faraday Society*, vol. 33, pp. 8b–26, 1937.
- [68] P. Hohenberg and W. Kohn, “Inhomogeneous electron gas,” *Physical Review*, vol. 136, no. 3B, p. B864, 1964.
- [69] W. Kohn and L. J. Sham, “Self-consistent equations including exchange and correlation effects,” *Physical Review*, vol. 140, no. 4A, p. A1133, 1965.
- [70] J. Harris, “Simplified method for calculating the energy of weakly interacting fragments,” *Physical Review B*, vol. 31, no. 4, p. 1770, 1985.
- [71] M. Weinert, R. Watson, and J. Davenport, “Total-energy differences and eigenvalue sums,” *Physical Review B*, vol. 32, no. 4, p. 2115, 1985.
- [72] W. M. C. Foulkes and R. Haydock, “Tight-binding models and density-functional theory,” *Physical Review B*, vol. 39, no. 17, p. 12520, 1989.
- [73] C. G. Broyden, “A class of methods for solving nonlinear simultaneous equations,” *Mathematics of Computation*, vol. 19, no. 92, pp. 577–593, 1965.
- [74] D. D. Johnson, “Modified Broyden’s method for accelerating convergence in self-consistent calculations,” *Physical Review B*, vol. 38, no. 18, p. 12807, 1988.
- [75] D. Vanderbilt and S. G. Louie, “Total energies of diamond (111) surface reconstructions by a linear combination of atomic orbitals method,” *Physical Review B*, vol. 30, no. 10, p. 6118, 1984.

- [76] J. P. Perdew, K. Burke, and Y. Wang, “Generalized gradient approximation for the exchange-correlation hole of a many-electron system,” *Physical Review B*, vol. 54, no. 23, p. 16533, 1996.
- [77] M. Gell-Mann and K. A. Brueckner, “Correlation energy of an electron gas at high density,” *Physical Review*, vol. 106, no. 2, p. 364, 1957.
- [78] C. Bowen, G. Sugiyama, and B. J. Alder, “Static dielectric response of the electron gas,” *Physical Review B*, vol. 50, pp. 14838–14848, 1994.
- [79] E. H. Lieb and S. Oxford, “Improved lower bound on the indirect Coulomb energy,” *International Journal of Quantum Chemistry*, vol. 19, no. 3, pp. 427–439, 1981.
- [80] E. H. Lieb, “A lower bound for Coulomb energies,” *Physics Letters A*, vol. 70, no. 5-6, pp. 444–446, 1979.
- [81] G. K.-L. Chan and N. C. Handy, “Optimized Lieb-Oxford bound for the exchange-correlation energy,” *Physical Review A*, vol. 59, no. 4, p. 3075, 1999.
- [82] M. Lewin, E. H. Lieb, and R. Seiringer, “Improved Lieb–Oxford bound on the indirect and exchange energies,” *Letters in Mathematical Physics*, vol. 112, no. 5, p. 92, 2022.
- [83] J.-D. Chai and M. Head-Gordon, “Long-range corrected hybrid density functionals with damped atom–atom dispersion corrections,” *Physical Chemistry Chemical Physics*, vol. 10, no. 44, pp. 6615–6620, 2008.
- [84] B. Axilrod and E. Teller, “Interaction of the van der Waals type between three atoms,” *The Journal of Chemical Physics*, vol. 11, no. 6, pp. 299–300, 1943.
- [85] C. Lee, W. Yang, and R. G. Parr, “Development of the Colle-Salvetti correlation-energy formula into a functional of the electron density,” *Physical Review B*, vol. 37, no. 2, p. 785, 1988.
- [86] A. D. Becke, “Density-functional exchange-energy approximation with correct asymptotic behavior,” *Physical Review A*, vol. 38, no. 6, p. 3098, 1988.

- [87] C. Herring, “A new method for calculating wave functions in crystals,” *Physical Review*, vol. 57, no. 12, p. 1169, 1940.
- [88] D. Hamann, M. Schlüter, and C. Chiang, “Norm-conserving pseudopotentials,” *Physical Review Letters*, vol. 43, no. 20, p. 1494, 1979.
- [89] M. Frigo and S. G. Johnson, “FFTW: An adaptive software architecture for the FFT,” in *Proceedings of the 1998 IEEE International Conference on Acoustics, Speech and Signal Processing, ICASSP’98 (Cat. No. 98CH36181)*, vol. 3, pp. 1381–1384, IEEE, 1998.
- [90] J. W. Cooley and J. W. Tukey, “An algorithm for the machine calculation of complex Fourier series,” *Mathematics of Computation*, vol. 19, no. 90, pp. 297–301, 1965.
- [91] G. Pizzi, V. Vitale, R. Arita, S. Blügel, F. Freimuth, G. Géranton, M. Gibertini, D. Gresch, C. Johnson, T. Koretsune, *et al.*, “Wannier90 as a community code: new features and applications,” *Journal of Physics: Condensed Matter*, vol. 32, p. 165902, jan 2020.
- [92] P. E. Blöchl, O. Jepsen, and O. K. Andersen, “Improved tetrahedron method for Brillouin-zone integrations,” *Physical Review B*, vol. 49, no. 23, p. 16223, 1994.
- [93] J. Heyd, G. E. Scuseria, and M. Ernzerhof, “Erratum: “Hybrid functionals based on a screened Coulomb potential” [J. Chem. Phys. 118, 8207 (2003)],” *The Journal of Chemical Physics*, vol. 124, no. 21, p. 219906, 2006.
- [94] M. Dion, H. Rydberg, E. Schröder, D. C. Langreth, and B. I. Lundqvist, “Van der waals density functional for general geometries,” *Physical review letters*, vol. 92, no. 24, p. 246401, 2004.
- [95] O. K. Le, V. Chihaiia, M.-P. Pham-Ho, and D. N. Son, “Electronic and optical properties of monolayer MoS₂ under the influence of polyethyleneimine adsorption and pressure,” *RSC Advances*, vol. 10, no. 8, pp. 4201–4210, 2020.

- [96] M. Kan, J. Wang, X. Li, S. Zhang, Y. Li, Y. Kawazoe, Q. Sun, and P. Jena, “Structures and phase transition of a MoS₂ monolayer,” *The Journal of Physical Chemistry C*, vol. 118, no. 3, pp. 1515–1522, 2014.
- [97] C. Ataca, H. Sahin, E. Akturk, and S. Ciraci, “Mechanical and electronic properties of MoS₂ nanoribbons and their defects,” *The Journal of Physical Chemistry C*, vol. 115, no. 10, pp. 3934–3941, 2011.
- [98] Y. Li, Z. Zhou, S. Zhang, and Z. Chen, “MoS₂ nanoribbons: high stability and unusual electronic and magnetic properties,” *Journal of the American Chemical Society*, vol. 130, no. 49, pp. 16739–16744, 2008.
- [99] H. E. Swanson, *Standard X-ray diffraction powder patterns*, vol. 5. US Department of Commerce, National Bureau of Standards, 1955.
- [100] K. T. Park, M. Richards-Babb, M. Freund, J. Weiss, and K. Klier, “Surface structure of single-crystal MoS₂ (0002) and Cs/MoS₂ (0002) by X-ray photoelectron diffraction,” *The Journal of Physical Chemistry*, vol. 100, no. 25, pp. 10739–10745, 1996.
- [101] R. Gordon, D. Yang, E. Crozier, D. Jiang, and R. Frindt, “Structures of exfoliated single layers of WS₂, MoS₂, and MoSe₂ in aqueous suspension,” *Physical Review B*, vol. 65, no. 12, p. 125407, 2002.
- [102] J. A. Wilson and A. Yoffe, “The transition metal dichalcogenides discussion and interpretation of the observed optical, electrical and structural properties,” *Advances in Physics*, vol. 18, no. 73, pp. 193–335, 1969.
- [103] V. Nagarajan and R. Chandiramouli, “MoSe₂ nanosheets for detection of methanol and ethanol vapors: a DFT study,” *Journal of Molecular Graphics and Modelling*, vol. 81, pp. 97–105, 2018.
- [104] C.-H. Chang, X. Fan, S.-H. Lin, and J.-L. Kuo, “Orbital analysis of electronic structure and phonon dispersion in MoS₂, MoSe₂, WS₂, and WSe₂ monolayers under strain,” *Physical Review B*, vol. 88, no. 19, p. 195420, 2013.

- [105] G. Wang, I. C. Gerber, L. Bouet, D. Lagarde, A. Balocchi, M. Vidal, T. Amand, X. Marie, and B. Urbaszek, “Exciton states in monolayer MoSe₂: impact on interband transitions,” *2D Materials*, vol. 2, no. 4, p. 045005, 2015.
- [106] A. Jäger-Waldau, M. Lux-Steiner, R. Jäger-Waldau, R. Burkhardt, and E. Bucher, “Composition and morphology of MoSe₂ thin films,” *Thin Solid Films*, vol. 189, no. 2, pp. 339–345, 1990.
- [107] D. Muoi, N. N. Hieu, H. T. Phung, H. V. Phuc, B. Amin, B. D. Hoi, N. V. Hieu, L. C. Nhan, C. V. Nguyen, and P. Le, “Electronic properties of WS₂ and WSe₂ monolayers with biaxial strain: a first-principles study,” *Chemical Physics*, vol. 519, pp. 69–73, 2019.
- [108] V. Q. Bui, T.-T. Pham, D. A. Le, C. M. Thi, and H. M. Le, “A first-principles investigation of various gas (CO, H₂O, NO, and O₂) absorptions on a WS₂ monolayer: stability and electronic properties,” *Journal of Physics: Condensed Matter*, vol. 27, no. 30, p. 305005, 2015.
- [109] H. E. Swanson, *Standard X-ray diffraction powder patterns*, vol. 9. US Department of Commerce, National Bureau of Standards, 1960.
- [110] D. Le, A. Barinov, E. Preciado, M. Isarraraz, I. Tanabe, T. Komesu, C. Troha, L. Bartels, T. S. Rahman, and P. A. Dowben, “Spin-orbit coupling in the band structure of monolayer WSe₂,” *Journal of Physics: Condensed Matter*, vol. 27, no. 18, p. 182201, 2015.
- [111] L. H. Brixner, “Preparation and properties of the single crystalline AB₂-type selenides and tellurides of niobium, tantalum, molybdenum and tungsten,” *Journal of Inorganic and Nuclear Chemistry*, vol. 24, no. 3, pp. 257–263, 1962.
- [112] S. Mathew, A. R. Abraham, S. Chintalapati, S. Sarkar, B. Joseph, and T. Venkatesan, “Temperature dependent structural evolution of WSe₂: A synchrotron X-ray diffraction study,” *Condensed Matter*, vol. 5, no. 4, p. 76, 2020.

- [113] N. T. Nguyen, P. A. Berseth, Q. Lin, C. Chiritescu, D. G. Cahill, A. Mavrokefalos, L. Shi, P. Zschack, M. D. Anderson, I. M. Anderson, *et al.*, “Synthesis and properties of turbostratically disordered, ultrathin WSe₂ films,” *Chemistry of Materials*, vol. 22, no. 9, pp. 2750–2756, 2010.
- [114] R. Campbell, J. M. Robertson, and J. Trotter, “The crystal and molecular structure of pentacene,” *Acta Crystallographica*, vol. 14, no. 7, pp. 705–711, 1961.
- [115] R. Endres, C. Fong, L. Yang, G. Witte, and C. Wöll, “Structural and electronic properties of pentacene molecule and molecular pentacene solid,” *Computational Materials Science*, vol. 29, no. 3, pp. 362–370, 2004.
- [116] E. S. Kadantsev and P. Hawrylak, “Electronic structure of a single MoS₂ monolayer,” *Solid State Communications*, vol. 152, no. 10, pp. 909–913, 2012.
- [117] W. S. Yun, S. Han, S. C. Hong, I. G. Kim, and J. Lee, “Thickness and strain effects on electronic structures of transition metal dichalcogenides: 2H-MX₂ semiconductors (M= Mo, W; X= S, Se, Te),” *Physical Review B*, vol. 85, no. 3, p. 033305, 2012.
- [118] D. S. Koda, F. Bechstedt, M. Marques, and L. K. Teles, “Tuning electronic properties and band alignments of phosphorene combined with MoSe₂ and WSe₂,” *The Journal of Physical Chemistry C*, vol. 121, no. 7, pp. 3862–3869, 2017.
- [119] S. Horzum, H. Sahin, S. Cahangirov, P. Cudazzo, A. Rubio, T. Serin, and F. Peeters, “Phonon softening and direct to indirect band gap crossover in strained single-layer MoSe₂,” *Physical Review B*, vol. 87, no. 12, p. 125415, 2013.
- [120] A. J. Bradley, M. M. Ugeda, F. H. da Jornada, D. Y. Qiu, W. Ruan, Y. Zhang, S. Wickenburg, A. Riss, J. Lu, S.-K. Mo, *et al.*, “Probing the role of interlayer coupling and Coulomb interactions on electronic structure in few-layer MoSe₂ nanostructures,” *Nano Letters*, vol. 15, no. 4, pp. 2594–2599, 2015.
- [121] A. Klein, S. Tiefenbacher, V. Eyert, C. Pettenkofer, and W. Jaegermann, “Electronic band structure of single-crystal and single-layer WS₂: Influence of interlayer van der Waals interactions,” *Physical Review B*, vol. 64, no. 20, p. 205416, 2001.

- [122] Q. H. Tran, T. N. Tran, T. T. Luong, V. T. Ngo, V. B. T. Phung, and V. A. Dinh, “Band valley flattening and exciton appearance/disappearance under isotropic strain in monolayer WS₂,” *The European Physical Journal Plus*, vol. 137, no. 12, p. 1317, 2022.
- [123] C. Ballif, M. Regula, P. Schmid, M. Remškar, R. Sanjines, and F. Lévy, “Preparation and characterization of highly oriented, photoconducting WS₂ thin films,” *Applied Physics A*, vol. 62, pp. 543–546, 1996.
- [124] D. Voß, P. Krüger, A. Mazur, and J. Pollmann, “Atomic and electronic structure of WSe₂ from ab initio theory: Bulk crystal and thin film systems,” *Physical Review B*, vol. 60, no. 20, p. 14311, 1999.
- [125] S. Sharifzadeh, A. Biller, L. Kronik, and J. B. Neaton, “Quasiparticle and optical spectroscopy of the organic semiconductors pentacene and PTCDA from first principles,” *Physical Review B—Condensed Matter and Materials Physics*, vol. 85, no. 12, p. 125307, 2012.
- [126] J. Lee, S. Kim, K. Kim, J. H. Kim, and S. Im, “Correlation between photoelectric and optical absorption spectra of thermally evaporated pentacene films,” *Applied Physics Letters*, vol. 84, no. 10, pp. 1701–1703, 2004.
- [127] J. Lee, D. Hwang, C. Park, S. Kim, and S. Im, “Pentacene-based photodiode with Schottky junction,” *Thin Solid Films*, vol. 451, pp. 12–15, 2004.
- [128] K. Kim, Y. Yoon, M.-O. Mun, S. Park, S. Kim, S. Im, and J. Kim, “Optical properties of solid pentacene,” *Journal of Superconductivity*, vol. 15, pp. 595–598, 2002.
- [129] S. Ahmad and S. Mukherjee, “A comparative study of electronic properties of bulk MoS₂ and its monolayer using DFT technique: application of mechanical strain on MoS₂ monolayer,” *Graphene*, vol. 3, no. 04, p. 52, 2014.
- [130] Z. Wu, S. Xu, H. Lu, A. Khamoshi, G.-B. Liu, T. Han, Y. Wu, J. Lin, G. Long, Y. He, *et al.*, “Even–odd layer-dependent magnetotransport of high-mobility Q-

- valley electrons in transition metal disulfides,” *Nature Communications*, vol. 7, no. 1, p. 12955, 2016.
- [131] D. W. Latzke, W. Zhang, A. Suslu, T.-R. Chang, H. Lin, H.-T. Jeng, S. Tongay, J. Wu, A. Bansil, and A. Lanzara, “Electronic structure, spin-orbit coupling, and interlayer interaction in bulk MoS₂ and WS₂,” *Physical Review B*, vol. 91, no. 23, p. 235202, 2015.
- [132] Y. Zhang, T.-R. Chang, B. Zhou, Y.-T. Cui, H. Yan, Z. Liu, F. Schmitt, J. Lee, R. Moore, Y. Chen, *et al.*, “Direct observation of the transition from indirect to direct bandgap in atomically thin epitaxial MoSe₂,” *Nature Nanotechnology*, vol. 9, no. 2, pp. 111–115, 2014.
- [133] Z. Y. Zhu, Y. C. Cheng, and U. Schwingenschlögl, “Giant spin-orbit-induced spin splitting in two-dimensional transition-metal dichalcogenide semiconductors,” *Physical Review B*, vol. 84, no. 15, p. 153402, 2011.
- [134] M. A. U. Absor, H. Kotaka, F. Ishii, and M. Saito, “Strain-controlled spin splitting in the conduction band of monolayer WS₂,” *Physical Review B*, vol. 94, no. 11, p. 115131, 2016.
- [135] H. Sahin, S. Tongay, S. Horzum, W. Fan, J. Zhou, J. Li, J. Wu, and F. Peeters, “Anomalous Raman spectra and thickness-dependent electronic properties of WSe₂,” *Physical Review B*, vol. 87, no. 16, p. 165409, 2013.
- [136] A. Ramasubramaniam, “Large excitonic effects in monolayers of molybdenum and tungsten dichalcogenides,” *Physical Review B*, vol. 86, no. 11, p. 115409, 2012.
- [137] W.-T. Hsu, L.-S. Lu, D. Wang, J.-K. Huang, M.-Y. Li, T.-R. Chang, Y.-C. Chou, Z.-Y. Juang, H.-T. Jeng, L.-J. Li, *et al.*, “Evidence of indirect gap in monolayer WSe₂,” *Nature Communications*, vol. 8, no. 1, p. 929, 2017.
- [138] C. Zhang, Y. Chen, A. Johnson, M.-Y. Li, L.-J. Li, P. C. Mende, R. M. Feenstra, and C.-K. Shih, “Probing critical point energies of transition metal dichalcogenides:

- surprising indirect gap of single layer WSe₂,” *Nano Letters*, vol. 15, no. 10, pp. 6494–6500, 2015.
- [139] H. Liu, J. Chen, H. Yu, F. Yang, L. Jiao, G.-B. Liu, W. Ho, C. Gao, J. Jia, W. Yao, *et al.*, “Observation of intervalley quantum interference in epitaxial monolayer tungsten diselenide,” *Nature Communications*, vol. 6, no. 1, p. 8180, 2015.
- [140] E. Black, P. Kratzer, and J. M. Morbec, “Interaction between pentacene molecules and monolayer transition metal dichalcogenides,” *Physical Chemistry Chemical Physics*, vol. 25, no. 43, pp. 29444–29450, 2023.
- [141] S. R. Kachel, P.-M. Dombrowski, T. Breuer, J. M. Gottfried, and G. Witte, “Engineering of TMDC–OSC hybrid interfaces: the thermodynamics of unitary and mixed acene monolayers on MoS₂,” *Chemical Science*, vol. 12, no. 7, pp. 2575–2585, 2021.
- [142] N. Shen and G. Tao, “Charge transfer and interface engineering of the pentacene and MoS₂ monolayer complex,” *Advanced Materials Interfaces*, vol. 4, no. 6, p. 1601083, 2017.
- [143] S. S. Batsanov, “Van der Waals radii of elements,” *Inorganic Materials*, vol. 37, no. 9, pp. 871–885, 2001.
- [144] J. Krumland and C. Cocchi, “Conditions for electronic hybridization between transition-metal dichalcogenide monolayers and physisorbed carbon-conjugated molecules,” *Electronic Structure*, vol. 3, no. 4, p. 044003, 2021.
- [145] Q. Guan, H. Yan, and Y. Cai, “Flatten the Li-ion activation in perfectly lattice-matched MXene and 1T-MoS₂ heterostructures via chemical functionalization,” *Advanced Materials Interfaces*, vol. 9, no. 7, p. 2101838, 2022.
- [146] E. Black and J. M. Morbec, “Effect of molecular rotation and concentration on the adsorption of pentacene molecules on two-dimensional monolayer transition metal dichalcogenides,” *Electronic Structure*, vol. 6, no. 2, p. 025008, 2024.

- [147] F. Tumino, A. Rabia, A. L. Bassi, S. Tosoni, and C. S. Casari, “Interface-driven assembly of pentacene/MoS₂ lateral heterostructures,” *The Journal of Physical Chemistry C*, vol. 126, no. 2, pp. 1132–1139, 2022.
- [148] D. Holmes, S. Kumaraswamy, A. J. Matzger, and K. P. C. Vollhardt, “On the nature of nonplanarity in the [N] phenylenes,” *Chemistry—A European Journal*, vol. 5, no. 11, pp. 3399–3412, 1999.
- [149] Y. Sakamoto, T. Suzuki, M. Kobayashi, Y. Gao, Y. Fukai, Y. Inoue, F. Sato, and S. Tokito, “Perfluoropentacene: high-performance p-n junctions and complementary circuits with pentacene,” *Journal of the American Chemical Society*, vol. 126, no. 26, pp. 8138–8140, 2004.
- [150] I. G. Lezama, A. Ubaldini, M. Longobardi, E. Giannini, C. Renner, A. B. Kuzmenko, and A. F. Morpurgo, “Surface transport and band gap structure of exfoliated 2H-MoTe₂ crystals,” *2D Materials*, vol. 1, no. 2, p. 021002, 2014.
- [151] J. P. Perdew, R. G. Parr, M. Levy, and J. L. Balduz Jr, “Density-functional theory for fractional particle number: Derivative discontinuities of the energy,” *Physical Review Letters*, vol. 49, no. 23, p. 1691, 1982.